UNIVERSITY OF SOUTHAMPTON

# Nanostructured Polymers: Morphology and Properties

by

Gabriele Gherbaz

A thesis submitted for the

degree of Doctor of Philosophy

in the

Faculty of Engineering, Science and Mathematics

School of Electronics and Computer Science

March 2009

UNIVERSITY OF SOUTHAMPTON

ABSTRACT

FACULTY OF ENGINEERING, SCIENCE AND MATHEMATICS

SCHOOL OF ELECTRONICS AND COMPUTER SCIENCE

Doctor of Philosophy

by Gabriele Gherbaz

This study is aimed to investigate the relationship between morphology and properties of non polar polymers in the presence of polar additives of different nature. The addition of the physical gel dibenzylidene sorbitol (DBS) in a polyethylene (PE) blend has shown to act as a nucleation site on the polymer. Electron microscopy was used to reveal the fibrillar network formed by the DBS and its interaction with the PE. Moreover, the nucleation density in each material was obtained as a function of the crystallization temperature, which showed an increase in the number of nuclei in the clarified system compared to the unclarified one. However, this was found to be temperature dependent. The nucleation of PE on DBS was also studied through the induction time, which revealed a reduced surface energy of the polymer nucleus in the presence of the DBS. Space charge measurements were taken to investigate the charge transport in PE/DBS blends and the space charge at low concentration of the gelator was found to improve the space charge distribution. The same polyethylene blend has then been studied also upon addition of relatively polar ethylene/ vinyl acetate copolymers (EVA), with a VA content varying from 9 % to 40 %. Morphology studies showed that three main factors control the phase separation, namely the the time the blend is kept in the melt, the PE:EVA ratio and also the EVA molecular weight. However, breakdown testing demonstrated that the polarity of EVA decreased the breakdown strength of the blends, independently on the morphology. Finally, a preliminary study was conducted with

EVA based nanocomposites to determine the effect of filler on the dielectric properties of the nanocomposite. Two relatively polar copolymers, EVA9 and EVA18, were processed by solution blending together with 5 % of o-MMT ( I30P and I44PA), and the time of solution blending was varied from 10 min to 100 min. X-ray scattering data showed intercalation in the case of EVA9 based nanocomposites and potential exfoliation for EVA18 based nanocomposites. However, X-ray results suggest that the solution blending could extract a fraction of the organo-modified ions from in between the MMT galleries, leading to shrinkage of the clay spacing. The nanocomposite was also analysed from the point of view of its breakdown properties, which were shown to be unaffected by the presence of fillers.

# Contents

# List of Figures

# List of Tables

# Author's Declaration

I, Gabriele Gherbaz, declare that the thesis entitled **Nanostructured Polymers: Morphology and Properties** and the work presented in the thesis are both my own, and have been generated by me as the result of my own original research. I confirm that:

- this work was done wholly or mainly while in candidature for a research degree at this University;
- where any part of this thesis has previously been submitted for a degree or any other qualification at this University or any other institution, this has been clearly stated;
- where I have consulted the published work of others, this is always clear attributed;
- where I have quoted from the work of others, the source is always given. With the exception of such quotations, this thesis is entirely my own work;
- I have acknowledged all main sources of help;
- where the thesis is based on work done by myself jointly with others, I have made clear exactly what was done by others and what I have contributed myself;
- parts of this work have been published as:

  1. A.S. Vaughan, G. Gherbaz, S.G. Swingler and N. Abd Rashid, *IEEE Conference CEIDP 2006, Kansas City*:161-164, 2006.

  2. G. Gherbaz and A.S. Vaughan , *IEEE Conference ICSD 2007, Winchester*:526-529, 2007.

  3. G. Gherbaz, G. Chen and A.S. Vaughan, *IEEE conference CEIDP 2008, Quebec City*:161-164, 2008.

Signed: _ _ _ _ _ _ _ _ _ _ Date: _ _ _ _ _ _ _ _ _ _

# Acknowledgements

I would like to thank my supervisor, Professor Alun S. Vaughan, for all the support, the discussions, the enthusiasm and the help given to me during my PhD. I would also like to thank all the people that I met within the EPE and HV group. In particular, I like to thank Ian Hosier and Chris Green for the interesting discussions that we had in the past years.

A big thank goes to my parents that supported me not just during my PhD, but during all my life. If I reached this target, it is thanks to them and my brothers. I would like to thank my closest friends who enrich my life every day. Thanks Andy for everything you have done: support, proof reading and general help. Thanks to Giovanna, Filippo and Giulia for their friendship and constant contact from all over the world.

*To my parents*

# Chapter 1

# Introduction

## 1.1 Polymers and Structure

A polymer consists of a large number of repeated units, connected together to give a macromolecule. The most fundamental and widespread example of a natural polymer is DNA, whilst polyethylene is an example of a synthetic polymer. Polyethylene was discovered fortuitously, as a direct side effect of producing ammonia under high pressure in the early 1930's [1]. Later in the 1950's, Ziegler and Natta produced the first polyolefin using an organometallic catalyst, which allowed the production of this polymer under more feasible conditions, i.e. atmospheric pressure and room temperature [2, 3, 4, 5]. Polyethylene derives from the ethylene monomer, which is also used for the production of other polymers when combined with chlorine and styrene.

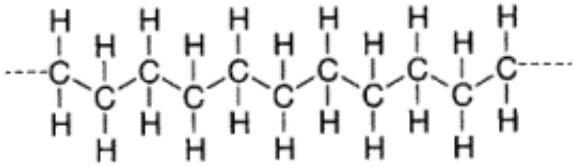

FIGURE 1.1: The basic structure of bonding patterns of polyethylene atoms showing Carbon (C) and hydrogen (H): From [6].

A few years after, another fundamental step was achieved in polymer science; Keller successfully grew single crystals of polyethylene [7]. Polyethylene is known to consist of a chain of carbon and hydrogen atoms held together by covalent bonding, as shown in Figure 1.1. The H-C-C bond angle is 112°, the C-C-C bond angle is 107° with a bond length of 0.15 nm, while the H-C-H bond length is 0.11 nm [6, 8, 9]. The chains are attracted to each other by van der Waals forces. These latter forces determine most of the physical properties, such as crystallisation, melting, flow and deformation. Single macromolecules can exist as linear or branched chains, and these chains can also form a three dimensional network.

Polymeric chains composed of the same repeated unit are termed homopolymers, whereas polymers formed by different types of monomer are termed copolymers. The simplest copolymer is composed by two different repeating units, A and B. However, the sequence can differ from:

- random copolymer, when A and B are positioned randomly (A-A-A-B-A-B)
- alternating copolymer, when A and B are positioned alternately (A-B-A-B-A-B)
- block copolymer, when long sequences of each monomer are present in a chain (A-A-A-B-B-B)
- graft polymer, when a homopolymer chain is branched to another different polymer

### 1.1.1 Polymer Crystal

Polyethylene is able to crystallise when it is cooled down from the melt, but not completely; therefore, it is called a semi-crystalline polymer. In fact, once

crystallised, the polymer contains a mixture of crystalline and amorphous regions [6]. In the solid state the molecules adopt a zig-zag structure, in which the carbon atoms arrange into an all-trans conformation within the crystal. The unit cell for polyethylene is orthorombic with dimensions a = 0.736 nm, b = 0.492 nm and c = 0.254 nm (Figure 1.2) [6]. However, polyethylene can also form monoclinic or hexagonal unit cells under different conditions. Hexagonal structures derive from crystallisation under high pressure, whilst monoclinic cells are observed upon crystallisation under deformation [10].

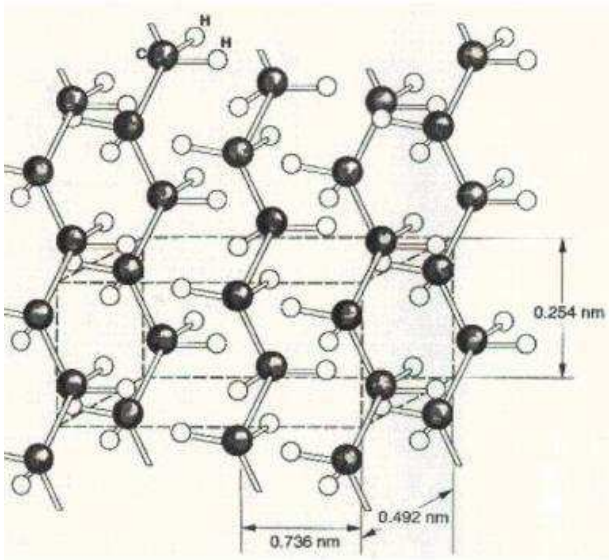


FIGURE 1.2: Unit cell of PE repeated in xyz; from [6].

The initial stages of polymer crystallisation involve the formation of thin platelets, commonly referred to as lamellae. These lamellae are of the order of 10 nm thick and $\sim 10\ \mu$m in the lateral extent [8]. Keller, Fisher and Till [7, 11, 12], in three independent works, deduced that these molecules must be folded many times within the crystal and described that the crystal can also twist (Figure 1.3). The space between the crystals, known as inter-lamellar regions, are not crystalline. The inter-lamellar regions may therefore be weak and contain tie molecules, defective species and impurities.

Three main models were proposed to account for lamellar folding. In a first model,

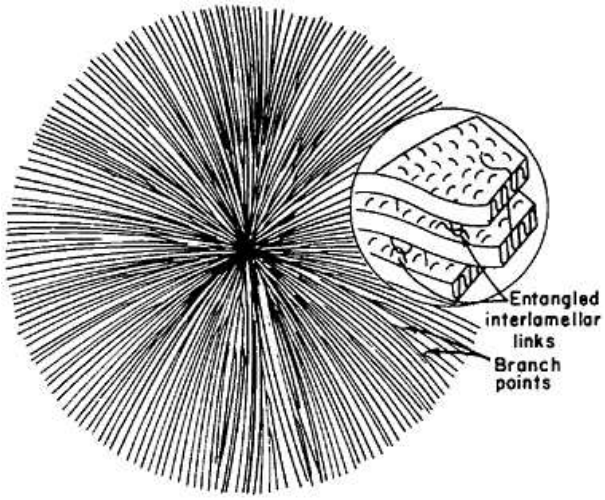


FIGURE 1.3: Diagram of polymer spherulite with chain-folded lamellae. From [10].

referred to as the switchboard model, Flory suggested a random folding of the chain on the same lamella and on other adjacent lamellae [13]. A second more idealised model is referred to as the smooth surface model, where the chain folded lamellar surfaces are smooth with just a few defects. A variation is represented by the rough surface model, where the length of chain folding can vary and multiple nucleation can occur [10]. These interpretations of chain folding contradict each other in several aspects; however, a detailed discussion of the origin of the chain folding is beyond the scope of this thesis.

Crystals develop into lamellae, which then act as nucleation sites for the formation of more lamellae. A screw dislocation process then drives the development of more complex objects, like spherulites [14, 15], as shown in Figure 1.3. During this latter stages of polymer crystallisation a spherulite can grow up to $50 - 500\mu m$ depending on the undercooling temperature [9, 7, 16]. Depending on the crystallisation temperature, a spherulite can grow until impinging upon neighbouring spherulites.

### 1.1.2 Thompson-Gibbs Equation and Chain-Folded Crystals

In order to describe the conditions under which polymer crystals can be formed, a thermodynamic model is necessary. The Thompson-Gibbs equation applies the principles of thermodynamics to the model of crystal lamellae as shown in Figure 1.4.

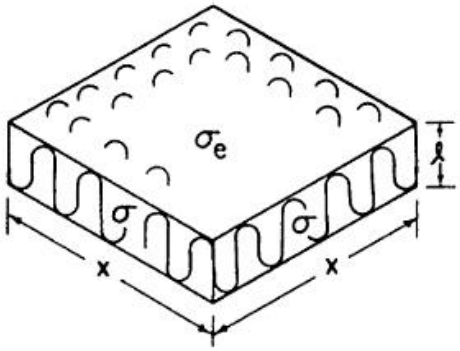


FIGURE 1.4: Thin Chain-folded crystal showing $\sigma$, $\sigma_e$ with dimensions $l$ and $x$. From [10].

The importance of this equation derives from the fact that it relates the melting point to the crystal thickness. Therefore, for a finite crystal lamella, the change in free energy upon melting, $\triangle G$, is equal to:

$$\triangle G = 4xl\sigma + 2x^2\sigma_e - x^2 l\left(\Delta G^*\right) \tag{1.1}$$

where $l$ is the dimension of the crystal, $x$ the largest dimension, $\sigma_e$ the folded surface free energy, $\sigma$ the lateral surface energy and $\Delta G^*$ is the free energy of fusion at the equilibrium melting point. Thus, $\Delta G^*$ is equal to:

$$\triangle G^* = \triangle H_{fus} - T\triangle S_{fus} = \triangle H_{fus}\left(\triangle T\right)/T_m^0 \tag{1.2}$$

where $\triangle H_{fus}$ and $\triangle S_{fus}$ are the enthalpy and entropy of fusion per unit volume of crystal, respectively. $T_m^0$ is the equilibrium melting point of a crystal with infinitive thickness $l$, and $\triangle T$ is the undercooling ( $T_m - T$ ). At the melting point, $\triangle G$ is equal to 0 and the dimension of $x$ is much larger than $l$ ( $x \gg l$), hence:

$$T_m = T_m^0 \left[1 - 2\sigma_e / \left(\triangle H_{fus}\right) l\right] \tag{1.3}$$

Plotting $T_m$ agaist $1/l$ yields the value of $T_m^0$ and $\sigma_e$. In the case of polyethylene, the value of $T_m^0$ is $\sim$ 142 °C and $\sigma_e$ is 0.93 $J/m^2$ ([17]).

### 1.1.3 Polymer Nucleation and Growth

Polymer nucleation can be divided into two processes, the primary and the secondary nucleation. In general, the formation of primary nuclei is followed by secondary nucleation of the polymer, which is described by Hoffman and Lauritzen theory. Stable nuclei can be formed only if the free energy barrier is overcome as shown in Figure 1.5.

In order to define the critical size of the nucleus, a differentiation of the free energy is necessary:

$$\frac{\triangle G}{dr} = 0 \tag{1.4}$$

where $r$ represents the size of the embryo. The maximum is defined as the activation energy barrier which has to be overcome in order to form a stable nucleus, which will form the first layer of nulcei. Afterwards, a second layer can nucleate and grow on the surface of the first layer, which will have a lower free enthalpy barrier, due to a smaller size of the surface area. Most nucleation and crystallisation theories are based on the secondary nucleation concept. Hoffman and Lauritzen were among the first to explain the growth rate of polymer crystals [10, 17, 18].

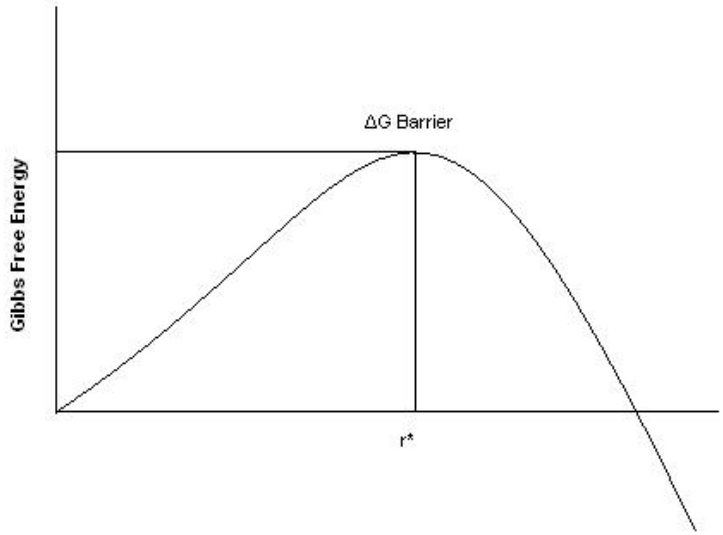


FIGURE 1.5: Schematic diagram of Gibbs Equation. Nuclei are unstable for r $< r^*$, where $r^*$ is the critical nuclei size.

Although other nucleation theories have also been proposed, such as the molecular nucleation model developed by Wunderlich [19] and rough surface growth model of Sadler and Gilmer [20], the Hoffman and Lauritzen (HL) theory is the most widely adopted.

The HL theory expresses the linear growth rate ($G$) of a secondary nucleus as a function of degree of supercooling ($\Delta T = T_m^0 - T_c$), where $ab$ is the cross-sectional area of the polymer chain, $a$ the width of the molecule, $b$ is the fixed thickness of the nucleus and $l$ is the height fixed at different undercooling which spreads laterally at the rate $g$. The surface nucleus grows up to the thickness $L$ and causes the crystal to grow in $G$ direction as illustrated in Figure 1.6. From this it has been shown that the growth rate, $G$, results in an equation of the following form:

$$G(T) = G_0 exp\left[-U^*/\left(R\left(T_c - T_\infty\right)\right)\right] exp\left[-K_g/\left(fT_c\Delta T\right)\right] \tag{1.5}$$

where $G_0$ is the pre exponential factor; $U^*$ is the activation energy to transport a

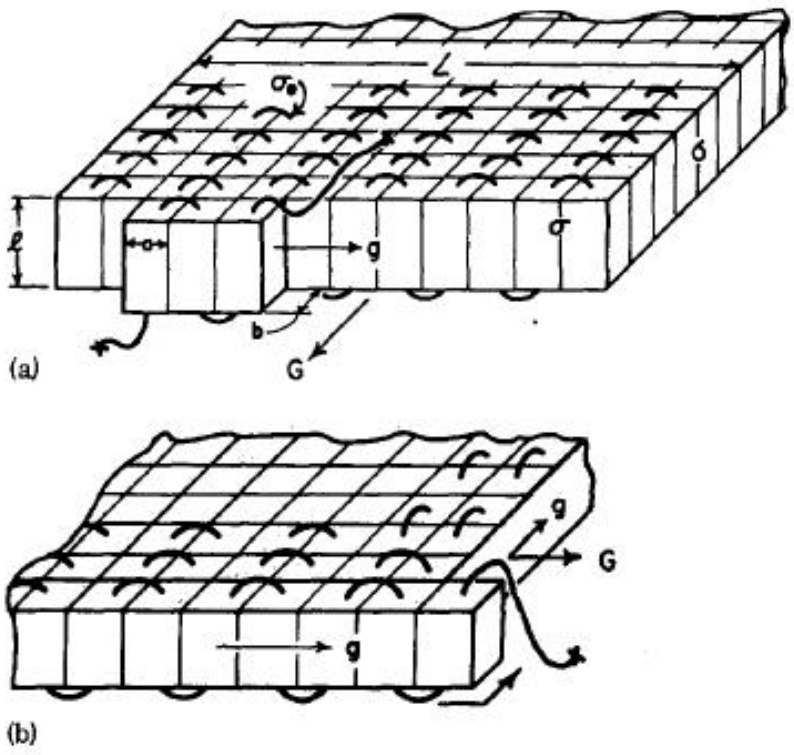


FIGURE 1.6: Model for crystal growth induced by chain-folded surface nucleus. (a)Model of surface nucleus growing in $g$ direction causing layer $b$ to grow in $G$ direction. (b) Surface nucleus growing a new layer. From [21].

polymeric segment across the liquid-crystal interface, which is taken as 1500 cal/-mol; $R$ is the gas constant and $T_\infty$ is the theoretical temperature which is assumed to be equal to $T_g = -30°C$ [22]. The term $f = 2T_c/(T_c + T_m^0)$ is a correction factor to account for the temperature dependence of the heat of crystallisation. $K_g$ accounts for the crystal growth, which can assume a three growth regime depending on the undercooling conditions. At high temperatures, the lateral growth rate is dominant with respect to the formation of new nuclei. This temperature range corresponds to the so-called regime I and $G$ can be written as follow:

$$G_I = b_0 i L \tag{1.6}$$

where $b_0$ is defined as the thickness of the layer, $i$ is the surface nucleation rate and $L$ the substrate length. At intermidiate rage of temperautures, the growth

rate is controlled by both $i$ and $g$ and it is termed regime II:

$$G_{II} = b_0(2iL)^{1/2} \tag{1.7}$$

At low temperatures, growth occurs through multiply nuclei, such that the growth rate is determined by the nucleation rate, as in the case of regime I (see eq. 1.6). Expressing $i$ and $g$, the overall growth rate $G$ can be found. In regime I and III, $K_g$ assumes the value of:

$$K_{gIII} = K_{gI} = 4b_0\sigma\sigma_e T_m^0/\left(\Delta H_m k\right) \tag{1.8}$$

Whereas in regime II, $K_g$ assumes the value of:

$$K_{gII} = 2b_0\sigma\sigma_e T_m^0/\left(\Delta H_m k\right) \tag{1.9}$$

Plotting $log(G)$ against $1/T_c\Delta T$ would yield a graph for the growth regime as shown schematically in Figure 1.7. Some experimental observations have confirmed HL theory, whilst in other system, sharp changes in the growth regime have been not detected. This could be attributed to the complexity of the polymer systems used, where morphological changes occur gradually. Moreover, HL theory has and still provides criticisms from some researchers [20, 23].

### 1.1.4 Crystallisation Kinetics

In order to describe the evolution of the crystallisation, Avrami analysis remains a popular approach [24, 25, 26]. It is based on the Poisson probabilistic equation. Gedde [8] described how a general formula can be derived starting from $t = 0$, taking into account that the crystallisation of a semicrystalline polymer is always

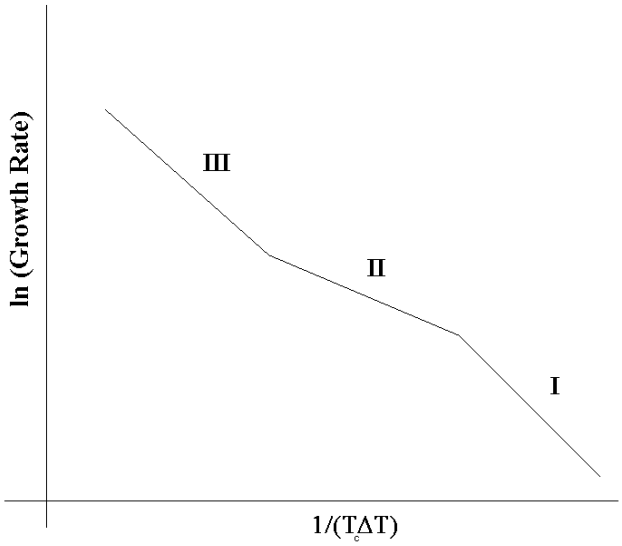


FIGURE 1.7: Schematic diagram showing the three regime changes of G in function of $1/T_c\Delta T$.

incomplete and that the volume of the system changes during crystallisation. From this point, the following equation can be derived:

$$1 - \frac{V_c}{V_\infty} = \exp\left(-K_{exp}\left(t - t_0\right)^n\right) \tag{1.10}$$

where $V_c$ and $V_\infty$ are the instantaneous and final crystallinity volume fractions, $n$ is the Avrami exponent, which depends on the dimensionality and type of the crystallisation; $n$ typically assumes values of 1, 2, 3 and 4 according to the nature of nucleation and growth process. For spherical growth, $n$ is equal to 3 or 4, for plate or disc types is 2 or 3 and for fibrilar ones is 1 or 2. Morgan [27] reported how the Avrami exponents are associated with different nucleation modes and structures. Three mechanisms of crystallisations were related with different nucleation events, as shown in Table 1.1. where $d$ is the diamater of fibre, $G$ is the linear growth rate, $N$ is the nucleation density, $\Omega$ is the nucleation rate and $h$ is the lamellar thickness. From experimental data the value of $n$ rarely corresponds to the values shown in table 1.1, due to erroneous determinations of zero time, baseline and overestimation of fusion [28], secondary crystallisation and mixed

TABLE 1.1: Avrami parameters for different cases of polymer growth (fibrilar, laminar, sphere) in athermal condition or thermal.

| **Mechanism of Growth** | **Nucleation (n)** | **Course of crystallisation** |
|---|---|---|
| Fibrillar Growth - athermal | 1 | $-\frac{\pi}{2}d^2N$ |
| Fibrillar Growth - thermal | 2 | $-\frac{\pi}{4}d^2G\Omega$ |
| Laminar Spherulitc Growth - athermal | 2 | $-lG^2N$ |
| Laminar Spherulitc Growth - thermal | 3 | $-lG^2\frac{\Omega}{2}$ |
| Initial sheaf-like Growth - athermal | 3 | $-\frac{4}{3}\pi NG^3$ |
| Initial sheaf-like Growth - thermal | 4 | $-\frac{\pi}{3}\Omega G^3$ |

nucleation modes. Furthermore the erroneous value of $n$ can affects $k_{exp}$.

## 1.2 Polymer Blends

The production of blends has attracted considerable interest because, in this way, the macroscopic physical properties of a material can be modified. Systems can contain two or more components and they can be miscible or immiscible. Macroscopic phase separation can occur within the blend and this process can be enhanced by crystallisation, so influencing the morphology [8].

In the case of polyethylene (PE), many studies have been conducted on blends of high and low density polyethylene [9, 29, 30]. In fact the phenomenon of phase separation has been proposed to occur when varying the blend composition; this is referred to as liquid-liquid phase separation (LLPS)[31]. Differential scanning calorimetry (DSC) was used to study such blends, and at low concentrations of high density PE two peaks were present. Studies attributed the presence of two peaks to phase separation [9]. Other studies have shown the presence of co-crystallisation in blends of branched low density polyethylene (BPE) and high density linear polyethylene (LPE)[32]. These data suggest that phase separation occurs for more highly branched grades of branched polyethylene. In the study by Greenway [29] blends containing 20 % LPE and 80 % of BPE were examined and found to exhibit continuous spherulitic morphologies at specific crystallisation temperatures. These are the same blends used in this work.

### 1.2.1 Thermodynamics of Polymer Blends

Multicomponent polymeric systems have been traditionally, and at the simplest level, studied with reference to polymer solutions. A first attempt to explain the theory of solution thermodynamics was given by Hildebrand and Wood in 1932 [33]. They developed the so called regular solution theory, which is not valid for polymer solution. In 1941, Flory and Huggins developed an improved theory: Flory-Huggins lattice theory. The essence of this theory is based on a lattice containing the different components. This model assumes no change of volume during mixing, the entropy is given by rearrangements during the mixing process and the enthalpy is caused by interaction between the repeating unit of the polymer, called segments and the solvent. The Flory-Huggins theory, therefore, was able to estimate the miscibility of polymeric systems [34, 35]. From the lattice theory, the entropy of mixing of two polymers, considered $\triangle V_{mix} = 0$, results:

$$\triangle S_{mix} = -R \left[ \frac{\nu_1}{M_1} \lg \nu_1 + \frac{\nu_2}{M_2} \lg \nu_2 \right] \tag{1.11}$$

where $\nu$ is the volume fraction of the two polymers, $M$ is the molecular weight and R is the gas constant. The value of $\triangle H_{mix}$ is given by:

$$\triangle H_{mix} = RT\chi\nu_1\nu_2 \tag{1.12}$$

where $T$ is the temperature in Kelvin and $\chi$ is the Flory-Huggins binary interaction parameter. Polymer blends show improved technological application thanks to enhanced properties such as strength and optical clarity ([9, 29, 36, 37, 38]). However, when two polymers are mixed together they can exhibit phase separation due to the different nature of the polymers, as is the case for a mixture of a polar and a non-polar polymer. From a thermodynamical point of view, a complete

miscibility between two polymer can be achieved if the following expression holds:

$$\triangle G_{mix} = \triangle H_{mix} - T\triangle S_{mix} < 0 \tag{1.13}$$

where $\triangle G_{mix}$ is the free energy of mixing, $\triangle H_{mix}$ is the enthalpy of mixing and $\triangle S_{mix}$ is the entropy of mixing at the temperature $T$. The sign of $\triangle G_{mix}$ always depends on the value of the enthalpy of mixing, because the value of $\triangle S_{mix}$ is always positive and small. The polymer blend forms a single phase only if the entropic contribution to free energy exceeds the enthalpic contribution as follows:

$$\triangle H_{mix} < T\triangle S_{mix} \tag{1.14}$$

Considering a binary system the free energy formula can be expressed as follow:

$$\triangle G_{mix} = RT\left[\frac{\nu_1}{M_1}\lg\nu_1 + \frac{\nu_2}{M_2}\lg\nu_2 + \chi\nu_1\nu_2\right] \tag{1.15}$$

From this expression, it can be seen that, in the case of high molecular mass $M$ the entropy term becomes extremely small. Therefore the miscibility of two polymers is possible only if the value of $\chi$ is negative. For a blend of polymer, the miscibility can be achieved if $\chi = \chi_{cr}$ is met:

$$\chi_{cr} = \frac{1}{2}\left(\frac{1}{\sqrt{M_1}} + \frac{1}{\sqrt{M_2}}\right)^2 \tag{1.16}$$

where $M$ is the molecular weight of the polymers [39]. However the value of $\chi$ does not depend only on the molar masses, but depends on the pressure, temperature and concentration [40].

Figure 1.8 represents some schematic phase diagrams:

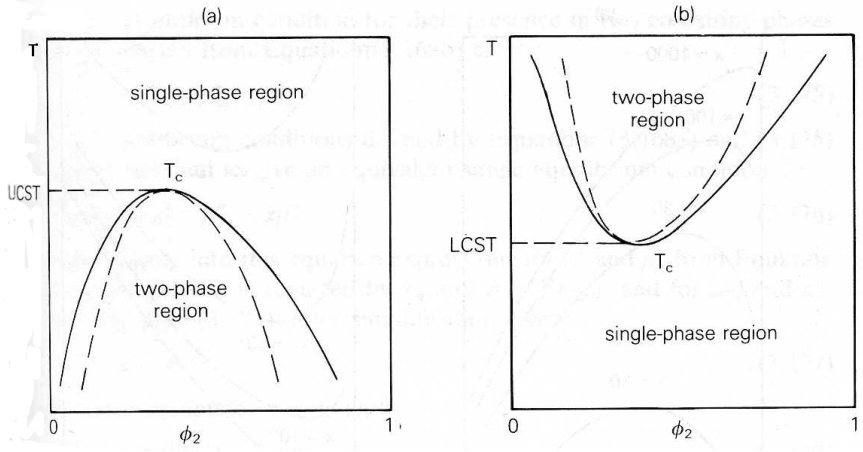


FIGURE 1.8: phase diagram for a mixture from [6].

The figure is composed of two lines called the binodal and the spinodal (dash line) that separate respectively the miscible and metastable phases, and the metastable and two phase region. The spinodal and the binodal curves meet at a point called upper critical solution temperature (UCST) and/or at lower critical solution temperature (LCST). Above the UCST point and below the LCST point the miscibility occurs at all compositions. When the polymer system enters the metastable phase from the single phase region, phase separation occurs by slow nucleation followed by growth of the phase separated domains [40]. When the polymer system enters, instead, from the single phase region to below the spinodal line, phase occurs spontaneously by the mechanism called spinodal decomposition.

## 1.3 Types of Polymer Blends

Polymer blends differ as a result of the different nature of one or more of the components, or as a result of the presence of different additives. Mechanical properties can be improved by adding nucleating agents, which increase the number of nuclei in the bulk [41]. In other cases, mechanical properties can be modified by the presence of partially non crystalline polymers, like ethylene vinyl acetate (EVA) copolymers [42]. Moreover, in the last decade polymers loaded with fillers, having

at least one dimension of nanometric size, have attracted considerable attention. Here are some examples of polymeric systems that having been studied as part of the investigation described in this thesis.

### 1.3.1 Polymer blends and Nucleating Agents

The inclusion of additives in polymers is a widely used method to improve the behaviour of polymers, such as mechanical and optical properties [43, 44]. However, only in the last few years has the inclusion of additives as morphology modifiers been studied. Dibenzylidene sorbitol (DBS) is an organic nucleant agent containing two benzene rings and two hydroxyl groups (Figure 1.9); a physical gel is obtained at room temperature when small quantities of DBS are added to many polymers, including polydimethylsiloxane [45, 46] and polyalkylene oxides [47]. In the presence of several semicrystalline polymers, DBS forms a gel at a temperature above the polymer melting temperature and promotes heterogeneous crystallisation of the polymer once the temperature is decreased. DBS forms nanofibrils of about 10 nm in diameter [48] upon which the polymer is able to crystalise forming small spherulites [49]; this gives enhanced mechanical and optical properties (depending on the spherulite size). Studies have shown an impressive nucleating efficiency of DBS most notably in system based on polypropylene [41].

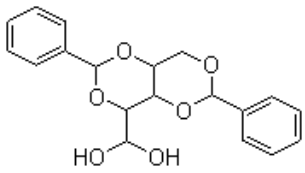


FIGURE 1.9: Dibenzylidene sorbitol structure.

The density of nuclei in iPP containing different quantities of sorbitol was increased by five orders of magnitude, as shown by Martin [50]. The crystallisation in commercial polymer is attributed to heterogeneous nucleation, such as impurities. For this reason nucleating agents play important roles. Beck [51] pioneered works in

this area, and suggested some criteria for nucleant agents, which include: stability, insoluble, and solid at temperatures above the melting point of the chosen polymer. DBS is a good example that meets these criteria. Subsequent studies proposed that nucleation is attributed to the epitaxial growth of lamellae on a substrate crystal of the nucleating agent [52, 53]. Kim *et al.* [54] have already demonstrated the efficiency of DBS in polyethylene at a concentration of 0.1 %. In this study the effect of DBS on blends of LPE and BPE will be analysed. Also, the effect of DBS on nucleation at different crystallisation temperatures will be investigated.

## 1.4 Immiscible Blends

Ethylene-vinyl acetate is a copolymer formed by a ethylene monomer and a vinyl acetate unit(VA). Different types of EVA can be found in commerce, which differ in terms of the relative proportions of the two monomers. On increasing the VA part, the crystallinity of the copolymer decreases becoming a rubber-like material. Up to 10 % wt VA content, the density decrease and the crystalline structure is still present. At 15-30 % VA the copolymer becomes very soft and flexible. At 40-50 % the rubber-like product predominates and the copolymer can be used as cable insulation, after cross-linking with an appropriate peroxide compound. For higher VA percentage, the copolymer becomes viscous and it can be used for paint or adhesive coatings. Whilst EVA itself has been studied as a potential nanocomposite materiel, a relative few studies have been concerned with PE/EVA blends; many of these studies have highlighted the immiscibility of the polyolefin polymers with EVA, due to the polarity of the acetate group [55].

However, some investigations revealed an interaction between the two materials when the VA content is present at low concentrations [56]. Some studies found that the addition of EVA to LDPE results in enhanced material toughness [42], while

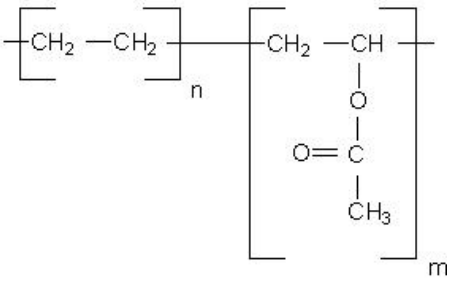


FIGURE 1.10: Ethylene-vinyl acetate structure.

others found that a phase separated microstructure develops with increasing VA content. In this study, a series of EVA systems will be investigated: this research will focus on the effect of VA on the microstructure of PE and the breakdown characteristic of the blends.

## 1.5 Polymer Nanocomposite

In the last decade polymers loaded with fillers, having at least one dimension of nanometric size, have attracted considerable attention. According to the first definition of nanocomposites, three types of nanocomposites can be distinguished, depending on how many particle dimensions are nanometers in size [57]:

- When the three dimensions are nanometric, we are dealing with isodimensional nanoparticles (e.g. spherical silica nanoparticles).
- When two dimensions are nanometric and the third is larger, forming an elongated structure, we speak about nanotubes and whiskers (carbon nanotubes and nanofibres or cellulose whiskers).
- When only one dimension is nanometric, the filler is present in the form of sheets, commonly of one to a few nanometers thick and of hundreds to thousands of nanometers in lateral exent, known as polymer/layered crystal nanocomposites (PLC).

There is a wide variety of both synthetic and natural crystalline fillers that are able, under specific conditions, to generate the final type of nanocomposites (e.g. montmorillonite, hectorite, saponite, hydrotalcite, fluoro-mica). However, those based on clays and layered silicates have been more widely investigated, probably because the starting clay materials are easily available and because their intercalation chemistry has been studied for a long time. Many studies focused on the processability of nanocomposites, others the interactions between polymers and fillers. Mechanical properties have been widely investigated, whilst electrical properties are still to be fully elucidated. Tanaka *et al.* [58] studied the effect of dispersed nanoparticles in thermoplastic polymers. Interfacial regions between the nanoparticles and the polymer are believed to have a high impact on the dielectric properties of the material, due to the surface to volume ratio [59]. Nelson and Hu [60] compared the space charge characteristics of micro and a nano $TiO_2$-epoxy systems. The nanocomposite showed a much faster space charge decay than the microcomposite, suggesting that the interface states enhance charge transport processses. This investigation highlighted the potential of this new material as an insulator, which could have a high impact from a technological point of view, due to the potential for a more compact designs in electrical equipment. However, including nanocomposite in non polar polymers such as polyethylene can be difficult, due to the limited compatibility of the polymer nature with the filler [61]. This obstacle is often partially alleviated through the addition of grafted maleic anhydride, which enhances the polarity of the matrix and therefore increases the dispersion of filler into the polymer. This can however, have a penalty in the case of dielectrics, due to the increased polarity of the system. In this project the addition of different degrees of polarity has been considered and the effect of this on dielectrics properties has been studied.

## 1.6 Aim of the Thesis

This work focuses on the interaction between PE-based blends and polar compounds. The incorporation of nanostructure compounds can modify both the structure and electrical properties of the polymer. The aim of this thesis is to investigate the effect of nanostructured polymers on the physical properties by making use of traditional morphology characterisation and by analysing the electrical properties of the material. Chapter 2 of the thesis outlines all the methods which have been applied in this study. First, the preparation procedure is explained, followed by the structural characterisation and by the description of the electrical methodology.

The third chapter focuses on the interaction between polyethylene and DBS. Studies of microstructures of different PE:DBS systems in combination with isothermal crystallisations are examined. Chapter 4 is focused on the effect of the polarity in the system is explored in combination with electrical properties. The fifth chapter of the thesis focuses on the interaction between PE blend and a macromolecular polar copolymer, EVA. A series of blends have been prepared varying both the EVA and the VA content. The morphology and the phase separation have been studied. Breakdown strength of the blends examined in Chapter 5 are analysed in Chapter 6. Finally Chapter 7 studies EVA/organoclay nanocomposites and their potential as nanodielectrics. Two commercially modified and an unmodified clay have been mixed with EVA systems of varying the VA content. A first attempt of a masterbatch of EVA/MMT was explored, but many difficulties in preparing and dispersing the clay in the polymers were encountered. Therefore this aspect of the project concentrated on the interaction and dispersion of 5 % MMT in EVAs. Finally, Chapter 8 summarises all the general conclusions and presents some possible future developments.

# Chapter 2

# Methods and Analysis

In this section, all the techniques used to prepare and analyse the materials examined in this study will be described. The preparation methods will first be described, followed by the structural characterisation and, finally, by the electrical testing methods.

## 2.1 Sample Preparation: Solution Blending

Generally, to prepare a polymer blend, the polymer must first be melted and mixed in an extruder. However, in order to prepare small quantities of polymer blends in a laboratory and to avoid any shear history, the material is commonly dissolved in a suitable solvent and subsequently precipitated-out of the blend using a non-solvent. When the non-solvent is added to the solution, it interacts with the solvent component, expelling the polymer blend in the form of a gel. During this project, xylene was used as the solvent, due to its commercial availability and extensive characterisation in many previous studies[9, 15, 50]. Methanol or hexane was chosen as the non-solvents.

During the preparation of blends, a concentration of 1 % w/v (polymer/xylene)

was used. The experiments were performed under reflux conditions to avoid evaporation of the solvent. Once the boiling temperature was reached, the solution was left to cool down for 10 min, and then poured into methanol to precipitate the blend out of solution. The precipitate was removed from solution via filtration, left to dry at room temperature and then sealed under vacuum for 24 h. Finally, the blends were dried in a dynamic vacuum oven for 48 h at a temperature of 40 °C to remove any residual solvent.

When a blend of polymer was prepared in the presence of DBS, hexane was chosen as the non-solvent. Unsuccessful attempts were made using methanol; due to the polarity of sorbitol it was also extracted during the filtration stage together with the xylene, such that methanol could not be used. Finally, all the blends obtained were examined by differential scanning calorimetry to ensure uniformity of the material. Once the blend had been prepared, further preparation steps were required depending upon the final experimental requirements.

### 2.1.1 Samples Preparation for Optical Microscope

Samples for polarised optical microscopy studies were prepared from solution. A small quantity of blend was added to xylene, heated and stirred until the polymer was completely dissolved in the solvent. Typically, 200 mg of blend was dissolved in 100 ml of solvent. Small aliquots were then pipetted onto microscope slides and left on the hot stage for approximately 2 min to allow the xylene to evaporate. At this point, a coverslip was placed onto the sample and pressure was gently applied to avoid any undue stress being transferred to the polymer.

Finally, all the samples were crystallised using a Mettler FP90 hot stage. All samples were heated to a melting temperature of 200 °C and left at this temperature for 5 min, allowing the polymer to relax, and thereby avoiding a high degree of stress within the sample. Samples were then cooled and isothermally

crystallised. Following crystallisation, samples were quenched in liquid nitrogen, ready for study using the optical microscope. Preliminary information was also obtained by observing the sample via the microscope during crystallisation within the hot stage.

### 2.1.2 Microtomy

Samples for study in the scanning electron microscope (SEM) required special preparation. Specimens of defined dimension were melted and crystallised at the required temperature in the differential scanning calorimeter (DSC), before being cut using an ultra-cryo-microtome [9, 50]. The specimens were first mounted in the sample holder in a cryo-chamber. Before cutting, samples were cooled to a temperature of -100 °C, thereby making them harder, and hence, easier to cut. Glass knives were prepared using a RMC ultramicrotome glass knife maker. However, the surface, after being cut, is not representative of the internal microstructure as it contains artifacts related to the cutting process. For this reason, all the samples were etched, so that that structure of the blends was revealed.

## 2.2 Structural Characterisation

The materials were studied using a range of techniques including optical microscopy, scanning electron microscopy (SEM), differential scanning calorimetry (DSC) and X-ray diffraction (XRD).

### 2.2.1 Optical Microscopy

During the project a Leitz transmission light optical microscope was used. The aim was to study the morphology of the samples crystallised in the Mettler hot

stage.

Light can be seen as a wave having an oscillation field ($E$), a polarisation direction ($P$), a propagation direction ($x$) and a defined wavelength ($\lambda$) (see Figure 2.1a) [62].

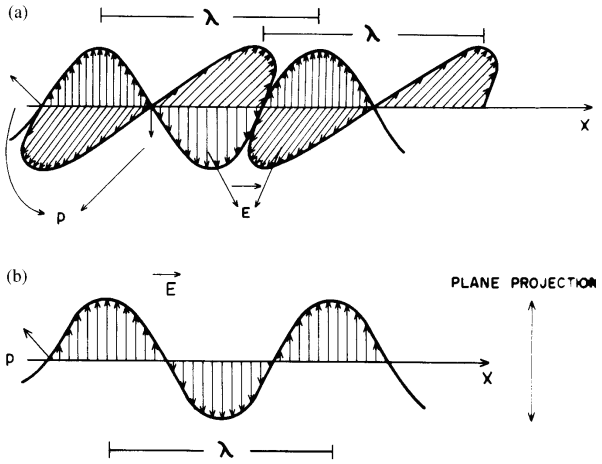


FIGURE 2.1: Diagram of light wave (a); linear polarised light wave (b); From [62].

Natural light is unpolarised, but it can be linearly polarised using a polariser, as shown in Figure 2.1b. Linearly polarised light is when the electric vector of the wave $E$, is confined to a single plane of oscillation. In this case it will be confined to the plane determined by the polariser.

A polarising transmission optical microscope consists of condenser optics, field and substage apertures, two polarisers, the objective lenses and the ocular lenses. One polariser is placed below the condenser, while the second one, termed the analyser, is positioned between the objective and the ocular lenses. The orientations of the polarisers are perpendicular to each other (crossed polar) such that no light is transmitted in the absence of a sample or retarder. When the light enters the material, it can be considered to split into two components (ordinary ($o$) and extraordinary ($e$) rays) which propagate through the sample at different speeds. This phenomenon is called bifringence [63]. As a result, a phase difference is introduced between the two rays. Upon emerging from the sample, these two rays

combine (as a result of super position of the *e*- and the *o*-waves) into a single beam; however, due to the phase difference introduced by the sample, the polarisation of the wave differs slightly from that of the incident linearly polarised beam. Only light parallel to the plane of polarisation of the analyser will be transmitted, while the rest will be absorbed or partially transmitted. This generally accounts for a variety of shades of grey, black and white observed in the absence of a chromatic retarder. When a chromatic retarder is introduced between the sample and the analyser, an additional phase shift between the o- and e-waves is introduced, the magnitude of which shift depends on the retarder in use. For example, in this experiment a $\lambda$ wave plate was used, which means that at a wavelength of an additional phase difference of $2\pi$ is introduced between the e- and the o-waves. This phase difference varies for any other wavelength, meaning that if white light is used (as is the case here), all the other wavelengths will undergo some retardance and will accordingly emerge from the waveplate as various forms of ellipticaly polarised light [64]. Upon reaching the analyser, some particular wavelengths will be blocked while others will be transmitted. The end result is a variety of colours due to colour interference effects.

Polymer spherulites, studied at the polarised microscope, present a so called maltese cross pattern, as shown in Figure 2.2 [16].

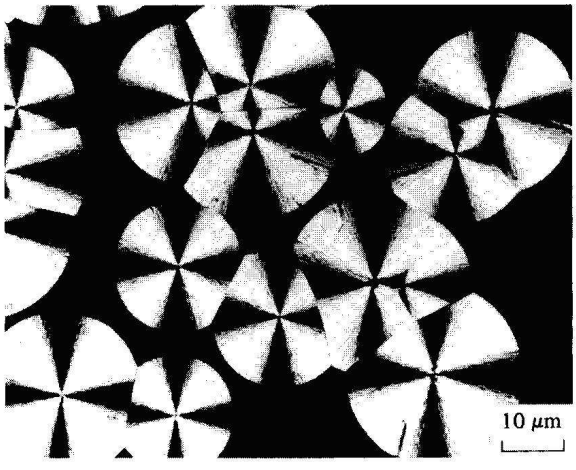


FIGURE 2.2: Optical image of spherulites in PE taken at 114° C; scale bar 10$\mu$ m; from [16].

### 2.2.2 Etching

The method used in this study to prepare samples prior to electron microscopy is that of permanganaic etching [65]. In this, specimens are immersed and agitated in a solution containing potassium permanganate, sulphuric acid, orthophosphoric acid and water. After 2 h the low crystallinity and amorphous parts have been preferentially removed from the surface, revealing the high crystallinity ones. The mixture used in this study consisted of a 1 % solution of potassium permanganate, in five parts concentrated sulphuric acid, two parts orthophosphoric acid to one part distilled water (5:2:1) [66, 67]. The reaction was terminated by the addition of a chilled mixture of two parts concentrated sulphuric acid to seven parts water, with the addition of hydrogen peroxide. The sample was then washed several times with distilled water and twice in methanol to remove etching residues.

### 2.2.3 Scanning Electron Microscope

The optical microscope was routinely used to observe the morphology of materials, but due to its relatively low resolution, further studies with a scanning election microscope were necessary. For these, a Cambridge Instrument S360 scanning electron microscope (SEM) and a FEI Quanta FEG 600 Environmental Scanning Electron Microscope (ESEM), housed at the University of Reading, were used. The wavelength of an electron is smaller than that of visible-light, so that it enables a higher resolution to be achieved [68]. The wavelength of accelerated electrons follows the formula (2.1):

$$\lambda = \frac{h}{p} \tag{2.1}$$

where $h$ is Plank's constant and $p$ is the momentum of the electron. An electron with charge $e$, subjected to a voltage $V$ follows the formula (2.2):

$$eV = \frac{p^2}{2} \tag{2.2}$$

and substituting the Equation 2.2 into Equation (2.1) the following Equation (2.3) results:

$$\lambda = \sqrt{\frac{h^2}{2meV}} \tag{2.3}$$

The resolution ($d$) of an SEM is a function of the short wavelength of the electrons:

$$d = \sqrt{\left(\frac{0.61\lambda}{\alpha}\right)^2 + (C_s\alpha^3)^2} \tag{2.4}$$

where $\alpha$ is half the angular aperture and $C_s$ is the spherical aberration coefficient. At an operation voltage of 20 kV the resolution of an SEM can reached 0.5 nm [8, 62, 69].

The electrons for the SEM can be produced by a heated tungsten filament, a so-called thermionic electron gun, or by a field emission gun (FEG). The electron beam scans the sample surface and the re-emitted electrons are collected by a detector. When electrons hit the coated surface of the samples, they generate secondary and backscattered electrons [70, 71]. Both emitted electrons can be used to acquire images. At this point the detector signal is amplified and converted to an image on the screen. X-ray radiation is also produced and, if the SEM is furnished with an X-ray microanalyser, material composition can be examined.

In this study, samples were first examined at a low magnitude to give an overview of the sample, and the stigmators were adjusted using a circular feature on the sample if necessary. The magnification was then increased to focus on a particular area of interest. All images were acquired using an accelerating voltage close to

18 kV for the SEM S360 and 20 kV for the ESEM.

The previously etched samples were mounted onto an SEM holder. All specimens were coated with a layer of gold to provide the sample with a degree of electrical conductivity (charge dissipation) and to improve image quality (minimise secondary electron escape depths). A sputter coater was used and the coating, according to the instruction manual, was around 70-100 nm thick. The thickness of the gold coating is important, for two main reasons: the first because an excess of gold coating would conceal microstructural details, and the second, because the coating becomes more brittle and could easily crack during the examination.

## 2.3 Differential Scanning Calorimetry (DSC)

DSC is a technique used for measuring the enthalpy variations in a sample, as a function of time, when the experiment is conducted under isothermal conditions, or as function of temperature, if a temperature ramp is used [9, 29, 50]. A Perkin-Elmer DSC-7 was used for this study. The instrument consists of two sample furnaces; one contains the studied material and the other a reference sample, the latter normally being an empty aluminium can. The cans were previously weighed, and cans of similar mass were used. The sample holders are connected to two different and independent heating systems [72]; one applies a ramped or constant temperature selected by the user, while the other ensures that both sample and reference are at the same temperature. The power to maintain this thermal balance is equal to the instantaneous heat flux, and it is recorded by a computer. In order to obtain accurate results, the instrument was calibrated prior to each batch of experiments. Calibration was performed using high purity indium that has a known melting temperature of 156.6 °C, which allowed for proper temperature calibration. For accurate calibration, the effect of ramp rate has to be taken into account. An ideal instrument would keep a zero temperature difference between

the sample and reference temperatures at all times. For isothermal calibration, it was necessary to record the melting point of indium at 1.25 °C/min, 5 °C/min and 10 °C/min before extrapolating to zero ramp rate as shown in Figure 2.3. Melting traces, instead, required a 10 °C/min offset to be used.

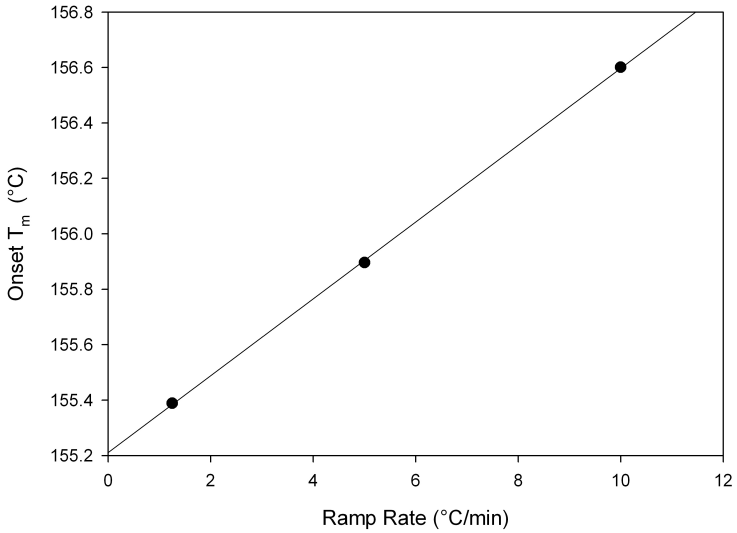


FIGURE 2.3: High purity indium calibration at different ramp rate.

All scans were performed under a nitrogen atmosphere to ensure that any volatiles evolved from the sample during the experiments did not accumulate in the furnace. The nitrogen atmosphere also helps to prevent sample decomposition, which could lead to aberrations in the data collected. In this way, crystallisation and melting phenomena in semi-crystalline polymers, like PE, can be studied [8, 16, 64]. In particular, isothermal runs were performed and the data were then analysed.

## 2.4 Avrami Analysis

All DSC isothermal crystallisation curves were integrated as a function of time using a Simpson's Rule approach. This makes it possible to analyse the kinetics of crystallisation using Avrami analysis [8, 24, 25, 26], whereby:

$$1 - \frac{V_c}{V_{inf}} = \exp\left(-K_{exp}\left(t - t_0\right)^n\right) \tag{2.5}$$

where $V_c$ and $V_{inf}$ are the instantaneous and final crystallinity volume fraction, $n$ is the Avrami exponent, which depends on the dimensionality and type of the crystallisation, as described in the previous chapter.

In this work experimental data were plotted on both double log plots and by non-linear curve fitting. The values of $n$, $K_{exp}$, and $t_0$ were found. In order to interpret the data correctly, it is important to identify the crystallisation modes for polymers. In the case of spherulitic crystallisation under athermal conditions the theoretical value of $K_3$ is [73]:

$$K_3 = \frac{4}{3}\pi N G^3 \tag{2.6}$$

where $N$ is the nucleation density and $G$ the growth rate. However, in practise, $n$ is rarely found to be equal to 3. Then, Kowalewski *et al.* [74], assuming that the crystal growth is really three-dimensional, suggested that the effective three-dimensional crystallisation constant $K_3'$ can be determined from the experimental value of $K_{exp}$:

$$K_3' = \frac{4}{3}\pi N G^3 \cong \left(K_{exp}\right)^{\frac{3}{n}} \tag{2.7}$$

In this $N$ is the number of nucleation sites per unit volume and $G$ is the growth rate of the crystallising object. Using the value of $G$ obtained from previous works [75], the nucleation densities were determined.

## 2.5 Induction Time

Muchova and Lednicky [73, 76] developed a theory that relates induction time, $t_i$, to the thermodynamics of nucleation at the early stage of heterogeneous crystallisation of polymers, which is based upon secondary nucleation theory (see Chapter 1.1.3). In this, induction time is defined as:

$$t_i = t_h + t_s \tag{2.8}$$

where

$$t_h = A_1 exp \frac{\left[16\sigma_{b1}\sigma_{ab}\Delta\sigma\left(T_m^0\right)^2\right]}{\left[kT\left(\Delta H_m \Delta T\right)^2\right]} exp\left(\Delta G_\eta / kT\right) \tag{2.9}$$

and

$$t_s = A_2\left[2\Delta\sigma T_m^0 / \Delta H_m \Delta T b_0 - 1\right] exp \frac{\left[4\sigma_{b1}\sigma_{ab}b_0 T_m^0\right]}{\left[kT\Delta H_m \Delta T\right]} exp\left(\Delta G_\eta / kT\right) \tag{2.10}$$

$t_h$ is the time for the formation of the first layer on a filler surface and $t_s$ is the time for the formation of further layers untill the growth of a stable nucleus is completed [73]. $A_1$ and $A_2$ are proportionality constants, $\sigma_{b1}$ and $\sigma_{ab}$ are the Gibbs specific surface energies of the nucleus, $\Delta\sigma$ is the difference energy paramenter, $T_m^0$ is the equilibrium melting temperature, $\Delta H_m$ the enthalpy of crystal melting, $\Delta T$ is the undecooling, $b_0$ is the thickness of one layer of folding chains, and $\Delta G_\eta$ is the activation energy of diffusion. When crystallisation occurs rapidly, the uncertainty in $t_i$ is likely to be significant [50]. At higher crystallisation temperature the time taken to form of the first layer ($t_h$) can be neglected in relation to the time taken for the remaining layers to be formed. Therefore Muchova and Lednicky argued that Equation 2.8 is approximately equal to $t_s$ and consequently be written in

logarithmic form as:

$$ln\left(t_i\Delta T\right) = ln\left[C\Delta\sigma T_m^0/\Delta H_m\Delta T b_0\right] + \frac{\left[4\sigma_{b1}\sigma_{ab}b_0T_m^0\right]}{\left[kT\Delta H_m\Delta T\right]}\left[\Delta G_\eta/kT\right] \tag{2.11}$$

Thus Equation 2.11 can be simplified and expressed as $ln\left(t_i\Delta T\right) - f\left(1/T\Delta T\right)$, where $K$ represents the slope and $Q$ the intercept:

$$K = \left[4\sigma_{b1}\sigma_{ab}b_0T_m^0/kT\Delta H_m\right] \tag{2.12}$$

$$Q = ln\left[C\Delta\sigma T_m^0/\Delta H_m\Delta T b_0\right] \tag{2.13}$$

The values of $K$ and $Q$ can therefore be determined easly from experimental data. The values of induction time can be determined by fitting the Avrami equation to experimental data [77]. Plots of induction time against temperature can be obtained and changes in the nucleation process may consequently be observed. The equilibrium melting temperature $T_m^0$ is normally used as a parameter in induction time plots and it is derived from Hofmann and Weeks analysis [78]. According to this method, the melting temperature $T_m$ is obtained from the following equation:

$$T_m = \left(1 - \frac{1}{\lambda}\right)T_m^0 + \frac{T_c}{\lambda} \tag{2.14}$$

where $\lambda$ is the ratio of the crystal thickness to the thickness of the initial nucleus [79]. $T_m$ is plotted against $T_c$ (crystallisation temperature) and together with the line representing $T_m = T_c$ on the same graph. $T_m^0$ is then given by the intercept of these two plots.

## 2.6 X-Ray Scattering

X-ray diffraction was performed on samples loaded with clay in order to obtain information about the state of the filler within the matrix. Different types of X-ray techniques can be used. Wide angle X-ray scattering (WAXS) is able to detect chain segment on a scale of 1 to 10 Å. Conversely, small angle X-ray scattering (SAXS) can determine lamellar spacing of the order of 100 Å in size. In this work only WAXS was used.

In this work a sealed tube source was used at the university of Trieste. The X-ray tube contains a hot filament, cathode, and a copper target, anode. An electric field accelerates electrons from the cathode, which hit the anode such that X-rays are produced by excited electrons in the metal target. A graphite monochromator is used to select the $CuK_\alpha$ line at a wavelength of 0.154 nm.

### 2.6.1 X-Ray Scattering Theory

X-rays are electromagnetic radiation with typical energies in the range of 1 keV - 100 keV [80]. Because the wavelength of these X-rays is comparable to the size of atoms, they are ideally suited for probing the structural arrangement of atoms and molecules in a wide range of materials [80]. From the X-ray source, an incident beam enters a polymer sample of defined thickness, X-rays will be scattered by electrons around each atomic nucleus, and the intensity of scattering depends on the number of atoms. Figure 2.4 shows a schematic representation of X-ray diffraction:

where X-rays scattered at $A$ will travel a shorter distance than the X-ray scatter at $B$, therefore the path difference is equal to:

$$(AB + BC) - AC' \tag{2.15}$$

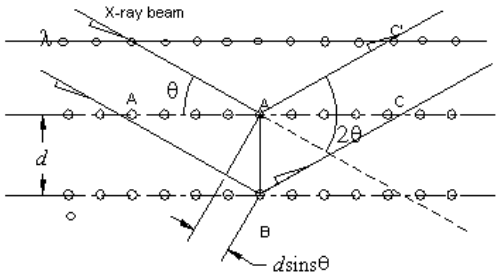


FIGURE 2.4: Schematic X-ray diffraction pattern.

If this path difference is equal to any integer value of the wavelength then the two separate waves will arrive at a point with the same phase, and hence undergo constructive interference:

$$n\lambda = (AB + BC) - (AC') \tag{2.16}$$

therefore the path difference is equal to an integral number of wavelengths $\lambda$, which leads to the Bragg equation:

$$2dsin\theta = n\lambda \tag{2.17}$$

Thus, the interplanar spacing can be written as:

$$d = 2\pi/Q \tag{2.18}$$

where scattering vector $Q$ is equal to:

$$Q = 2\pi/d \tag{2.19}$$

### 2.6.2 Wide Angle X-Ray Scattering

Wide angle X-ray scattering (WAXS), is a non-destructive technique that is often used to determine the crystalline structure of polymers [6]. This technique specifically refers to the analysis of Bragg peaks scattered to wide angles, which are, by Bragg's law, caused by sub-nanometer sized structures. According to this method, the sample can be scanned in a wide angle X-ray goniometer, and the scattering intensity is plotted as a function of the 2 $\theta$ or scattering vector $Q$. A crystalline solid consists of regularly spaced atoms that can be described by crystal planes introduced above; the distance between these planes is called the d-spacing. The intensity of the d-space pattern is directly proportional to the electron densities that are found in the appropriate crystal planes. Every crystalline solid will have a unique pattern of d-spacings.

X-ray patterns were recorded in the range of 1.4-7 nm $^{-1}$. The X-ray tube was running at 40 kV and 30 mA. Steps were in increments of 0.02°, and counts were collected for 1 s at each step.

## 2.7 Electrical Testing

Specimens for electrical testing were prepared with a Grasby-Specac hydraulic press to produce film samples of known thickness. In the case of breakdown tests, the thickness was $\sim$ 70 $\mu m$, while for the space charge tests, the sample thickness was $\sim$ 200 $\mu m$. Samples prepared as described in section 2.1, were placed between two aluminium foils and pressed between the two parallel plates. Each sample was melted at a desired melting temperature for a period of 2 min to erase the previous thermal history. Subsequently, some samples were immersed in an oil bath at a temperature of 117 °C for a period of 20 min, to allow complete crystallisation of the blend. Other sample were directly quenched into distilled water from the melt.

To avoid any damage of the sample surface, the aluminium foils were dissolved in a hydrochloric acid solution 10 % HCl in $H_2O$ and subsequently washed in distilled water and then in acetone. Finally, all the samples were degassed in a vacuum oven overnight.

Crystallised samples of PE/EVA blends for breakdown testing were prepared as described above. However, since it was thought that the hydrophilic nature of the VA compound may offset the behaviour of these systems, a further investigation of the effect of the absorbed water was also undertaken. For this, a batch of disks was immersed in distilled water for 50 h at room temperature before being tested in the breakdown rig.

### 2.7.1 Breakdown Testing

Samples 70 $\mu$m in thickness were placed between two steel ball bearing electrodes (6.3 mm diamater) immersed in Dow-Corning 200/20cs silicon oil, to avoid partial discharge due to the presence of air, and a 50 g load was applied to the upper electrode. The choice of ball bearing was determined to reduce the problem of flashover at the edges of the sample [81] and secondly, because this electrode geometry has been widely used in the past by Hosier and Greenway [9, 29]. Moreover, the ball bearings were substituted every 5 tests in order to avoid pitting on the electrods [9]. Alternating current (AC) voltage ramps of 50 $Vs^{-1}$ at 50 Hz were applied and the time to failure were measured. A schematic diagram of the instrumention is given in Figure 2.5.

A warm up time of 1 h was used before performing a calibration of the instrument. To calibrate the ramp rate, a thick sample of PE was place between the electrodes and the voltage was increased to 25 kV and a series of times were collected corresponding to different voltages, until the desired ramp rate was achieved. After calibration, voltage ramps of 50 $Vs^{-1}$ rate were applied to a disc sample until a

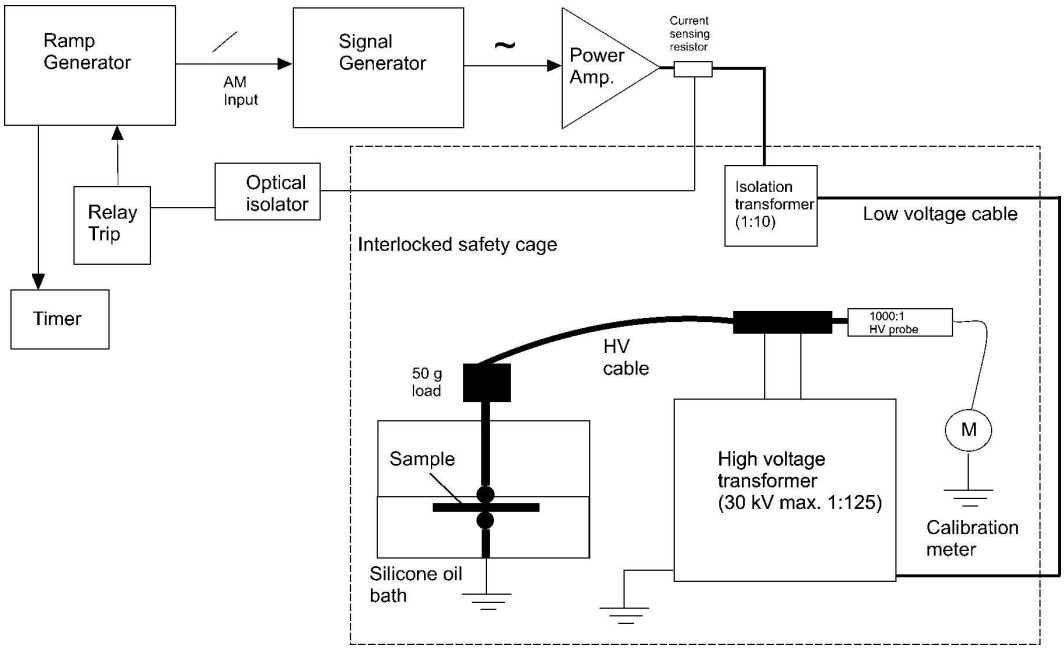


FIGURE 2.5: Schematic diagram of breakdown test instrument.

breakdown current was recorded. Five tests were performed on each sample and the oil was changed for each batch of samples tested. Each sample was tested with new ball bearings in order to avoid the possibility of damage to the electrode surface created by discharges influencing the measured data. The voltages obtained were divided by the average disk thickness to produce a value of breakdown strength. 20 breakdown tests were performed on each material type.

### 2.7.2 Breakdown Analysis: the Weibull Distribution

Breakdown tests have been analysed in the past using a number of different statistical distributions [82]. Dissado and Fothergill [83] have described the use of the Weibull distribution and it is now accepted as the standard by the Institute of Electrical and Electronics Engineers (IEEE) [84]. Therefore, this probability distribution has been chosen for the purpose of this thesis.

Weibull introduced the distribution in 1951 [82], as a distribution that is applicable to a wide variety of situations. In the case of breakdown, the probability of failure,

$P_f$, of a sample before reaching the time or voltage $x$ is defined as:

$$P_f(x) = 1 - \exp\left(\frac{x - x_t}{\alpha}\right)^{\beta}, 0 \geq x_t \geq x \tag{2.20}$$

where $\alpha$ is termed the scale parameter, $\beta$ the shape parameter and $x_t$ defines the threshold below which the sample will not fail. If $x_t = 0$ the Weibull distribution is called a two parameter Weibull. The differential of $P_f(x)$ with respect to $x$ gives the probability density equation:

$$g(x) = \beta\alpha^{-\beta}x^{\beta-1}\exp - \left(\frac{x}{\alpha}\right)^{\beta} \tag{2.21}$$

Dividing Equation 2.21 by the probability of survival $(1 - P_f)$ gives the rate of failure:

$$h(x) = \beta\alpha^{-\beta}x^{\beta-1} \tag{2.22}$$

When plotting these three functions for different value of $\beta$ and for $\alpha = 1$ the following diagrams are obtained (see Figure 2.8). For values of $\beta$ less than one the sample fails as soon as the experiment starts. When $\beta$ is equal to one, the distribution becomes exponential and the rate to failure is constant and it is defined as the ideal case for an insulator. A maximum value of the distribution appears when the value of $\beta$ is increased and the peak becomes progressively narrower as $\beta$ increases. In this case, the samples fails by a single mechanism as they have a narrow distribution of lifetimes.

However, although the 2 parameter Weibull distribution is widely used, it is not the only statistical procedure proposed. Dang *at al* [85] suggested an exponential model, while some claimed the benefit of using a three parameter Weibull distri-

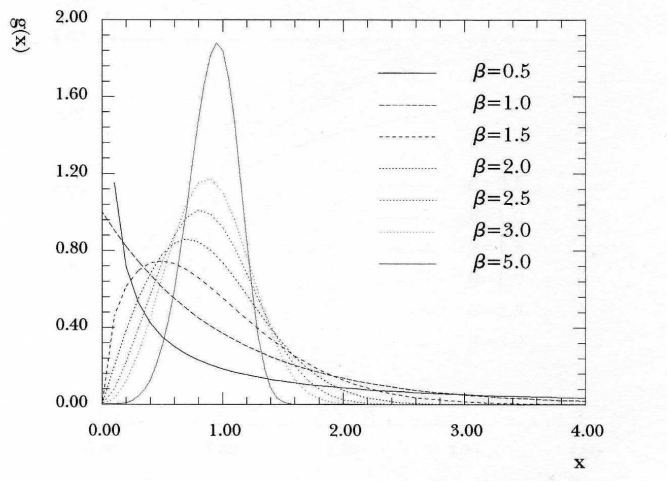


FIGURE 2.6: Probability of failure to the extend of $\beta$.

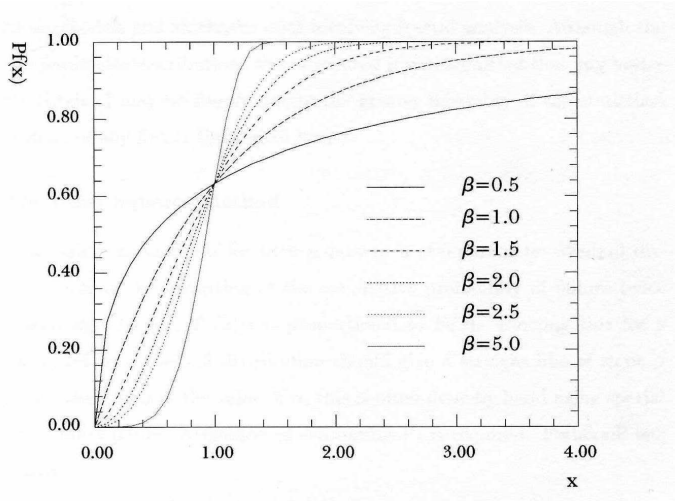


FIGURE 2.7: Probability density equation.

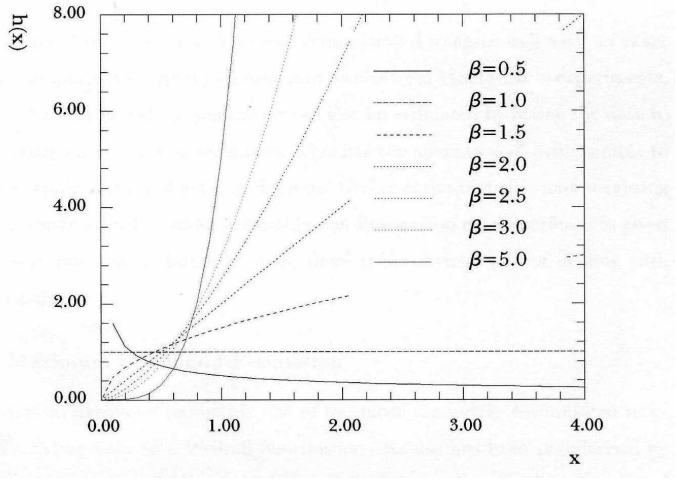


FIGURE 2.8: Rate of failure. From Greenway [29].

bution thanks to a better fit [83, 86]. However, a study by Cacciari *at al* [87] showed that the better fit of a three parameter Weibull distribution is due to an artefact.

In order to fit the two parameter Weibull distribution, several method can be used. The least squares method takes the logarithm of the cumulative probability of failure twice $\ln(-\ln(1 - P_f(x)))$ and generates a straight line and in order to estimate the Weibull parameters a method of estimating $P_f$, proposed by Fothergill [88] is used:

$$P_f(i, n) = \frac{i - 0.3}{n + 0.4} \tag{2.23}$$

where $i$ is the progressive order of failed specimens of the sample and $n$ the sample size. However, linear regression would be biased at the extremes of the distribution and therefore the Maximum Likehood Method (LME) is used to give better estimates value for $\alpha$ and $\beta$. The likehood function is defined as the product of the probability density function 2.21 at each data point.

$$L(p) = f(x_1 : \alpha, \beta) \times f(x_2 : \alpha, \beta) \times \ldots \times f(x_n : \alpha, \beta) \tag{2.24}$$

Maximising the $\log(L(p))$ and making a substitution, $\alpha$ can be eliminated [83] so that the equation for a two parameter Weibull distribution is:

$$\frac{1}{\beta_{LM}} = \frac{\sum_{i=1}^{n} x_i^{\beta} \ln x_i}{\sum_{i=1}^{n} \beta} - \frac{1}{n} \sum_{i=1}^{n} \ln x_i \tag{2.25}$$

According to Dissado and Fothergill [83] this provides a first guess for the $\beta$ value. Once $\beta$ has been found the value of $\alpha$ is then given by:

$$\alpha = \left( \frac{1}{n} \sum_{i=1}^{n} x_i^{\beta} \right)^{\frac{1}{\beta}} \tag{2.26}$$

Even if the maximum likehood method is easy to implement, it does not lead to good value of $\beta$ for small $n$ and introduces a bias in $\alpha$. Ross [89] observed this phenomenon performing Monte-Carlo simulations to the maximum likehood method. Several studies have examined bias in the two Weibull parameter, and have proposed methods to remove this [87, 90].

In this study, Weibull software supplied by ReliaSoft®was used.

### 2.7.3 Pulse Electro Acoustic Technique

Space charge is considered to be one of the potential reasons for the electrical failure of polymeric materials. When a polymer is subjected to a high electric stress, some charge can be generated and trapped in the bulk of the material. This modifies the electric field, enhancing the local field within the material, and leading to faster degradation and premature breakdown of the insulation.

Consequently, techniques have been developed to study this phenomenon; the dominant technique is the pulsed electro acoustic (PEA), which was developed by Takada in 1987 [91]. Figure 2.9 represents schematicly the principle behind the PEA. The sample is subjected to a high DC voltage, such that two charge layers are formed at the surface of the electrodes. When an external high voltage pulse $V_p(t)$ of amplitude from 0.1 to 2 kV and duration of 5-200 ns is applied between the electrodes, acoustic pulsed pressure waves are produced at the charged regions [92].

In the case of the charge on the electrode A, for example, the pressure wave travels through the sample into electrode B and then is transmitted to a piezoelectric

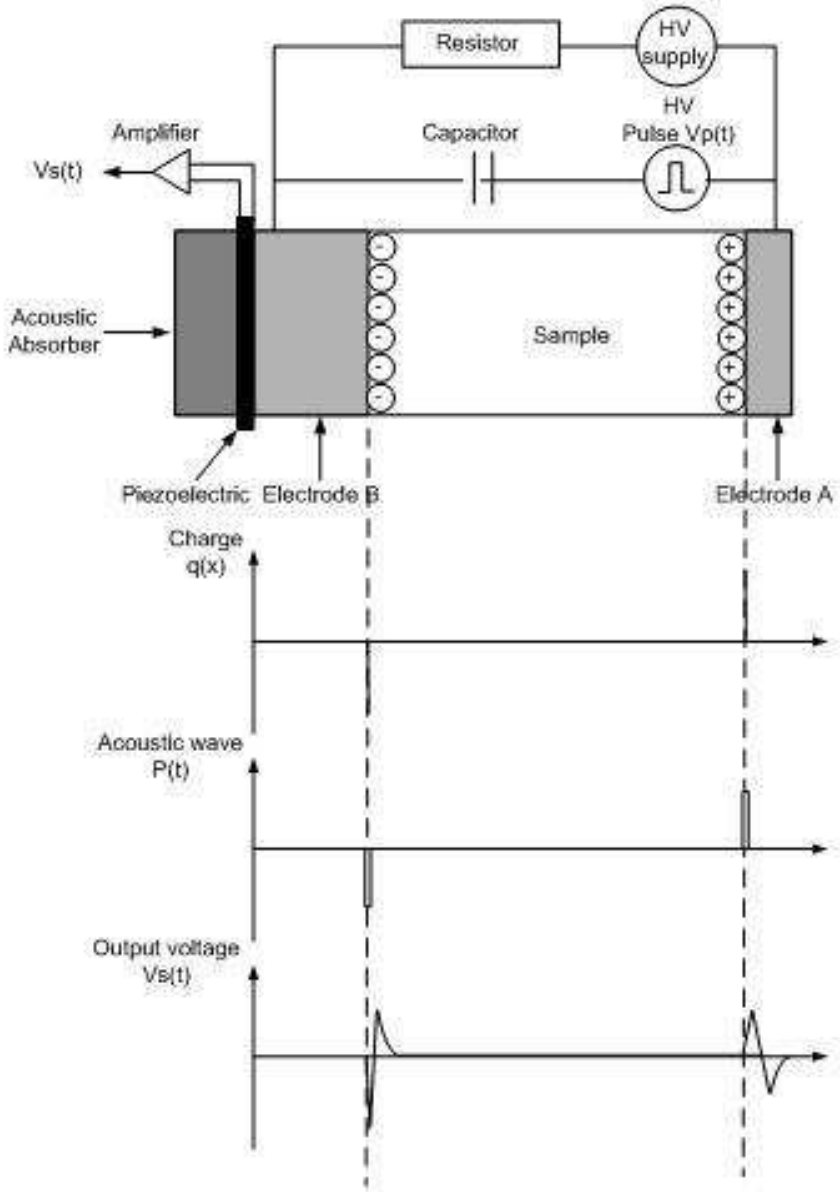


FIGURE 2.9: Schematic diagram of PEA principle

transducer. This converts the mechanical signal into an electrical one. Then the signal is amplified and captured with a digital oscilloscope. The voltage trace obtained is a measurement of the wave profile as a function of time, which is proportional to the one dimensional charge density distribution in the sample. The dc field generates surface sheet charges equal in magnitude but opposite in sign, while the space charge in the bulk induces surface sheet charges of the same sign but different in magnitude. For a thin sample, the electrode charges $\sigma_1$ and $\sigma_2$ results in:

$$\sigma_1 = -\sigma_2 = \varepsilon_0 \varepsilon_r E \tag{2.27}$$

where $\varepsilon_0$ is the permittivity of free space and $\varepsilon_r$ is the relative permittivity of the material. $E$ is given by the Poisson's equation for quasi static field:

$$\nabla E = \frac{\rho(x)}{\varepsilon_0 \varepsilon_r} \tag{2.28}$$

Hence the value of $\sigma_1$ is equal to the integral of the front peak in charge density distribution ($\rho(x)$):

$$\sigma_1 = \int_{z=0}^{z=FrontPeak} \rho(x) dx \tag{2.29}$$

Due to the frequency response of the system, the signal results are distorted, therefore a deconvolution is required. The theory behind the deconvolution is largely described by Maeno *et al.* [92].

During this study an automated PEA system equipped with a LAbVIEW programme was used to analyse samples. In this system, the specimen of interest is inserted between the lower and upper electrodes and a pulse voltage is applied to the sample, in order to generate an acoustic wave. The thickness of the specimen was set to 200 $\mu m$, in order to avoid signal dispersion [93]. Silicone oil was used to make a good acoustic contact between the sample and the electrodes. Calibration was carried out at 2 kV with a short period of voltage application time to minimise the influence of space charge. Space charge accumulations were conducted at 5 kV for a period of 1 h at room temperature. After this time, the voltage was removed and the discharge process was recorded over 1 h. During the charging phase, data were acquired every 30 s over the first 5 min, and then subsequently every 5 min for the remaining time. For a clearer interpretation of these results, data with

voltage on and off were gathered during the charging process. In the discharging phase data were acquired every 5 minutes. The resulting space charge data were analyzed using the calibration trace and a deconvolution technique was applied in order to restore the original signal.

# Chapter 3

# Effect of DBS on Polyethylene

## 3.1 Introduction

This chapter will focus on the morphology and crystallisation behaviour of polyethylene blends. The effect of changes in the composition will also be described. This work starts from a brief description of the DBS and its application in different polymer systems, and then proceeds with a description of the experimental procedures. The investigation takes into consideration a wide rage of compositions of PE and DBS in order to observe the variation of the nucleation of the polymer on the fibrils, using differential scanning calorimetry (DSC), optical microscopy (OP), scanning electron microscopy (SEM).

## 3.2 DBS Gellation

Sorbitols are organic compounds possessing un-reacted additive OH groups, which allow fibrils to form within the melt [45]. The dibenzylidene derivates are obtained by condensation of benzaldehyde and D-glucitol. DBS dissolves in an organic liquid at a temperature above the gelation temperature and undercooling leads

to the formation of a fibrillar network in the solution. The resulting material is a gel that is defined as follows: *a substance is a gel if (1) it has a continuous structure with macroscopic dimensions that is permanent on the time scale of analytical experiment and (2) is solid-like in its rheological behaviour* [94]. Gels are classified into two groups: chemical and physical gels. In the first class, the network is developed through a chemical reaction (normally non-reversible), whilst the physical gels are thermally and mechanically reversible. Studies on dry DBS gels estimated a 10 nm diameter of fibrils [95]. The morphological characteristics of DBS gel networks in different solvent/polymer systems have been studied by Yamasaki *et al.* and by Watase and Itagaki [95, 96]. These studies highlighted a helical structure of the fibrils depending on the solvent polarity. A similar study by Shepard *et al.* [49] on isotactic polypropylene (iPP) and DBS confirmed a helical twist of the fibrils with nanofibrils measuring of the order of 10 nm in diameter; in contrast, other studies claimed the presence of flat sheet-like fibrils, and furthermore, they reported the presence of some remenants of solid particles in a solution containing 1 % DBS [46]. However, TEM images taken by Mercurio and Spontak [97] supported the helical twist and revealed that DBS is electron-transparent (clear) relatively to a poly(propylene glycol) (PPG) background. Two possible explanations for this result have been suggested. First, it might be due to the phenyl rings being stacked together within the nanofibrils, consistent with the observation of Wilder *et al.*[98]. Alternatively, the observation might be influenced by the technique used to obtain the TEM images. All these results introduce another subject of ongoing argument: the formation of the nanofibrils.

The formation of a nanofibrillar network occurs upon cooling from the melt. DBS molecules self assemble creating a gel. Gelation, however, depends on several factors, such as DBS concentration, temperature and solvent polarity. The process of formation of the gel is still unclear. Yamasaki and Tsutsumi [95] have underlined the importance of the hydrogen bonding in the formation of the gel. A later study

by Yamasaki *et al.* [99] has suggested that the 6-hydroxyl group seems to be important in the formation of 1,3:2,4 Dibenzylindene-D-Sorbitol (D-DBS) aggregates. Infrared spectroscopy and molecular modeling calculations of DBS molecules in organic solvents confirmed the role of hydrogen bonding in the network formation and consequently gellation [97]. Others claimed that the stabilisation of the network is more likely due to a delicate balance of the symmetric structure of a DBS molecule, which has a rigid and chiral ten-member ring symmetrically connected with two benzylidene groups in equatorial positions. In short, Watase *et al.* [96] attributed the formation of the network to a $\pi$ electron overlap of the benzylidene rings. This is clearly in contrast with what is suggested by Yamasaki [99]. Molecular dynamic simulations provide an insight into the above. Wilder *et al.* [100] suggested that both the hydrogen bonding and the $\pi$ interactions are the cause of the formation of fibril network, confirming in this way the work of Watase and Yamasaki. Although many studies have improved our understanding of gelation and of the ability of DBS to self assemble, the molecular interactions governing the gelation remain, at present, not fully solved.

The extent to which DBS molecules interact with the solvent and or macromolecular matrix has not been completely addressed. Watase's work suggested that the solvent molecules are not assimilated within the fibrillar network and that a phase separation could occur [96]. Nevertheless, an interaction seems possible. Instead, Wilder *et al.* [98] supported the idea of interaction between DBS and matrix. They considered the combination of DBS with a series of poly(ethylene glycol) systems differing in their termination. Reportedly, changing the nature of the end group from polar to non polar has an effect on the DBS. The polarity seems to have an impact on the gel formation and furthermore the polarity was found to have an effect on the activation energy of DBS. This result indicates an interaction between the fibrils and the matrix. Similar works supported this hypothesis, attributing to the clarifier an epitaxial interaction of PE vapour deposited onto

the fibrils [101]. Moreover, Nogales *et al.* [102] have suggested that the DBS fibrils can drive the nucleation process in polyethylene.

Although some questions are still unsolved, DBS has been shown to be able to create a fibrillar network at low concentrations in various polymer melts, including poly(dimethylsiloxane) [45],poly(propylene oxide) [103], poly(propylene glycol) [97, 104], polycarbonate [105], isotactic polypropylene [41, 106] and a series of small molecular organic liquids [46, 107].

Martin *et al.* [41, 50] proved that the presence of a clarifying additive in polypropylene greatly increases the nucleation density, whilst Vaughan and Hosier [38] observed a drastic drop in the nucleation density at a certain crystallisation temperatures in a polyethylene system. A similar study has been conducted here, using a polyethylene blend containing varying quantities of DBS. In this case, much attention has been devoted to the interaction between the polymer and the nucleating agent. The choice of polyethylene is based on industry-related reasons, in that polyethylene is one of the most widely used materials in technological applications and it can be a model for future studies. This project began with studies using hot stage, optical microscopy, followed by an investigation by SEM, and finally by analysis with the DSC.

## 3.3 Material and Experimental Procedure

The following materials were used in this work: the high density, linear polyethylene (LPE) Rigidex 160-25 from BP; the low density, branched polyethylene (BPE) LD100BW from Exxon and the 1,3:2,4-dibenzylidene sorbitol, obtained from Milliken under the trade name of Millad 3095. LPE and BPE were first melted, mixed and extruded to give a blend containing 20 % LPE and 80 % BPE, termed PE. DBS was added to the polyethylene blend by dissolution in xylene and precipitation in

hexane; blends of PE containing 0 %, 0.3 %, 1 % and 3 % DBS were prepared. The above materials were characterized by differential scanning calorimetry (DSC), using a Perkin Elmer DSC7 running Pyris software. This instrument was routinely calibrated using high purity indium. Samples were normally melted at 200 °C and held at this temperature for 5 min in order to erase any previous thermal history. They were then cooled at a nominal rate of 100 °C/min to the desired temperature and crystallized up to completion. Samples for optical microscopy were prepared by melting thin layers of the blends between a glass slide and a cover slip on a hot plate at different melting temperatures. Specimens for growth rate data were crystallised at the desired temperatures in a Mettler FP82HT hot stage and the morphology evolution was recorded via a video camera. Isothermal growth rate data were obtained from PE 0% DBS in a temperature range between 113-122 °C. Samples for optical examination between crossed polars were prepared on the hot stage and quenched or crystallised at different temperatures, and images were recorded using a Leitz optical microscope equipped with a digital camera. Microstructures were examined with a Cambridge S360 SEM and a FEI Quanta FEG 600 Environmental Scanning Electron Microscope (ESEM). Specimens were prepared using an RMC CR21/MT7 cryo-ultramicrotome and then etched using 1 % w/v solution of potassium permanganate in an acid mix containing five parts of concentrated sulphuric acid, two parts of orthophosphoric acid and one part of water. Etching and sample recovery were performed according to standard procedures [66, 67].

## 3.4 Result and Discussion

### 3.4.1 Morphology: Macroscopic Optical Properties

As described in chapter 2, all the blends were heated up to 200 °C in the hot stage and then crystallised isothermally. The temperature range taken into consideration was between 112 °C and 125 °C. At first the polyethylene blend without DBS was examined. Figure 3.1 shows samples of PE crystallised isothermally at 114 °C and 116 °C. The microstructures are typical of polyethylene, and agree with other studies [16, 29]; figure 3.1(b) shows a typical banded spherulitic morphology that is space filling. Spherulites were present on the surface and some quenched effects were observed. Therefore this result provides a reference point from which to judge the morphological effect of the clarifier.

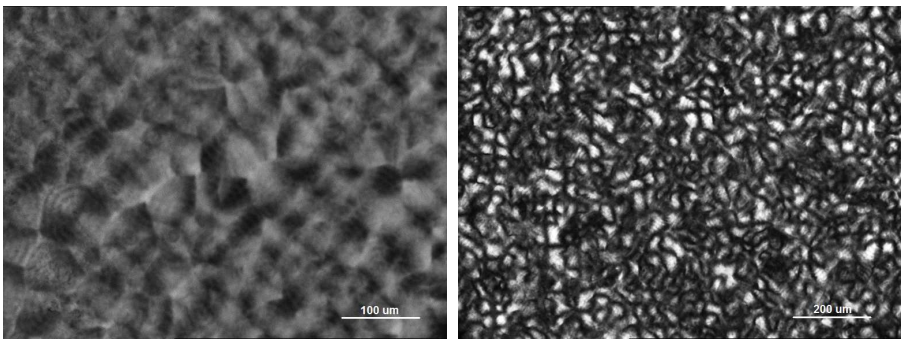


(a) spherulitic texture with maltese effect, crystallised at 114 °C.

(b) space filling spherulitic texture, crystallised at 116 °C.

FIGURE 3.1: Transmission optical micrograph (crossed polar) showing typical spherulitic morphology that develops in polyethylene blend in the absence of DBS. Sample melted at 200 °C before being isothermally crystallised

Figure 3.2 shows a series of polarised light micrographs obtained from PE blends containing two different concentrations of DBS: 1 % ( Figure 3.2 a, b, c) and 3 % ( Figure 3.2 d, e, f). Images have been taken over a broad range of crystallisation temperatures, but only three of these are included here for illustration. Figure 3.2(a) highlights the classical spherulitic features of the organogel and not of the polyethylene, as reported by other works [97, 98, 108]. Figure 3.2(d) shows a

similar fine scale pattern as Figure 3.2(a) but now there is no evidence of DBS spherulites. One of the reasons for this result could be the high concentration of fibrils, which does not allow the formation of spherulites. However, applying a slightly defocus, macrofibrils were detectable in both samples. They appear as opaques fibrils without a predominant direction. This result has suggested the presence of a 3-D network within the polyethylene with ribbon-like and ordered macrofibrils; nanofibrils were not detectable due to the technique used. All the samples were melted again at 200 °C and subsequently re-crystallised at the previous temperature. In this case, it was possible to detect again the appearance of birefringent microstructures and the presence of fibrils. Thus, the organogel was verified to be thermally reversible, as expected.

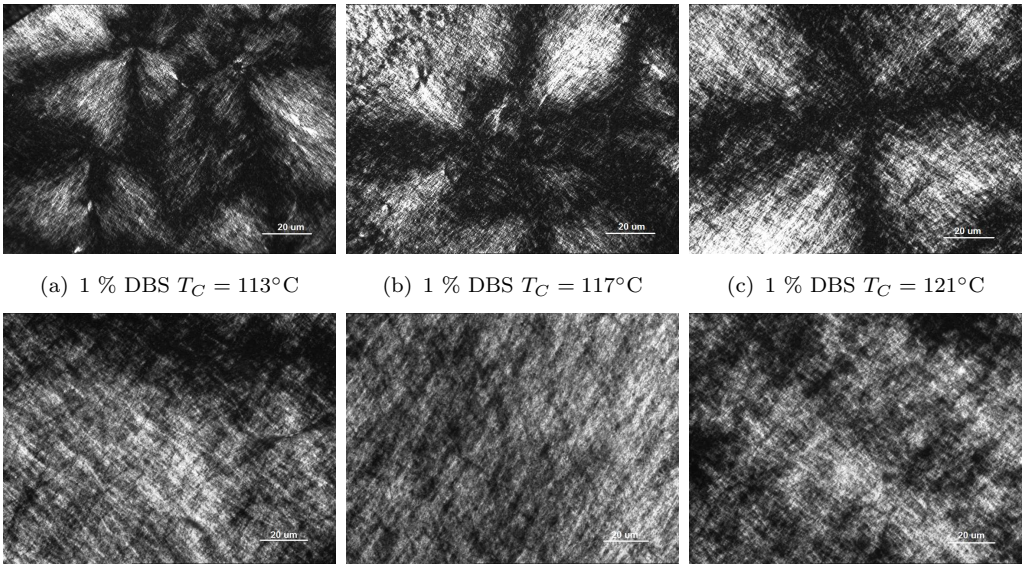


(a) 1 % DBS $T_C = 113°C$ (b) 1 % DBS $T_C = 117°C$ (c) 1 % DBS $T_C = 121°C$

(d) 3 % DBS $T_C = 113°C$ (e) 3 % DBS $T_C = 117°C$ (f) 3 % DBS $T_C = 121°C$

FIGURE 3.2: Transmission optical micrograph (crossed polar) showing morphology that develops in polyethylene blends containing 1 % and 3 % DBS. Sample melted at 200 °C before being isothermally crystallised; scale bar 20 $\mu m$.

Furthermore, during the cooling from the melt it was possible to notice the appearance of discrete macrofibrils in a temperature range between 150-180 °C in the sample with 1-3 % DBS. This suggested the formation of a network already in the melt, as proposed in rheology and birefringence intensity works by Yamasaki and Tsutumi [95] and Wiler *et al.* [98]. In contrast, samples containing 0.3 % DBS

did not show any birefringence in the polymer melt or evidence of macrofibrils in the crystallised samples. This result could be attributed to either the formation of nanofibrils that does not affect the crystallisation of the polymer as stated from Kristiansen *et al.* [106], or just to the intrinsic limitations of the observation method used. However, these preliminary results require further analysis in order to elucidate the interaction between PE and DBS.

### 3.4.2 Scanning Electron Microscopy (SEM)

In order to elucidate the activity of the nuclei at high crystallisation temperatures, an investigation of the detailed microstructure has been conducted at SEM. All the samples were prepared following the procedure described in section 2.2.3. Figure 3.3 shows the morphology of a sample without DBS at two different crystallisation temperatures. Figure 3.3(a) shows the typical morphology of the sample crystallised at 117 °C; spherulites, formed from sheaf-like embryos, developed and expanded up to impingement against other spherulites. The presence of bands with a period of ∼5 $\mu$m are evident throughout the sample, which is in agreement with the crystallisation temperature [9]. Figure 3.3(b) represents the same material crystallised at 122 °C. Although the same general behaviour occurs as in the previous sample, in this case, spherulites are separated by distinct quenched zones formed mainly by BPE. In some cases, they do not reach the classical form of a spherulite. On the border some bands are visible and they are associated with quench halos from the crystallisation temperature. Quench halos correspond to a low molecular mass LPE fraction, which crystalise onto the isothermal lamellae during quenching [30, 109].

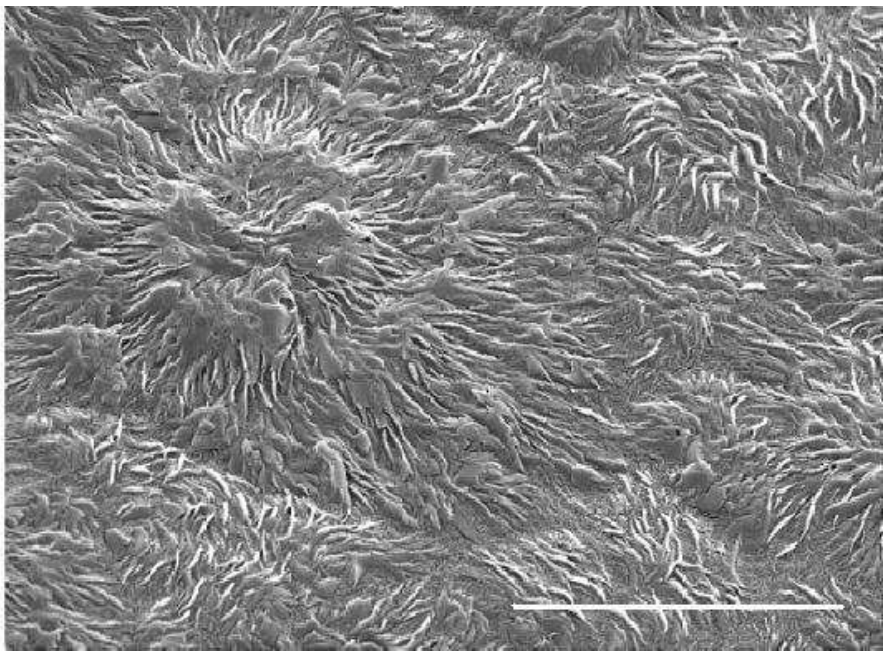

(a) PE crystallised at 117 °C: presence of fully developed spherulite; scale bar 10 $\mu$m.

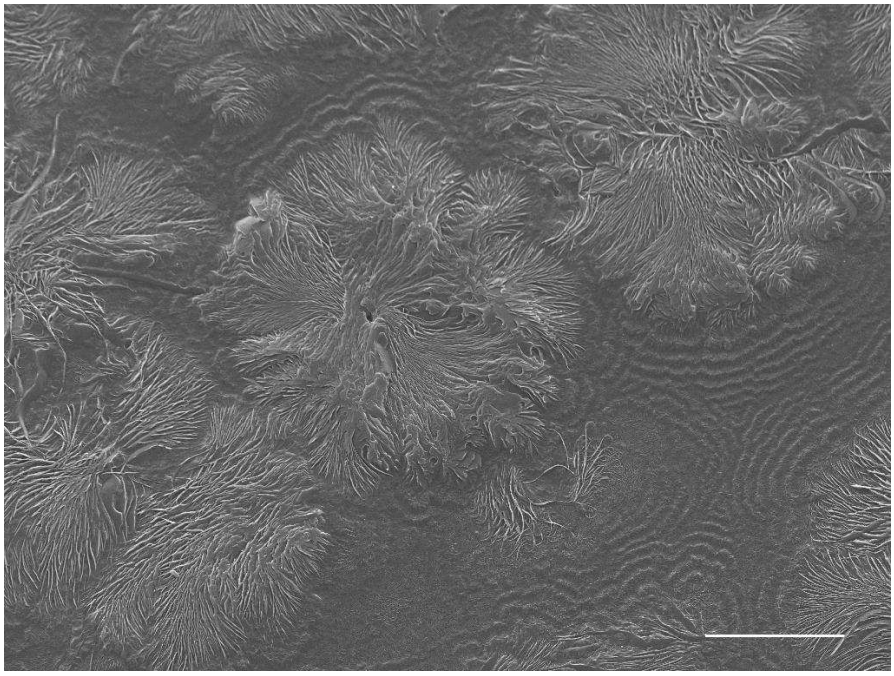

(b) PE crystallised at 122 °C: presence of spherulite separated by quenched PE; scale bar 10 $\mu$m.

FIGURE 3.3: Crystallisation of PE 0 % DBS at 117 and 122 °C.

Figure 3.4 shows polyethylene containing 0.3 % DBS after crystallisation at 122 °C. The presence of isolated axialities composed of a densely packed array of isothermal lamellae is visible. In addition, the quenched matrix includes some features which are linear in shape (see arrow) and resemble structures reported in the same system by Vaughan and Hosier [38]. The origin of these features can be related to the presence of DBS in an unknown form surrounded by crystals composed of low molar mass LPE. Figure 3.5(a), instead, shows a sample containing 1 % DBS

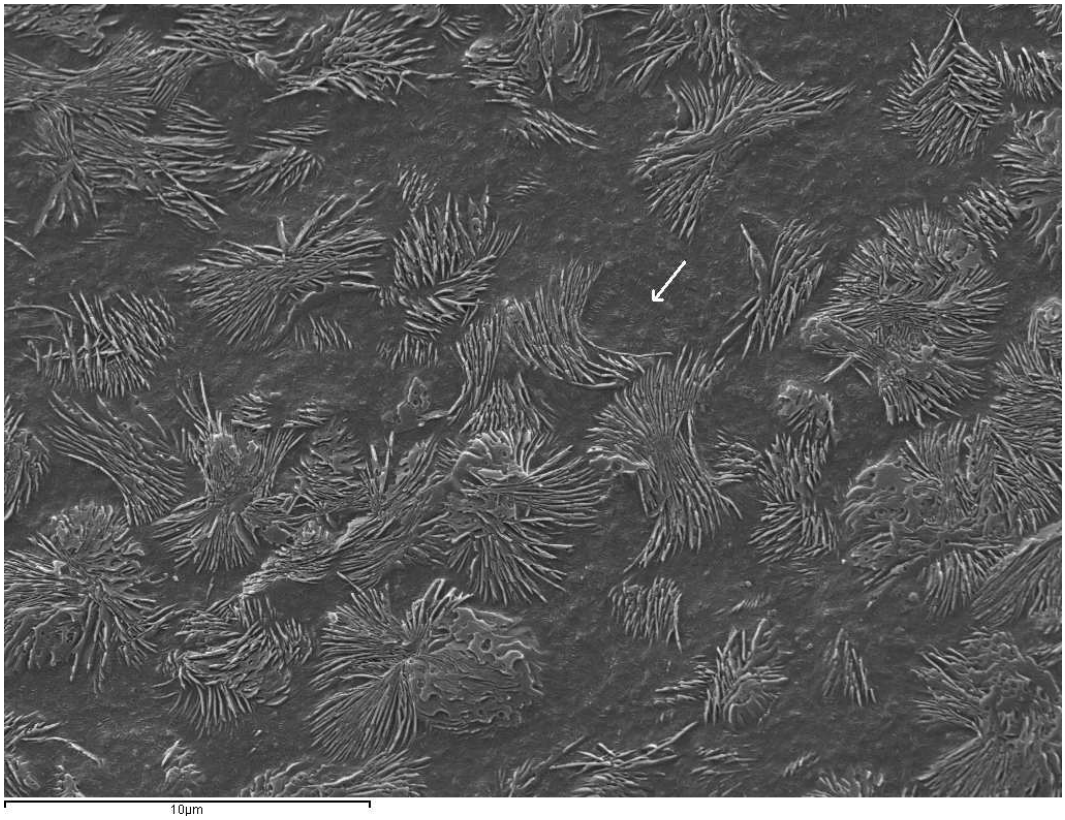


FIGURE 3.4: PE 0.3 % DBS crystallised at 122 °C.

crystallised at 122 °C. The morphology is composed of PE lamellae crystallised around clear fibrils. The diameter of the fibrils is of the order of 100 nm, which is in line with previous published data [106, 108]. Polymer lamellae grow perpendicular to the fibrils in a radial form. The nucleation and subsequent growth of the polymer on the fibrils have been studied by Nogales *et al.* [102]. They found a significant anisotropy related to the lamellar texture. They suggested that the texture developed in this way arises from so-called parent and daughter lamellae.

The first one grows perpendicular to the fibril, whilst the second one will crystallise from the parent lamella. Figure 3.5(b) shows a PE containing 3 % DBS crystallised at 126 °C. The micrograph shows the same texture as figure 3.5(a). However, in

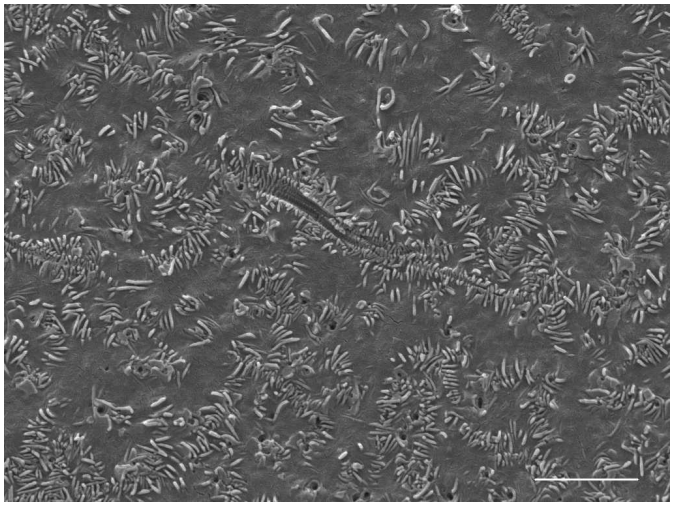

(a) PE/ 1 %DBS crystallised at 122 °C: presence of polymer lamellae crystallised perpendicular to the DBS fibrils; scale bar 10 $\mu$m

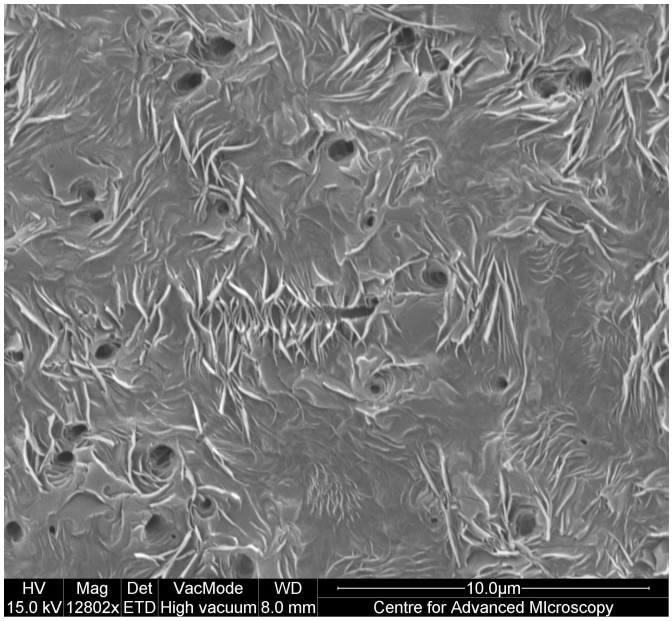


(b) PE/ 3 %DBS crystallised at 126 °C: presence of well developed lamellae perpendicular to the fibrils; scale bar 10 $\mu$m

FIGURE 3.5: Crystallisation of PE 3 % DBS from 200 °C at a rate of 100 °C/min

this case, the fibril diameters are up to 1 $\mu$m, which evidences bundle fibrils in this sample. However, the diamater can be consequence of the etching method used and therefore the fibril are much smaller than the observed. As numerous studies

have reported, the diameter of the fibrils depends mainly on the DBS concentration as a result of them bundling together, upon increasing the DBS content [106, 108].

The same specimen containing 3 %DBS was heated to 250 °C, significantly above the temperature at which the DBS melts and subsequently crystallised again at 126 °C as shown in Figure 3.6. In this case, the micrographs show an additional form of behaviour involving the formation of large craters after etching. The origin of these craters could be attributed to a collapse of the DBS fibrils into aggregates as proposed by Shepard *et al.* [49].

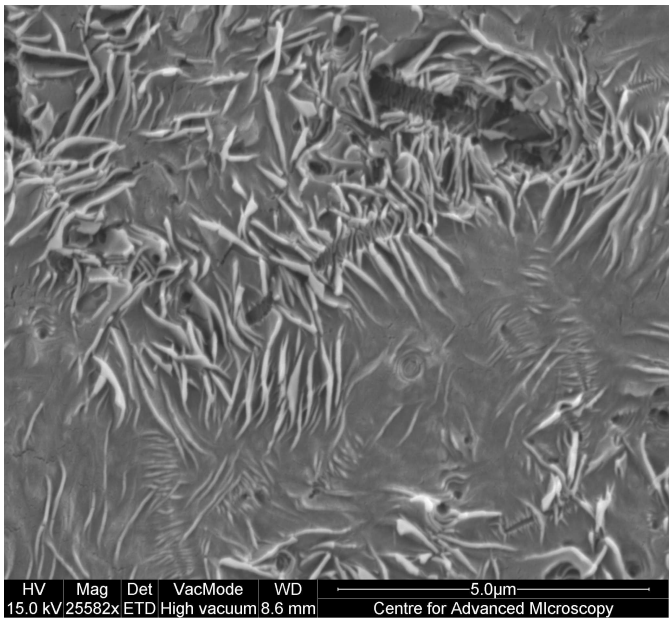


(a) PE/ 3 %DBS melted at 250 °C and crystallised at 122 °C: presence of polymer lamellae crystallised perpendicular to the DBS fibrils; some cavity are visible due to DBS aggregates scale bar 10 $\mu$m

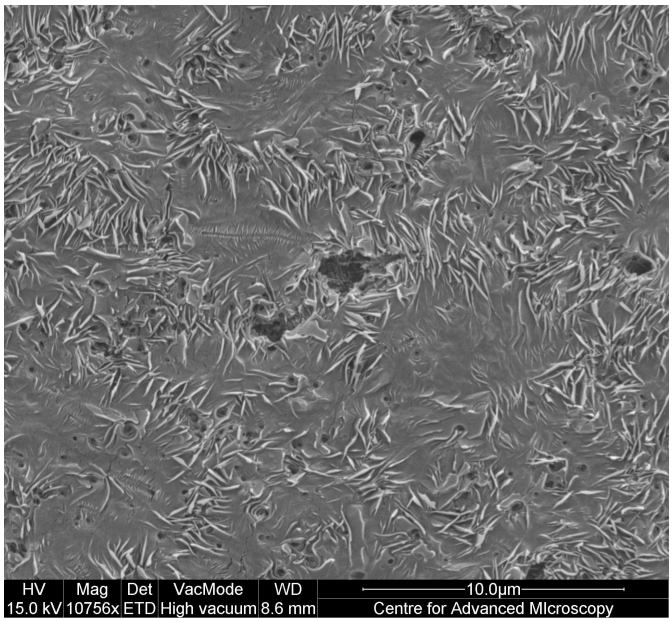


(b) PE/ 3 %DBS melted at 250 crystallised at 126 °C: presence of well developed lamellae perpendicular to the fibrils; scale bar 10 $\mu$m

FIGURE 3.6: Crystallisation of PE 3 % DBS from 250 °C at a rate of 100 °C/min

### 3.4.3 Differential Scanning Calorimetry

DSC melting scans from 50 °C to 150 °C at 10 °C/min were performed on isothermally crystallised samples of the polyethylene blends without DBS and, subsequently, on PE samples containing DBS. Figure 3.7 represents traces for the PE blends after being isothermally crystallisesd at four different temperatures. Two main melting peaks are observed. A first broad peak is detectable at $\sim$ 108 °C corresponding to BPE, whilst a second, narrow peak is detected at variable temperatures (depending on the crystallisation temperature used). The latter peak corresponds primarily to the linear polyethylene (LPE) which, at low temperatures, shows appears as a double peak. This split, rather than a double peak, is associated with co-crystallisation and reorganisation effects involving the linear material and the more linear fractions of the BPE. This finding has been confirmed by the work of Greenway [29] and is also in line with other published data [30, 110]. Moreover, Hosier *et al.* [111] explained a similar result as co-crystallisation of LPE with some linear parts of BPE. Increasing the crystallisation temperature, the co-crystallisation effect disappears and a shift of the LPE peak at higher temperatures is caused by thickening of the crystal, as previously suggested by Martinez-Salzar *et al.* [32].

With the increase of crystallisation temperature, a third peak, marked as C, becomes apparent below the crystallisation temperature and therefore must be attributed to quenched material. Consequently, the origin of this peak can be related to the LPE that crystallises onto lamellae during quenching, to form the quench halos observed in Figure 3.3(b).

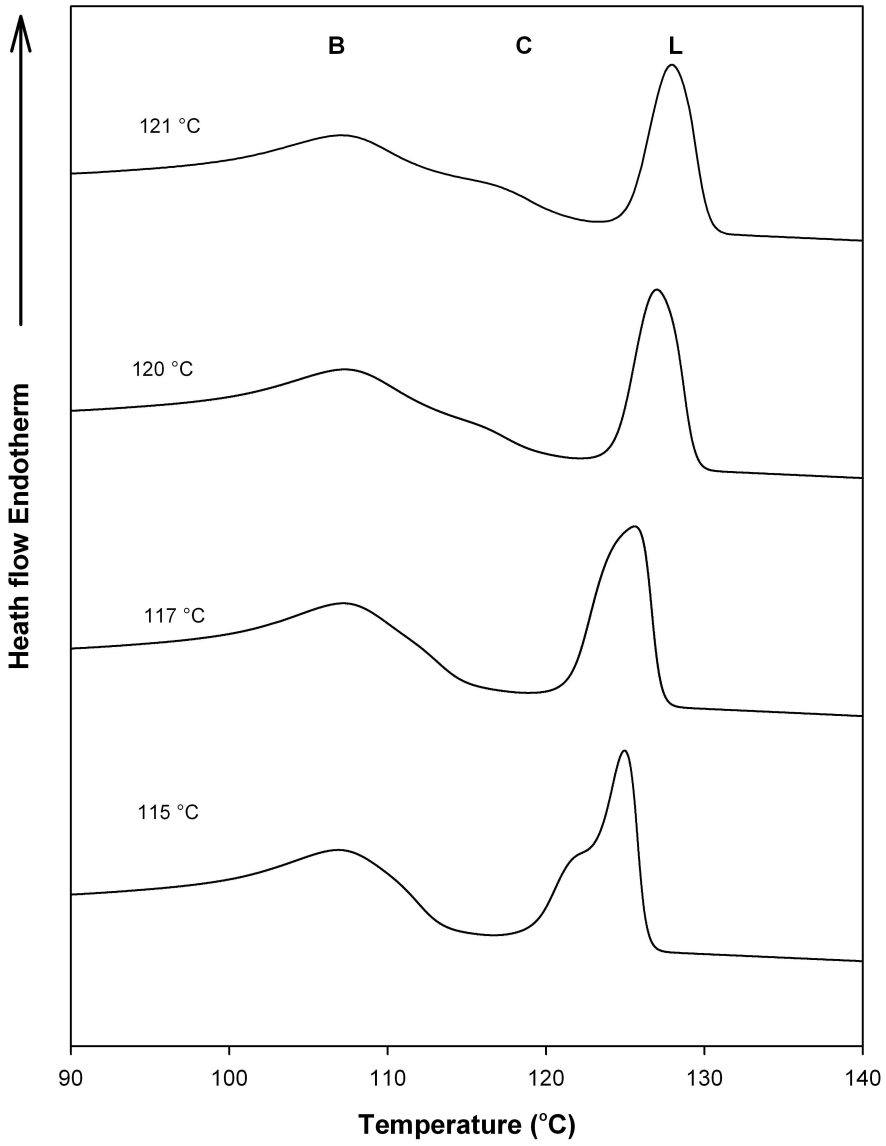


FIGURE 3.7: DSC melting curves for crystallised PE 0 % DBS.

Figure 3.8 shows melting traces for the system containing 0.3 % DBS. In this case, an additional well developed feature is present already at 118 °C and it develops progressively at higher $T_c$'s. This third peak can have two possible causes. First, it could be due to the presence of some low molar mass PE fraction that does not normally crystallise at such temperatures, as explained above. Alternatively, the cause might be the DBS network dissolving at this temperatures, but this conclusion would disagree with most of the published works [49, 102]. Vaughan and Hosier [38] examined the morphological behaviour of a polyethylene system con-

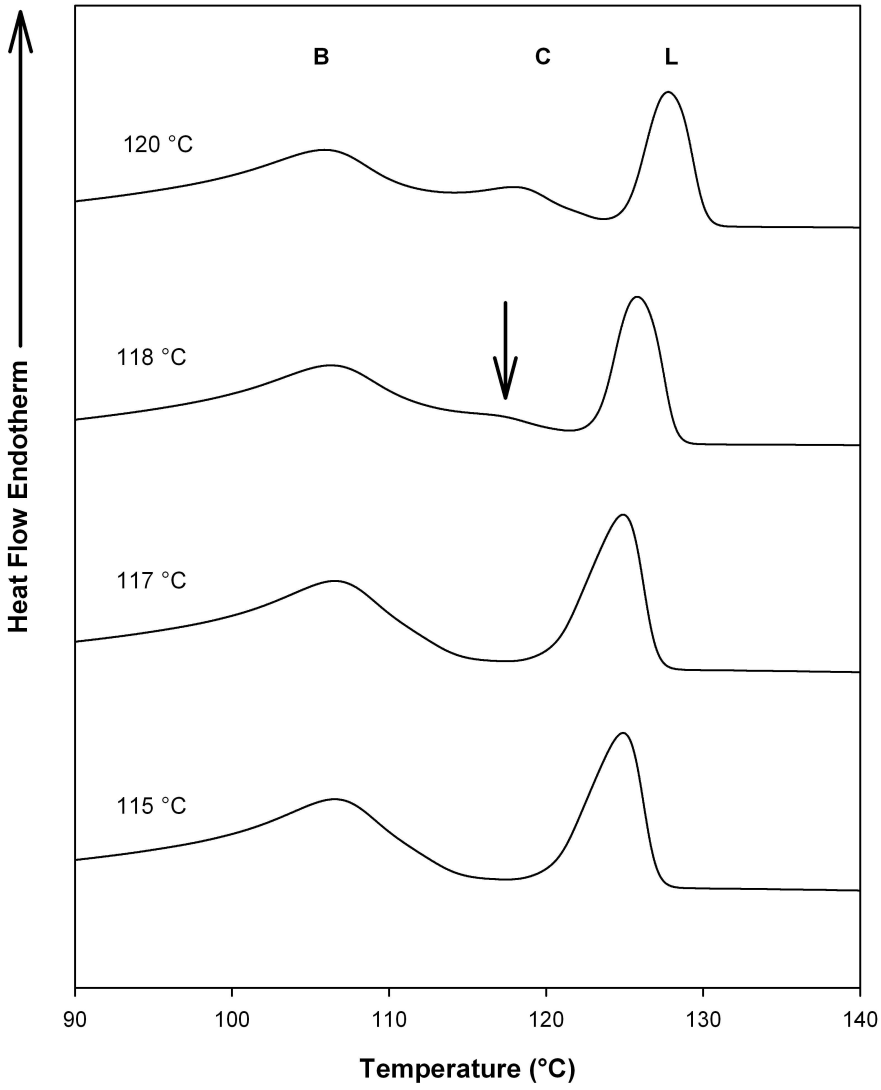


FIGURE 3.8: DSC melting curves for crystallised PE 0.3 % DBS.

taining 0.3 % DBS and suggested that low molar mass linear polyethylene fractions crystallise upon fibrils of DBS during quenching. A similar effect was observed by Martin *et al.* [41] in a propylene/ethylene co-polymer, where a progressive change in the crystallisation process was reported to occur with increasing $T_c$ leading to similar suggestion. Figure 3.9 presents melting traces of blends containing 3 % DBS (similar results were found for 1 % DBS). The LPE and BPE peaks are again present in all the traces, in addition a third intermediate peak develops as a function of the crystallisation temperature. Again, the this final peak can be

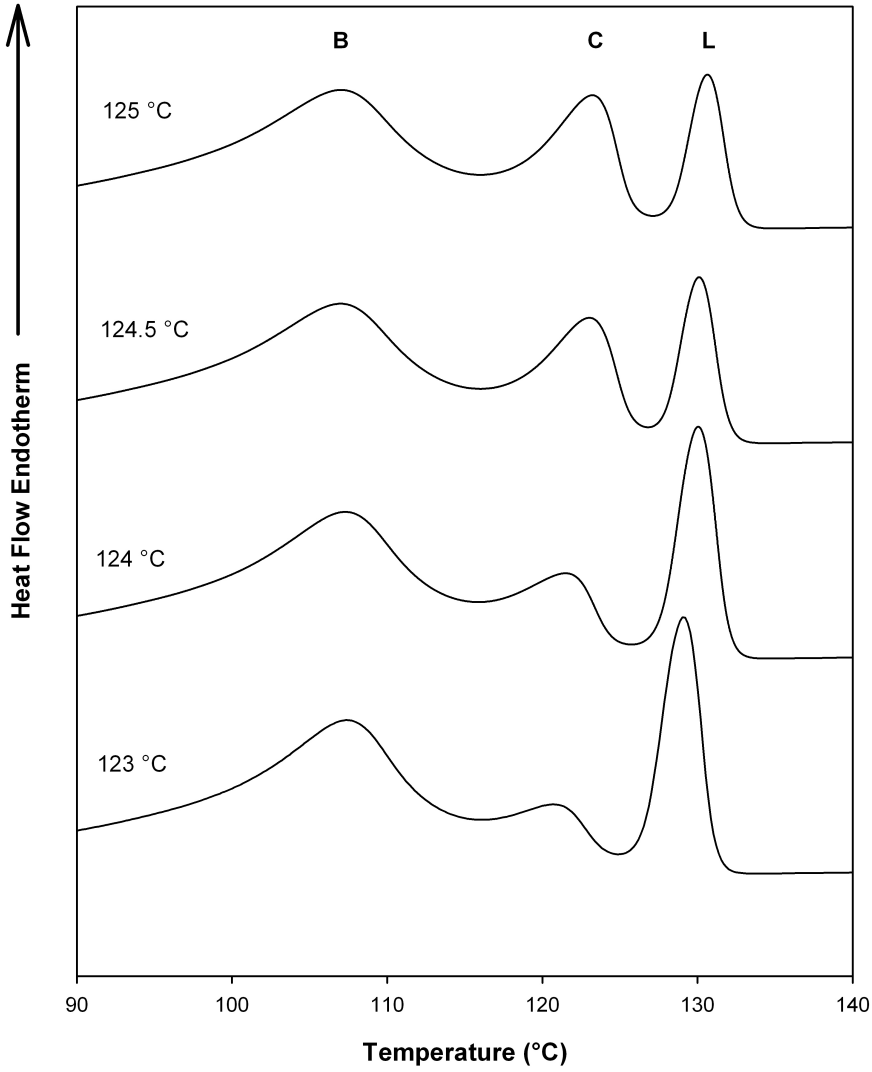


FIGURE 3.9: DSC melting curves for crystallised PE 3 % DBS.

associated with the crystallisation of polyethylene upon DBS during quenching. A further quantitative analysis was performed on the melting enthalpies, $\Delta H_m$, of the LPE peak and the intermediate peak (marked as C) from all the blend examined here. Therefore, plotting the $\Delta H_m$ of the LPE peak against the crystallisation temperature a monotonic decrease can be observed, as shown in Figure 3.10. However, when similarly plotting the enthalpy of the quenched intermediate peak, shown in Figure 3.11, a few observations can be made. First, there is no presence of the peak at temperatures below ∼118 °C. Second, whilst the increase of the co-crystallisation peak is relative low for 0 % DBS, a rapid increase can

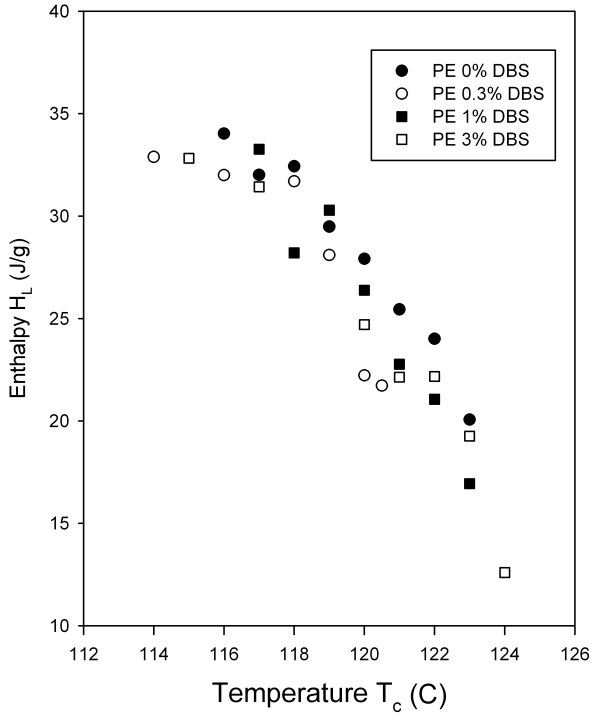


FIGURE 3.10: $\Delta H_m$ of LPE peak (L) plotted against the crystallisation temperature.

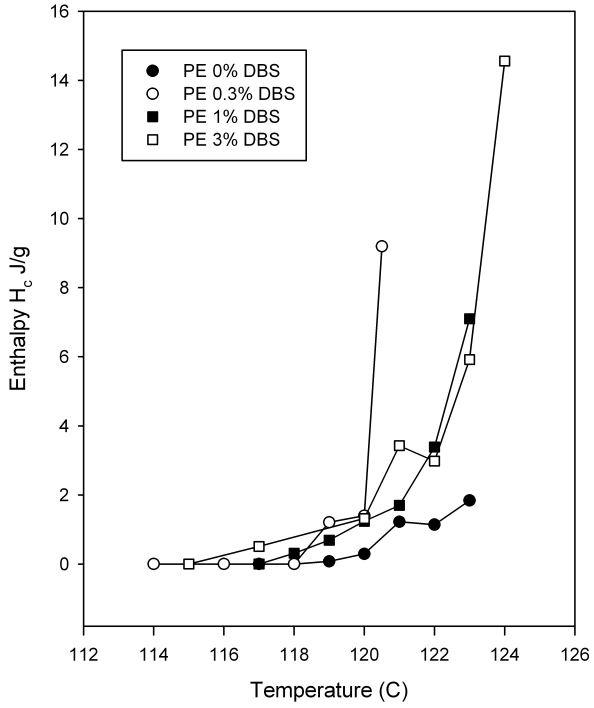


FIGURE 3.11: $\Delta H_m$ of quenched intermediate peak (C) plotted against the crystallisation temperature.

observed in the presence of DBS. Thus, this finding supports the idea that part of the LPE that normally does not crystallise at the increase of crystallisation temperature, is able to crystallise upon the presence of DBS fibrils.

In a further study the temperature of the peak corresponding to LPE has been plotted against the crystallisation temperature for all the specimens. The data have been analysed with a standard Hoffman-Weeks theory extrapolating $T_m^0$ at $T_m = T_c$. Figure 3.12 represents the scatter data from all the four blends. If a linear fit were applied to the entire set of data, an estimated $T_m^0$ of 133.5±2 °C would be extrapolated. However, this value is unrealistically low compared to most published data [10, 16, 19]. This low melting point could be originated from co-crystallisation and reorganisation effects, which affect the observed melting point at lower crystallisation temperatures, as described above. Subsequently, the data lower than 118.5 °C can be related to the co-crystallisation effect, as shown from the melting traces, and therefore were treated separately from the other data . The extrapolated values of $T_m^0$ for the data above 118.5 °C is found to be 137.8±5 °C, whilst the value for the co-crystallisation affected data is 127.9±1 °C, as shown in Figure 3.12. The uncertainties correspond to the 90 % confidence limits and clearly indicates two separate melting processes. Moreover, Marco *et al.* [112] reported that $T_m^0$ of a iPP/DBS system can be considered identical to that of iPP alone since the nucleating agent did not extent any detectable influence in the slope of the linear fitting process. Although the best fit melting point is still lower than the commonly accept theoretical melting point of 142.2 °C [10], agreement exists within experimental errors. In order to test if the method used could be responsible for the lowered melting point, the data were also analysed by applying directly the Hoffman Weeks equation, as explained in section 2.5:

$$T_m = \left(1 - \frac{1}{\lambda}\right) T_m^0 + \frac{T_c}{\lambda} = T_m^0 \tag{3.1}$$

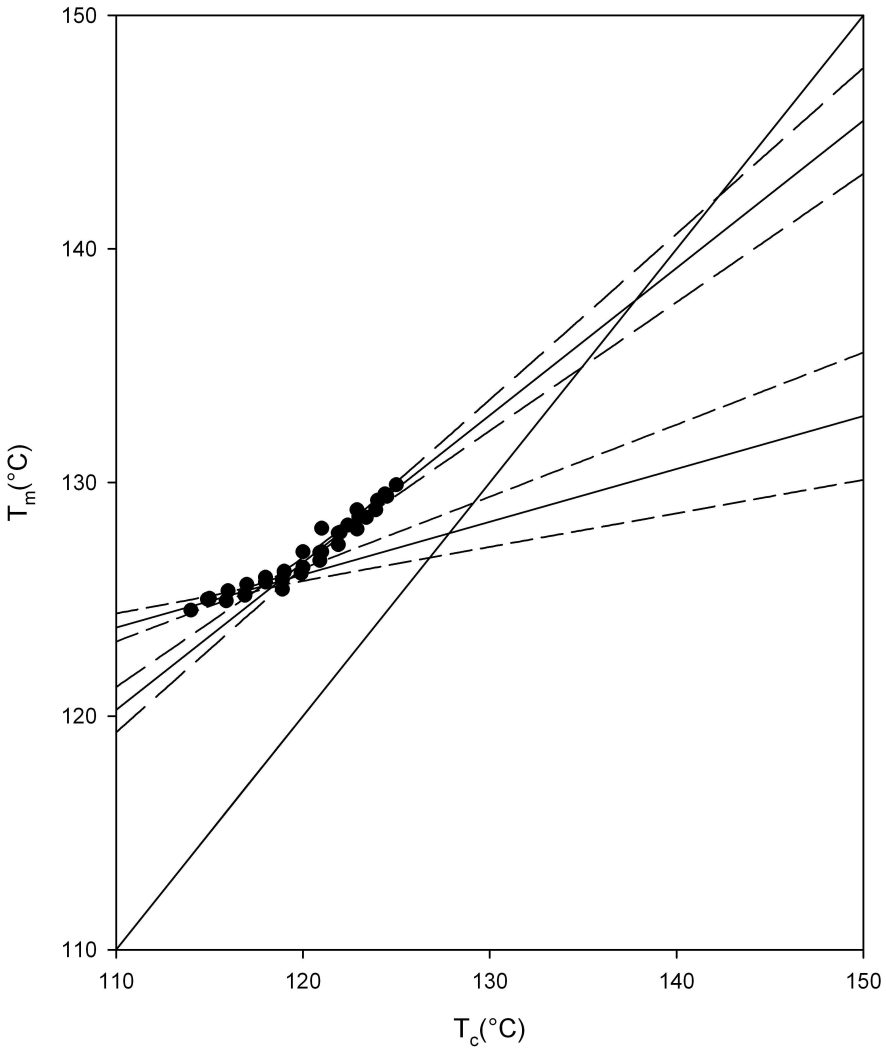


FIGURE 3.12: Plot of $T_m$ (highest-temperature melting peak L) against $T_c$ for all the systems. Scatter data show a change in the slope at around 118.5 °C due to co-crystallisation effect.

This equation can also be written as:

$$T_m - T_c = (1 - \frac{1}{\lambda})T_m^0 + \frac{T_c}{\lambda} - T_c \tag{3.2}$$

hence:

$$T_m - T_c = (m - 1)T_c + C \tag{3.3}$$

where m is equal to $\frac{1}{\lambda}$ and C is a constant. Figure 3.13 represents the linear fitting of the above equation and the value of $T_m^0$ is equal to 138.6±6 °C, just 1°C higher

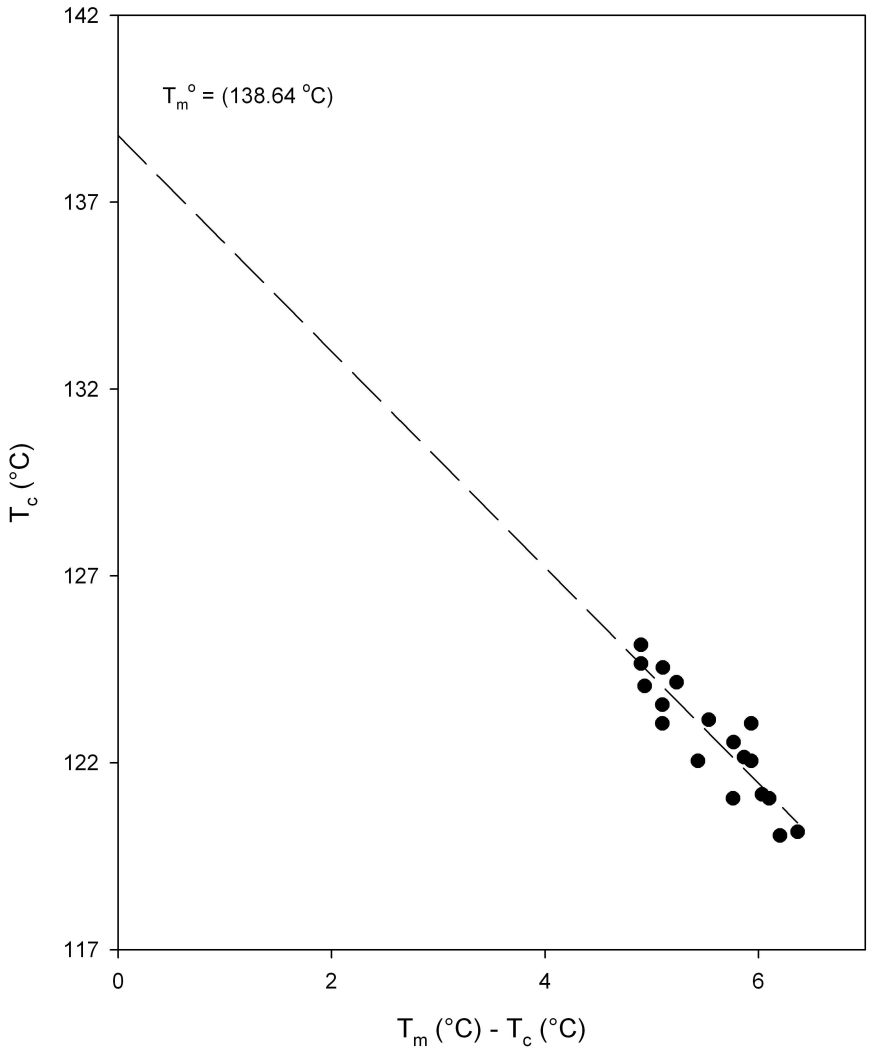


FIGURE 3.13: Plot of $T_m - T_c$ against $T_c$ for all the systems. The extrapolated value for $T_m^0$ is equal to 138.64 °C.

than the previous one, therefore it can be concluded that both methods reaches the same conclusion. Nevertheless, Marand [113] examined the melting point for polyethylene by using a linear and a non linear extrapolation and suggested that the HW approach leads to an underestimation of the equilibrium temperature, which would explain the lower melting point found here. For these reasons, the commonly accepted $T_m^0$, equal to 142.2 °C, was used throughout this work [10].

## 3.5 Effect of DBS on isothermal crystallisation

Results obtained from DSC isothermal crystallisation experiments were analysed according to Avrami theory [24, 25, 26] and its later revision [74], by applying the following equation:

$$1 - \frac{V_c}{V_{inf}} = \exp\left(-K_{exp}\left(t - t_0\right)^n\right) \tag{3.4}$$

From this equation, the values of $n$, $K_{exp}$ and $t_0$ were found. Figure 3.14(a) represents the Avrami data on a double log plot for the pure PE system. The crystallisation process is well described by the formula above. However, in the clarified systems, the gradient of the plots changes at about 50 % of the maximum crystallinity. The behaviour is often interpreted as being due to a change in the nature of the crystallisation process, possibly due to impingement of spherulites. However, in this case, it could be the consequence of a larger number of nucleation sites, as previously reported by Martin *et al.* [41], Zhao *et al.* [114] and more recently by Vaughan and Hosier [38]. For this reason, data from non linear Avrami plots up to 50 % crystallinity were fitted using the above formula and representative examples are shown in Figure 3.15. From this, the Avrami equation fits all the scattered data obtained by DSC at a crystallisation temperature of 121 °C. Also, comparing the unclarified system with the clarified ones, a marked decrease in the half time can be observed in the latter materials and the 1-3 % DBS data overlap. For example, PE 0% DBS takes 280 s to reach the half time at 121 °C, whilst PE containing 1-3% DBS takes 77 s at the same crystallisation temperature. It appears clear that such behaviour can be ascribed to the interaction of the fibrils with the matrix. Moreover, as the DBS content increases a decrease in the induction time is also observed. Mucha *et al.* [77] studied a PP system loaded with carbon black and observed a decrease in the induction time when carbon black

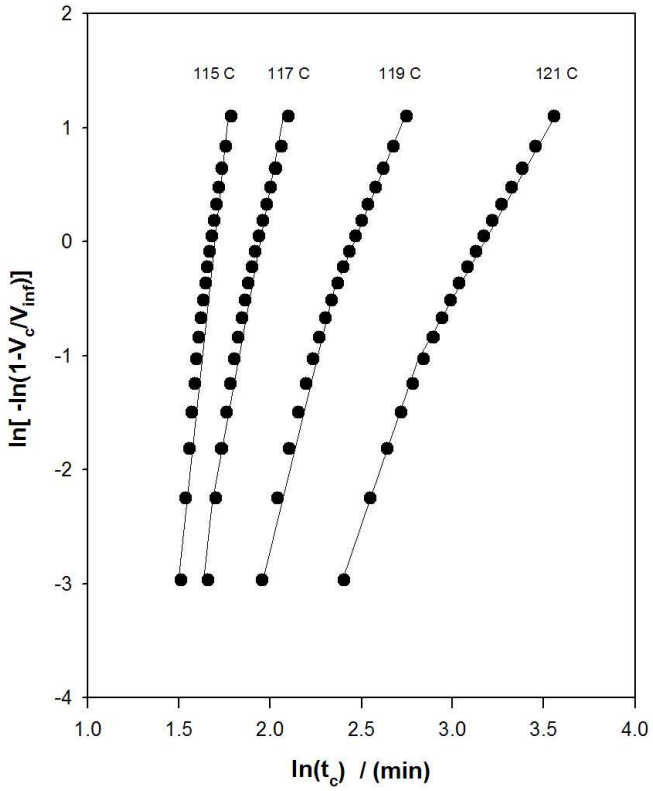


(a) Four different isothermal non linear avrami for PE 0% DBS.

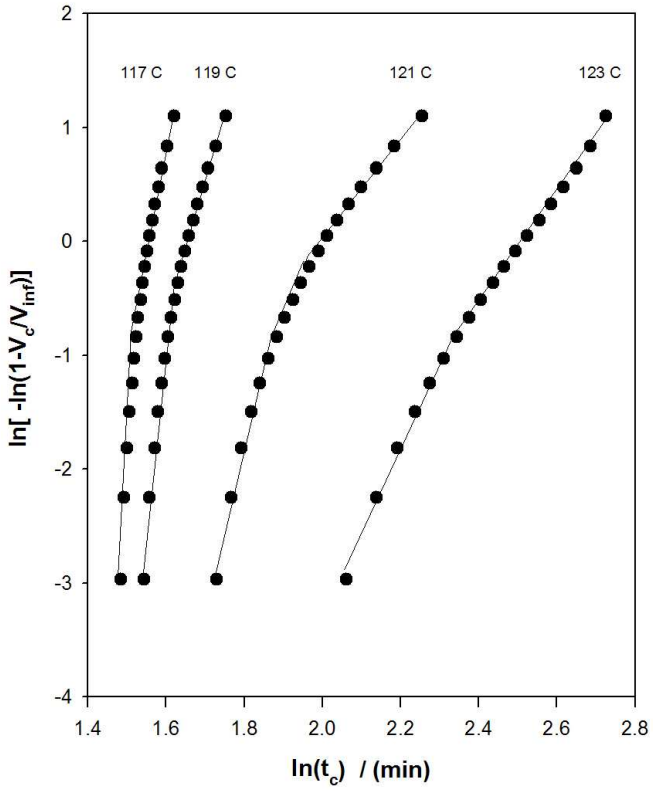


(b) Four different isothermal non linear avrami for PE 3% DBS.

FIGURE 3.14: Linear Avrami best fit lines to typical crystallisation data obtained from: a) PE 0 % DBS; b) PE 3 % DBS.

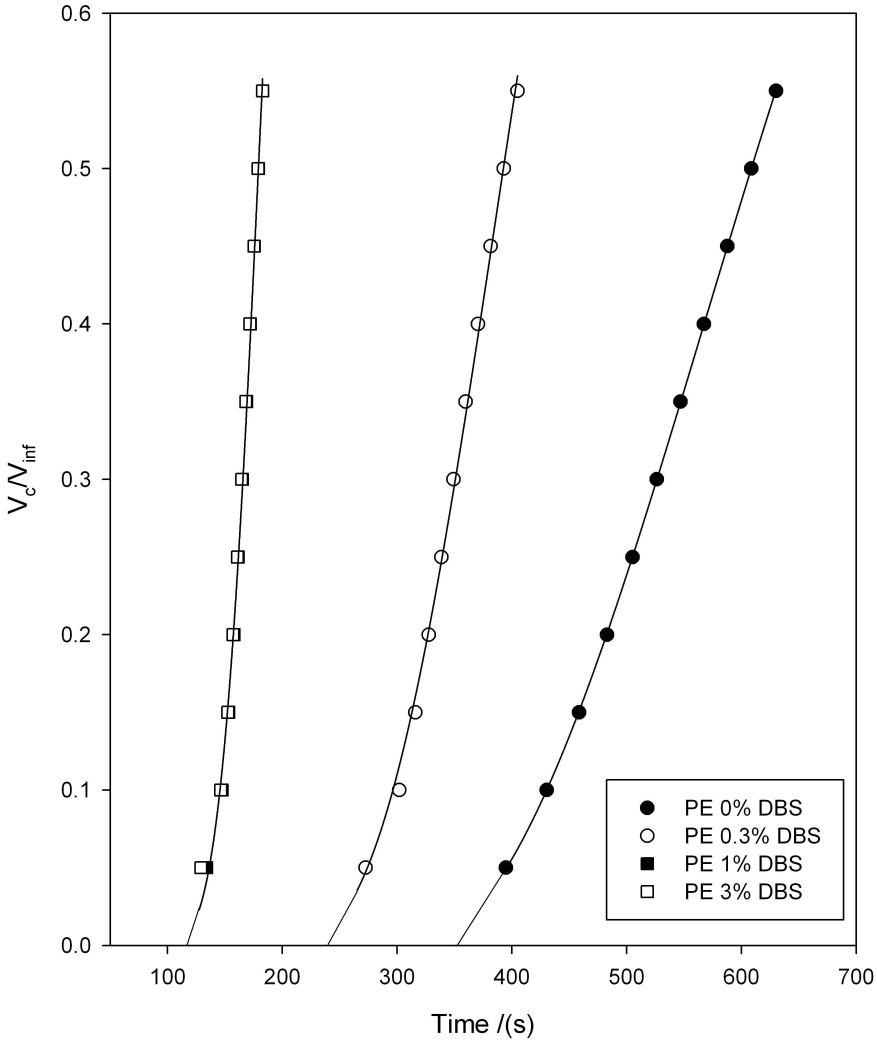


FIGURE 3.15: Non linear Avrami best lines to typical crystallisation data obtained at 121 °C.

was added. They suggested that the carbon black reduces the surface energy $\sigma_e$ and the nucleus size of the polymer crystal (decreasing the induction time), which is in agreement with the concept of a nucleating agent. Tables 3.1 and 3.2 list the parameters derived from two selected PE:DBS systems fitting Equation 1.10 to the data. The value of $n$ in both cases varies monotonically, in agreement with previous studies [41, 115]. According to Morgan, 3-dimensional growth is dominant in the case of 0 % DBS and perhaps a 2-dimensional growth for 1% DBS. However, according to Kowalewski and Galeski [74], the value of non-integer values of $n$ are associated with factors such as the nucleation mode, secondary crystallisation.

Furthermore the estimation of $n$ can be affected by the erroneous determination of the "zero" time ($t_0$), therefore $n$ can have a considerable impact on $K_{exp}$.

TABLE 3.1: Avrami parameters derived from PE 0 % DBS using the nonlinear fitting technique

| $T_C$ | $n$ | $K_{exp}$ | $K'_3$ |
|---|---|---|---|
| 114 | 3.01 | 4.16e-6 | 2.24e-6 |
| 115 | 2.77 | 5.86e-6 | 4.42e-6 |
| 116 | 2.56 | 6.86e-6 | 9.28e-7 |
| 117 | 2.48 | 3.63e-6 | 2.72e-7 |
| 118 | 2.25 | 5.11e-6 | 9.19e-8 |
| 119 | 2.31 | 1.00e-6 | 1.73e-8 |
| 120 | 2.13 | 7.47e-7 | 2.39e-9 |
| 121 | 2.16 | 2.23e-7 | 6.33e-10 |
| 122 | 1.91 | 2.81e-7 | 5.39e-11 |

TABLE 3.2: Avrami parameters derived from PE 1 % DBS using the nonlinear fitting technique

| $T_C$ | $n$ | $K_{exp}$ | $K'_3$ |
|---|---|---|---|
| 121 | 2.63 | 5.25e-5 | 1.34e-5 |
| 122 | 2.411 | 4.43e-5 | 3.81e-6 |
| 123 | 2.41 | 2.08e-5 | 7.40e-7 |
| 124 | 2.237 | 3.81e-6 | 5.41e-8 |
| 125 | 2.222 | 4.12e-7 | 2.39e-9 |
| 126 | 2.23 | 1.70e-8 | 3.65e-9 |

In addition to experimentally derived parameters, Table 3.1 and 3.2 also contain values of $K'_3$ as obtained from the theoretical assumption that the crystallisation process occurs at constant dimensionality (i.e. $n = 3$) and that it is characterised by instantaneous nucleation [74]. From this, the number of the effective nuclei, $N$, can be estimated. Figure 3.16 contains the value of $K'_3$ plotted as a function of crystallisation temperature for all the different concentrations of DBS. From Figure 3.16, a monotonic decrease in the $K'_3$ parameters is observed with increasing temperature. As the DBS content increases, $K'_3$ values also increase. Moreover, $K'_3$ can depend only on two factors, the nucleation $N$ and the growth rate $G$. If we consider that the growth rate is the same for all the systems, there must be a change in nucleation density, which would be higher in the presence of DBS.

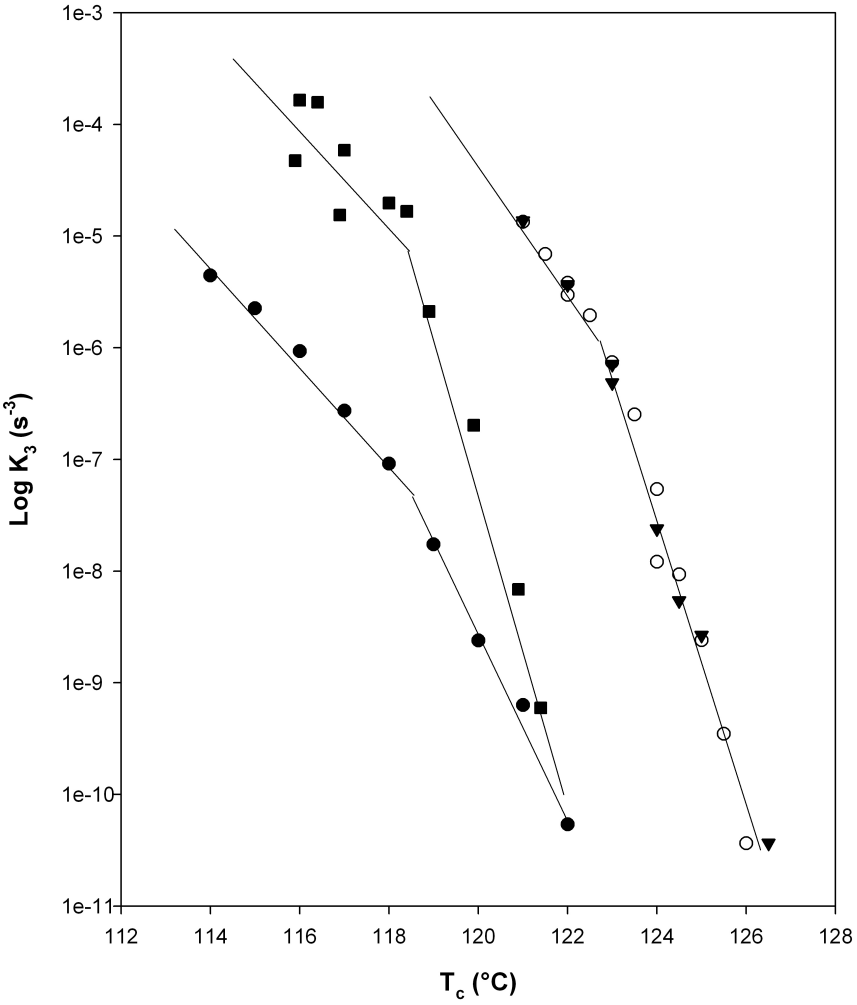


FIGURE 3.16: Variation of $K_3$ vs isothermal crystallisation for: PE (•); PE 0.3 % DBS (■); PE 1 % DBS (○) ; PE 3 % DBS (▼).

All the scatter data in Figure 3.16 follow a curve, but for simplicity, straight lines are fitted to the data. From this, 0 % and 0.3 % DBS change the slope at around 118 °C and then the lines converge, having similar $K_3'$ values, at around 122 °C. For, 1-3 % DBS a change in the slope occurs around 122 °C, followed by an abrupt decrease in $K_3'$ values. This result leads to a series of considerations. A possible explanation could be that the 0.3 % DBS acts as an intermediate case, whereas the effect of the clarifying system becomes irrelevant at the increase of crystallisation temperature. This finding would mean that the 0.3 % DBS does not act as effective nucleating agent at high crystallisation temperatures. If such

phenomenon is true, this could be related to the template mechanism suggested by other authors [38, 102, 116]. Similar conclusion could be reached for the 1-3% DBS, but the template mechanism is delayed due to presence of bundles of DBS which are still able to act as nucleation site, as seen from the micrographs. Otherwise it could be the consequence of a change in the microstructure but we will come back on this point later.

If the above data are processed further to give absolute nucleation density values, this parameter can be seen to drop progressively as $T_C$ increases, whilst in the presence of 0.3 % DBS the nucleation density remains constant up to 118 °C at $\sim$ 5x10$^{10}$ $cm^{-3}$ and then falls abruptly, as shown in Figure 3.17. Regarding the nucleation density of 1-3 % DBS, it is constant up to 124 °C at $\sim$ 3x10$^{12}cm^{-3}$ and subsequently it falls dramatically, like the 0.3 % system. This finding is in agreement with Vaughan and Hosier results on a similar system [38], where the nucleation efficiency was found to be temperature dependent. Nonetheless, these results are significant in several respects. First, the addition of 0.3 % DBS has increased the nucleation density by 3 orders of magnitude confirming the high nucleating efficiency of DBS for polyethylene. Second, a saturation occurs for DBS content more than 1 % DBS, which is in line with other works. Wilder *et al.* [98], from rheology studies on PPG/DBS, found a network saturation at 1.5 % DBS. According to their work, the increase of DBS is accompanied by a saturation due to thicker bundles of fibrils. This is in agreement with Fahaländer *et al.* [103] on PEG/DBS. Thierry *et al.* demonstrated a PE/DBS epitaxial relationship, which could provide a nucleation mechanism for PE on the fibrils. However, Mitchell and co-workers have studied the crystallisation of different polymers in the presence of DBS by WAXS and SAXS and have suggested that neither chemical interactions nor precise lattice dimensions are the real reason of the polymer nucleating on DBS [102, 116]. They have suggested that the nucleation occurs through a graphoepitaxy type mechanism [116].

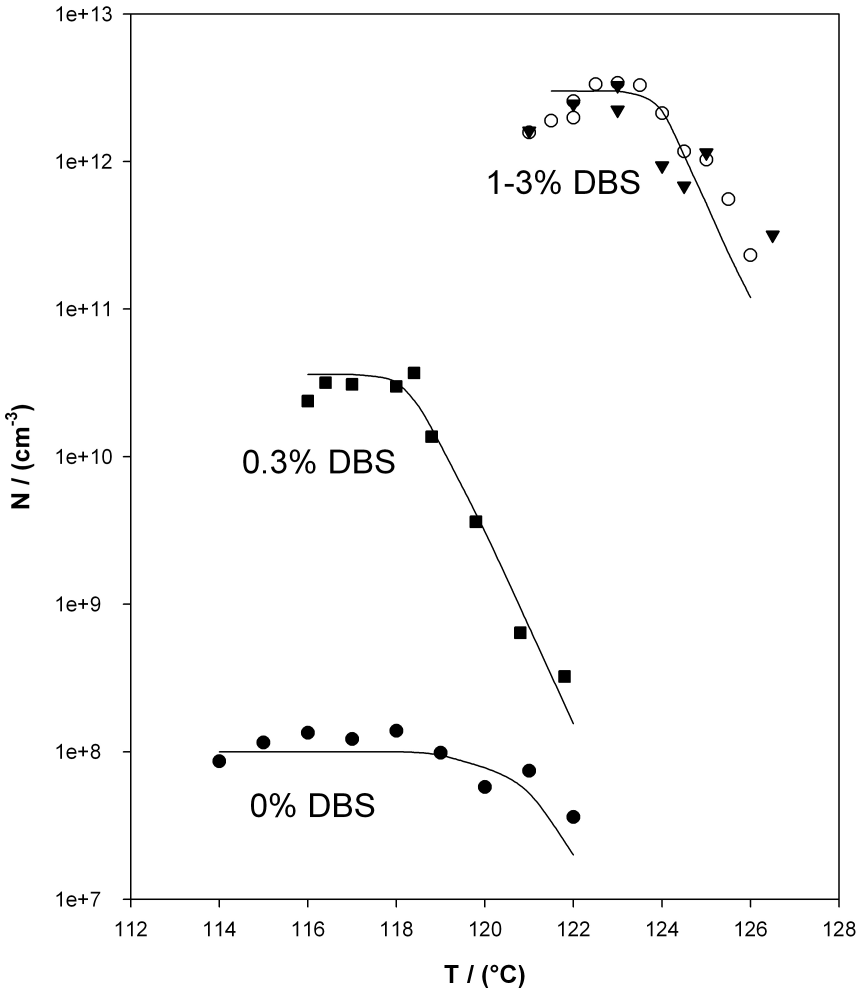


FIGURE 3.17: Calculated nucleation densities with respect to the $T_c$ in case of $k_3$ for PE 0 % DBS, PE 0.3 % DBS, PE 1 % DBS and PE 3 % DBS.

In contrast to the present result, nucleation density of a propylene/ethylene copolymer clarified with DBS increased by 3 orders of magnitude with respect to the unclarified polymer and there was no evidence of a dramatic fall in efficiency with increasing $T_c$. Martin *et al.* [41] proposed that DBS forms nucleation centres that are of larger dimensions than the critical-growth nuclei at all the temperature studied. However, in the case reported here, the nucleation densities fall for all clarifier concentrations at different temperatures. This phenomenon could be attributed to several effects. The first explanation could be the formation of thicker PE lamellae at higher crystallisation temperatures, which would not interact with smaller DBS fibrils. This is in agreement with the work of Wilder *et al.*

[98]. Again, the graphoepitaxy mechanism proposed by Mitchell and co-workers would not be efficient at high crystallisation temperature. Vaughan and Hosier [38] have recently studied a similar system to the one investigated here and they have suggested that the drop in the nucleation density is caused by increase of critical nucleus of the polyethylene such that the DBS fibril is not able to act as nucleation site. Gresco and Philips also suggested that the nucleation ability does not depend only on lattice matching and local interactions but also on available dimensions; this phenomenon was termed the template mechanism [117]. A second explanation could derived by the work of Kristiansen *et al.* [106]. They proposed a monotectic phase diagram of a binary system iPP-DBS. From this, they suggested that the DBS can phase-separate upon cooling, though the microstructure seen on 0.3 % DBS by SEM did not show this effect and therefore this hypothesis appears unlikely. A third possible explanation could be inappropriate data analysis.

From kinetic data, $n$ assumed values of $\sim$2 and following Morgan's work [27] we could be in a case of laminar spherulitic (athermal) case. According to Morgan [27], nucleation can be considered to occur at a random point P at time $t = 0$ followed by the development of concentric shells of thickness $dr$. The shell can be integrated between $r = 0$ and $r = vt$, where $v$ is the constant radial velocity of growth. Therefore, depending on the growth mode (i.e. $n = 2$) a series of case were tested as described in chapter 1. In the case of a laminar spherulitic shape in athermal condition, the thickness of the crystal layer is considered constant and using the theory of an expanding sphere, Morgan proposed that the new $K_2$ is equal to $-hG^2N$.

However, in the present work the nucleation occurs on extended fibrils and the lamellae grow radially outwards as observed from the SEM images. Therefore we propose a new 2-dimensional growth theory of a cylinder growing radially outwards from the fibril. The growing cylinder will have an area equal to $\pi r^2$, where $r$ is

the radius. Thus, $K_2'$ is equal to:

$$K_2' = -\pi G^2 N_{2D} \approx K_{exp}^{\frac{2}{n}} \tag{3.5}$$

$G$ is the linear growth rate and $N_{2D}$ is the nucleation density.

Consequently, the crystallisation data were analysed by considering the 2-D growth model. As shown from the Equation 3.5, the nucleation density can be found once known $K_2'$ and considering the same growth rate $G$. The result in Figure 3.18 shows 0.3 % and 1-3 % DBS data treated with the new theory. The fitting lines of the 3-dimensional case have also been plotted (grey dashed lines) in order to highlight potential differences between the two method. Although the nucleation density values are dimensionally different in the two approaches, it is clear that numerical offset and temperature dependencies are consistent across all specimens. Therefore, it must be concluded that changing from a 3-dimensional to a 2-dimensional growth, does not affect the temperature dependency of the PE/DBS fibrils. However, the nucleation density could be just the consequence of our assumptions and to test it further, we also compared the values of nucleation densities derived from the SEM images. In the case of 0 % DBS at 122 °C (Figure 3.3(b)), the morphology shows axialities that are several microns in lateral extent. Such micrographs suggest a nucleation density of about $10^8$ cm$^{-3}$, in line with the values reported in Figure 3.17. Comparing the nucleation density from the SEM for the 0.3 % DBS at the same temperature, the nucleation density falls around 4x10$^9 cm^{-3}$. From Figure 3.5(a), the calculated value for $N$ for 1 % DBS system at 122 °C is $\sim$ 4x10$^{12} cm^{-3}$, which again is in line with the analyses proposed above. Therefore there is no real reason to reject such values and different interpretations for the drop in the nucleation density can be proposed. The first can be related to the graphoepitaxy mechanism where DBS fibrils are unable to act as nucleation site due to the fibril size and the critical nucleus dimension. Otherwise, the dropping

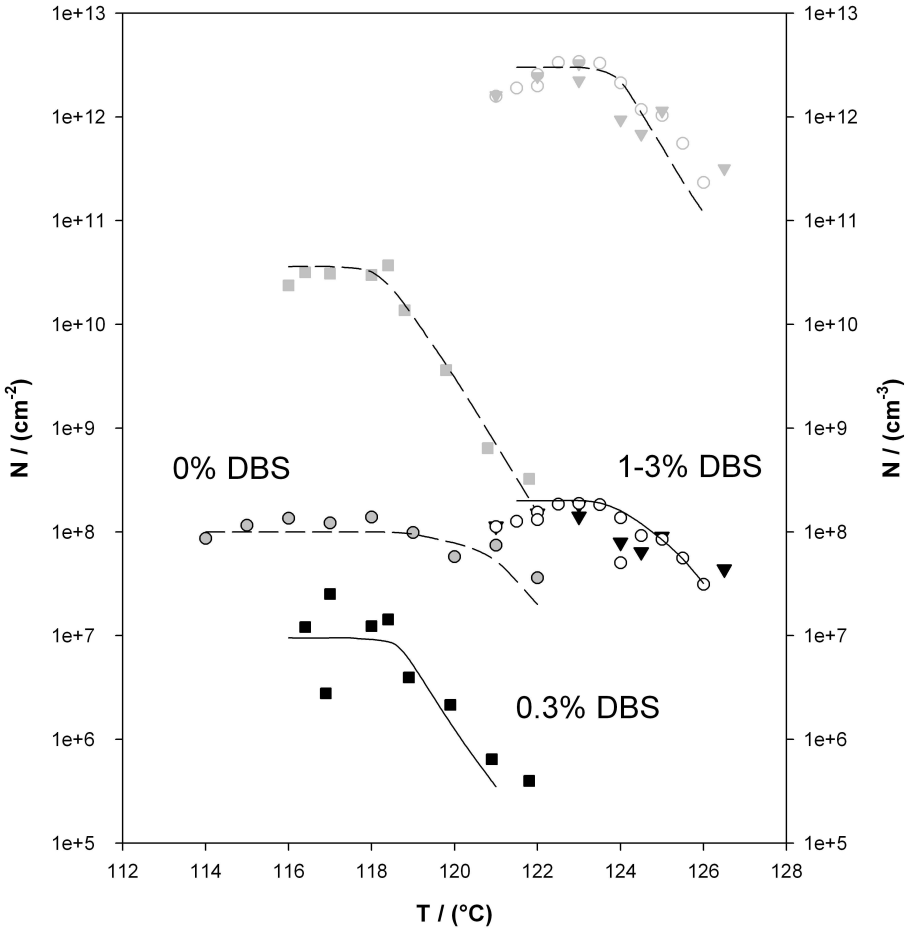


FIGURE 3.18: Calculated nucleation densities with respect to th $T_c$ in case of $k_2$ for PE 0 % DBS, PE 0.3 % DBS, PE 1 % DBS and PE 3 % DBS.

effect at high crystallisation could occur due to a transition in the crystallisation regime. Celli *et al.* [118] studied a PP system and reported a drop in nucleation density at $T_c = 138$ °C. A transition in the crystallisation regime was observed at a temperature $\sim 138$ °C, which has as consequence a drop in the nucleation density.

To test such hypothesis, a study of the kinetics of crystal growth was undertaken using the Hoffman Lauritzen equation:

$$G(T) = G_0 exp\left[-U^*/\left(R\left(T_c - T_\infty\right)\right)\right] exp\left[-K_g/\left(f T_c \Delta T\right)\right] \tag{3.6}$$

where $G_0$ is the pre-exponential factor; $U^*$ is the activation energy to transport a polymeric segment across the liquid-crystal interface, which is initially assumed to be as 1500 cal/mol; $R$ is the gas constant and $T_\infty$ is the theoretical temperature, which is assumed to be equal to $T_g$ = -30 °C [22]. The term $f = 2T_c/(T_c + T_m^0)$ is a correction factor which accounts for the temperature dependence of the heat of crystallisation. $K_g$ controls the crystal growth and is equal to:

$$K_{gIII} = K_{gI} = 4b_0\sigma\sigma_e T_m^0/\left(\Delta H_m k\right) \tag{3.7}$$

$$K_{gII} = 2b_0\sigma\sigma_e T_m^0/\left(\Delta H_m k\right) \tag{3.8}$$

where $b_0$ is the thickness of a single stem on the crystal, $\sigma$ and $\sigma_e$ are the lateral and the folded surface-free energies and $k$ is the Boltzmann constant.

Figure 3.19 represents a linearised form of equation 3.6, from which there is no evidence of a regime change, though the scatter in the data could be interpreted as falling on a slight curve. From this result an apparent change could occur at $\backsim$ 120 °C, which might explain the falls in the nucleation density of PE 0 % DBS after that temperature. The curvature could alternatively derive from the co-crystallisation effect seen up to ~118.5 °C. Moreover, we treated $U^*$ and $T_\infty$ as fitable parameters and the linearity was not improved. From this, it must be supposed that the trend is just the consequence of random experimental uncertainties and there is not evidence of regime change. Thus, the only reasonable conclusion that can be drawn from here is the one reached previously, of a reduction in the DBS fraction able to act as nucleation site for the polymer.

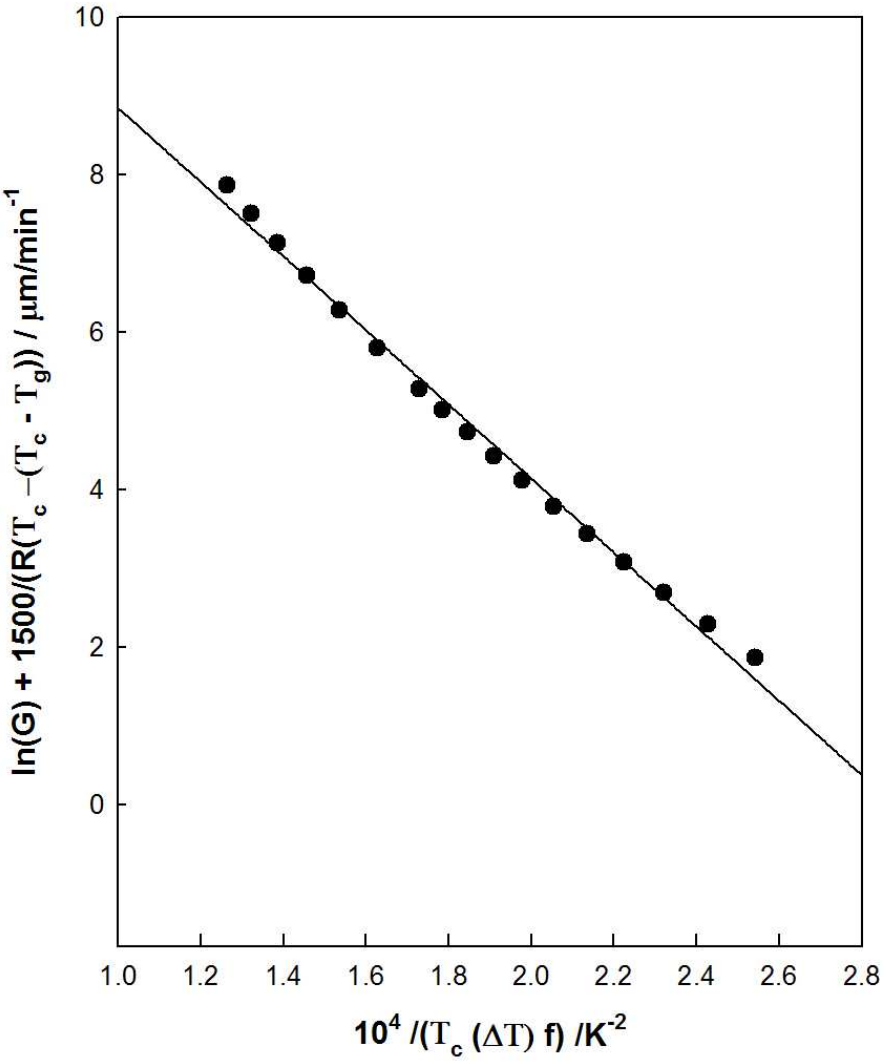


FIGURE 3.19: Variation of spherulite growth rate $G$, with $T_c$ obtained from unclarified PE.

### 3.5.1 Nucleation and Crystallisation of Nucleated Polyethylene Blends

The results so far have shown an enhanced nucleation of PE in the presence of DBS fibrils. Furthermore, a drastic morphological change as a result of the nucleation has been observed in the micrographs. In order to elucidate the influence of the fibrils on the crystallisation behaviour of the polymer, a study of the induction time has been performed. Several studies on the nucleation and crystallisation of polymers on fibers have been reported. Ishida and Bussi [119] observed a tran-

scrystalline zone between PE/PE fibers followed by spherulites. Moreover, they studied the nucleation and growth of the polyethylene by optical microscope and noticed a high nucleation ability of the fiber and associated this with the free energy difference between fiber and polymer. Recently Ratner *et al.* [120] investigated the morphology of the transcrystalline layer by microbeam synchrotron X-ray diffraction. In their work, the X-ray results revealed a gradual twisting of the lamellae at different radial distances from the fiber. Furthermore, the X-ray results supported the idea of an epitaxial mechanism between the fiber and the polyethylene chains. More recently, Okada *et al.* [121] studied the nucleation of a polyethylene/nucleating system by SAXS, which suggested that the reduced in induction time is related to the nucleus dimension. Moreover, they claim that the polyethylene nucleates in form of 2-dimensional loose fold from which macro crystals subsequently develop in 3-dimensions. Nogales *et al.* [102] found that the epitaxial growth also occurs in sheared clarified PP.

In this study, the induction time has been analysed by applying the theory of Muchova and Lednický [73, 76]. In the case of heterogeneous nucleation, the induction time, $t_i$, derives from the sum of the time necessary for the formation of the first layer ($t_h$) plus the time period for the formation of other layers ($t_s$):

$$t_i = t_h + t_s \tag{3.9}$$

The induction time can be determined as a function of the temperature $T$ and from the work of Ishida and Bussi [119], the induction time is related to the nucleation rate in the following form:

$$I(T) * t_i(T) = K = Constant \tag{3.10}$$

where $I$ is the rate of nucleation. In the theory of Muchova and Lednický the

nucleation of a polymer on a substrate is considered. From the Gibbs energy function, once the size of the nucleus exceeds that corresponding to the value of the nucleation barrier ( $\frac{\Delta G}{dr} = 0$), it will be stable. From this consideration Muchova and Lednický added an extra term to the Gibbs energy equation due to the presence of a foreign substrate, such that:

$$\Delta G = abl\Delta G_v + 2ab\sigma_{ab} + 2bl\sigma_{bl} + al\Delta\sigma \tag{3.11}$$

where $\Delta G_v$ is the change in the Gibbs energy of crystallisation of a unit volume, $\sigma_{ab}$ and $\sigma_{bl}$ are the specific surface energy parameters, and $a$, $b$ and $l$ are the dimension of the growing nucleus ( as shown in Figure 3.20). Differentiating $\Delta G$

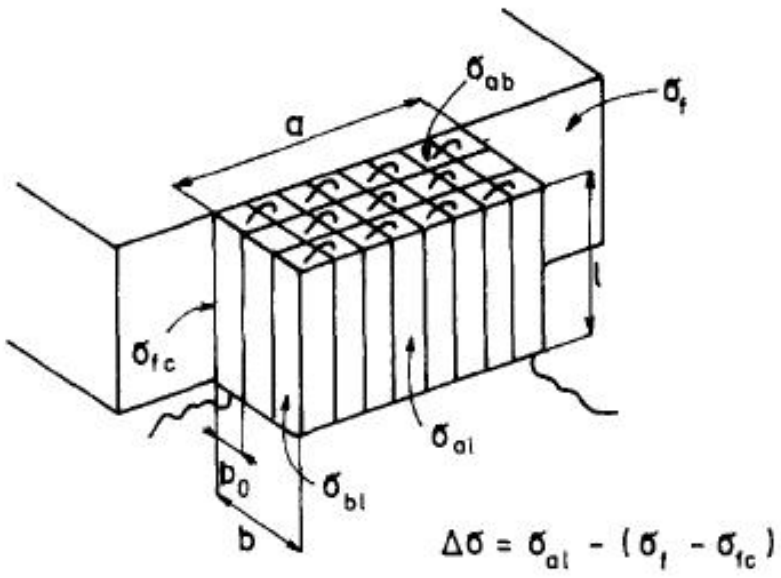


FIGURE 3.20: Growth of a heterogeneous crystallisation nucleus a,b, l nucleus dimensions, $b_0$ thickness of layer,$\sigma_{ab}$ and $\sigma_{bl}$ are the specific surface energy parameters, $\sigma_f$ is the specific surface energy of the foreign substrate in the polymer melt and $\sigma_{fc}$ is the specific Gibbs energy of the foreign substrate-crystal interface. From [73]

as a function of $a$, $b$ and $l$, the critical nucleus can be found and once substituted into Equation 3.11 the critical value of the change in the Gibbs energy for the

heterogeneous nucleation can be written as following:

$$\Delta G^* = 16\sigma_{ab}\sigma_{bl}\Delta\sigma(T_m^\circ)^2/(\Delta H)^2(\Delta T)^2 \tag{3.12}$$

Afterwards, a hypothetical dimension of nucleus is considered for the formation of the first layer with two variable dimensions, $a^*$ and $l^*$ and a fixed $b_0$ ( the thickness of the single layer). Moreover these workers considered the induction time to be equal to $t_s$ in the case of high temperature. From Equation 3.9:

$$t_i = (b_h/b_0 - 1)exp(\Delta G_s + \Delta G_\eta) \tag{3.13}$$

where $\Delta G_s$ is the change in the Gibbs energy of the critical secondary nucleus and $\Delta G_\eta$ is the activation energy of diffusion. $\Delta G_s$ can be easily found applying Equation 3.11 without the last term. Once all the terms are substituted in Equation 3.13, the induction time can be written in a logarithmic form:

$$ln(t_i\Delta T) = lnQ + K/(T\Delta T) \tag{3.14}$$

where $K$ and $Q$ are respectively:

$$K = \left(4\sigma_{b1}\sigma_{ab}b_0T_m^0/kT\Delta H_m\right) \tag{3.15}$$

$$Q = ln\left(C\Delta\sigma T_m^0/\Delta H_m\Delta T b_0\right) \tag{3.16}$$

Figure 3.21 shows plot of $ln(t_i\Delta T)$ against $10^4/(T_c\Delta T)$ where $\Delta T = (T_m^0 - T_c)$, assuming 142.2 °C, as explained previously [78, 122].

From Figure 3.21, it is clear that the slope $K$ does not vary significantly between the unclarified and clarified systems. Rather, $Q$ decreases with the increase of DBS in the polymer matrix. This result provides evidence of the efficiency of nucleating

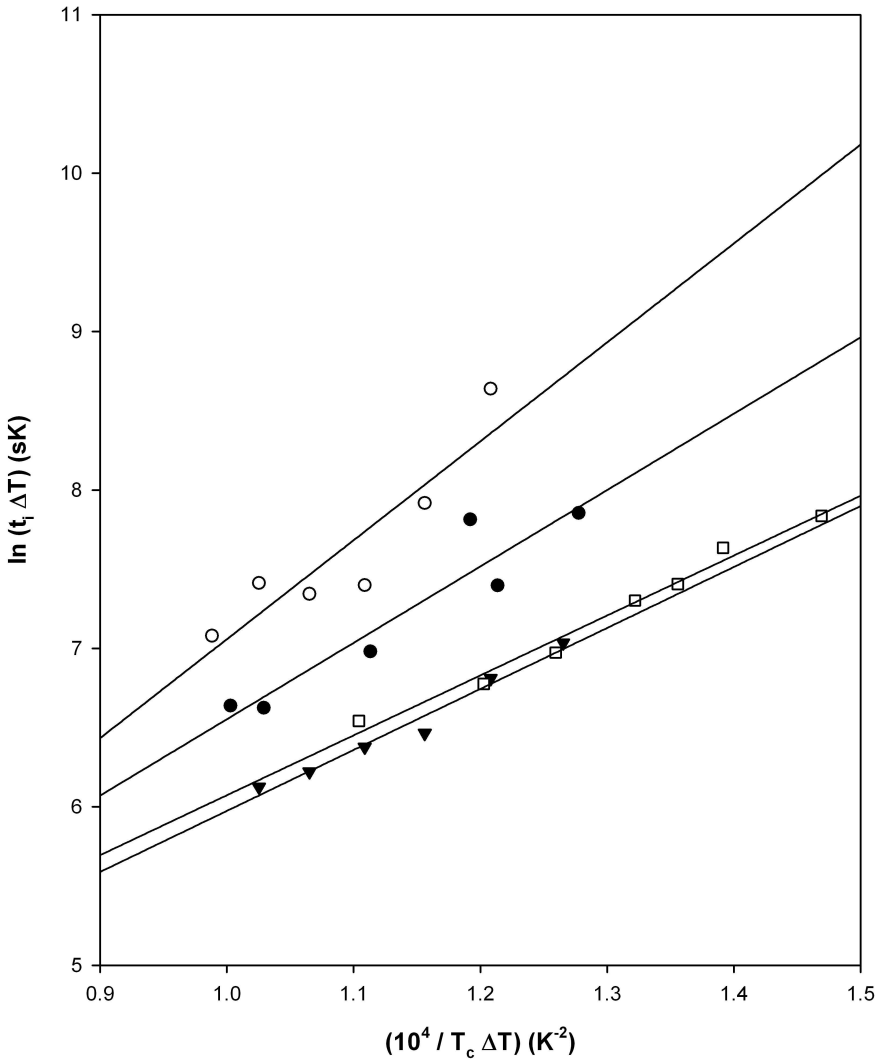


FIGURE 3.21: Analysis of crystallisation induction times for PE O% DBS (○), PE 0.3 % DBS (●), PE 1% DBS (▼) and PE 3 % DBS (□)

agent on the polymer but, according to Muchova and Lednický, does not imply a change in the nucleation process, which is in contradiction with the conclusion drawn from the nucleation density studies. $Q$ is effected by the energy parameter $\Delta\sigma$ which suggests only a decrease in the activation energy in the presence of DBS. From Figure 3.21 it can be clearly seen that the PE 0 % DBS results are similar to 0.3 % DBS, whilst 1 % DBS and to 3 % DBS are indistinguishable. This can suggests that there is a saturation in the nucleation process around 1 %, as has been shown previously for nucleation densities (figure 3.17). A similar result was

found by Martin *et al.* [41] but in their case the result was not as distinct.

However, a detailed consideration of the assumptions and approximations present in the above theory reveals a number of issues. For example, in the case where $\Delta\sigma \rightarrow 0$ (when an external substrate is not present) the intercept would tend to infinity. This is in contrast with Muchova and Lednický experimental test and our analysis. Moreover $\Delta G_\eta$ is treated as a constant term, which is not the case due to its dependence on the temperature $T$. From all these considerations we propose a different approach to consider the induction time. The induction time is equal to the time for the polymer to form a critical nucleus on the substrate. Therefore from Equation 3.9, the induction time is equal to:

$$t_i \approx t_h \tag{3.17}$$

$t_h$ is equal to:

$$t_h = A_1 exp\left[16\sigma_{b1}\sigma_{ab}\Delta\sigma\left(T_m^0\right)^2\right] / \left[kT\left(\Delta H_m \Delta T\right)^2\right] exp\left(\Delta G_\eta / kT\right) \tag{3.18}$$

and substituting $t_h$ in Equation 3.17, it can be expressed in logarithmic form as:

$$ln(t_i) = lnA_1 + 16\sigma_{ab}\sigma_{bl}\Delta\sigma(T_m^0)^2 / \left[(\Delta H)^2 (\Delta T)^2 kT\right] + \left([\Delta G_\eta (\Delta T)^2]\right] / \left[(\Delta T)^2 kT\right] \tag{3.19}$$

From the above equation it can be clearly seen that it assumes the form of a parabola. However, the weight of the last term at high temperature can be considered negligible; hence the equation can be written as:

$$ln(t_i) = lnA_1 + 16\sigma_{ab}\sigma_{bl}\Delta\sigma(T_m^0)^2 / \left[(\Delta H))^2 (\Delta T)^2 kT\right] \tag{3.20}$$

Figure 3.22 shows a plot of $ln(t_i)$ against $1/(T_c \Delta T^2)$. From the regression data presented in Table 3.3, it is evident that there is considerable uncertainty in the

intercepts. From Equation 3.18, $A_1$ is a constant and, therefore, should be independent of DBS concentration. Intercepts weighted according to the standard error was therefore calculated and the regression lines were recalculated using the mean of the intercept as a constraint ( see Table 3.4).

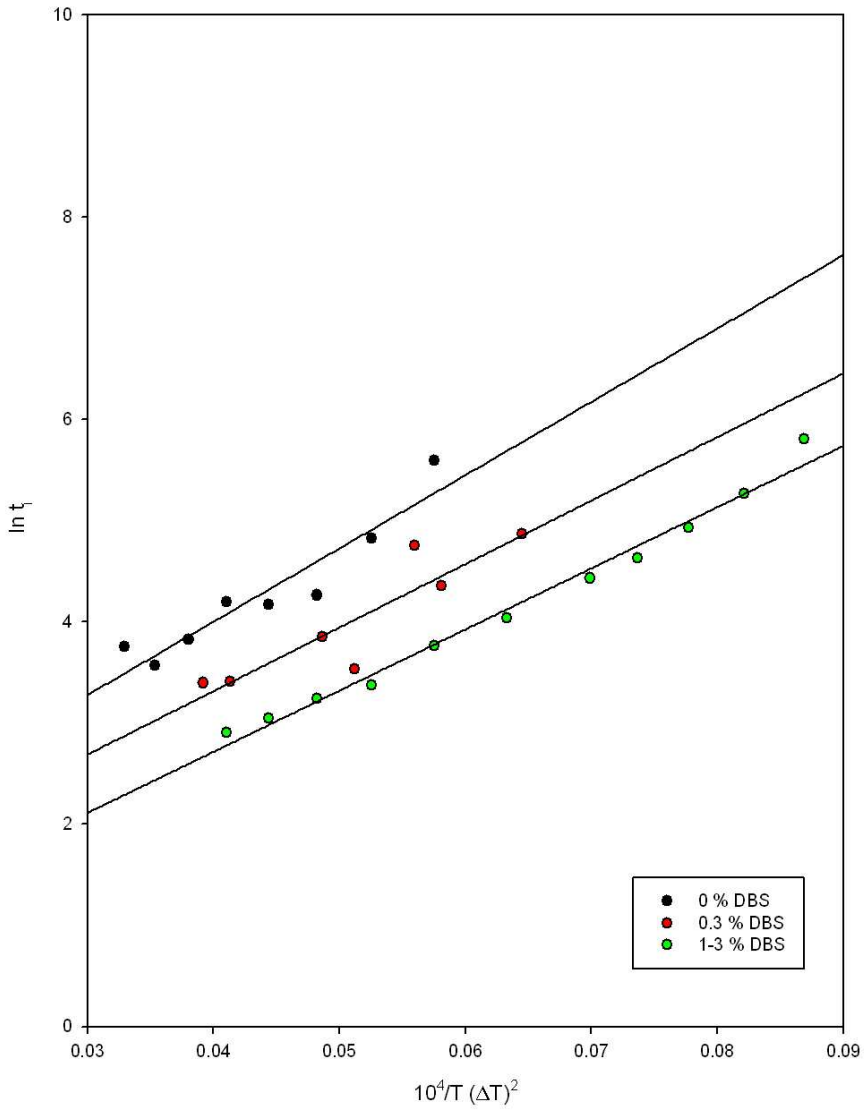


FIGURE 3.22: Analysis of crystallisation induction times for PE O% DBS (○), PE 0.3 % DBS (●), PE 1% DBS (▼) and PE 3 % DBS (□).

From the results, it is evident that $\Delta\sigma$ decreases as the percentage of DBS increases up to 1 % DBS. That is, $\Delta\sigma$ decreases as the fibril size increases. However, a quantitative evaluation $\Delta\sigma$ did not result in any sensible number, compared

TABLE 3.3: Value of the slope and the intercept for the new induction time.

| **Material i =1,2,3** | **a (slope)** | **± Δ a** | $m_i$ **(intercept)** | **±** $\Delta m_i$ |
|---|---|---|---|---|
| PE 0 %DBS 1) | 72.4474 | 10.4538 | 1.1045 | 0.4650 |
| PE 0.3 %DBS 2) | 62.7593 | 13.5695 | 0.8069 | 0.7050 |
| PE 1-3 %DBS 3) | 60.4371 | 2.4310 | 0.3000 | 0.1584 |

TABLE 3.4: Value of the slope and the intercept for the new induction time, using the mean of the intercept as constrain.

| **Material i =1,2,3** | **a (slope)** | **± Δ a** | $m_i$ **(intercept)** | **±** $\Delta m_i$ |
|---|---|---|---|---|
| PE 0 %DBS 1) | 88.0043 | 10.4538 | 0.4010 | 0.5465 |
| PE 0.3 %DBS 2) | 70.4700 | 13.5695 | 0.4010 | 0.7280 |
| PE 1-3 %DBS 3) | 58.9297 | 2.4310 | 0.4010 | 0.1619 |

to published data [121], even though the above analysis suggest, qualitatively, that the addition of DBS results in a reduction in $\Delta\sigma$, and that 1-3 % DBS are indistinguishable. However, 0.3 % DBS shows an intermediate case between 0 % and 1-3 % DBS. This result leads to a few interpretations. First, 0.3 % could result different from 1-3 % DBS simply because there is not enough fibrils in the system to form a network to act as nucleating agent. Nogales *et al.* [102] studied iPP containing different levels of DBS by SAXS and noticed a strong lamellar orientation in the presence of DBS ( above 0.5 % DBS). This was not the case for the polymer containing 0.3 % and therefore they suggested that DBS network at really low concentrations may be loose such that the overall lamellar orientation is undetectable. Otherwise, the above result could be explained by considering that at 0.3 % the DBS could exist in a different form from that in the 1-3 % DBS. This hypothesis can be supported by the non direct evidence of fibrils in the optical and SEM images. Moreover, some quenching experiments were carried out in the attempt to image DBS fibrils in the melt. Each specimen containing DBS has been melted at 150 °C, held at this temperature for 5 min and subsequently quenched into isopentane ( cooled down to - 80 °C with liquid nitrogen). Figure 3.23 shows the relative results for each specimen tested. The sample containing

0 % DBS show no features, as expected due to the rapid quenching rate. 1-3 % DBS show well developed network of fibrils throughout the sample, whilst 0.3 % again exhibits no feature. This result could suggest that at 0.3 % the DBS exists in a non birefringent (i.e. disordered) state as supposed before, or simply that the presence is so sporadic that we are not able to detect it.

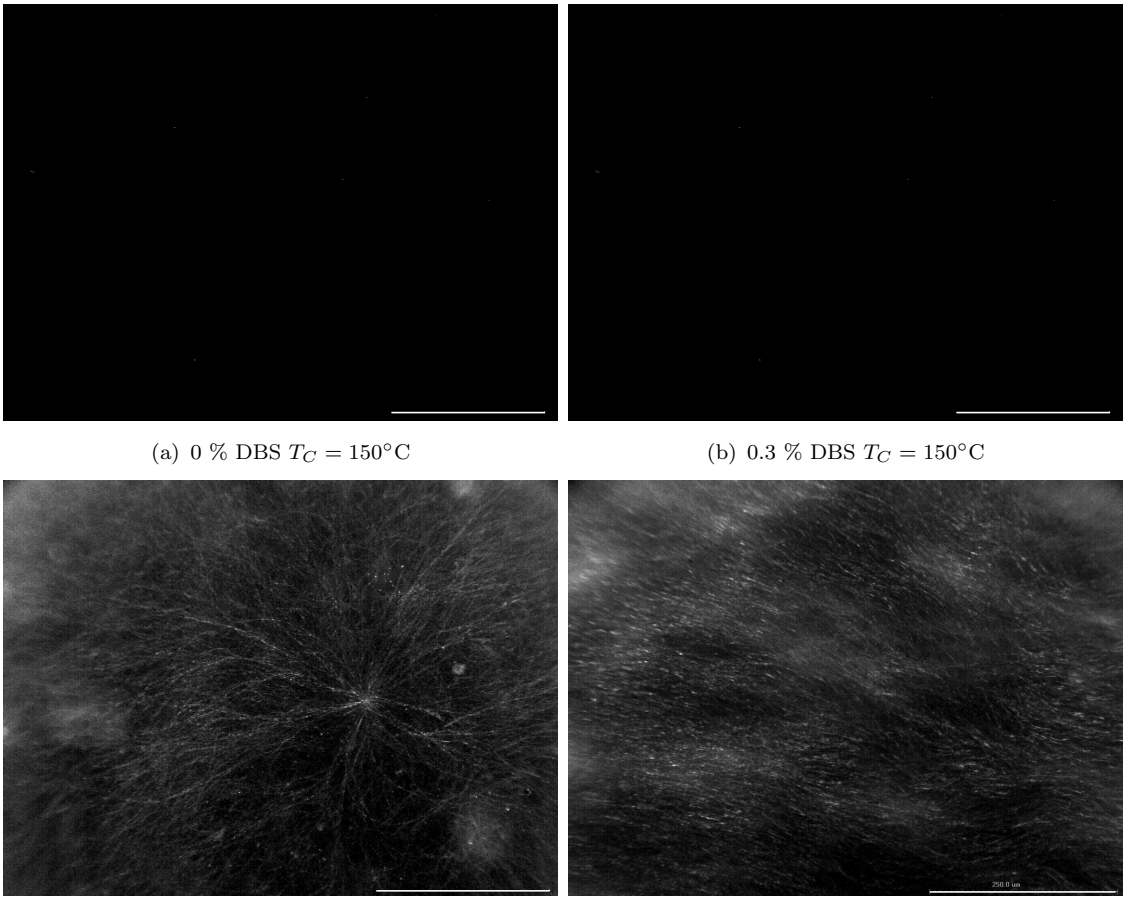

(a) 0 % DBS $T_C = 150°C$ (b) 0.3 % DBS $T_C = 150°C$

(c) 1 % DBS $T_C = 150°C$ (d) 3 % DBS $T_C = 150°C$

FIGURE 3.23: Transmission optical micrograph (crossed polar) showing morphology that develops in polyethylene melt containing 0-0.3 % and 1-3 % DBS. Sample melted at 150 °C before being quenched in isopentane at - 80 °C; scale bar 250 $\mu m$.

From the results presented here, it is possible to conclude that DBS fibrils are able to decrease the surface energy and become site of nucleation for polyethylene nuclei. However, the nucleation ability is temperature dependent because of a increase in the critical nucleus size and as consequence a reduce fraction of DBS

is available as nucleation site , as seen from the nucleation density experiments.

## 3.6 Conclusion

Enhanced nucleation of polyethylene has been shown to occur over a range of DBS concetrations and, as previously observed by Vaughan and Hosier [38], a temperature dependency was shown to occur for all different amount of DBS studied here. Whilst a decrease in nucleation density was observed at around 124 °C for 1-3 %, this was not the case of 0.3 % DBS. In fact, the latter has shown an abrupt decrease in the range of 118-120 °C and it is suggested that this may be related to the ratio of the size of the critical polymer nucleus and the DBS fibrils. This would explain also the decrease of 1-3 % at higher temperature due to the presence of bundle of fibrils as directly observed from SEM images and supported by other works [106]. A second element of this study concerned an analysis of the effectiveness of DBS as nucleating agent by studying the induction time using Muchova and Lednický's theory. However, we believe that some of their assumptions can alter the result. Therefore we proposed an alternative approach and observed a decrease in the surface energy between the DBS and the polymer crystal. Moreover, the surface energy was found to be dependent on the amount of DBS, but we were not able to explain if this is the result of a different nature of the DBS at low percentage or just due to a loose network as suggested by others [102].

# Chapter 4

# Charge Transport in Unclarified and Clarified Polyethylene

## 4.1 Introduction

In the previous chapter the nucleation and crystallisation of a polyethylene blend on DBS fibrils was described. A range of morphologies was produced and crystallisation of polyethylene on DBS fibrils was demonstrated. In particular, it was seen that the nucleation density was increased by some 5 order of magnitude for polymer containing 1-3 % DBS, although, a temperature dependency was observed above particular temperature, depending on the amount of DBS present. In this work, the same PE/DBS systems are considered and the dielectric properties are investigated by the pulsed electro acoustic (PEA) technique.

Under high voltage (HV) conditions, trapped or low mobility electrically charged species within the bulk of polymeric materials may develop, resulting in a localised electric stress enhancement. Space charge is believed to be a major contributing factor leading to initiation of electrical trees and consequently to catastrophic dielectric breakdown under an applied electrical field [123, 124]. The space charge

distribution in polyethylene has been shown to have a strong dependency on additives, crosslinking and oxidant products [125, 126]. Nonetheless, the morphology of the polymer appears to play an important role in increasing the breakdown strength of the material [127]. Studies have shown a significant increase in electrical strength in the presence of spherulites in the bulk [111, 127]. At the same time, an increase in the size of spherulites can decrease significantly the electric strength of the material [128]. Dibenzylidene sorbitol was shown previously to increase the number of nuclei in polyethylene and as a result the microstructure that develops is considerably different from that of the unclarified polymer. Recently Li *et al.* [129] have studied space charge behaviour in a low density polyethylene (LDPE) containing 0.3 % sorbitol and demonstrated improved space charge distributions in the presence of the nucleating agent. They attributed the improvement in space charge characteristics to the introduction of shallow traps.

In this work, the space charge behaviour will be studied using a wider range of DBS concentrations in order to study the influence of the DBS and the morphology of the polyethylene on the transport of charges under an applied electric field. Samples were prepared at the Specac press of 200 $\mu$m in thickness and subsequently crystallised in an oil bath at 117 °C. This specific crystallisation temperature was chosen because all PE/DBS samples investigated showed a maximum in nucleation density and, morphologically all the samples exhibited space filled microstructures. Space charge distributions were measured using the pulse electro-acoustic (PEA) system as described in section 2.7.3. Calibration was carried out below a threshold voltage, at which no space charge is present in the bulk. In this case an optimum was found at 2 kV. For each PE/DBS system, space charge accumulations were conducted at 5 kV for a period of 1 h at room temperature. After this time, the voltage was removed and the discharge process was recorded over 1 h. During the charging phase, data were acquired every 30 s over the first 5 min, and subsequently, every 5 min for the remaining time. However, in order to represent the

space charge behaviour in a clear manner, each of the figures presented below includes only data recorded after 30 s, 5, 30 and 60 min after the voltage application. Moreover, for a clearer interpretation of these results, data with voltage on and off were gathered during the charging process. Subsequently, the samples were short-circuited upon the removal of the external voltage and the charge decays were monitored for 1h. In this phase, data were acquired every 5 min.

## 4.2 Space Charge

The data shown in Figures 4.1 show how the distribution of space charge in a crystallized PE blend 0 % DBS evolves with time during charging and discharging period at room temperature. Figure 4.1(a) reveals that after 30 s almost no charge is visible near the electrodes or in the bulk. After 5 min some positive charge injected near the cathode is visible, which is termed heterocharge, and it increases with the time of application of the electric field (see arrow) up to 30 min. Heterocharge is defined the charge having the polarity opposite to that of the adjacent electrode, whilst homocharge is the charge having the same polarity as the electrode. However, in order to have a closer profile of the net charge, measurements with voltage off ( Figure 4.1(b)) were also taken during the charging process. Figure 4.1(b) reveals an increasing presence of heterocharge close to the cathode, which gradually moves into the bulk, together with a small amount of heterocharge near the anode. Charge formation in the bulk depends on several factors, including electrode injection, charge movement and the trapping characteristics of the material [125]. On short circuiting after the 60 min voltage application, the accumulated charge from the cathode starts decaying, as can be observed in Figure 4.1(c), but most charge still remain trapped after 60 min. These results show that the LPE/BPE blend contains some deep charge trapped in the bulk, which is consistent with the work of Li *et al.* [129] who suggested that the formation of this

kind of charge is associated with short branch chains and impurities. However, Suh *et al.* [130] studied space charge evolution in an LDPE system and suggested that the heterocharge is determined by the polymerisation process. These authors suggested that oxygen and peroxides used for the polymerisation may behave like ionic species, increasing the overall heterocharge in the bulk.

Figure 4.2 compares space charge distributions in the three blends containing different amounts of DBS as a function of time during the charging phase and with voltage on. From this, it is evident that in the case of the 0.3 % DBS system (Figure 4.2(a)), heterocharge is injected from the cathode. Moreover, these data sets lie on top of the one another, indicating that the space charge distribution is established within the first 30 s. Nevertheless, the charges in PE 0 % DBS and PE 0.3 % DBS are of the same type, but they increase to a different extent. This is in agreement with the findings of Li *et al.* [129] and supports the idea that the charge re-distribution improves in the presence of 0.3% DBS . Figure 4.2(b) presents the space charge behaviour of PE 1 % DBS. These data differ markedly from the previous systems, in that an increase of injected homocharge near the cathode is observed, followed by an increased in heterocharge near the anode. Moreover, an increase with the time is observed, reaching a plateau at 30 min. A similar trend can be seen in figure 4.2(c)); in this, the homocharge next to the cathode is bigger than that seen in figure 4.2(b) and the charge next to the anode decreases from the one seen in 1 % DBS.

The change from heterocharge to homocharge in the latter two systems may be attributed to the presence of an established 3-dimensional network of DBS macrofibrils, as observed by SEM. A second explanation could be the injection of positive charge from the anode, which could enhance the diffusion of negative charge into the bulk from the cathode. From these data, it is not possible to distinguish the evolution of the space charge in the materials due to the presence of the charge at the electrode. The only consideration that can be made is that when the 3-D

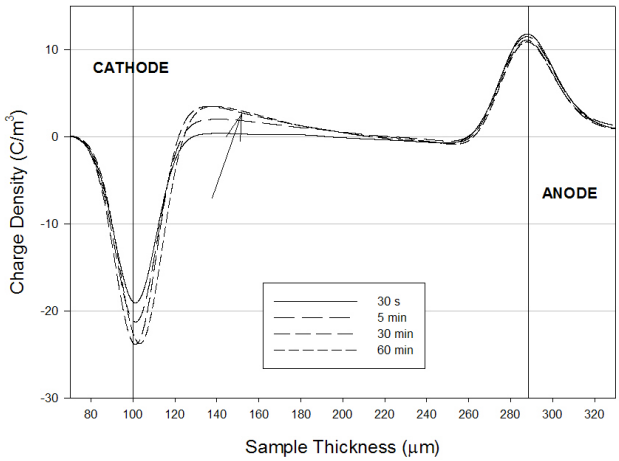


(a) PE crystallised at 117 °C: measurements taken with volt ON.

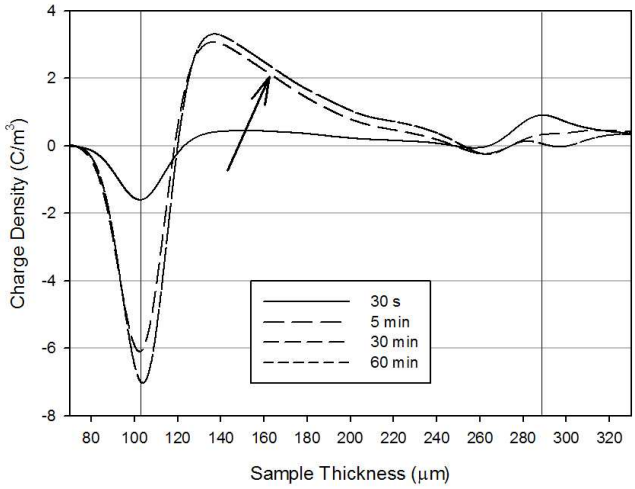


(b) PE crystallised at 117 °C: measurements taken with volt OFF.

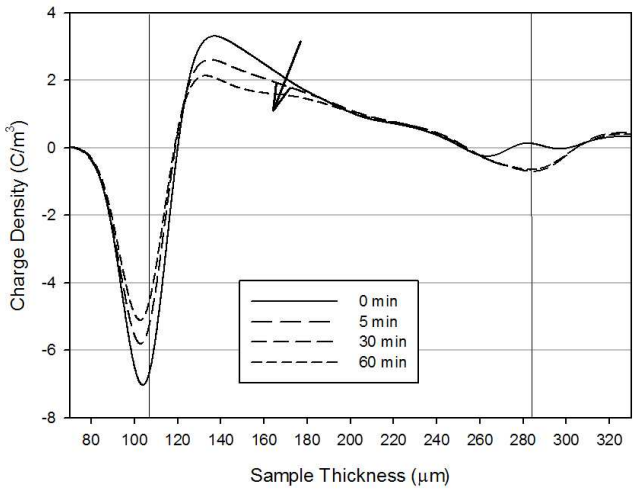


(c) PE crystallised at 117 °C: measurements taken during the 60 min decay.

FIGURE 4.1: Space charge distribution of PE 0 % DBS during the voltage application and 60 min decay process.

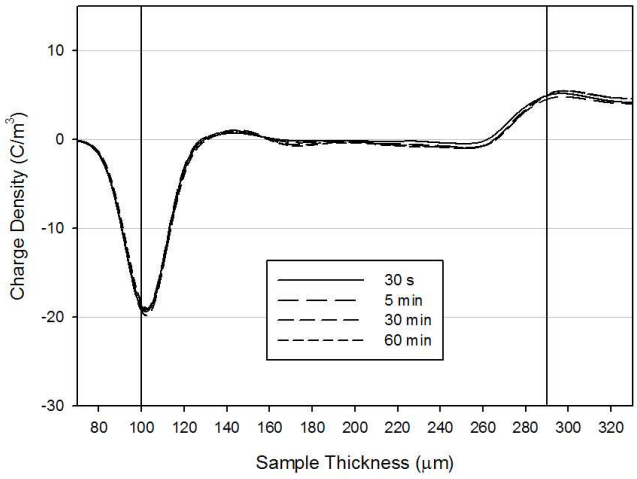


(a) PE/ 0.3% DBS crystallised at 117 °C: measurements taken with volt ON.

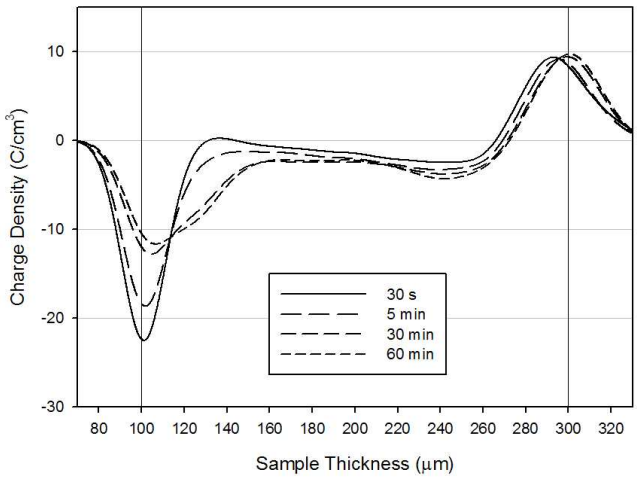


(b) PE/ 1% DBS crystallised at 117 °C: measurements taken with volt ON.

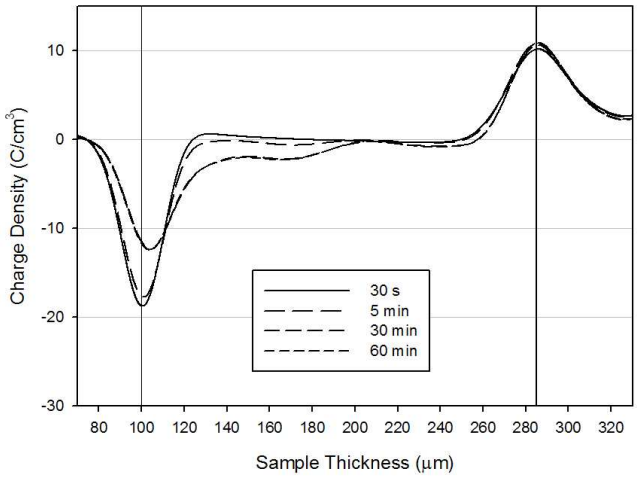


(c) PE/ 3% DBS crystallised at 117 °C: measurements taken with volt ON.

FIGURE 4.2: Space charge distribution of PE:DBS systems during volt ON.

network is established and the presence of DBS is higher than 0.3 %, an inverted charge develops as a consequence, we suggest, of enhanced charge injection at the cathode. Therefore from the above data, it suggests that the evolution of space charge is strongly influenced by the presence and the nature of the DBS fibrils.

Consequently, we chose to investigate further the charge process with volts off during the charging process in order to obtain a better insight of the charge formation. Figure 4.3(a) shows some heterocharge present near the cathode but overall the charge density is really small compared to the PE 0% DBS charge distribution. In this case it can be observed that the charge density increases from 30 s to 60 min, but the magnitude of the increase is negligible compared to the one seen in Figure 4.1(b). Tanaka *et al.* [126] studied the evolution of space charge in LDPE at different temperatures and suggested that an increase in thermal energy enhances the charge carrier mobility, promoting de-trapping. In our case instead, the presence of 0.3 % DBS could enhance the mobility of charge carrier. In fact, Li *et al.* [129] have suggested the presence of shallow traps from the observation of charging evolution in LDPE 0.3 % DBS. In the case of 1 %DBS ( Figure 4.3(b)), the charge formation and transport seems different from the previous case, as suggested from the volt on data. At first there is formation of some homocharge near the cathode which increase with the time and is consequently injected into the bulk. This is followed by formation of heterocharge near the cathode. A similar phenomenon can be seen for 3 % DBS in Figure 4.3(c), even if the homocharge is predominantly on the cathode side and moves into the bulk as a function of the time.

The charging process of the PE/DBS systems has shown two distinct scenarios. In the absence of DBS, the presence of heterocharge injected from the cathode has been observed. Similarly, the 0.3 % DBS sample exhibited heterocharge, but its magnitude was smaller than that of the 0 % DBS. The 1 and 3 % DBS systems are, conversely, dominated by homocharge near the cathode, followed by the formation of heterocharge at the anode. In this work we also monitored the decay of the

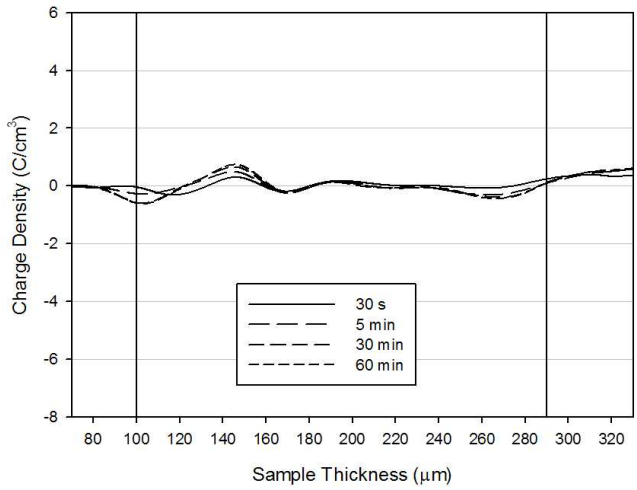


(a) PE/ 0.3% DBS crystallised at 117 °C: measurements taken with volt OFF.

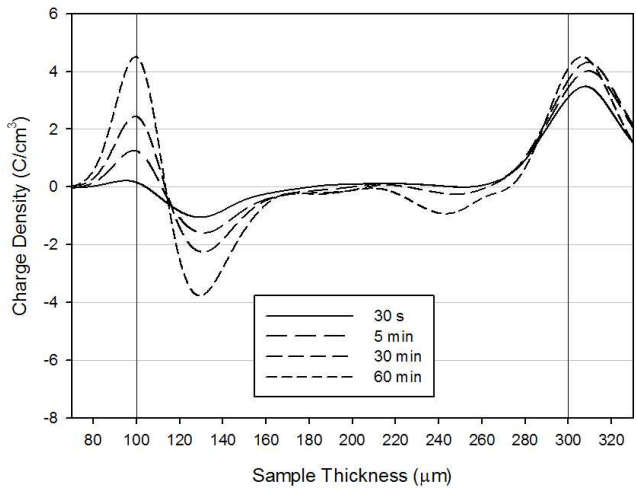


(b) PE/ 1% DBS crystallised at 117 °C: measurements taken with volt OFF.

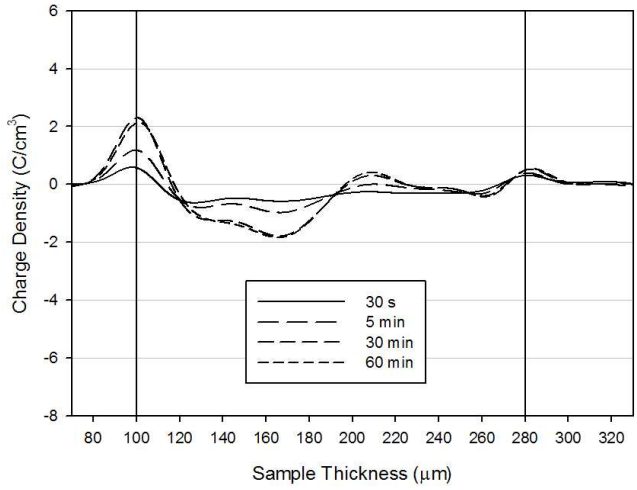


(c) PE/ 3% DBS crystallised at 117 °C: measurements taken with volt OFF.

FIGURE 4.3: Space charge distribution of PE:DBS systems during the 60 min charging process with volt OFF.

charge in our systems and compared with the slow decay present in the PE 0 % DBS system. Figure 4.4(a) shows the discharging process, after short circuiting, of the 0.3 % DBS system. A complete discharge, with almost no charge, is observed in the sample, in agreement with the result of Li and coworkers [129]. Therefore this result further suggests that the charge distribution is improved and that the nucleating agent may act as the site of shallow traps. Conversely, the charge decay in 1 % DBS decreases noticeably in the first 5 min, as than shown in Figure 4.4(b), after which a constant charge level is observed for the remaining time. This finding suggests the presence of deep charge in the bulk. Moreover Figure 4.4(c) shows the space charge decay for 3 % DBS. From this, it is evident that negligible decay of charge occurs within the allowed 60 min, suggesting again a number of deep charges trapping sites in the system, which could be ascribed to the polarity of the fibrils.

The data presented above can be interpreted in different ways. First, the presence of the DBS in the system modified the morphology of the material, as described in the previous chapter. This different morphology may have an effect on the charge dynamics which gives rise to the above effects. Indeed, Jones and coworker [131] have suggested that the transport of charge is influenced by the precise polymer chain configuration. Although, charge transport can be influenced by the morphology, Tanaka *et al.* [126] have suggested that the presence of foreign species is more important factor. Therefore we must consider the presence of the DBS as an element that directly influences the charge transport. This would also agree with the suggestions of Li *et al.* [129]. If this was true, it would not explain completely why the presence of DBS enhances charge transport giving fast discharge in 0.3 % DBS, whilst it acts as the site of deep trapped charge in the 1-3 % DBS systems. One hypothesis could be derived simply from the amount of DBS in the system, where at low concentration it is loose and the charge can be de-trap. Conversely, in the 1-3 % DBS systems, a 3-dimensional fibril network is well

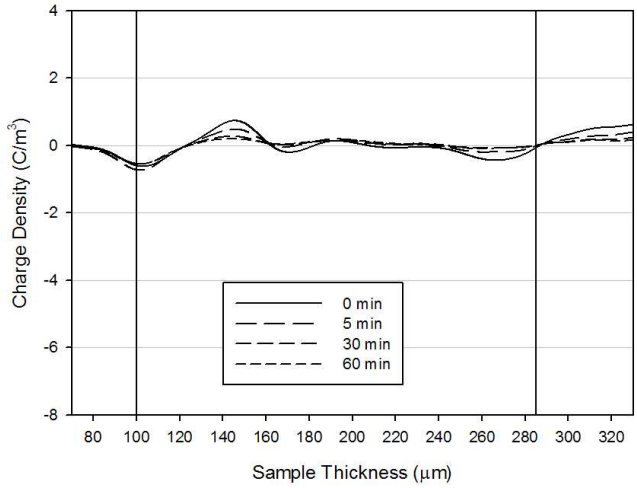


(a) PE/ 0.3% DBS crystallised at 117 °C: measurements taken during 60 mins decay.

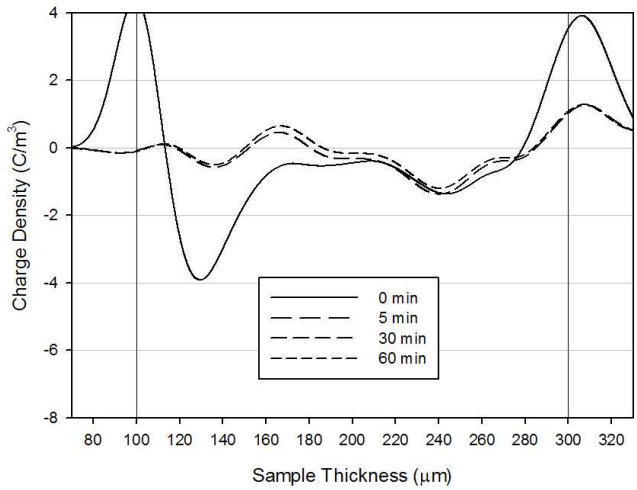


(b) PE/ 1% DBS crystallised at 117 °C: measurements taken during 60 mins decay.

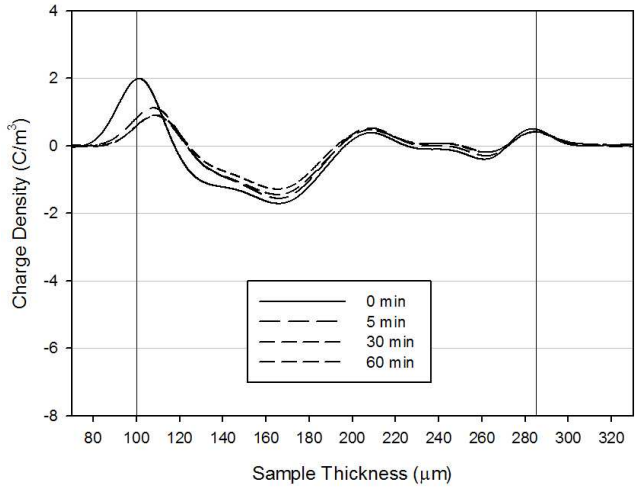


(c) PE/ 3% DBS crystallised at 117 °C: measurements taken during 60 mins decay.

FIGURE 4.4: Space charge distribution of PE:DBS systems during the 1 h discharging process.

established and being polar, could behave as the site of deep charge traps. There is another more intriguing hypothesis. The difference in these results, particularly at 0.3 %, could derive from a different nature of the DBS at this low concentration, as already suggested in the previous chapter. This means that the DBS acts as shallow trap up to 0.3 %, whilst forming fibrils at 1-3 % which introduce deep traps into the system. Although the precise origin of the different space charge characteristics are difficult to be explain mechanistically, the results are quite clear. Deep heterocharges are present in PE 0% DBS but can be modified through the introduction of 0.3 %, which enhance the de-trapping. However, increasing the amount of DBS in the system up to 3 % results in homocharge and the decay is slow.

## 4.3 Conclusion

Space charge distributions in PE/DBS systems have been measured using the PEA method. Heterocharge was observed in PE 0% DBS during the charging process and some deep trap charges were still present in the bulk after 60 min discharge. The 0.3 % DBS system still showed evidence of heterocharge, but smaller in magnitude than in the 0 % DBS, and an almost complete discharge was observed during the decay, suggesting that the DBS acts as the site of shallow charge traps, in agreement with Li *et al.* [129]. In contrast, the formation of homocharge near the cathode followed by some heterocharge at the anode was observed in 1-3 % DBS, which also shown a slow decay, suggesting some deeply trapped charges. We propose that the DBS is associated with the dynamic of charge transport in the bulk and that the presence of DBS at low concentration, when a fully evolved 3-dimensional network has not yet developed, enhances the de-trapping of charges. However, the formation of a mature polar network has negative consequences, because the fibrils induces deep trap charges within the

bulk.

# Chapter 5

# Polyethylene/ Ethylene Vinyl Acetate Blends

## 5.1 Introduction

The properties of polymers can be enhanced by mixing two or more different polymers together to form blends [8]. However, only a small number of combinations of polymers result in miscible blends, the majority tend to phase separate, modifying the mechanical properties. Some polymer blends can result in enhanced mechanical properties whilst others can reveal poor mechanical properties due to lack of interaction at the interface of the two or more polymers. This is more likely to occur when mixing polar and non polar polymers, as in the case of polyethylene/ethylene vinyl acetate blends. Other factors that can influence the phase separation at macroscopic level are: molecular weight, melting temperature, melting time and annealing temperature. Nevertheless, phase separation can still occur even in polymers that have similar physiochemical properties. In the case of polyethylene blends, if crystallisation takes place in the spinodal region (see section 1.2.1), phase separation will occur [8].

From a thermodynamic point of view, mixing two polymers can lead to phase separation due to the small combinationatorial entropy and positive enthalpy of mixing. Rheological studies have shown that the interfacial tension between two polymers plays a key role for partial miscibility/dispersion of the second phase in small particles [132, 133]. Moan *et al.* [134] reported that the interfacial tension depends mainly on the structural similarity of the components and blend composition. Khonakdar *et al.* [135] estimated the interfacial tension between LDPE/EVA and HDPE/EVA using a rheological model, known as the Palierne analysis [136]. This study enables the derivation of interfacial tension values for both system and demonstrated greater structural similarity in LDPE/EVA systems than in HDPE/EVA. Furthermore, Ray and Khastgir [137] observed a degree of miscibility within the amorphous region for LDPE and EVA. DSC melting traces have shown a decrease in the melting temperature of the PE peak, which is related to the partial miscibility of the two polymers [138]. Péon *et al.* [139] have also shown a correlation between the VA percentage, the molecular weight ($\bar{M}_w$) and the activation energy; however, they noticed a stronger bias of the $\bar{M}_w$ on the enhancement of viscosity of EVA copolymers than the VA content.

Other researches have concentrated their attention on high density polyethylene and ethylene vinyl acetate blends. Krause *et al.* [36] used the Hildebrand solubility parameter to predict a complete miscibility of HDPE/EVA for VA contents lower than 18 %. Experimental agreement was subsequently found by Na *et al.*, [56] which demonstrated a miscibility for HDPE/EVA with 16 % VA content. However, Na *et al.* [56] observed a phase separation already in the melt when the VA content was above 16 % . In contrast, John *et al.* [55] observed immiscibility in HDPE/EVA blends, but they increased the penetration of the two phases and reduced the interfacial tension by the addition of maleic anhydride (MA).

In brief, the morphology of blends of PE/EVA, depends on both the EVA content when mixed with polyethylene and the percentage of VA content present in the

copolymer. The EVA domain size increases with the extent of VA, generally resulting in lower mechanical properties, although, a study of LDPE/EVA by Serenko and Avinkin [42] highlighted an enhancement in toughness of this blend. Therefore, a potential strategy to enhance the dispersion EVA avoiding macro phase separation in polyethylene matrix could result from the mixing of EVA in a blend of LPE/BPE.

In this study, a series of blends of PE and EVA were considered. The interest in these blends is given by the potential use of the blends in the dispersion of a polar aluminium silicate, montmorillonite (MMT) clay. The polyethylene used in this study is a blend composed of 20 % high density polyethyelene (LPE) and 80 % low density polyethylene (BPE) and will be termed PE. The reference material used in this chapter is therefore the same polyethylene blend considered in the chapter 3 and 4. The three ethylene vinyl acetate (EVA) copolymers investigated here contain 9, 18 and 40 % vinyl acetate (VA) and will be refereed to, respectively, as EVA9, EVA18 and EVA40. All these were obtained from DuPont. According to the manufacturer, the 9 % and 18 % copolymers both have a melt flow index (MFI) values 2.16 Kg at 190 °C of 7, while the 40 % polymer has an MFI of 57 under the same conditions. This indicates that the first two copolymers are of a higher molecular weight than the latter. The PE:EVA ratios used were 80:20 and 60:40 in order to have polyethylene domains and the EVA as second phase. The first blend, containing 80 % PE and 20 % EVA, will be referred to as 80:20EVAs. The second blend contains 60 % PE and 40 % EVA is termed 60:40EVAs.

All the compounds were held in the melt for 5 min or 60 min in order to enhance the phase separation effect in the blends and subsequently characterised by DSC and SEM.

## 5.2 Results and Discussion

## 5.3 Differential Scanning Calorimetry

All samples were isothermally crystallised at a range of temperatures between 113 °C and 120 °C inclusive, and melting traces were subsequently acquired. The prior melting temperature was always set at 150 °C and two different batches of PE:EVAs were tested. The first batch of samples was held at the melting temperature for 5 min, whilst the second batch was held for 60 min. This was done in order to explore the kinetics of any phase separation in the blends.

Figure 5.1 shows the DSC melting behaviour of PE isothermal crystallised samples at 117 °C as a function of VA content. The high melting peak at ∼126 °C, corresponds to lamellae that are composed, principally, of LPE. These crystals correspond to the framework of so-called dominant lamellae [111]. The second peak at ∼110 °C corresponds to BPE. A third small peak is also visible in traces containing 9 and 18 % VA at variable temperatures. These peaks correspond to the different EVAs. In the case of 80:20EVA9-5m the EVA peak appears inside the BPE peak tail at a temperature of 98 °C. This feature could be interpreted as indicating a passive role of EVA in isothermal crystallisation and, as such, this component behaves effectively as an additional diluent. In this way, the LPE is only weakly influenced by the EVA and its melting behaviour is largely unaffected and the enthalpy remains constant. Alternatively, the above could indicate that the PE and EVA are immiscible and, therefore, phase separated in the melt, such that the PE and EVA occupy distinct spatial locations. The zones corresponding to each of the PE and EVA phase consequently crystallise separately, such that the EVA has minimal effect on the polyethylene (both LPE and BPE). Increasing the VA content, decrease the crystallinity of the EVA. Thus, a peak at ∼85 °C in 80:20EVA18 melted for 5 min, corresponds to the ethylene part of the EVA18 and

is in agreement with behaviour by Hosier *et al.* [140].

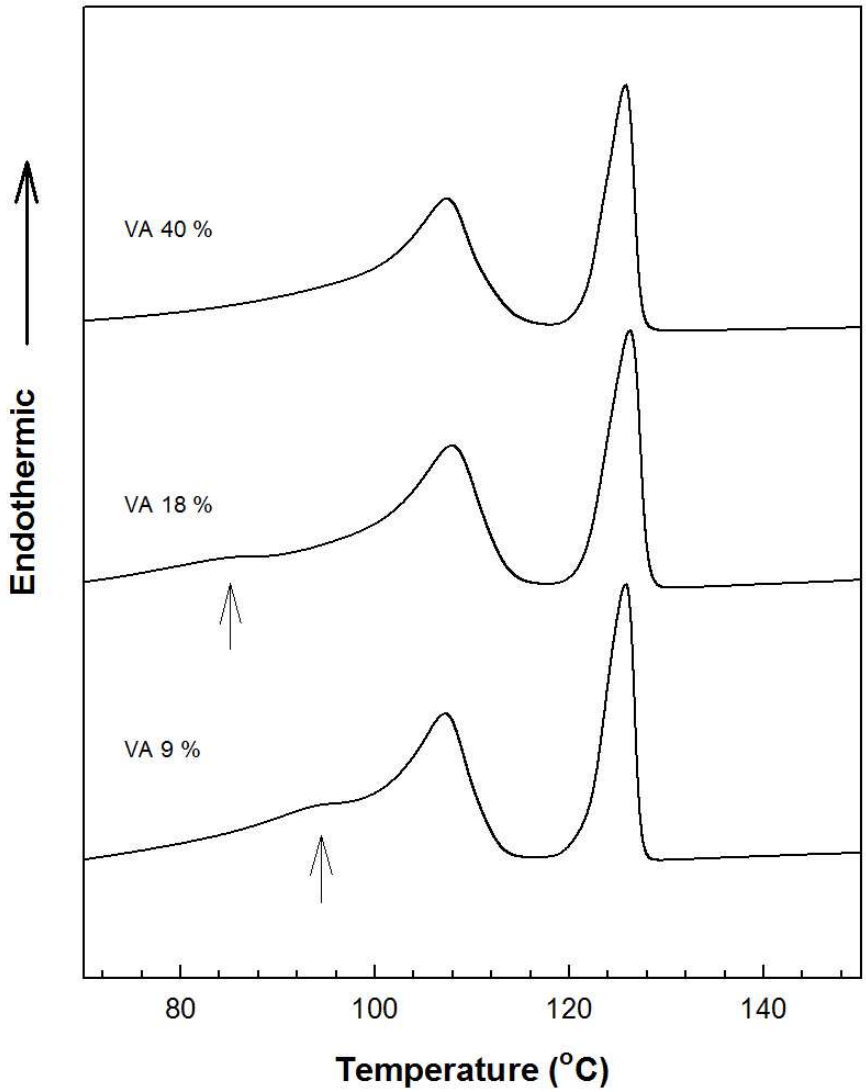


FIGURE 5.1: Differential Scanning Calorimetry of 80:20EVA in function of VA content after isothermal crystallisation at 117 °C. All melting traces show two distinct peaks at 126 °C and 110 °C relative to LPE and BPE, respectively. A third peak (arrowed) is observed at 98 °C and 85 °C relative to EVA9 and EVA18.

Although the peak corresponding to EVA18 and the peak relating to BPE are separate, some co-crystallisation with BPE is possible. In the uppermost trace, there is no evidence of an EVA peak because the melting peak of EVA40 is situated to a lower temperature. Hosier *et al.* [140] found that the crystallinity and melting point of EVA decreases with increasing VA content. In particular the melting point of quenched EVA40 was found at 40 °C, which is out of the temperature range investigated here.

Figure 5.2 represents the effect of EVA content on the melting behaviour of blends containing 9 % VA crystallised at 120 °C. Two features are evident in both traces; 80:20EVA9 and 60:40EVA9 show the a peak at 126 °C and another peak at 110 °C, corresponding to the LPE and BPE peaks respectively. A third peak is also present below the BPE peak at $\sim$ 110 °C and becomes more pronounced as the EVA content increases. As previously noted in Figure 5.1, the corresponding feature (arrowed) in the melting behaviour of 80:20EVA9 and 60:40EVA9 relates to both the BPE and the EVA components of each blend. These DSC data can be interpreted in two ways. The EVA plays a passive role in isothermal crystallization and, as such, behaves effectively as an additional diluent. In this way, the LPE is only weakly influenced by the EVA and, consequently, its melting behaviour is largely unaffected. The BPE and the EVA subsequently co-crystallize to give the broad, low temperature endotherm seen in Figure 5.1. Otherwise the polyethylene and EVA are immiscible and, therefore, phase separate in the melt such that each occupies distinct spatial locations. The zones corresponding to each phase consequently crystallize separately, such that the presence of the EVA has a minimal effect on the polyethylene (both LPE and BPE). The DSC trace obtained from each blend then merely constitute a suitably weighted addition of the traces obtained, separately, from the EVA and the polyethylene.

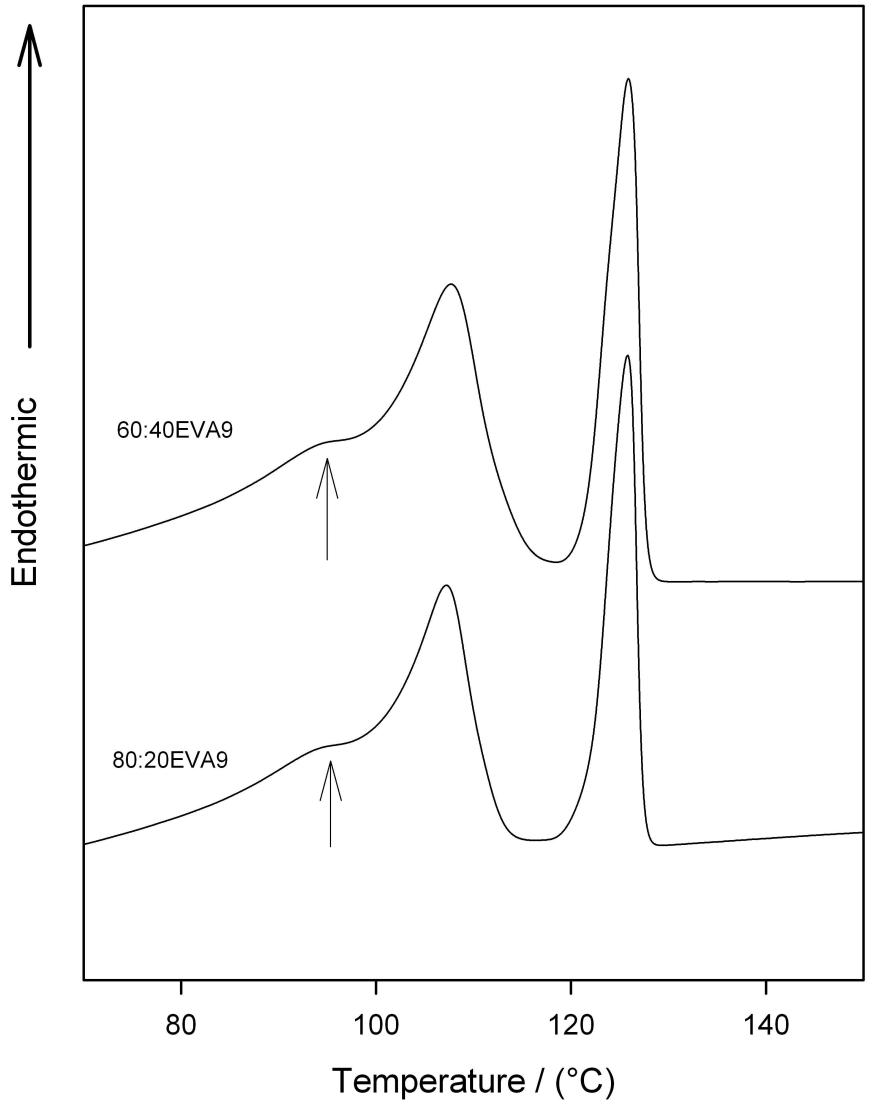


FIGURE 5.2: Differential Scanning Calorimetry of PE in function of EVA content after being crystallised at 120 °C. PE indicates the LPE and BPE peaks for a blend without EVA; same peaks are detected for 80:20EVA9-5m and 60:40EVA9-5m and an additional peak is present at 98 °C.

Figure 5.3 compares melting traces of the same material after being isothermally crystallised at range of temperature between 113 and 120 °C. For the sake of brevity only melting traces for 80:20EVA18 are shown here; all the others blends showed the same behaviour, except the EVA40 peak, which was not detectable as explained above. From all the traces, the three characteristic peaks corresponding to LPE, BPE and EVA are present at variable temperatures. After crystallisation at 113 °C, the melting temperature of the LPE peak is situated at 124.7 °C and exhibits a shoulder on the low temperature side. This secondary feature is believed to be a co-crystallisation/reorganisation effect of the linear material and the more linear fractions of the BPE, as described by other authors [9, 38]. The peak relating to BPE is situated at 110 °C and is associated with at the branch polymer that crystallises during quenching. A third peak, corresponding to the EVA, melts at 85 °C, not far from the melting point of EVA18 alone. As the crystallisation temperature was increased to 117 °C, the LPE peak becomes narrow and the co-crystallisation effect is reduced. At higher crystallisation temperatures, the LPE peak becomes narrower and the peak is shifted towards higher temperatures. This phenomenon can be associated with the formation of thicker LPE lamellae as the crystallisation temperature increases ([9, 110, 141]). This is not the case for the quenched BPE and EVA peaks, which remain at constant temperatures over the same temperature range; it is interesting to note that the extent of the BPE peak increases with the crystallisation temperature. In fact, a new feature appears on the right shoulder of the BPE peak after crystallisation at 120 °C. A co-crystallisation of low molecular mass LPE together with the BPE is a potential explanation, as seen in the PE blend described in the previous chapter. However, a segregation phenomenon during the crystallisation can be another possible interpretation, as described by Alamo *et al.* [142]. At this stage, the melting traces cannot explain which of the two interpretations is more probable.

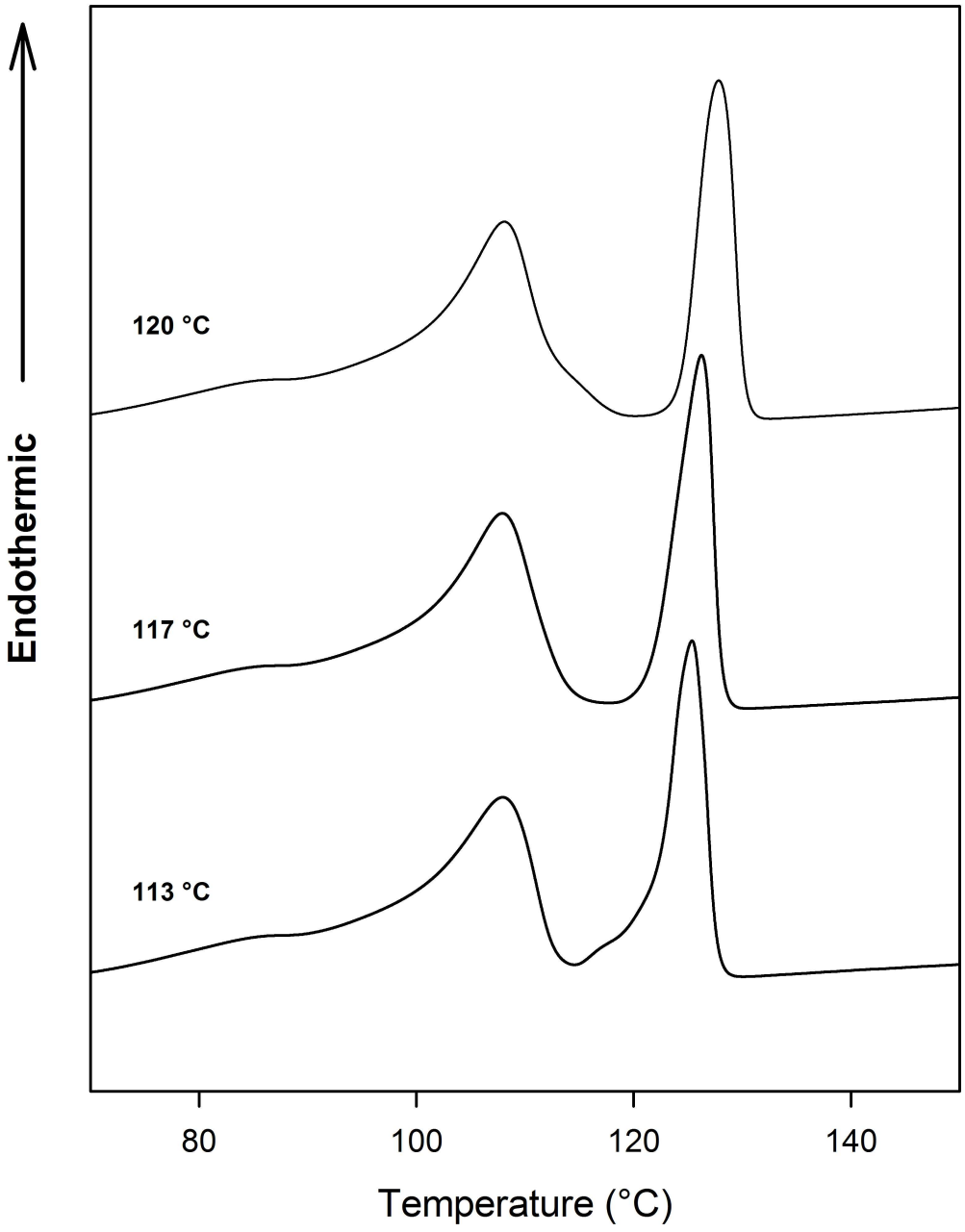


FIGURE 5.3: Differential Scanning Calorimetry of 80:20EVA18-5m in function of crystallisation temperature. LPE peak shift at higher melting temperature at the increase of crystallisation temperature, whilst the BPE and EVA peaks remain constant at the same temperature range.

The data presented in Figure 5.4 show melting traces of 80:20 and 60:40 EVA18 samples crystallised at 117 °C as a function of the melting time. The blends containing EVA9 and EVA18 are not represented because they showed the same trend as EVA40 apart from the additional presence of the low temperature EVA melting peak. Two main differences are observed in the melting traces shown here. The LPE peak position shows a slight depression after the samples were held in the melt for 60 min. This result could be interpreted in different ways:

- The depression is related to some interaction between the LPE and the EVA, which has assumed a different conformation during the relaxation time.
- Enhanced phase separation occured that has affected the crystallisation of LPE. Moreover, in the 60 min melt the BPE peaks are broader.

One explanation can derived from segregation of PE molecules of different molecular weight during the annealing time in the melt, therefore a co-crystallisation has occurred between BPE and the short chains of LPE. Comparing the enthalpy of the LPE peak for 5 and 60 min samples, a decrease in the LPE enthalpy can be noted at 60 min. Therefore, it seems that after 60 min in the melt a fraction of the LPE molecules do not crystallise in the same way as in the case of the 5 min melting traces. This would explain the increase in BPE peak area, which results form of low molecular weight LPE rejected from LPE peak. However, the behaviour shown in Figure 5.4 could also be the result of LLPS, which reduces the amount of LPE available for the the isothermal crystallisation. Li *et al.* [138] studied a binary blend of LLDPE/EVA and they observed an increase of phase separation with increasing annealing time at 180 °C. They suggested that the observed phase separation was due to LLPS.

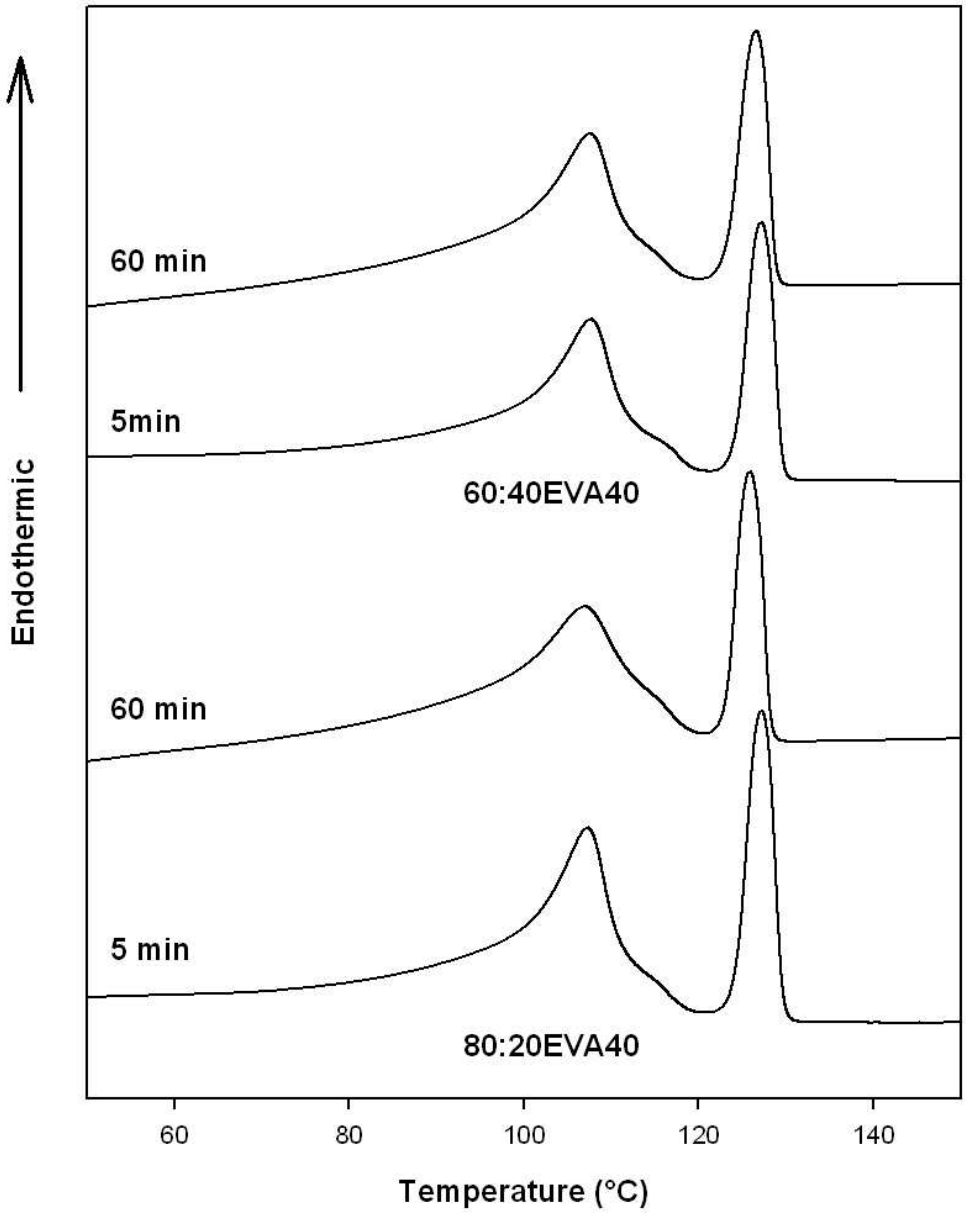


FIGURE 5.4: Differential Scanning Calorimetry of PE:EVA40 crystallised at 117 °C in function of melting time. LPE peak shifts at lower temperature when held in the melt for 60 mins and more co-crystallisation is observed on the right shoulder of the BPE peak.

## 5.4 Isothermal Crystallisation of PE/EVA blends

Isothermal crystallisation data obtained from DSC experiments were analysed by applying Avrami theory [24, 25, 26] and its subsequently revision [74]. Applying the kinetic equation on the data up to 50 % relative crystallinity:

$$1 - \frac{V_c}{V_{inf}} = \exp\left(-K_{exp}\left(t - t_0\right)^n\right) \tag{5.1}$$

the value of $n$, $K_{exp}$ and $t_0$ were found. The values of $n$ fall from 3.6 to 2.8 as the crystallisation temperature increases, for all the polymer systems, suggesting 3-dimensional growth. Assuming that the crystal growth is really three-dimensional, Kowalewski *et al.*[74] has suggested that the effective three-dimensional crystallisation constant $K_3'$ can be determined from the experimental value of $K_{exp}$ using the following formula:

$$K_3' = \frac{4}{3}\pi N G^3 \cong \left(K_{exp}\right)^{\frac{3}{n}} \tag{5.2}$$

In this Equation, $N$ is the number of nucleation sites per unit volume and $G$ is the growth rate of the crystallising object.

Figure 5.5 shows non linear Avrami plots of isothermal crystallisation data obtained at various temperatures for a PE:EVA blends melted for 5 min. Increasing the crystallisation temperature results in an increase in crystallisation time for all the blends examined, up to 50 % of the total crystallinity, in line with previous results found on PE 0 % DBS blend. Increasing the ratio of PE/EVA from 80:20 to 60:40 the latter blends showed a further increase of crystallisation time at the same isothermal temperatures compared to the 80:20EVAs blends. This behaviour is generally ascribed to blends containing a second phase that decreases the growth rate, which is reflected in the crystallisation time. Dreezen *et al.* [143] have shown

a drastic decrease in spherulitic growth rate in poly(ethylene oxide)/amorphous polyamide with an increase in the fraction of amorphous component. Nevertheless, increase of growth rate has also been reported in crystalline/amorphous blends. Bulakh and Jog [144] observed an increase in growth rate in poly(phenylenesulfide) (PPS)/amorphous polyamide (PA) blends. They attributed the enhancement of growth rate to the presence of the molten polyamide, which facilitates the mobility of PPS.

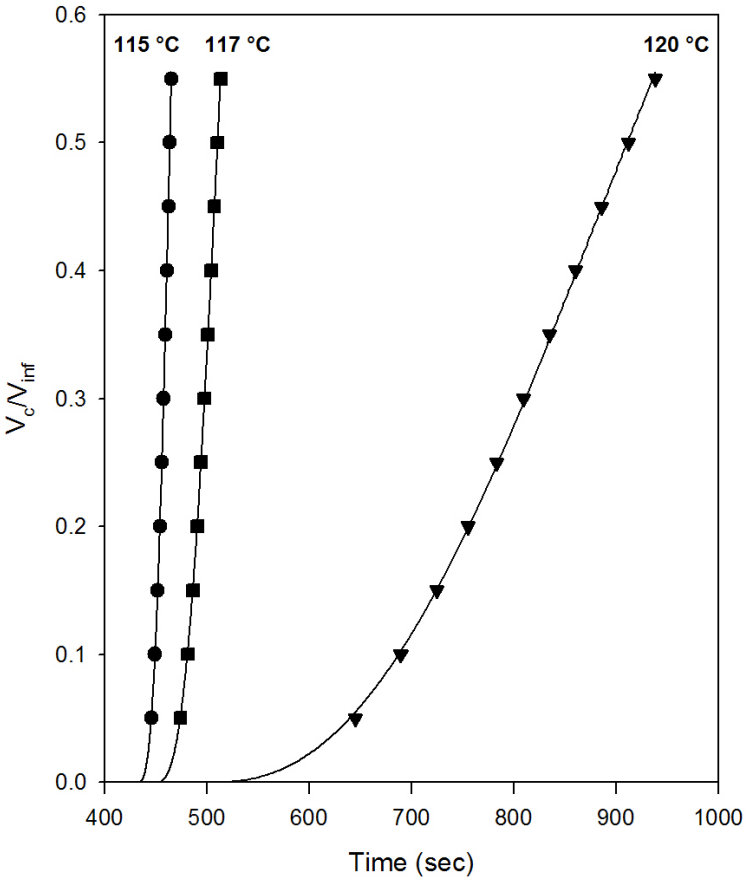


FIGURE 5.5: Non Linear Avrami fitting on 80:20EVA9 melted for 5 min at three different isothermal crystallisations

Li *et al.* [145] have have shown that poly(ethylene-butene)(PEB) can influence the crystallisation of LLDPE, suggesting that the PEB acts as a diluent for PE. Figure 5.6 shows non linear Avrami plot of 80:20EVAs blends for all three VA content after being held in the melt for 5 min. As can be seen, there are no main differences in terms of $n$, $K_{exp}$ for blends containing EVA9 and EVA40. On the contrary, the 80:20EVA18 blend takes longer to crystallise. This result is difficult to interpret, because at first sight, crystallisation may be expected to vary monotonically with VA content. This result suggests that the crystallisation process is comparable for EVA9 and EVA40 blends. Nonetheless, the melting traces in Figure 5.1 have shown

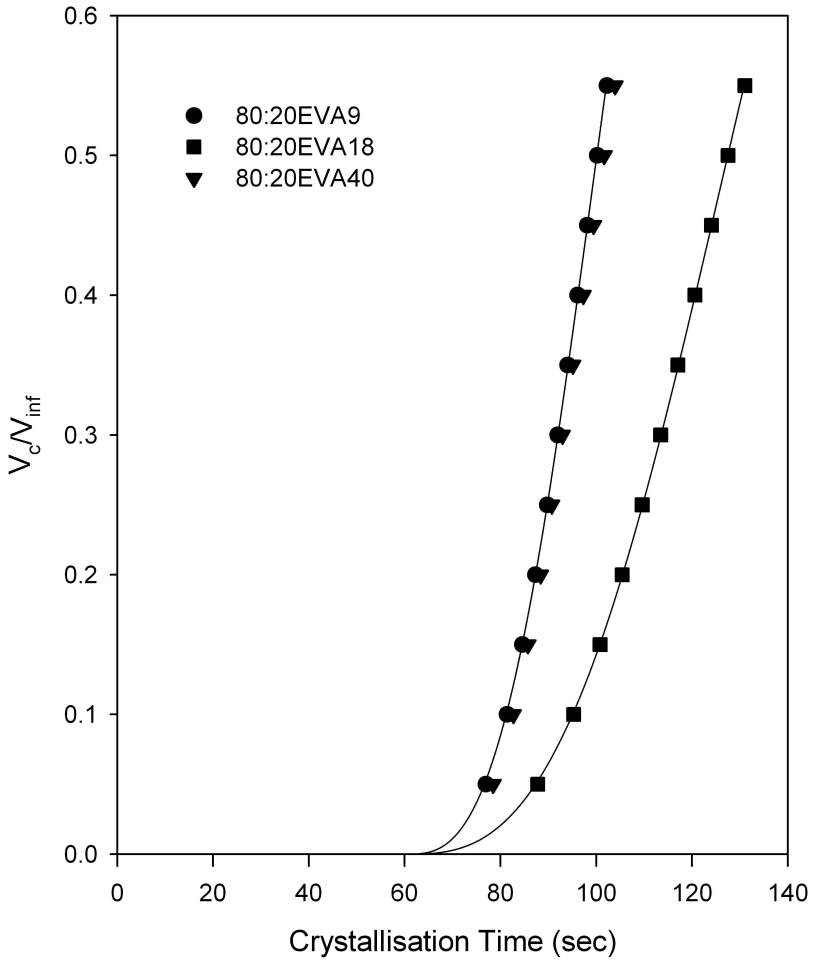


FIGURE 5.6: Non Linear Avrami fitting on 80:20EVA crystallised at 117 °C in function of VA content.

that 80:20EVA40 blend is immiscible and therefore the second phase does not play

a penalty in the crystallisation process. In contrast, the addition of 18 % VA content seems to affect the crystallisation process. This finding suggests that, the process of phase separation in 80:20EVA18 is different from that in 80:20EVA40. This could be due to engulfed EVA drops affecting the crystallisation of the PE blend, or due to a different growth rate of the blend. Nevertheless, at the present moment, although it cannot be speculated which is the cause, it is evident that the EVA18 system behave differently and therefore we will come back on this point after an investigation of blend microstructure.

Figure 5.7 shows $K'_3$ values for all the blends as a function of crystallisation temperature. Two distinctive trends are observed with a monotonic decrease in $K'_3$ as the crystallisation temperature increases. The top curve consists of $K'_3$ values for 80:20EVA9 and 80:20EVA40, whilst the second is composed of $K'_3$ of 80:20EVA18 and all the 60:40EVAs. A decrease of $K'_3$ occurs with increasing EVA content only for blends containing the 9 and 40 % VA materials. A decrease in $K'_3$ is observed for 60:40EVA18 compared to 80:20EVA18, but this is negligible.

This result leads to some hypotheses. First, the values of $K'_3$ could derived from an error due in processing of raw data. To test this hypothesis, the crystallisation half time was considered as method to verify $K'_3$. For this, a 3-dimensional growth model was chosen and the values of crystallisation rate were considered for three different crystallisation temperatures. From the Avrami equation, considering the half time of 80:20EVA9 at 117 °C and comparing to the one of 60:40EVA9 at the same crystallisation temperature, it can be found that:

$$ln0.5 = -K'_{3'}t_1^3 \quad ln0.5 = -K'_{3''}t_2^3 \tag{5.3}$$

where $K'_{3'}$ and $K'_{3''}$ are the 3-dimensional values of growth rate, $K'_3$, for 80:20EVA9

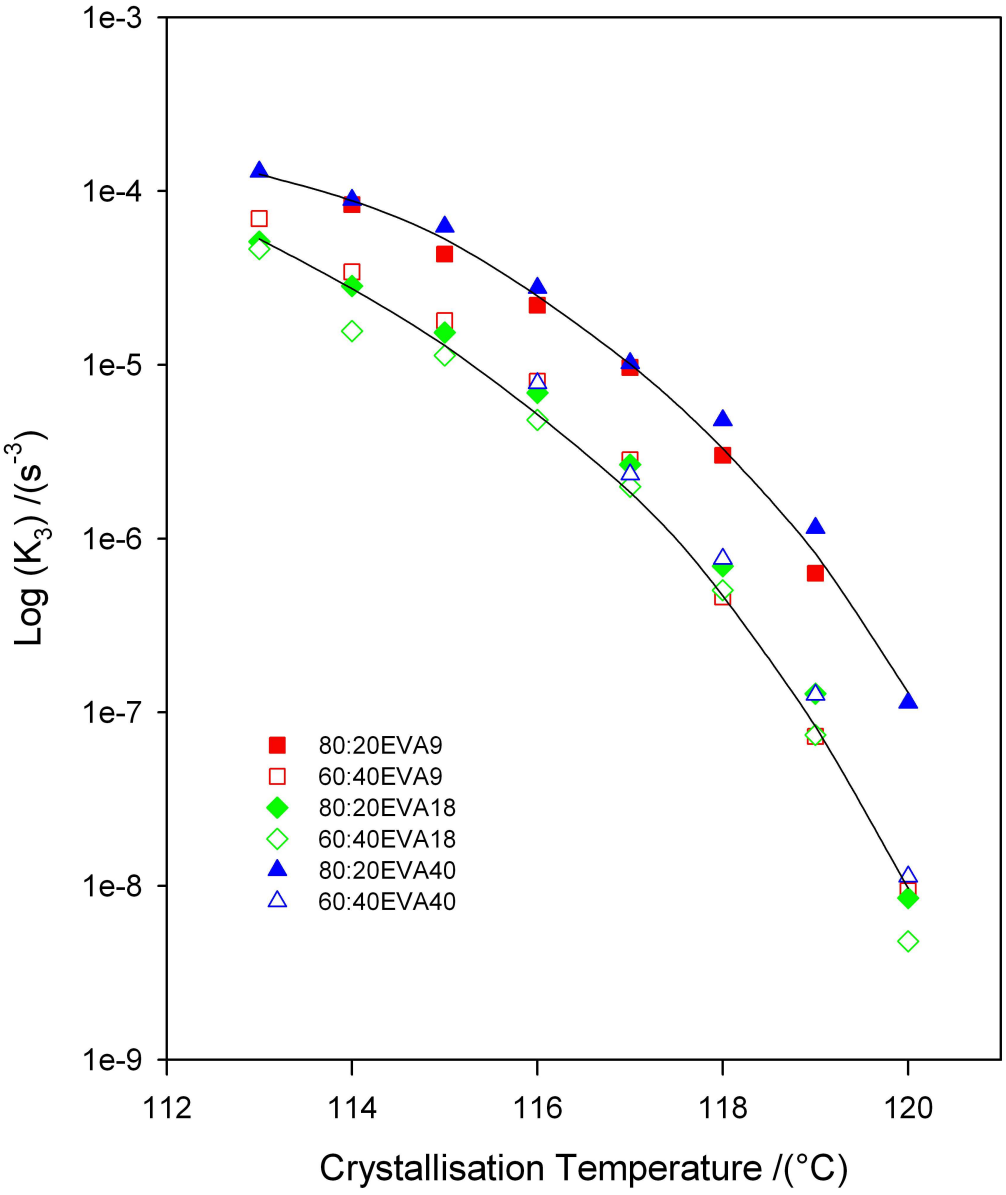


FIGURE 5.7: Crystallisation constant against crystallisation temperature for samples melted 5 min. Blends 80:20EVA9 and 80:20EVA40 show an higher crystallisation constant compared to 60:40EVA. All PE:EVA18 show similar behaviour.

and 60:40EVA9 respectively. Hence, this can be written as:

$$(K_{3''}/K_{3'})^{1/3} = (t_1/t_2) \tag{5.4}$$

From the Figure 5.7 it can be seen that the ratio of $K'_3$ differers by a factor $\sim$ 20, which means that the half times ratio differ by a factor of 2.7. Values for the temperatures tested did not show evidence of an error in processing the raw data. This point is further reinforced in Figure 5.8 which compares crystallisation exotherms obtained at 117 °C for 80:20EVA9, 60:40EVA9 crystallised at 117 °C. From here it can be seen that the 80:20EVA9 and EVA40 behave similarly while 60:40EVA9 and EVA40 take longer to crystallise. A second interpretation could be attributed to a different nucleation density and/or a slower growth rate. It is known that:

$$K'_3 = \frac{4}{3}\pi N G^3 \tag{5.5}$$

The review article on miscible and immiscible blends by Di Lorenzo [146], showed that the addition of an immiscible polymer generally produces a decrease of $G$ in the blend. However, other immiscible systems may show no affect of the amorphous component on the growth rate. Only few authors has observed an increase of growth rate in blend systems. For instance, Bulakh and Jog [144] observed an increase of $G$ with the addition of polyamide in poly(Phenylenesulfide). These authors suggested that the molten PA facilitates the movement of PPS chains and therefore an enhanced growth rate was observed. However, isothermal crystallisation data have shown an increase in crystallisation time, which would make difficult to believe in an increase of $G$. Hence, a decrease in nucleation density due to interaction between the two phases can affect the kinetic of the blends. However, such interpretation can be only verified by examining the morphology of the samples using the SEM technique.

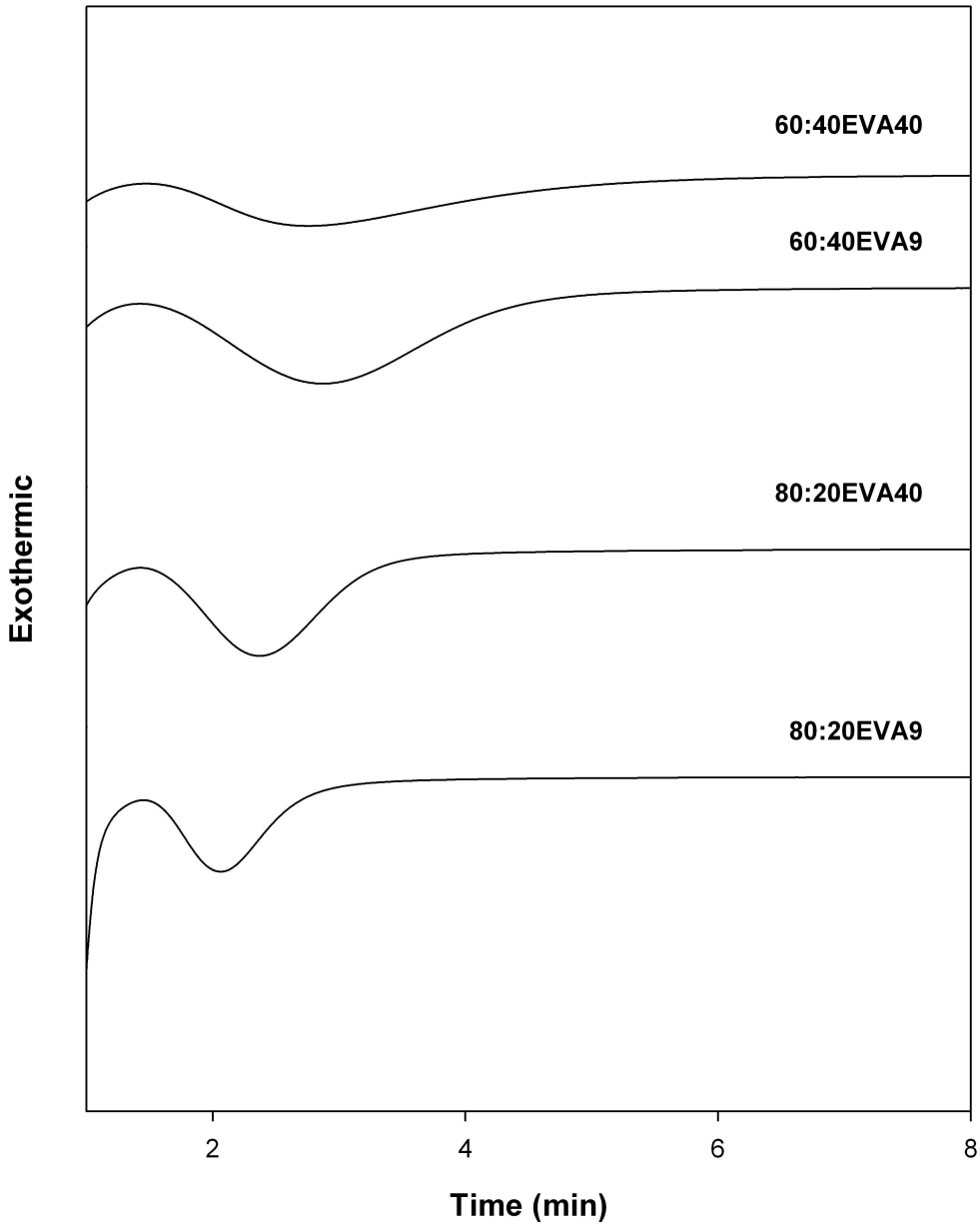


FIGURE 5.8: Exotherm for 80:20EVA9 and EVA40 against 60:40EVA9 and EVA40.

### 5.4.1 Morphology

A preliminary optical study was conducted on samples containing 9 % VA due to its potential miscibility with PE. Figure 5.9 shows a crossed polar optical micrograph that typifies all blends containing 9 % VA. This shows a banded spherulitic morphology that is space filling, despite the fact that 40 % of this system is made up of EVA. The same was true of 80:20EVA9 melted for 5 min, where 20 % of the

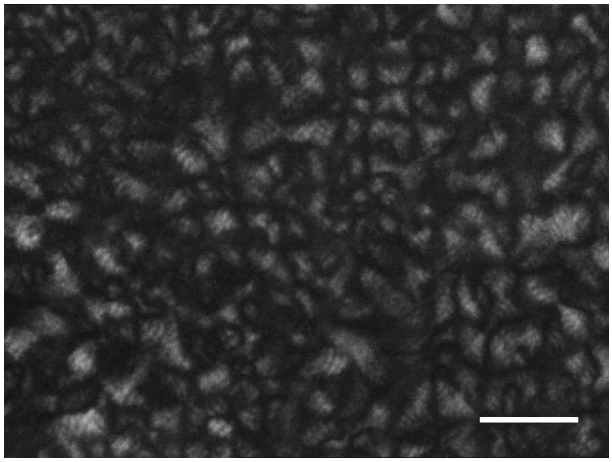

FIGURE 5.9: Polarized light transmission optical micrograph showing the space-filling spherulitic texture of 60:40EVA9 melted for 5 min and crystallised at 117 °C. Scale bar: 50 $\mu$m.

material in the blend was composed of the relatively amorphous polar copolymer. These results required further investigations at SEM resolution.

Figure 5.10 shows the internal micrograph of a 80:20EVA9 sample that was melted at 150 °C for 5 min and subsequently crystallised at 117 °C for the time corresponding to the total crystallisation time determined during the isothermal DSC analyses. This particular isothermal temperature was chosen because PE samples exhibit well known microstructures, and the crystallisation time is relative short. Sample 80:20EVA9-5m contains some spherulites that are banded on the scale of 5 $\mu$m and well ordered lamellae can be distinguished (Figure 5.10). The microstructure does not show evidence of macroscopic phase separation, confirming the above suggestion obtained by optical microscopy.

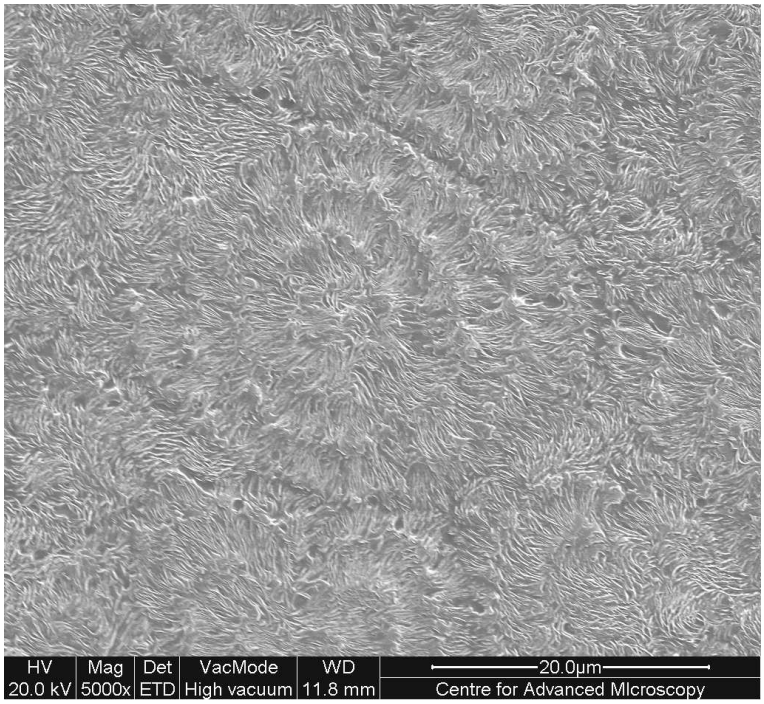


FIGURE 5.10: Scanning electron micrograph of 80:20EVA9 melted for 5 min and crystallised at 117 °C; no evidence of macroscopic phase separation. The microstructure is dominated by PE spherulite.

However, at higher magnification, some micro droplet-like objects could be observed at the boundary of spherulites, which could be related to a potential phase separation of EVA (Figure 5.11). At this temperature the PE spherulites grow rapidly and there is not much time for phase decomposition, as seen by Shabana *et al.* [147] in a different system. This confirms the previous hypothesis regarding the melting traces of PE:EVA9, where the EVA plays only a passive role in the crystallisation of the polyethylene blend. Nonetheless, in order to confirm if these features are caused by phase separation, the same sample was held in the melt for 60 min. In doing so, phase separation should be promoted, if present.

Figure 5.12 shows a predominant crystallised PE phase and a second phase, in the form of droplets. The featureless region is the effect of the etching method used and it can be related to the EVA being removed by the etchant. However, the precise composition of such regions remains unclear. According to Moan *et al.* [134], partial miscibility between EVA and LDPE is possible and, therefore, we

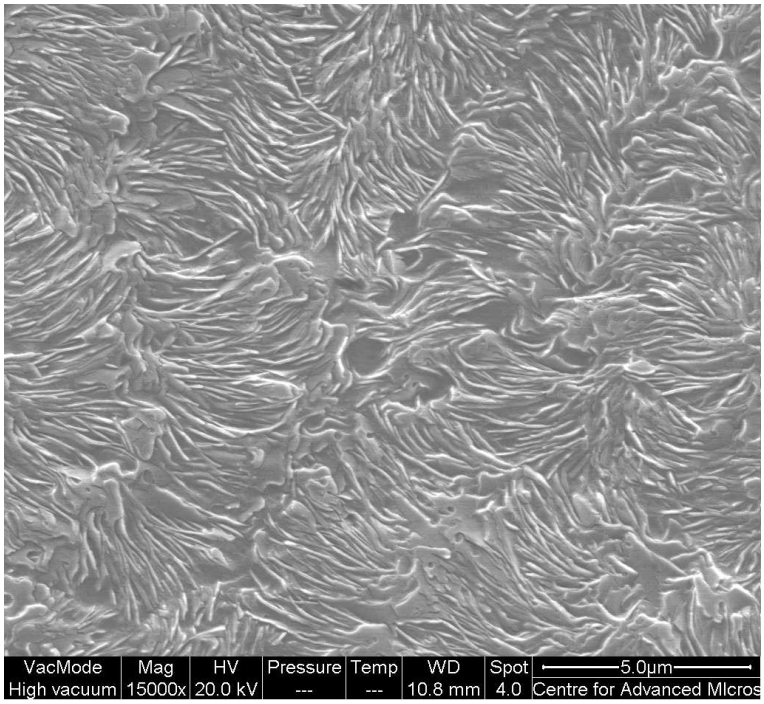


FIGURE 5.11: Scanning electron micrograph of 80:20EVA9 melted for 5 min and crystallised at 117 °C; evidence of microphase separation at the spherulites boundaries.

might expect an interaction with the LPE. Moreover, Okui and Kawai [148] studied EVA with different VA contents and observed the growth of crystals bundles up to 14 % VA. This result could suggest that the featureless droplet may be composed of VA while the more ethylene rich features have interacted with the matrix. A similar phenomenon was observed by Shabana *et al.* [147]. These authors studied poly($\varepsilon$-caprolactone)/polystyrene blends by optical and electron micrographs and showed segregation of PS outside spherulites of poly($\varepsilon$-caprolactone). Therefore, the results presented in the this work suggest that the long melting time allows the two polymers to phase separate and create a second phase. SEM images were analysed using Image Pro Plus software (work carried out at the University of Trieste), to measure the average diameter of the EVA droplets, which was found to be 0.6 $\mu$m for the sample melted for 5 min and 0.9 $\mu$m for the sample melted for 60 min. This result evinces an increase in phase separation with increased the melting time.

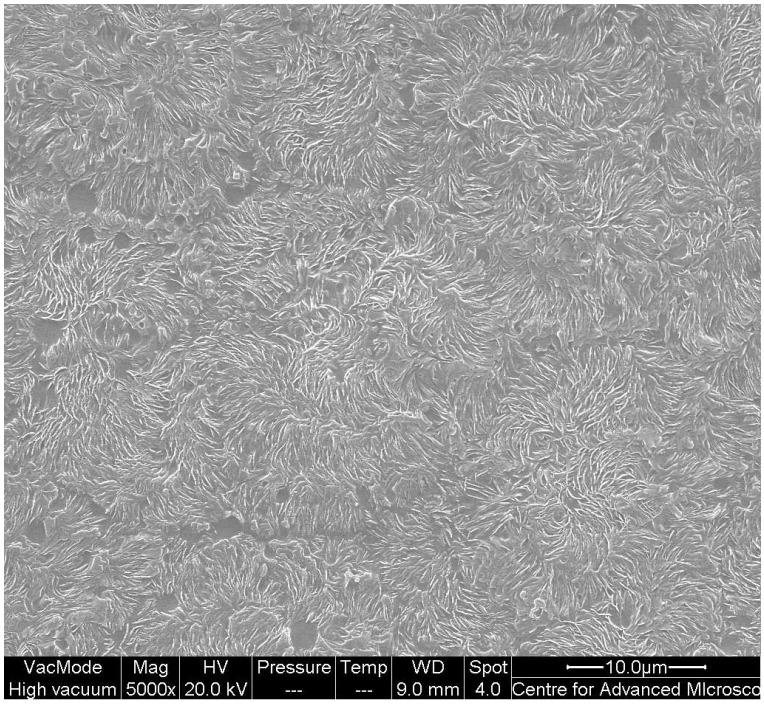


FIGURE 5.12: Scanning electron micrograph of 80:20EVA9 melted for 60 min and crystallised at 117 °C; evidence of microphase separation at the spherulites boundaries.

Subsequently, the effect of varying the ratio of PE:EVA was investigated in order to determine if the phase separation is just a time effect or it is also related to composition. Figure 5.13 shows a sample of PE:EVA9 60:40 melted for 5 minutes and subsequently crystallised at 117 °C, whilst Figure 5.14 represents the same material after being melted for 60 min. In the first micrograph, the dominant features are PE lamellae, alternated with droplets of EVA phase dispersed throughout the sample, with an average diameter of 1.2 $\mu$m. At the top of the micrograph, an incomplete spherulite can be observed, which appears deformed due to the presence of the second phase. This suggests that lamellae need to overcome the EVA phase during the crystallisation process and, therefore suggests that the growth rate can be affected, as seen from the decrease in $K_3'$ data compared to the 80:20EVA9. The second micrograph, instead, reveals a co-continuous structure, typical of spinodal decomposition. Well defined lamellar structures are visible, alternated with featureless regions typical of the EVA copolymer. These results suggest that the phase separation is affected by both time and composition. An

agreement with work of Li *et al.* [138] can be found, where LLPS was observed in LDPE/EVA9 (60:40) blend, varying the annealing time in the melt.

In summary, PE:EVA9 blends showed different morphologies, depending on both the EVA content and the melting time. A simply diagram can summarise the above findings:

TABLE 5.1: Schematic summary of PE:EVA9 morphologies in function of EVA content and melting time

| **Material** | **Melt 5 min** | **Melt 60 min** |
|---|---|---|
| 80:20EVA9 | Single Phase | Phase Sep./micro droplets |
| 60:40EVA9 | Macro Phase Sep. | Co-continuous Phase Sep. |

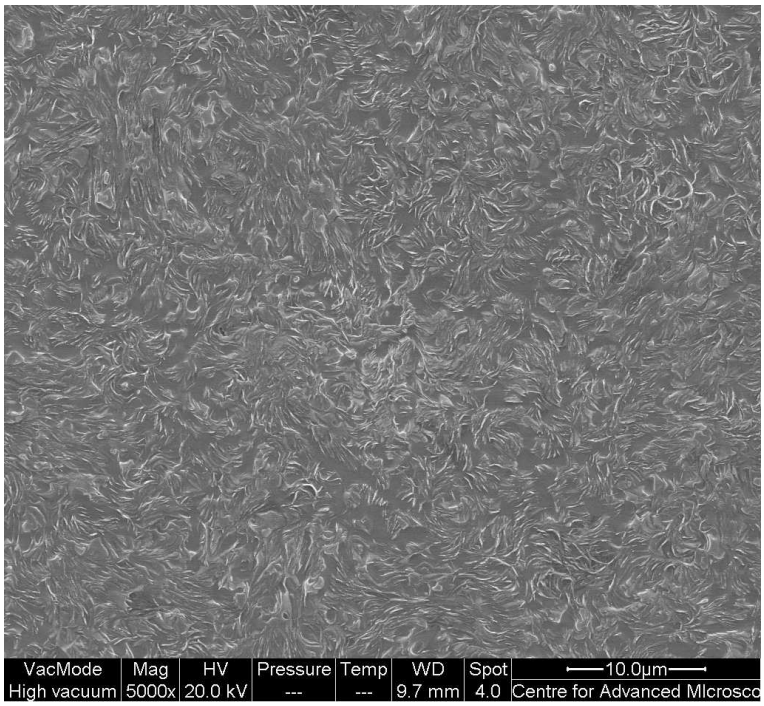


FIGURE 5.13: Scanning electron micrograph of 60:40EVA9 melted for 5 min and crystallised at 117 °C; presence of crystallised lamellae in polyethylene regions and featureless regions related to EVA.

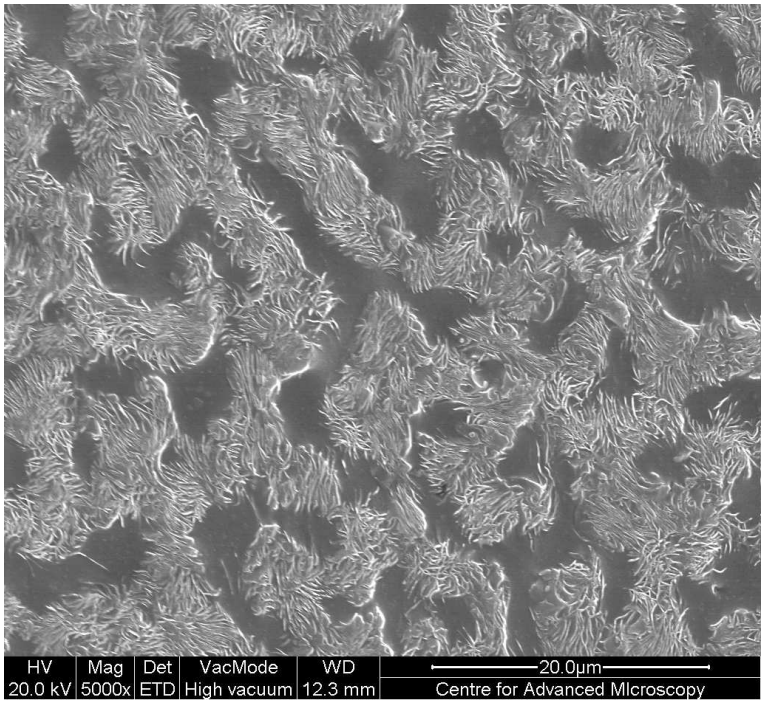


FIGURE 5.14: Scanning electron micrograph of 60:40EVA9 melted for 60 min and crystallised at 117 °C; presence of crystallised lamellae in polyethylene regions and featureless regions related to EVA.

### 5.4.2 PE:EVA with 18 % VA

On increasing the VA content up to 18 %, the microstructure shows a different scenario from the PE:EVA9 blends. Figure 5.15 shows a typical microstructure for 80:20EVA18 after being melted for 5 min and crystallised at 117 °C. A structure predominated by crystallised spherulites with a typical 5 $\mu$m banding is observed together with a second phase of EVA droplets. Moreover, it can be noticed that the second phase is present as inclusion inside the spherulites. In addition, micrographs at higher magnifications show the lamella texture penetrating into the inclusions ( Figure 5.16), which could be related to some interaction between the matrix and the second phase, as predicted by Peon [132]. Observing the microstructures around the phase separated regions, it can be noted that well defined lameallae are present. Otherwise, this could be simply an etching effect with the blend being immiscible. The diameters of the EVA droplets shown in Figure 5.16 vary from submicrom inclusions to others of the order of 2 $\mu$m. This result is

largely in agreement with micrographs shown by John *et al.* [55]. According to Krause *et al.* [36], we could still be in the case of one phase in the melt. This hypothesis could agree with the micrograph in figure 5.15 because the inclusion are present inside the spherulites which means that the PE occludes the EVA during crystallisation . Di Lorenzo [146] explained the case of binary blends where the crystallisable part is dominant over the amorphous one. In this case, a phenomenon termed *fractionated crystallisation* can occur leading to a reduction in crystallisation rates within the dispersed droplets. A similar result was observed in a blend of poly($\varepsilon$-caprolactone)/atactic polystyrene (PCL/aPS)[149]. Depending on the thermal treatment it was shown that aPS can remain trapped within the growing spherulite. The cause of this dispersion was attributed to the crossing of the binodal curve, causing subsequently LLPS within the spherulites. The fractionated crystallisation could reduce the growth rate of the matrix and this could result in the decrease of $K_3'$ shown in Figure 5.7. Returning to the morphology shown in Figure 5.15, this microstructure is in contrast with that found by Faker *et al.* [150] in LDPE/EVA blends, where they observed a PE matrix containing submicrom EVA droplets formed because of a favorable interfacial tension. Although the finding of Faker *et al.* [150] is in contrast to our present finding, we suggest that this is due to differences in material preparation. In particular, the submicrom EVA droplets result from the sample being quenched into liquid nitrogen, directly from a melting temperature of 180 °C. This would indicate that the EVA droplets can grow during the crystallisation of PE at 117 °C.

On increasing the EVA content to 40 %, the microstructure formed, after melting for 5 min, reveals a two phase co-continuous structure between the PE and EVA, as can be seen in Figure 5.17. Within the PE-rich regions, partial banded spherulites can be seen. This result indicates that the PE is still able to crystallise in the form of spherulite, despite the gross phase morphology.

Furthermore, on increasing the melting time to 60 min, the phase separation is

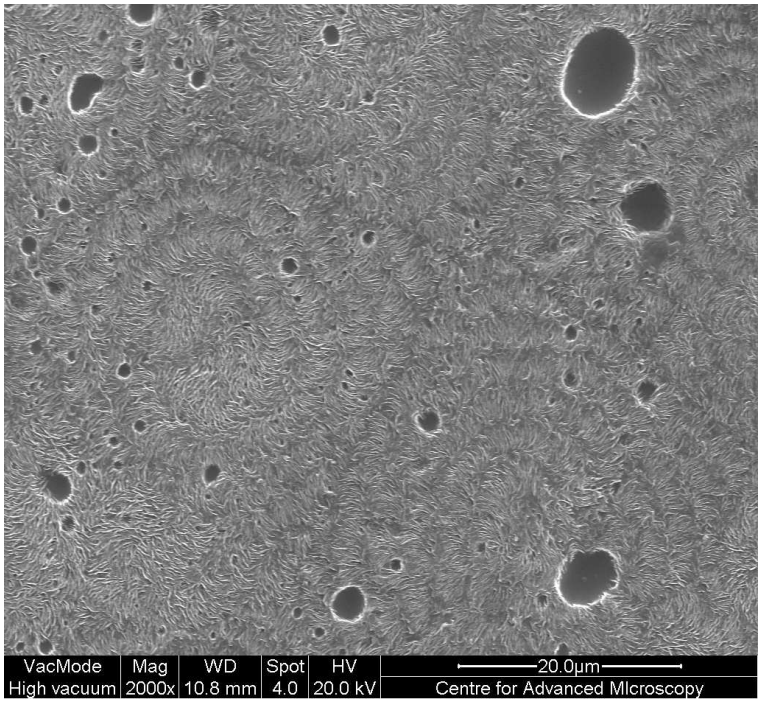


FIGURE 5.15: Scanning electron micrograph of 80:20EVA18 melted for 5 min and crystallised at 117 °C; Spherulites are visible throughout the specimen and well established phase separation is present within the PE matrix;PE and EVA result immiscible.

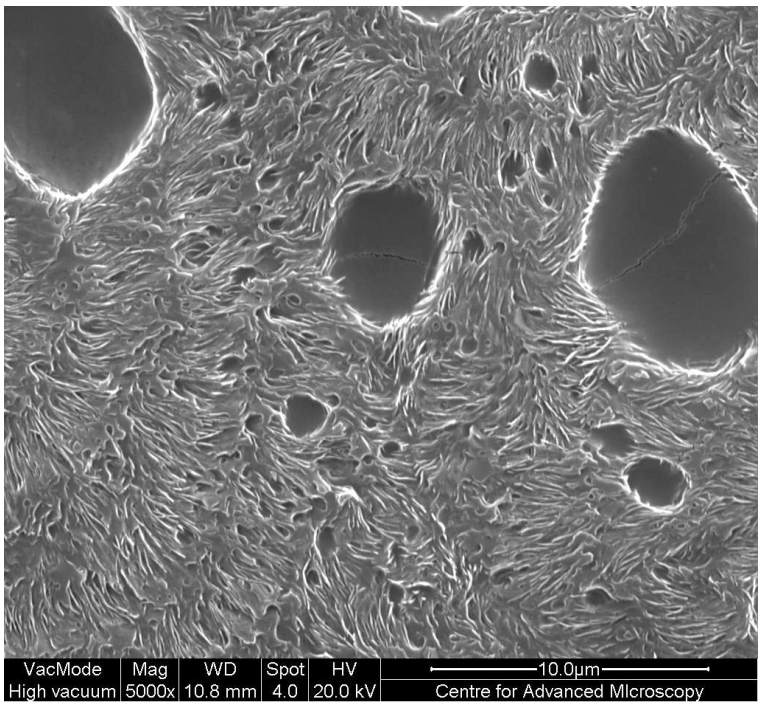


FIGURE 5.16: Scanning electron micrograph of 80:20EVA18 melted for 5 min and crystallised at 117 °C; Different size of second phase are observed, where some penetration of PE lamellae are visible.

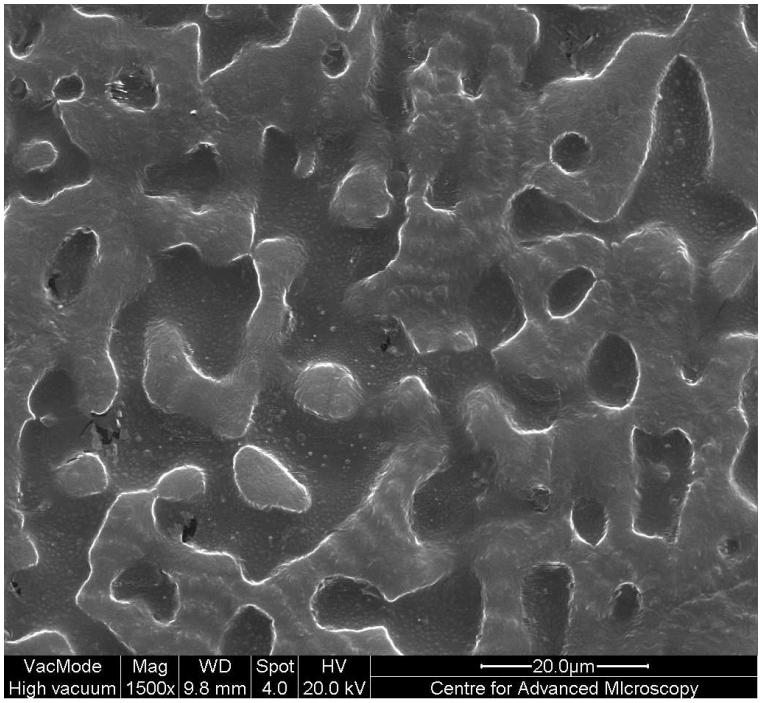


FIGURE 5.17: Scanning electron micrograph of 60:40EVA18 melted for 5 min and crystallised at 117 °C; phase separation present all around the specimen.

enhanced. Figure 5.19 typifies the 80:20EVA18 blends, where coarser phase separation is visible through all the sample; Figure 5.20 shows phase separation in 60:40EVA18 blends. The latter Figure demonstrates that the polyethylene again contains partial banded spherulites (as seen from Figure 5.20), while the EVA phase results as coarser structureless regions, compared with Figure 5.17. These results are in agreement with those reported in the literature by Na *et al.* [56], who observed a co-continuous polyethylene phase in a blend of 60:40 LDPE:EVA after short melting times.

In summary, PE:EVA18 blends showed different morphologies, depending on both the EVA content and the melting time. Table 5.2 summarises the above findings:

The range of morphologies seen from PE:EVA9 and PE:EVA18 start from an apparently miscible blend (80:20EVA9 melted for 5 min) through inclusion of EVA droplets, to co-continuous phase separation. On increasing the EVA content, more phase separation occur in all the systems. Submicrons droplets for blends

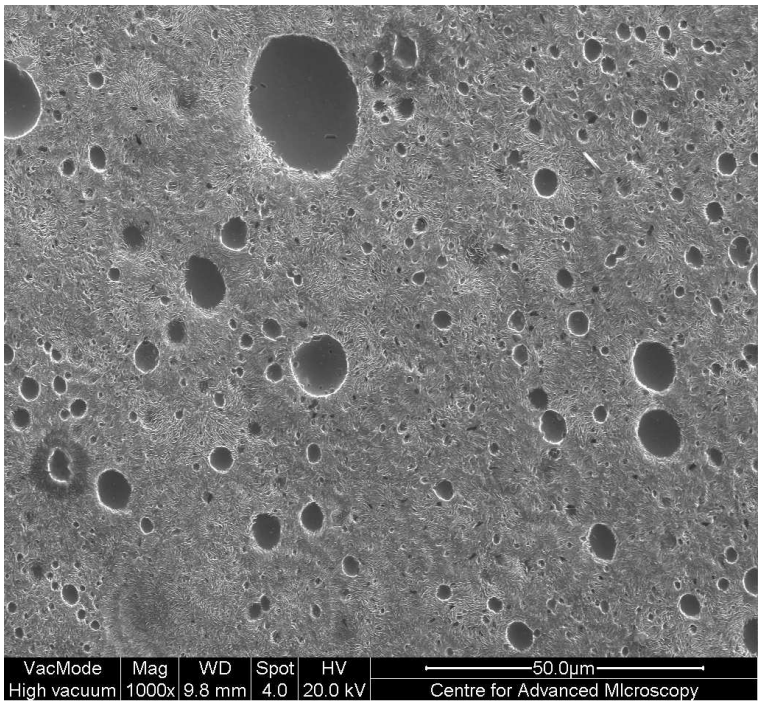


FIGURE 5.18: Scanning electron micrograph of 80:20EVA18 melted for 60 min and crystallised at 117 °C; Increase of EVA $R_d$ for 1 hr melting time.

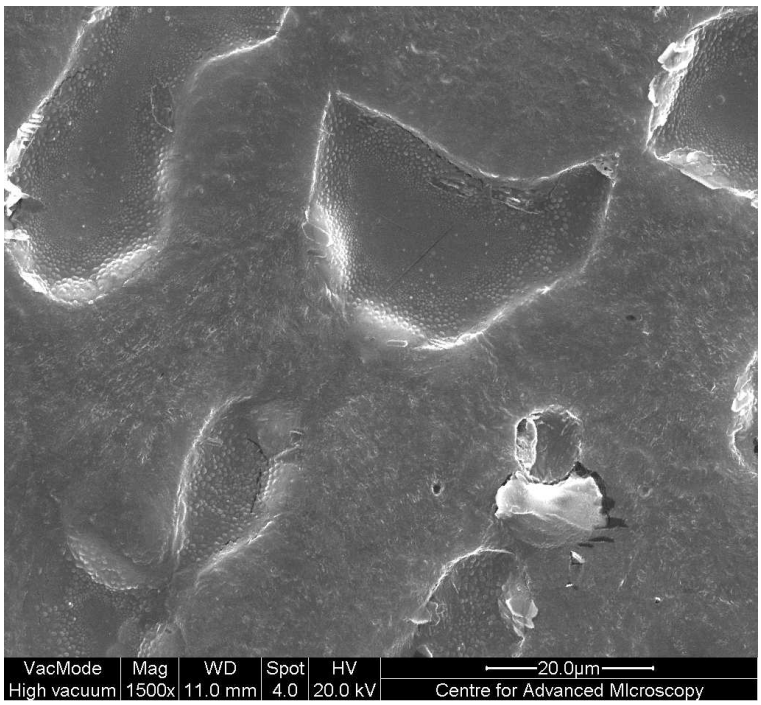


FIGURE 5.19: Scanning electron micrograph of 60:40EVA18 melted for 60 min and crystallised at 117 °C; Co-continuous phase separatation is present all over the sample.

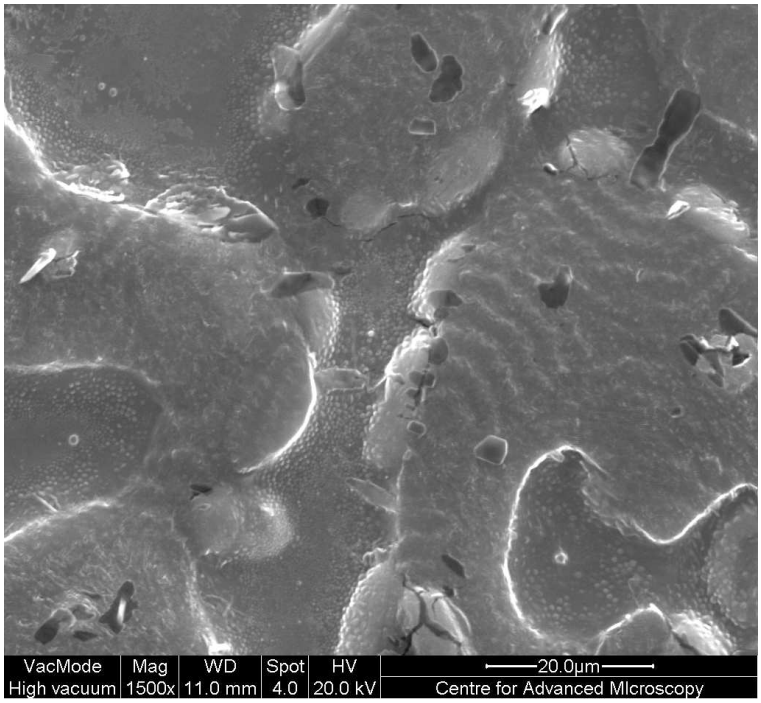


FIGURE 5.20: Scanning electron micrograph of 60:40EVA18 melted for 60 min crystallised at 117 °C.

TABLE 5.2: PE:EVA18 morphologies in function of EVA content and melting time.

| **Material** | **Melt 5 min** | **Melt 60 min** |
|---|---|---|
| 80:20EVA18 | Phase sep./micro droplets | Phase sep./coarser droplets |
| 60:40EVA18 | co-continuous Phase Sep. | Coarser Co-continuous Phase Sep. |

based on EVA9 to macro droplets in EVA18 based systems. On increasing the VA content in the EVA, phase separation is present in all the specimens as seen above. Increasing the melting time, separation was observed in all cases and co-continuous phase separation is present, which suggests a melt effect. This findings suggest that the phase behaviour is dominated by the EVA, VA content and the time in the melt.

### 5.4.3 PE:EVA with 40 % VA

The trends outlined above were expanded further with reference to the PE:EVA40 system. Figure 5.21 shows a micrograph of 80:20EVA40 melted for 5 min; crystallised polyethylene that resembles the form of spherulites is present with occluded EVA droplets on the order of 0.7 $\mu$m in radius ($R_d$), which are smaller than the droplets seen in PE:EVA18. Looking back at the previous trends, the increase of VA content in EVA showed coarser phase separation, which does not happen in the current case. An increase of time in the melt results in a well defined and coarser phase separated microstructure, containing EVA-rich droplets (Figure 5.22). A shorter melt time has been seen to result in a more homogeneous dispersion compared to that of longer melt times. The EVA particles have a radius of the order of 0.70 $\mu$m (Figure 5.21) for a 5 min melt and 3-4 $\mu$m for a 60 min melt (Figure 5.22). From Figure 5.21, spherulite shapes are still detectable; however, inclusions of EVA are present throughout the crystallised PE. If the size of the inclusions in PE:EVA40 are compared to those in PE:EVA18, it can clearly be seen that in this case the inclusions are smaller. Na *et al.* [56] related this phenomenon to reduced interfacial tension due to increased compatibility of LDPE with EVA. Another study suggested that the small size of the EVA phase domains is due to a higher viscosity of the PE matrix compared to the EVA [135]. Moreover, 80:20EVA40 has shown same values of $K_3'$ to 80:20EVA9 blends, which suggests that EVA40 affects neither the nucleation nor the growth rate of the polyethylene blend.

Figure 5.23 shows typical microstructures of 60:40EVA40 melted for 5 min. Coarser EVA droplets are present in the system but, again, the increase in EVA content has not produced co-continuous phase separation, as in EVA18 based systems. From the micrograph, it seems that the lamellae occluded the EVA phase while crystallising and a drop in $K_3'$ was observed, thus more energy needs to be dissipated to occlude the second phase. Martuscelli proposed a modification to the

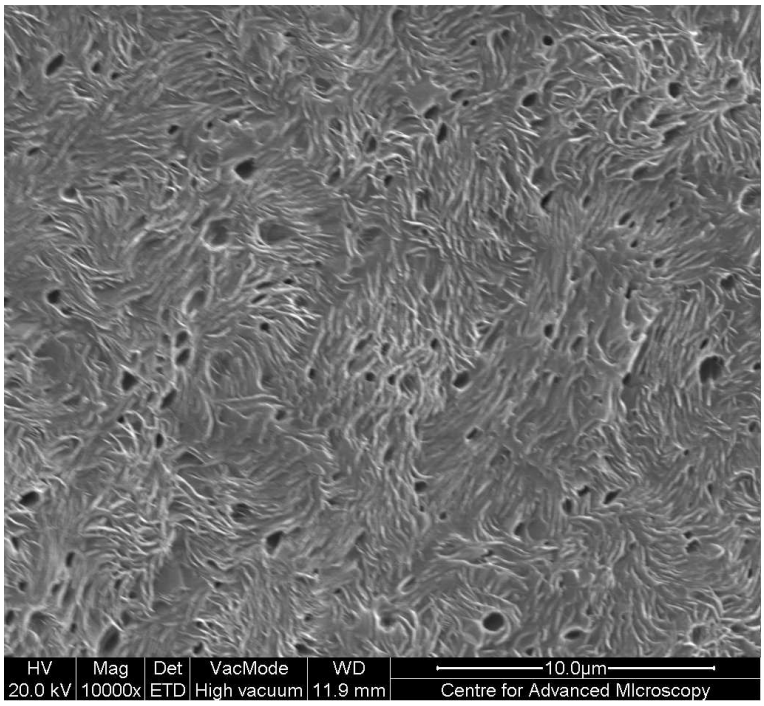


FIGURE 5.21: Scanning electron micrograph of 80:20EVA40 melted for 5 min and crystallised at 117 °C.

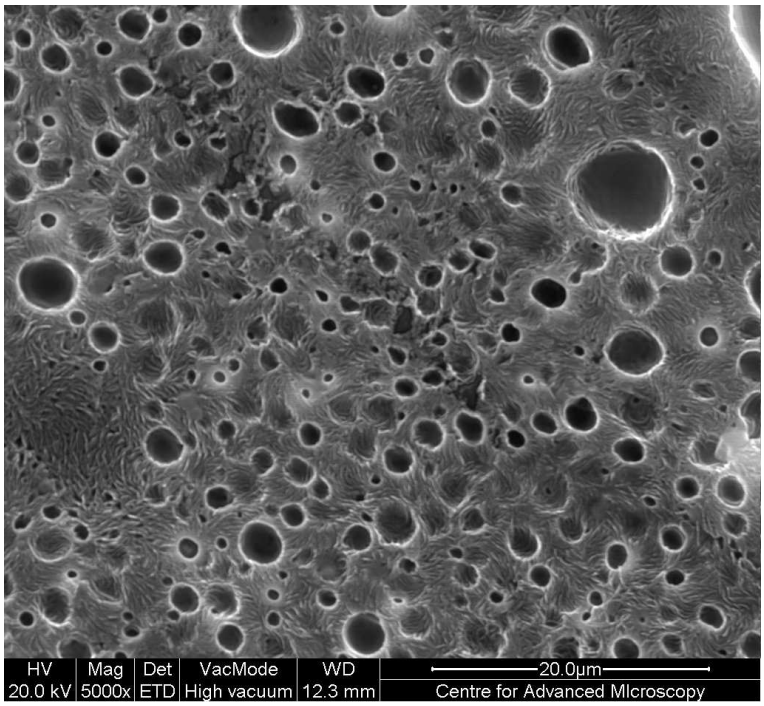


FIGURE 5.22: Scanning electron micrograph of 80:20EVa40 melted for 60 min and crystallised at 117 °C; Increase of EVA $R_d$ for 1 hr melting time.

Hoffman Lauritzen equation in order to include an the additional energy barrier, such that the growth rate equation becomes:

$$Ln(G)+\frac{U*}{R\left(T_c-T_{inf}\right)}=ln(G_0)-K_g/\left(fT_c\Delta T\right)-\left(E_1+E_2+E_3+E_4\right)/\left(fT_c\Delta T\right) \tag{5.6}$$

In this, the new terms are defined as: $E_1$ energy dissipated by rejection of domains, $E_2$ kinetic energy to overcome the inertia of the drops, $E_3$ energy required to form a new interface between a spherulite and the other phase and $E_4$ energy dissipated by deformation of the engulfed domain [151]. From this, it can be conclude that $G$ can be affected by presence of the second phase, which confirms an increase in growth rate is impossible in the PE/EVA systems studied here. This also explain why the PE:EVA18 systems show lower $K_3'$ compared to the 80:20EVA9 and 80:20EVA40. Nonetheless, Wang *et al.* [152] showed through self-consistent field theory (SCFT), that enhancement of nucleation is possible in polymer blends containing a diblock copolymer. Recently Zhang *et al.* [153] explained that the enhancement of nucleation depends on the orientation of the polymer chain with respect to the interfacial region and is proportional to the interfacial volume. Conversely, dynamic Monte Carlo simulations by Ma *at al* [154] attributed the enhancement to enthalpic, rather than entropic factors. With regards to the 60:40EVA40 blends, it is interesting to note that the second phase is present in droplet-like features and not as a co-continuous phase, as shown for 60:40EVA9 and 60:40EVA18. An explanation can be provided by the different molecular weight of the EVA40 compared with the other two copolymers. In fact, Potschke and Paul [155] showed that the phase inversion composition depends on both composition and viscoelastic factors. Therefore, the composition in the present work is the same as the other copolymer, whilst the viscosity will be affected by the different molecular weight of the materials. This seems in agreement with the morphology shown here, where at the same crystallisation temperature the droplets in EVA40 result different from the EVA18.

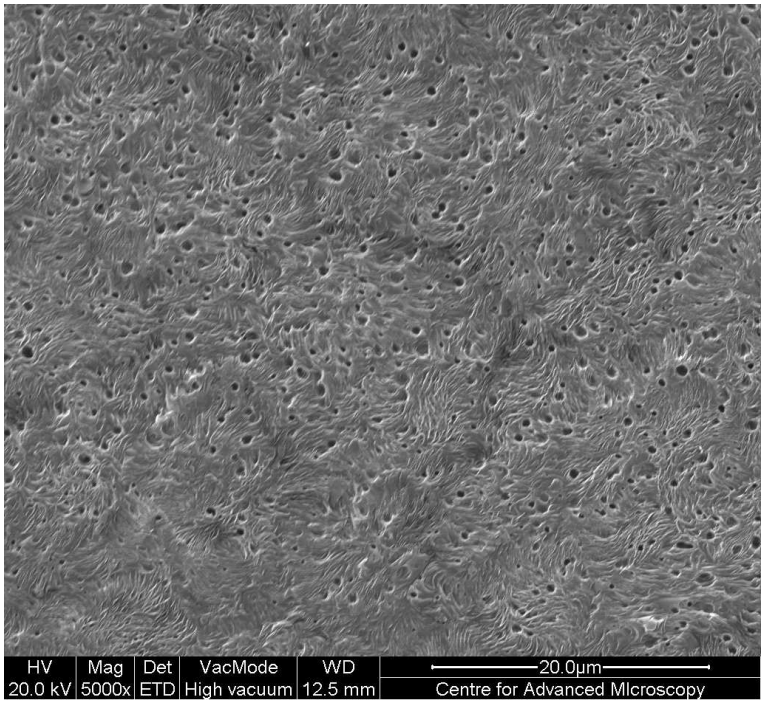


FIGURE 5.23: Scanning electron micrograph of 60:40EVA40 melted for 5 min and crystallised at 117 °C.

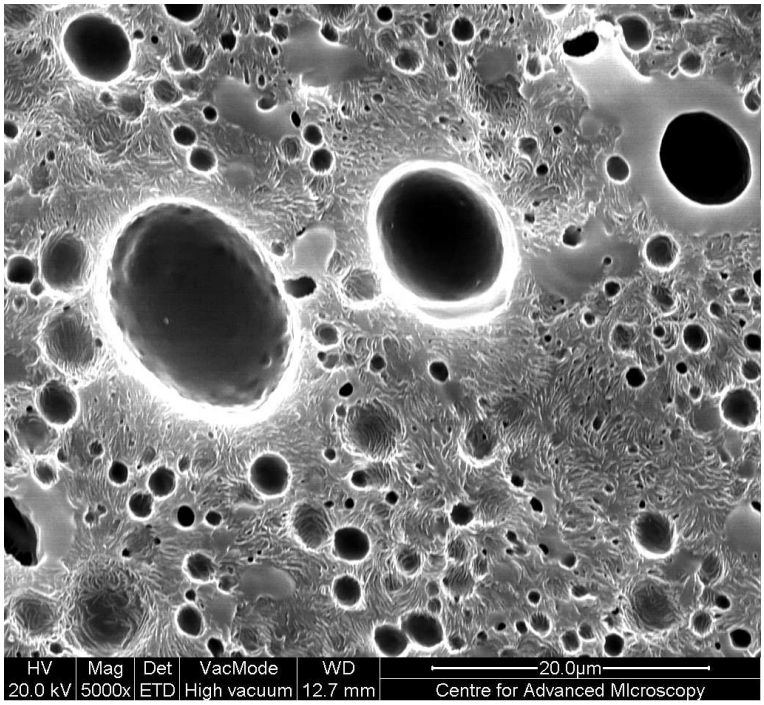


FIGURE 5.24: Scanning electron micrograph of 60:40EVA40 melted for 60 min and crystallised at 117 °C.

To summarise, two different blend ratios were studied by SEM. The Specimens varied in term of the EVA to PE ratio, the composition of the EVA itself and the annealing time at the melting temperature. From these results, some conclusions can be drawn:

- In the case of blend ratios of 80:20 melted for 5 mins, a PE-rich phase was observed for all VA content. In particular, the blend containing EVA9 showed limited phase separation of EVA rejected at the boundary of the spherulites. However, the size of inclusion increased with increase of VA to 18 %, which affected the growth rate.

- On increasing the EVA content, phase separation was present ranging from inclusions (60:40EVA9 melted 5 min) to co-continuous phase separation (60:40EVA18 melted 5 min), depending on the VA content. However, this was not the case for the EVA40 system, where phase separation was observed in the form of droplets.

- On increasing the time in the melt, phase separation was enhanced in all the cases, showing coarser droplets or co-continuous phase separation. Again, the EVA40 system showed no co-continuous phase separation.

Therefore, the first two PE:EVAs system showed similar trends, whilst the PE:EVA40 appeared different. The low molecular weight of the EVA40 is suggested to be the cause of such effect, which highlights how a non polar matrix can be effectively mixed with relative polar macromolecules.

## 5.5 Conclusions

Three different polymer blend systems have been studied here, in which we have varied the EVA content ( between 9, 18 and 40 %), the PE:EVA ratio ( between 80:20 and 60:40) and the time held in the melt. Melting traces have shown a potential passive role of EVA9 in both blends, whilst this was not the case for the EVA18 and EVA40. However, increasing the time in the melt, the enthalpy of the LPE peak decreased and a co-crystallisation peak arose on the right shoulder of the BPE peak. Being always present below the isothermal crystallisation temperature, this is believed to be a LLPS effect. Kinetic data supported a 3-dimensional growth rate of the polymer blends. Blends 80:20 containing EVA9 and EVA40 showed similar values of $K_3$, whilst all the 60:40 and the 80:20EVA18 showed lower values of growth rate. This result suggests that the the increase of EVA does not mean a decrease in the crystal growth rate. It is believed that the EVA phase disrupts the growth rate of the PE blend when present at 40 % or when the phase separation is present in the form of macrophase inclusions ( see 80:20EVA18). This hypothesis is strengthened by the morphology studies. That is, the EVA9 and EVA40 systems showed submicron EVA inclusion. However, it is believed that the EVA9 plays a passive role in the system, as seen from the melting traces, whilst the low molecular weight of the EVA40 allows the PE blend not to be disrupted by the inclusion of submicron EVA phase. On the contrary the higher molecular weight of EVA18 reduces the growth rate, as seen from the kinetic data and the macrophase separation in the SEM images. The increase of melting time increases the coalescence of the EVA droplets that ultimately result in co-continuous phase separation in EVA9 and EVA18 systems. Therefore we would like to emphasise that the design of specific morphologies are possible by varying the molecular weight and the polarity of the copolymer. This is a first potential step for the fabrication of nanocoposites based on a non polar matrix and a low polar second phase, in order to maximise the exfoliation of the filler.

# Chapter 6

# Electrical Breakdown in PE/EVA systems

In chapter 5 the effect of adding EVA copolymers to 20:80 LPE:BPE polyethylene blend (called PE) has been studied. In particular, the effect of VA content and the PE:EVA ratio has been described. By suitable processing, a range of morphologies was produced and it was shown that the EVA, VA content can have an influence on the microstructure. However, it was demonstrated that the molecular weight can play an important role in influencing mixing a non polar matrix with polar macromolecules. In this way, various morphologies with micro phase separation were produced on increasing the VA content to 40 %. The time in the melt was also used as variable in all the systems and this indicated a coarser phase separation, ranging from droplets to co-continuous phase separation, depending on the PE:EVA ratio and the molecular weight of the EVA.

So far, the previous study showed that it is possible to design tailored microstructure, without disrupting the morphological characteristics of the polyethylene blend. This is, however, only a first step towards designing nanocomposites materials, with particular interest in the dielectrics field. In fact, one of the ultimate

goals of this concept is to intercalate/exfoliate nanofillers in a non polar matrix with the through the addition of a relative polar macromolecule. However, before adding the filler into the blends described previously, a study of the electrical properties of the blends will follow in order to study the effect of the polarity of the EVA copolymers on the blends.

To date, only few studies have been undertaken on PE:EVA blends. Some breakdown tests have been performed on LDPE/EVA (22 % VA) composite under liquid nitrogen temperature, showing a better performance of the composite material than the single polymers [156]. Tu *et al.* [157] studied the electric breakdown and space charge of LLDPE/EVA blends and suggested that the incorporation of EVA reduces the concentration of deep trap charges such that the DC breakdown characteristics at liquid nitrogen temperature improve with the addition of EVA up to 4.6 % in weight. Lee *et al.* [158], instead, studied the mechanical properties of XLPE blended with EVA and related the improved mechanical properties to the retardation of water treeing growth in the blends examined. More recently, Go *et al.* [159] studied the effect on the AC dielectric strength of varying the ratio of LLDPE:EVA, finding an optimum at 70:30. However, details of morphologies were not shown. Only recently a more systematic work has been undertaken by Hosier *et al.* [140] on the morphology and the electrical breakdown of EVA copolymers and the effect of adding polyethylene. Hosier and co-workers showed that the breakdown behaviour can be improved by tailoring low VA content copolymer and adding a fraction of the same of PE blend considered here (10 % w/w). However, these authors suggested that a greater improvement of the electrical properties could be achieved through the introduction of more LPE into the system.

In summary, the above findings put some positive premises on the present work. From the blends studied in chapter 5, all the 60 min melted samples were eliminated, because all morphologies showed enhanced phase separation, which could adversely affect breakdown behaviour. Therefore the blends were prepared as pre-

viously varying the EVA and VA content. All the samples were tested using the standard procedure described in section 2.7. The polymer discs were melted at 150 °C for 5 min and then crystallised at 117 °C. Subsequently, the samples were quenched in water. For each type of material, two different batches were tested: a first batch was degassed in the vacuum oven, while a second was immersed in water for 50 hr. Due to the polarity of the EVA, the addition of the water could affect the breakdown behaviour adversely.

## 6.1 Results and Discussion

Samples prepared as described previously exhibited different morphologies, as described in detail in chapter 5. Nevertheless, a short description of the key microstructural characteristic of each blend used for breakdown measurement is provided here.

Figure 6.1 shows the morphology of 80:20EVA9 samples. Banded spherulites are present throughout all the sample and there is no evidence of macrophase separation. Figure 6.2 typifies the morphology of 60:40EVA9 blends. As can be seen, a different microstructure is observed from the 80:20EVA9. There is no evidence of sperulites, but a co-continuous phase separation is detachable. This result suggests that the addition of 40 % of EVA corresponds to phase inversion region. Figure 6.3 and Figure 6.4 show the typical microstructures of blend containing EVA18. In the case of 80:20EVA18, polyethylene is still able to form spherultites, but the presence of a second phase is visible throughout the sample. The radius of the second phase droplets are of the order of 2 $\mu$m, but some droplets reach a maximum of several micron in diameter, as shown in Figure 6.3. On increasing the EVA content, a co-continuous phase separation is observed. Figure 6.4 shows the morphology of 60:40EVA18 blend, where the co-continuous phase separation alternates between crystallised polyethylene and featureless EVA regions.

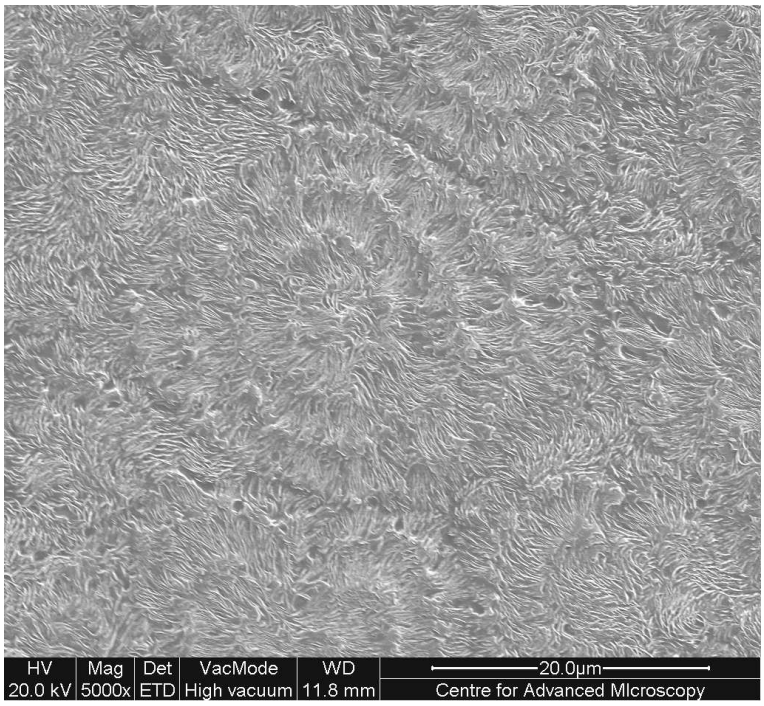


FIGURE 6.1: Scanning electron micrograph of 80:20EVA9 melted for 5 min and crystallised at 117 °C; no evidence of macroscopic phase separation. The microstructure is dominated by PE spherulite.

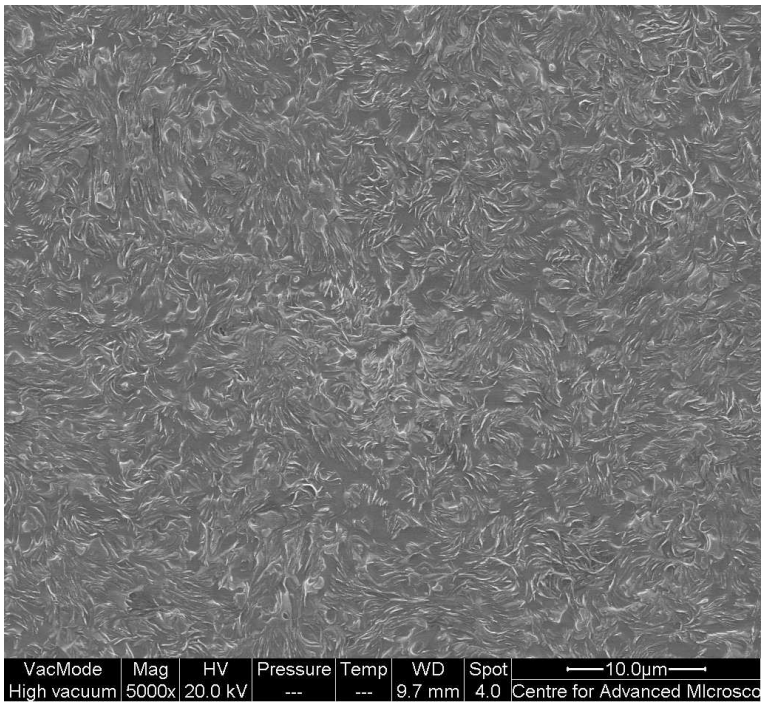


FIGURE 6.2: Scanning electron micrograph of 60:40EVA9 melted for 5 min and crystallised at 117 °C; presence of crystallised lamellae in polyethylene regions and featureless regions related to EVA.

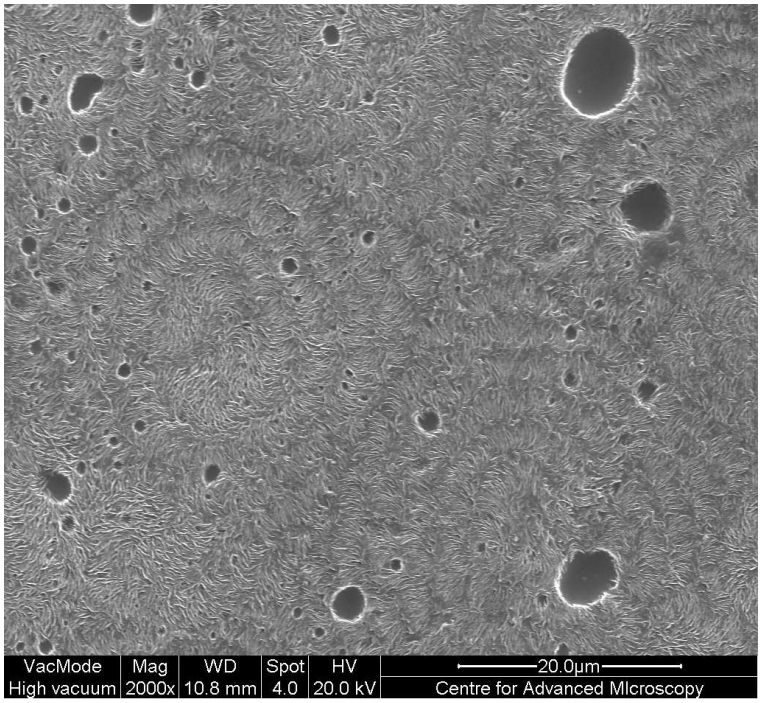


FIGURE 6.3: Scanning electron micrograph of 80:20EVA18 melted for 5 min and crystallised at 117 °C; Spherulites are visible throughout the specimen and well established phase separation is present within the PE matrix;PE and EVA result immiscible.

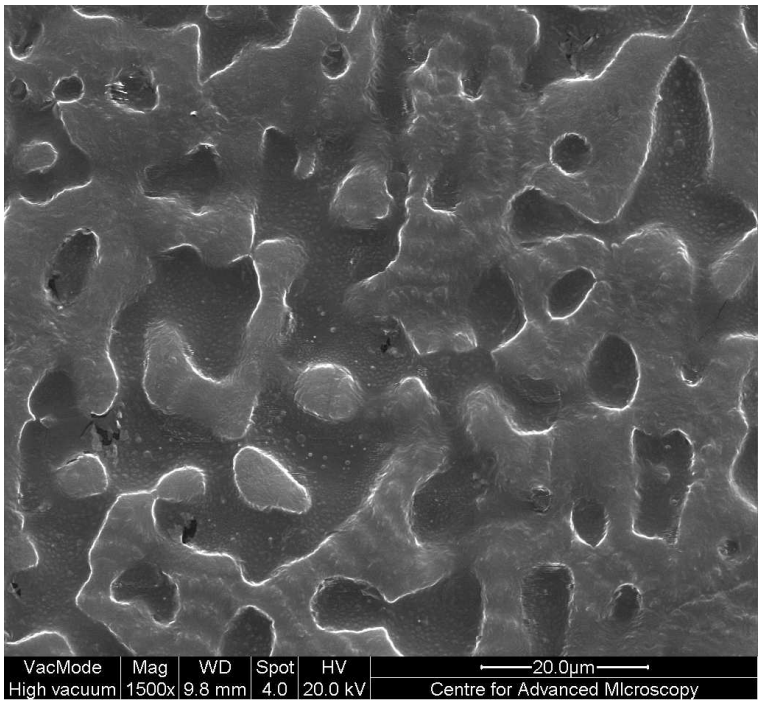


FIGURE 6.4: Scanning electron micrograph of 60:40EVA18 melted for 5 min and crystallised at 117 °C; phase separation present all around the specimen.

On increasing the VA content to 40 % in weight, different morphologies develop, compared with the previous two batches of blends. Figure 6.5 shows that crystallised polyethyelene lamellae and some submicron EVA droplets are present in the samples. Increaseing the EVA content does not produce a marked increase in droplet size, but, rather gives rise to an overall increase in the number of submicron droplets, as seen from Figure 6.6.

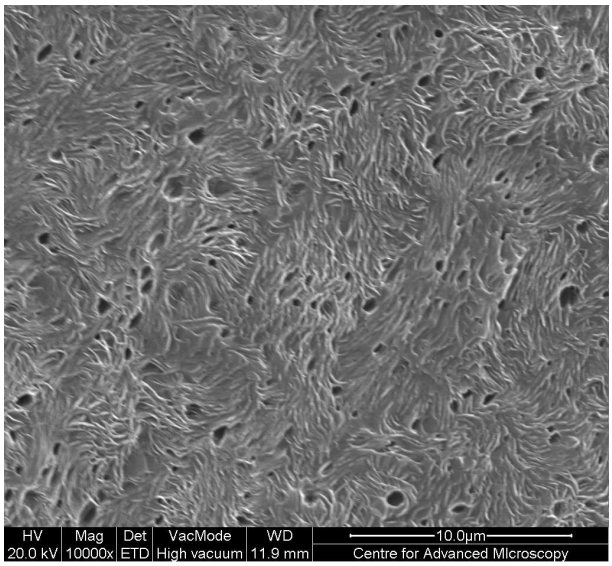


FIGURE 6.5: Scanning electron micrograph of 80:20EVA40 melted for 5 min and crystallised at 117 °C.

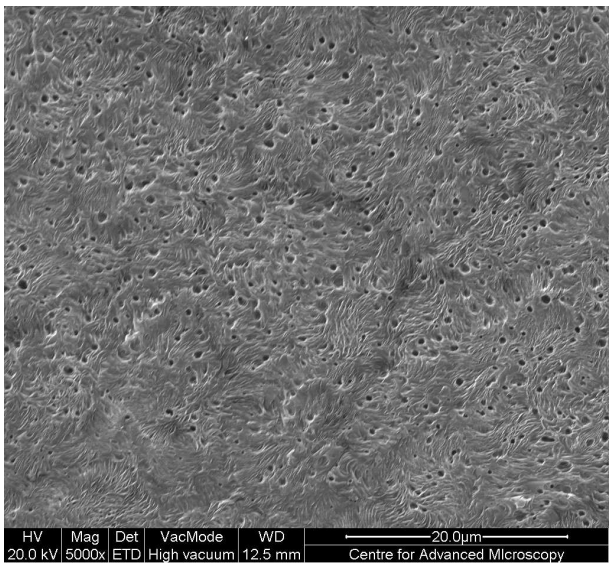


FIGURE 6.6: Scanning electron micrograph of 60:40EVA40 melted for 5 min and crystallised at 117 °C.

## 6.2 Electrical Breakdown Results

Figure 6.7 compares the breakdown behaviour of three PE:EVA9 blend systems with that of the PE blend alone, which was used here as a reference. From this, and the related data in Table 6.1, it is evident that the breakdown behaviour of these three materials is statistically equivalent and, in particular, is independent of the EVA content up to 40 %. The initial premise that, while the addition of polar EVA to polyethylene may be useful in connection with nanodielectric compounding, a combination of the resultant phase structure and the low crystallinity of the EVA would necessarily result in a reduction in breakdown strength is, evidently, not correct. Although the EVA used here contains a relatively low vinyl acetate content, as has been seen from the morphology studies, this is still sufficient to facilitate interactions with non-polar systems.

TABLE 6.1: Weibull data derived from the plots of all the PE:EVA9 systems

| *System* | *Degassed/Water* | $E_0(kV/mm)$ | $\beta$ |
|---|---|---|---|
| $PE$ | *Degassed* | 181± 5 | 12 |
| $80:20EVA9$ | *Degassed* | 178±4 | 11 |
| $60:40EVA9$ | *Degassed* | 182± 3 | 18 |

Figure 6.8 shows typical Weibull plots comparing the behaviour of all 80:20EVA described in this chapter. Although significant scatter is present in these, a pronounce decrease of $E_0$ from the 80:20EVA9 blend to 80:20EVA18 to 80:20EVA40. Nonetheless, despite a decrease in breakdown strength of the 80:20EVA18 compared to the blend containing EVA9, the difference is negligible, with a strength of 163 kV/mm. The 80:20EVA40, instead shows the lowest breakdown strength, with $E_0 = 137$ kV/mm. This result indicates that the increase of the polar group ( VA content) in the system affects the electrical strength of the blends adversely. Despite the fact that the 80:20EVA40 showed submicron droplets from the morphology ( Figure 5.21), the VA content plays a negative role for the electrical strength of the system. However, it seems reasonable that over the breakdown

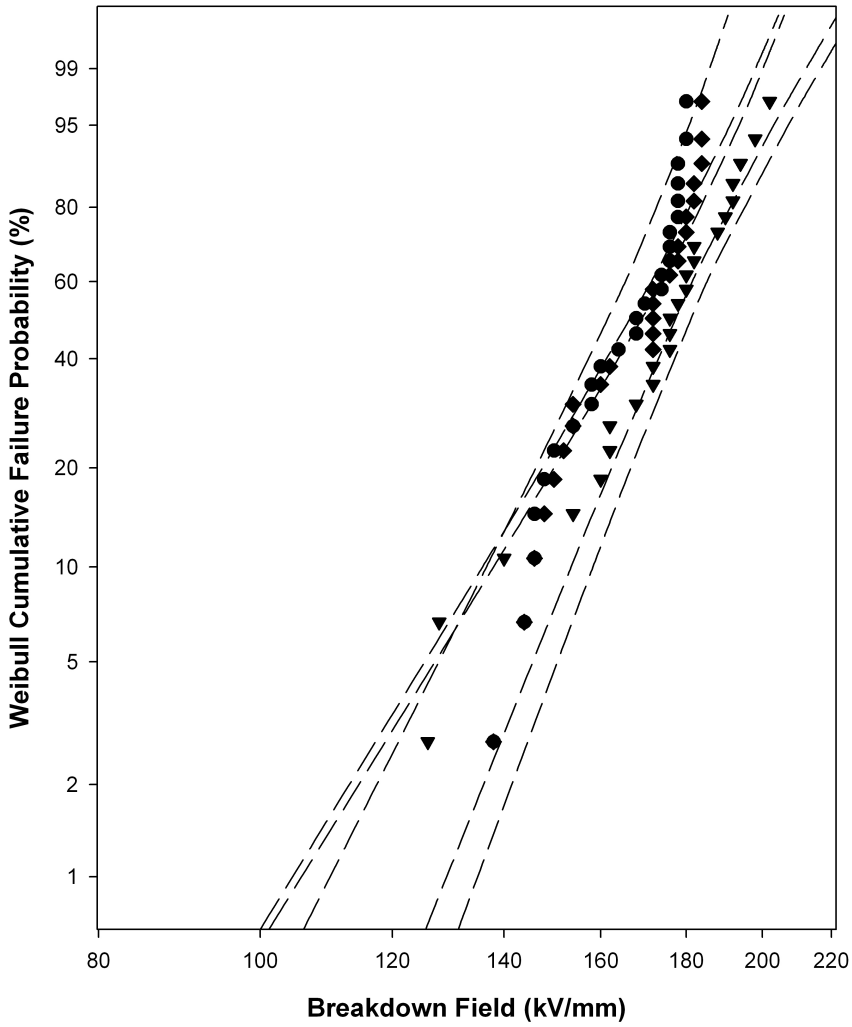


FIGURE 6.7: Weibull plots comparing the breakdown behaviour of PE (▼), 80:20EVA9 (●) and 60:40EVA9 (⧫).

strength has increased due to the presence of 80 part of PE. Indeed, Hosier *et al.* [140] studied the same materials with just 20 part of PE and found that blend of 20:80EVA40 exhibited a breakdown strength of 96 kV/mm after crystallisation at 117 °C. Nonetheless, from the present results and the related morphologies, it can be concluded that the polarity seems to affect more than the size of the second phase.

A further investigation was conducted using the composition to 60:40 PE:EVA systems. Figure 6.9 and Figure 6.10 compare the breakdown behaviour of 80:20EVA18

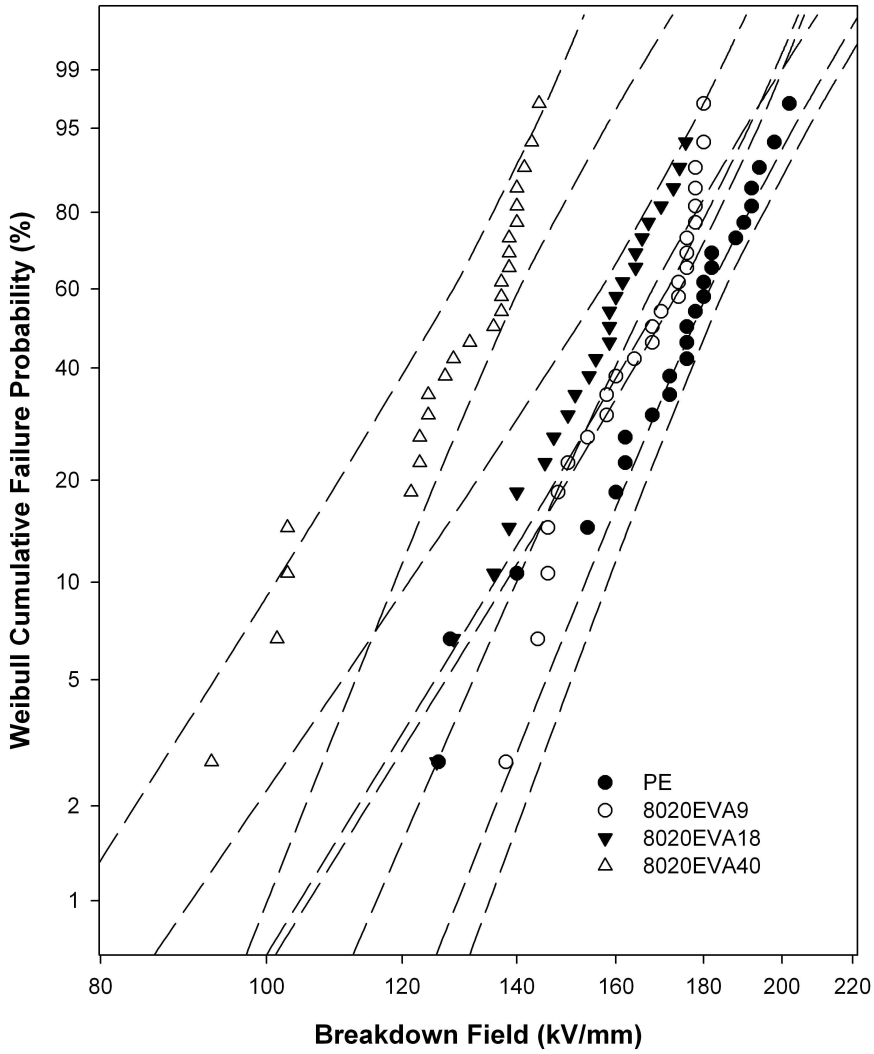


FIGURE 6.8: Weibull plots comparing the breakdown behaviour of 80:20EVA at variation of VA content.

and EVA40 with that of 60:40EVA18 and EVA40. In the case of EVA18, there are no major changes in the breakdown strength, so that the scatter data overlap within the uncertainty limits, whilst the EVA40 shows a different trend in the case of 60:40EVA40. In fact, even though the values of $E_0$ are similar, there is a change in the $\beta$ value that decreases with the increase of EVA in this system. This decrease is caused by the presence of few data points below 100 kV/mm; quantitative analysis provides no statistical justification for censoring the data set. Therefore, assuming that this effect is real, it could be related to both the

polarity and the presence of macrophase separation within the system, otherwise this result is just consequence of the outliers. Indeed, comparing the $\beta$ values of all the blend shown in Table 6.2, 60:40EVA40 blend is the only one with a much higher $\beta$, while the others are comparable. This would suggest that there are no differences in breakdown behaviour between 80:20EVA and 60:40EVA blends. As

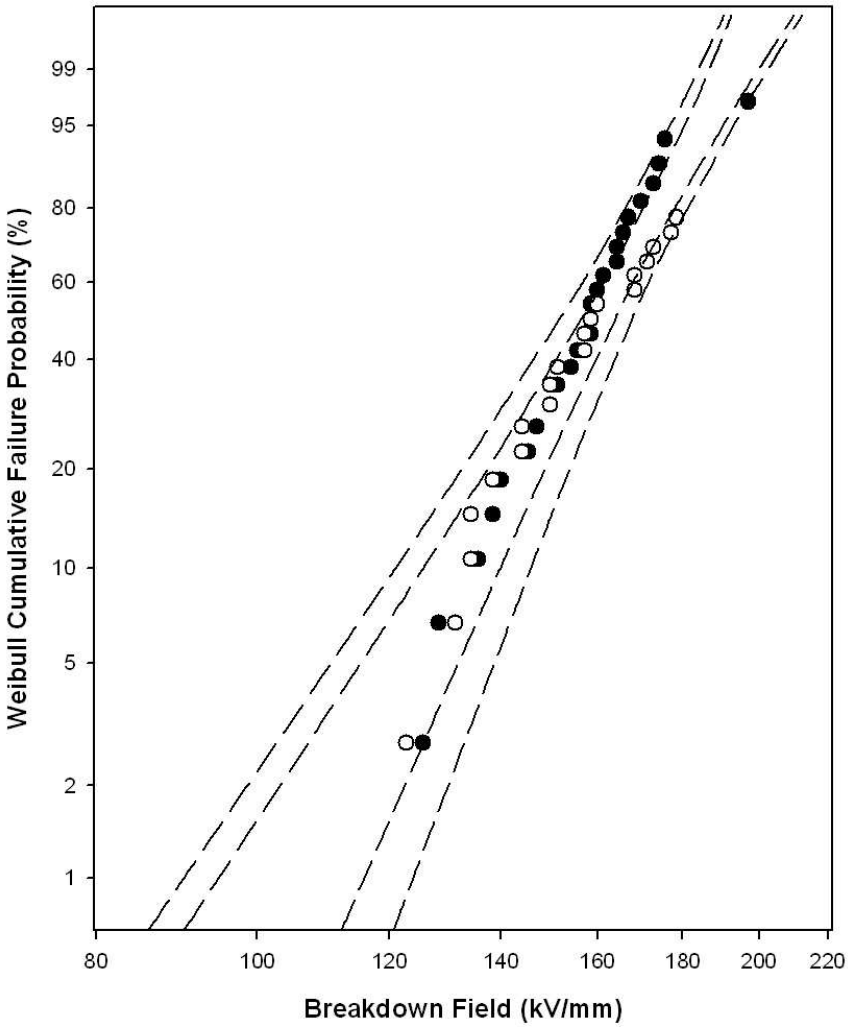


FIGURE 6.9: Weibull plots showing the effect on the breakdown behaviour of the PE:EVA18 system of varying the composition: 80:20EVA18 samples (•) and 60:40EVA18 (○).

mentioned at the beginning of this study, the effect of water has been considered here, in order to verify if the polar part of the blends would be affected by it. Typical data obtained from 60:40EVA9 samples that had been immersed in distilled

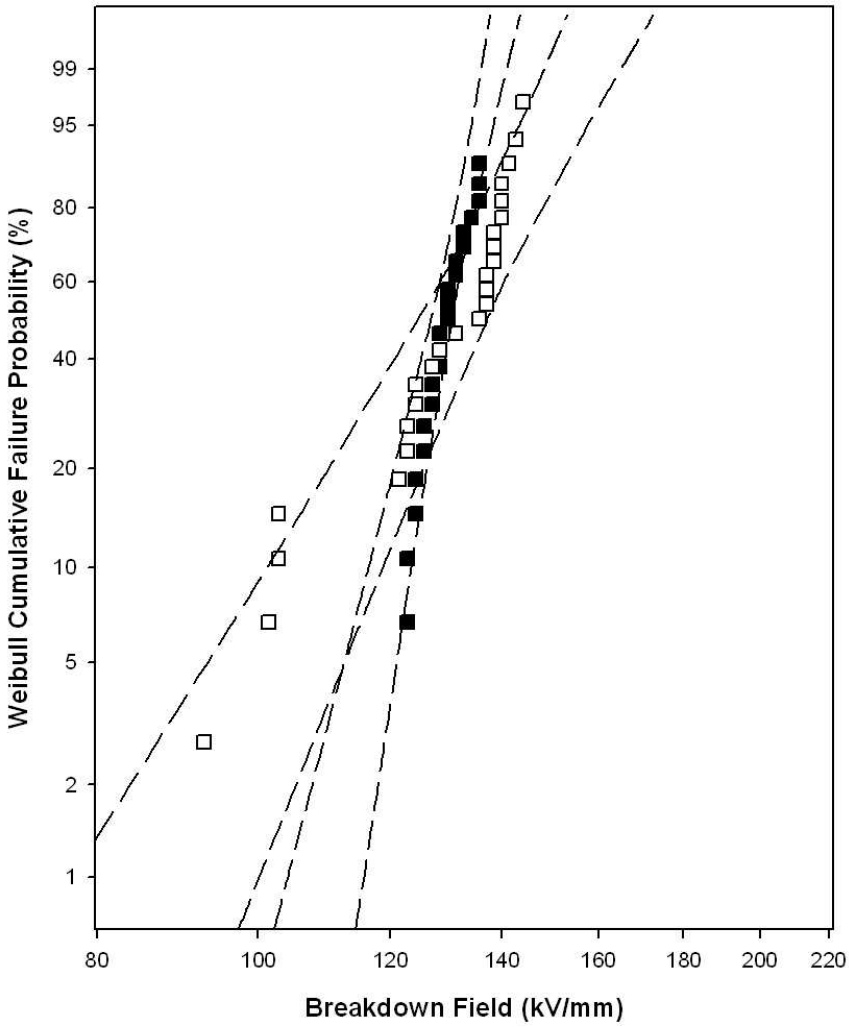


FIGURE 6.10: Weibull plots showing the effect on the breakdown behaviour of PE:EVA40 system of varying the composition: 80:20EVA40 samples (■) and 60:40EVA40 (□).

water for 50 hr at room temperature are shown in Figure 6.11; these data suggest that this has no adverse consequences, even in a system containing 40 % EVA, resulting independent of the presence of water. Figure 6.12(a) and 6.12(b) compare the breakdown behaviour of degassed 80:20EVA18 and 60:40EVA18 samples that have been immersed in distilled water. From this result it can be seen that all the samples show a decrease in the case of system immersed into water. Therefore the increase of of polarity allowed the penetration of water in the system which affected the the strength of the blends. Figure 6.13(a) and 6.13(b) compare the

breakdown behaviour of degassed 80:20EVA40 and 60:40EVA40 samples that have been immersed in distilled water.

From these results, despite the general decrease of breakdown from the PE:EVA9 system, it seems that the water has no effect in the case of 80:20EVA40 ( Figure 6.13(a), while it does affect the second system. To summarise the above results, Table 6.2 shows the quantitative data of $E_0$ and $\beta$:

TABLE 6.2: Weibull data derived from the plots of all the PE:EVA systems

| *System* | *Degassed/Water* | $E_0(kV/mm)$ | $\beta$ |
|---|---|---|---|
| $PE$ | *Degassed* | 181± 5 | 12 |
| $80:20EVA9$ | *Degassed* | 178± 4 | 11 |
| $80:20EVA9$ | *Water* | 181± 5 | 14 |
| $60:40EVA9$ | *Degassed* | 182± 3 | 18 |
| $60:40EVA9$ | *Water* | 186± 4 | 17 |
| $80:20EVA18$ | *Degassed* | 163± 4 | 10 |
| $80:20EVA18$ | *Water* | 137± 5 | 11 |
| $60:40EVA18$ | *Degassed* | 160± 6 | 12 |
| $60:40EVA18$ | *Water* | 145± 5 | 10 |
| $80:20EVA40$ | *Degassed* | 137± 5 | 11 |
| $80:20EVA40$ | *Water* | 137± 6 | 10 |
| $60:40EVA40$ | *Degassed* | 130± 2 | 27 |
| $60:40EVA40$ | *Water* | 123± 3 | 11 |

As it can be seen, the breakdown strength decrease with the presence of water, except for 80:20EVA9 and 80:20EVA40. In the first blend, the polar group is low and well dispersed in the system, therefore the water sorption is negligible. On the contraty, two explanations can be proposed from the result in 80:20EVA40 blend. First, it could be related to uncertainty in the technique used, but it would be strange that just one of the material do not show any affect from the water. In a second explanation, it is tempting to ascribe this phenomenon to the size of the EVA droplets in the system, which are at the sumicron dimension in the case of PE:EVA9 and 80:20EVA40 blends ( as seen in Figure 5.10 and 5.21), whilst the other blends show radius of several micron. Therefore, the water could penetrate easier in the second type of droplets than the first one. This would mean that

a tailored design of the morphology can influence both the breakdown strength and the water penetration. Marais *et al.* [160] studied the water permeation in non polar polymers ( LDPE and iPP) and some polar copolymers, included EVA varying the VA content. They found that the rate at which the water migrates in a polymer depends on the local concentration. From the micrographs, the local concentration of polar group is lower in the PE:EVA40 than PE:EVA9 and EVA18 due to the fine droplets dispersion and this allows a non permeation of water after 50 hr.

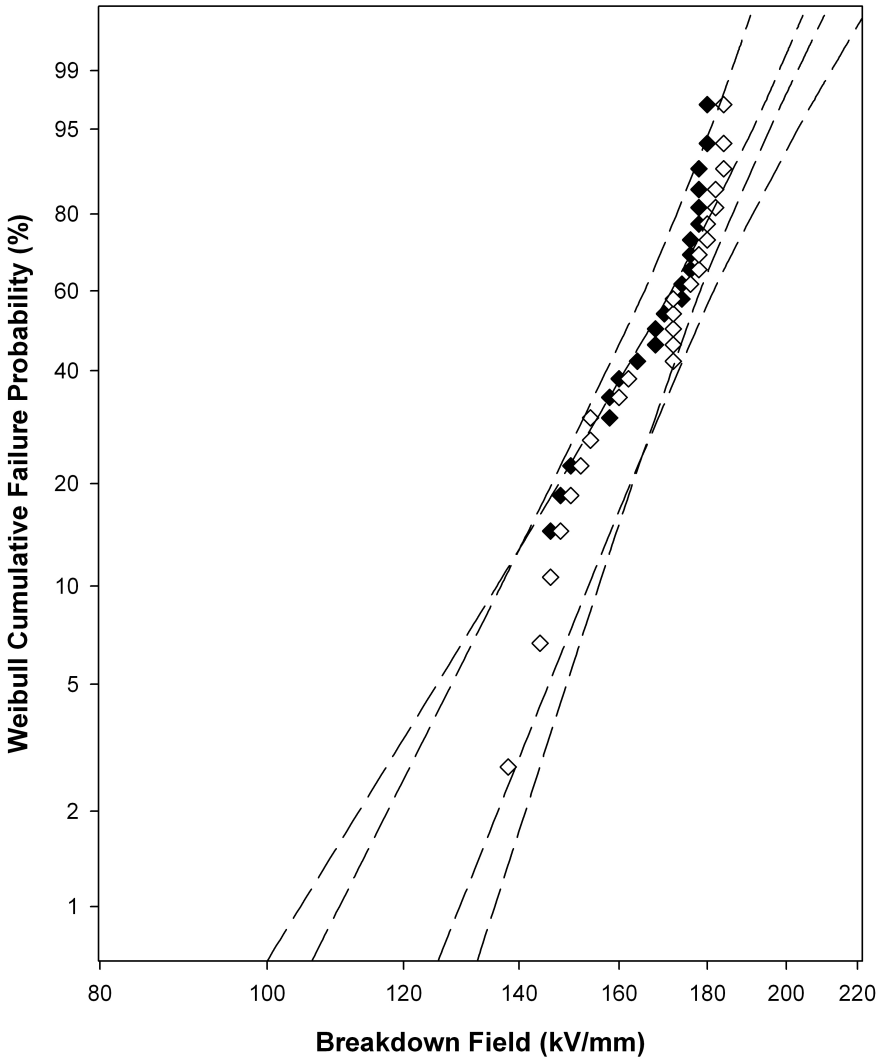


FIGURE 6.11: Weibull plots comparing the breakdown behaviour of 60:40EVA9 (♦) with that of the same material after immersion for 50 hr in distilled water (◊).

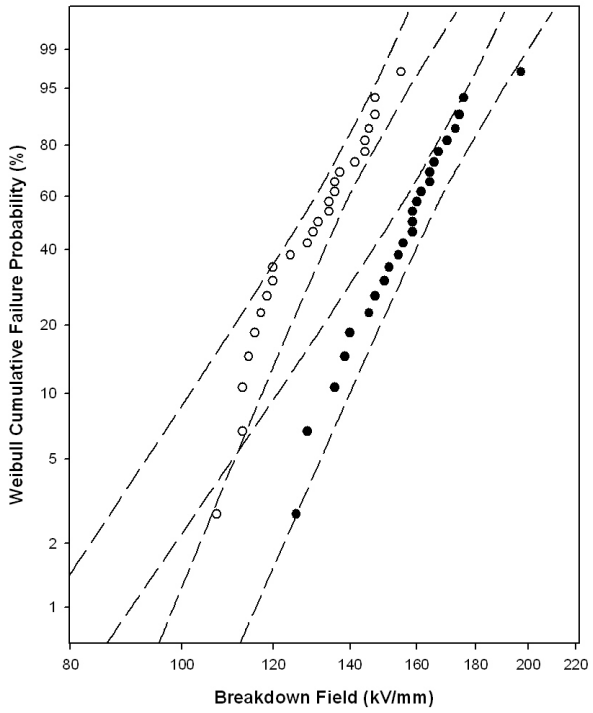


(a) 80:20EVA18

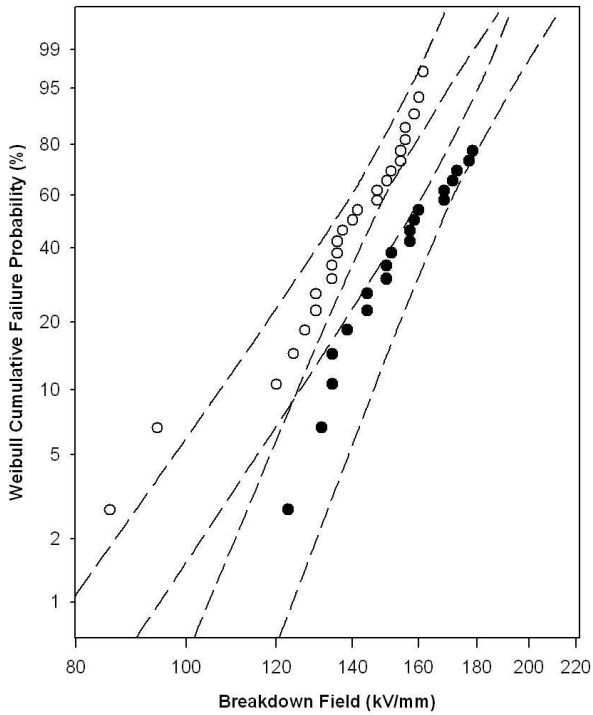


(b) 60:40EVA18

FIGURE 6.12: Breakdown plots of PE:EVA18 (•) varying the composition and the effect of water (○).

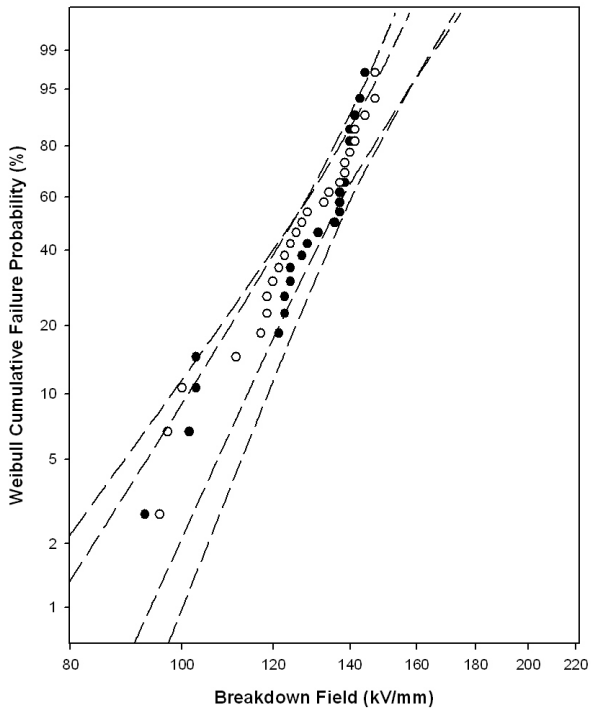


(a) 80:20EVA40

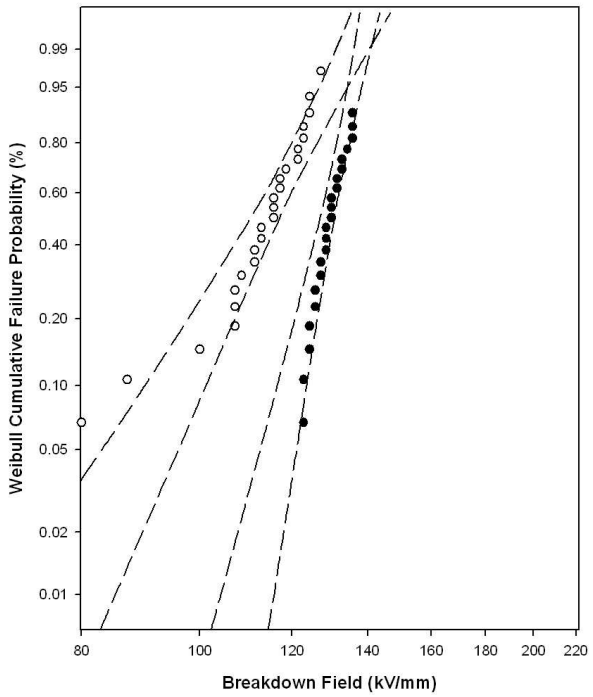


(b) 60:40EVA40

FIGURE 6.13: Breakdown plots of PE:EVA40 (•) varying the composition and the effect of water (○).

## 6.3 Conclusion

The breakdown behaviour of PE:EVA9 blend systems appears to be independent of composition, and a range of structural probes indicate an absence of macroscopic phase separation. All blends exhibit space-filling spherultic morphologies, irrespective of composition. If the addition of the EVA does not disrupt this element of the material's morphology, then short term breakdown does not appear to greatly affected. Thus, we can explain the observations reported above via the hypothesis that the added EVA is relatively miscible with PE at low vinyl acetate content.

The increase in VA content changes the morphology of the blend PE:EVA18, resulting in a macro phase separation. The breakdown behaviour of these systems are no longer independent of the EVA content. The EVA phase is dispersed into the PE matrix in micro particles, therefore the breakdown is affected by the EVA phase. Moreover exposure of the system to the water results in a penalty for the blend therefore it is not suitable as dielectric material. Although 80:20EVA40 blend showed a decrease in breakdown strength, suggesting a penalty due to the polarity of the EVA, it revealed behaviour that was indipendent of the immersion in water. This suggests that the morphology and dimension of the second phase plays an important role in the absorption of water by the system. While this interpretation is consistent with all the data, it is not intuitively obvious why a blend of polar and non-polar polymers should behave in this way.

# Chapter 7

# EVA/MMT nanocomposites

## 7.1 Introduction

In the previous chapter, the effect of the morphology of PE/EVA blends on dielectric breakdown was examined. By suitable processing and crystallisation at a specific temperature, a designed blend was demonstrated to maintain similar breakdown strength to the virgin PE blend. In particular EVA9 and EVA18 based blends were found to be suitable for further dielectric applications. On the contrary, PE:EVA40 showed low brewakdown strength and for that reason no further studied will be undertaken. However, PE:EVA9 blends showed a single phase structure at the micro dimension, whilst PE:EVA18 resulted in a two phase system. In this chapter the possibility of designing a polyethylene based nanocomposite through the presence of a relative polar EVA in the system will be investigated. A preliminary study was conducted with the EVA based nanocomposite to determine if, in the presence of a filler, the dielectric properties of the nanocomposite would decrease. Before undertaking this study, a short review of the nature of nanocomposites is presented.

Nanocomposites are a relative recent class of composite materials in which the

dispersed particles have at least one nanometric dimension. This is the most widely used definition of nanocomposites, even if other criteria can also be used to identify nanocomposites [161], based on the huge surface area generally associated with these nano-fillers instead of on the linear dimensions of the particles. The surface area plays a major role in the modification of the matrix properties. As explained at the beginning of this work, several types of filler are used and they can have from one to three of their dimensions of nanometer size.

## 7.2 Polymer Layered Silicate (PLC) Nanocomposites

Although the intercalation chemistry of polymers when mixed with appropriately modified layered silicate has been known for a long time, the field of polymer/layered silicate (PLS) nanocomposites has gained considerable interest only relatively recently. Two major findings stimulated the interest in these materials. Firstly, in 1986 the first nylon-6-clay hybrid (NCH) was created at Toyota Central Research and Development Laboratories (TCRDL). The idea of combining nylon and a clay mineral arose from the inspiration of Dr. Kamigaito at TCRDL [162]. This work led to the preparation of the first exfoliated nylon 6 nanocomposite via in-situ polymerization of $\varepsilon$-caprolactam in which alkylammonium modified montmorillonite (MMT) was thoroughly dispersed in advance [163]. The resulting composite with a loading of only 4.7% wt of clay showed excellent properties. Nowadays these hybrid techniques have been successfully applied to various polymer systems, and other industrial applications have been developed, especially in the fields of automotive interior and exterior panels, barrier films for packaging and flame retardant plastics.

### 7.2.1 Structure and Properties of PLC

The commonly used layered silicates that are used for the preparation of PLS nanocomposites belong to the same general family of 2:1 layered phyllosilicates, whose most widely known members are talc and mica. Phyllosilicates are constituted of large irregular aggregates (0.1-10 $\mu$m in diameter) formed by primary particles (8-10 nm thick). These, in turn, are formed by five to ten high aspect ratio lamellae (of about 100-200 nm in diameter and 1 nm in thickness) associated by interlayer ions (figure 7.1). The crystal structure of each lamella [57, 164]

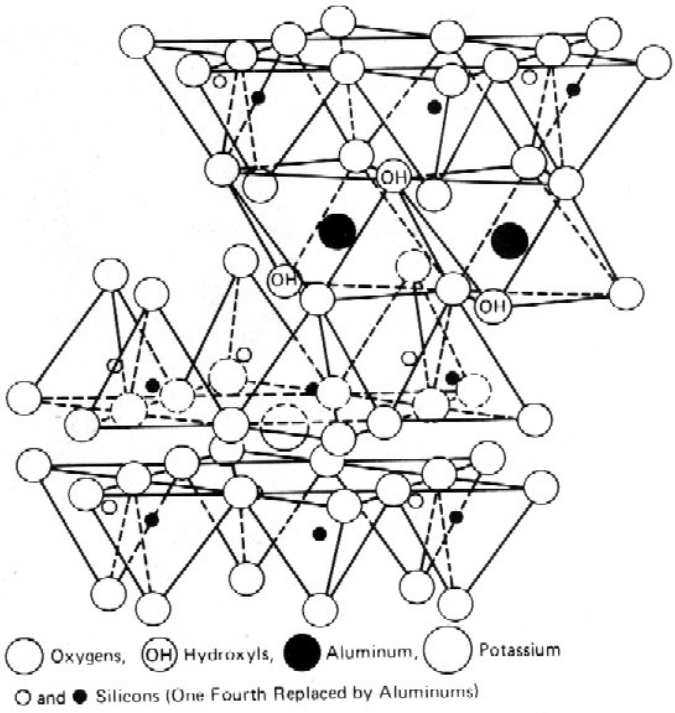


FIGURE 7.1: Schematic structure of a montmorillonite clay.

consists of two tetrahedrally coordinated silica sheets fused to an edge-shared octahedral sheet of either aluminium or magnesium hydroxide. The layer thickness is 0.1 nm and the lateral dimensions may vary from 30 nm to several microns or larger, depending on the particular layered silicate. Stacking of the layers leads to a regular Van der Waals gap between the layers called the interlayer region or gallery.

Isomorphic substitution within the layers (for example in montmorillonite $Al^{3+}$ is replaced by $Mg^{2+}$ or by $Fe^{2+}$, or in hectorite $Mg^{2+}$ replaced by $Li^{1+}$) generates negative charges that are counterbalanced by alkali and alkaline earth cations situated inside the galleries. Due to the high hydrophilicity of the clay, water molecules are usually also present between the layers. Layered silicates have two types of structure: tetrahedral-substituted and octahedral substituted. In the case of tetrahedrally substituted layered silicates, the negative charge is located on the surface of silicate layers, and hence the polymer matrices can interact more readily with these than with octahedrally-substituted material [164]. Montmorillonite, hectorite, and saponite are the most commonly used layered silicates since they are easily available from natural minerals. These types of layered silicates are characterized by a moderate surface charge, deriving from isomorphic substitution, known as the cation exchange capacity (CEC) and generally expressed as milliequivalent (meq) per 100 g ( meq/100 g). This charge is not locally constant, but varies from layer to layer, and must be considered as an average value over the whole crystal. CEC represents the maximum amount of cations that can be taken up by the clay. For instance, the CEC of montmorillonite varies from 80 to 150 meq/100 g.

### 7.2.2 Organically Modified Clays (Organoclays)

In order to render layered silicates more organophilic, and thus compatible with other polymer matrices, the normally hydrophilic silicate surface must be converted to organophilic, which makes the intercalation of many polymers possible. Generally, this can be done by ion-exchange reactions with cationic surfactants (organic modifiers). The first organic modifiers used in the synthesis of nanocomposites (nylon-6-clay hybrids at Toyota) were amino acids [165]. Other types of compatibilising agents have been used since then in the synthesis of nanocomposites. The most popular are primary, secondary, tertiary and quaternary alkyl-

phosphonium and especially alkyl-ammonium cations, because they can be exchanged easily with the ions situated between the layers. The role of organic cations in the organo-modified silicate (organoclay) is to lower the surface energy of the inorganic host and to improve the wetting characteristics of the polymer matrix. Additionally, alkyl-ammonium or alkyl-phosphonium cations can provide functional groups that can react with the polymer matrix or, in some cases, initiate the polymerization of monomers to improve the strength of the interface between the inorganic host and the polymeric matrix. The replacement of pristine inorganic cations by organic onium ions on the gallery surfaces of layered clays not only serves to match the clay surface polarity with the polarity of the polymer, but it also expands the clay galleries. This facilitates the penetration of the clay gallery space (intercalation) by polymers. Depending on the charge density of the clay (CEC) and on the chain length of the ionic surfactant, different arrangements of ions are possible [57]. In general, the longer the surfactant chain length and the higher the charge density of the clay, the further apart the clay layers will be forced [166]. In a given temperature range, the charge density of the clay and the chain length of the ions determine also the orientation of the ions [167].

The first ideas concerning the orientation of ion chains in organoclays were deduced from infrared and X-ray diffractometry measurements [167]. Later, a more detailed description was proposed by Vaia and Giannelis [168]. Based on Fourier transform infrared spectroscopy (FTIR) experiments, they found that alkyl chains can vary from liquid-like to solid-like, with the liquid-like structure dominating as the interlayer density or chain length decreases or as the temperature increases. This results from an increase in the gauche/trans conformer ratio. Besides playing a major role in determining the interlayer arrangement of the ions, the chain length of the organic modifier has a strong impact on the resulting structure of nanocomposites.

### 7.2.3 Structure of Polymer/Layered Silicate Nanocomposites

Depending on the nature of the components used (layered silicate, organic modifier and polymeric matrix) and on the method of preparation, different types of polymer/layered silicate nanocomposites [45] are thermodynamically achievable (Figure 7.2):

- Agglomerated nanocomposites: the polymeric matrix is not able to expand the distances between the iterlayer galleries, such that clusters are present within polymer that are commonly called tactoids.
- Intercalated nanocomposites: in this type of nanocomposites, the insertion of the polymer matrix into the layered silicate structure occurs in a crystallographically regular manner, regardless of polymer to organoclay ratio. Intercalated organoclay sheets are normally interlayered by a few molecular layers of extended polymer chains.
- Exfoliated nanocomposites: in an ideally exfoliated nanocomposite, the individual clay layers are completely and uniformly dispersed in a continuous polymer matrix by an average distance that depends on clay loading.

In an exfoliated nanocomposite the interlayer expansion is comparable to the radius of gyration of the polymer rather than to that of an extended chain as in the case of intercalated hybrids. Usually, the clay content of an exfoliated nanocomposite is much lower than that of an intercalated nanocomposite. The exfoliated configuration is of particular interest because it maximises the polymer-clay interactions, making the entire surface of the layers available to the polymer. When the polymer is unable to intercalate between the silicate sheets, a phase separated composite is obtained, whose properties stay in the same range as traditional microcomposites.

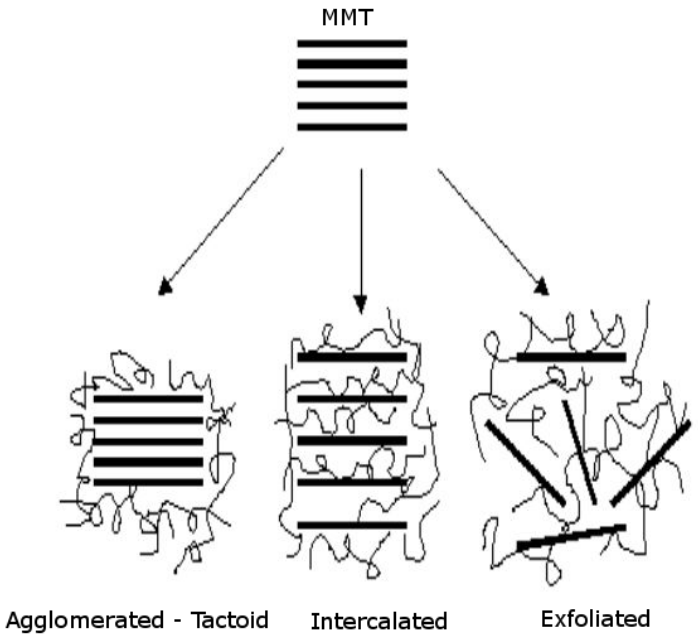


FIGURE 7.2: Schematic structure of a montmorillonite clay within a polymer.

### 7.2.4 Properties of Polymer/Layered Silicate Nanocomposites

Polymer/layered silicate nanocomposites often exhibit attractive improvement of material properties when compared with pure polymer or conventional composites (both micro and macro-composites). These improvements can include high moduli, increased strength and heat resistance, reduced solvent uptake, decreased gas and vapour permeability and reduced flammability ([169, 170, 171]). The main reason for the improved properties of nanocomposites is the interfacial interaction between the polymer matrix and organoclays compared with conventional composites. Layered silicates have layer thickness of the order of 1 nm and very high aspect ratios [57].

Although the mechanical, flame retardant, gas barrier properties etc have been widely studied, the same cannot be said for dielectric properties. Cao *et al.* [172] showed improved breakdown strength for polyamide loaded with alumina nanoparticles. It has been shown that nanofillers with proper orientation can act as bar-

rier. Gustavino *et al.* [173] studied EVA loaded with modified MMT and noticed a longer life time under high voltage application than the pure EVA. In a later study Gustavino *et al.* [174] observed changed tree propagation in EVA based nanocomposites and attributed this phenomenon to the presence of the nanofiller, which was acting as barriers. Lewis attributed the improved properties of such new classes of materials to the interface between the polymer and the filler [59]. Various theories concerning the role of the interface have been proposed, but the mechanisms by which charges move in a polymer nanocomposite remains unclear ([126, 175, 176]). Recently, Vaughan *et al.* [177] investigated the effect of MMT clay on structural properties in polyethylene and observed improved breakdown strength when the material was processed through extrusion. However, Green *et al.* [61] showed the presence of tactoids through TEM technique, although the material was processed through extrusion. One of the reason for this result could be attributed to the non polar nature of the polyethylene.

The purpose of this study is the fabrication of a nanocomposite based on a PE matrix. The intercalation and exfoliation of MMT is rather difficult in a pure PE blend, due to the non polar nature of the matrix and, therefore, the addition of EVA to the PE could result a strategic way to obtain a nanocomposite. Moreover, the previous chapter has shown that blends containing EVA9 and EVA18 are suitable for dielectric applications. Therefore, a study on the dispersion of two organo modified MMT in EVA9 and EVA18 is reported here.

## 7.3 Experimental

All the specimens were prepared via solution blending; the time for which the compounds were left in solution was varied from 10 min to 100 min. At first, all the specimens were prepared as shown in section 2.1. However, clay was observed at the bottom of the flask once the solution was poured out. Consequently, a series

of test was conducted on the clay using different solvents. An optimum solvent was identified in cholorobenzene. For that reason, the clay was dispersed in a 10 % solution of chlorobenezene with the aid of ultrasonication for 30 min before being added to the solution of polymer in xylene. The materials so produced were based on EVA9 and EVA18 and the two organomodified clays are I30P and I44PA, obtained from Nanocor (USA). Samples were dried in the vacuum oven overnight and disks of 500 $\mu$m thickness were prepared for X-ray scattering and disks 70 $\mu$m thick were prepared for breakdown testing.

## 7.4 Results and Discussion

### 7.4.1 X-Ray Scattering

All the samples were investigated using the Brucker D5005 diffractometer at the University of Trieste. WAXS patterns were recorded in the range of $Q$ = 1.4-7 nm$^{-1}$, where the scattering vector $Q$ is given by the Equation:

$$Q = \frac{2\pi}{d} = \frac{4\pi}{\lambda} sin\theta \tag{7.1}$$

where $d$ is the inter planar spacing, $\lambda$ is the X-ray wavelength and $\theta$ is the scattering angle.

Figure 7.3 shows diffraction patterns obtained from the I30P and I44PA clays and the relevant EVA9:MMT nanocomposites processed in solution for different times. The same X-ray data are presented in two different Figures in order to highlight the main differences in the scattering data. Figure 7.3(a) shows the diffraction peak of I30P at $Q$ = 3.1 nm$^{-1}$ which corresponds to the interlayer spacing of 2.02 nm, whilst the I44PA peak corresponds to 2.3 nm. From Figure 7.3(b), EVA9:I30P processed through solution blending for 10 min show little evidence of diffraction

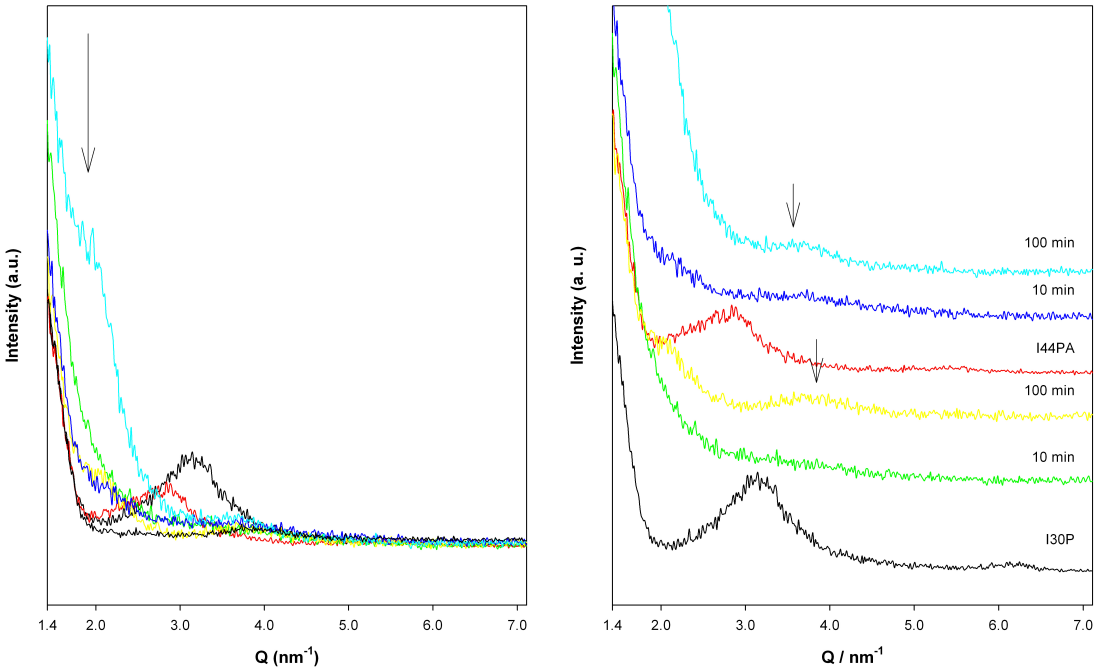


(a) WAXS on EVA9:MMT intercalation arrowed

(b) WAXS on EVA9:MMT: 2nd order peak after 100 min solution blending

FIGURE 7.3: WAXS data of EVA9 5 % wt o-MMT: From the bottom I30P and I44PA reference clay, respectively. EVA9:o-MMT processed for 10 min show no evidence of diffraction peaks, whilst same materials processed for 100 min show diffraction peaks at 3.8 $nm^{-1}$.

peak. However, a peak may can be observed in the range of $Q$ = 1.8-2 $nm^{-1}$ (green line). Increasing the time of solution blending to 100 min, EVA9:I30P still shows an intercalation peak at around $Q = 2$ $nm^{-1}$ and an additional second peak at $Q = 3.8$ $nm^{-1}$. EVA9:I44PA processed for 10 min may show an increase in the scattering at around 2 $nm^{-1}$, indicating intercalation with partial disorder of the clay. This result could indicate a potential exfoliation of the I44PA clay in the system after 10 min. However, Green *et al.* [61] correlated potential WAXS results with TEM images and concluded that this is not always the case. Increasing the solution blending time to 100 min, a peak is present at 2.8 $nm^1$ which could indicate some intercalation of EVA chains between the galleries of the MMT. However, an additional peak is present at 3.8 $nm^{-1}$. This peak corresponds to an interlayer distance of 1.7 nm. This secondary peak could derive from a fraction of clay that has not increase the distance of the galleries. Otherwise it could be consequence

of the solution blending process that washes out the surfactants from the galleries.

Figure 7.4 shows diffraction data obtained for the EVA18 based nanocomposites. As for the EVA9 diffraction patterns, the two MMT reference are shown ( black and red patterns). Figure 7.4(b) shows no or little presence of peaks at low Q values, therefore it can be concluded that the increase of VA content increase the disorder of the platelets. Chaudhary *et al.* [178] showed that the increase of polarity in EVA copolymers increase the intercalation of the clay and exfoliation is reached at 28 % of VA content. Moreover, De Souza *et al.* [179] reported that the VA content together with the mobility of the chain plays an important role in the dispersion of the MMT. The above result is also in agreement with the work of Morgan and Harris [180] on the preparation of polymer/clay nanocomposite via solution blending. These workers reported a higher intercalation/exfoliation of clay in polystyrene when accomplished with sonication. Whilst specimens prepared in solution for 10 min show no evidence of a diffraction peak, EVA9:I44PA processed for 100 min shows two broad peaks between 3.5 and 3.8 $nm^{-1}$, as shown in Figure 7.4(b) (arrowed). Acharya *et al.* [181] studied ethylene propylene diene terpolymer/EVA/MMT nanocomposite and also observed the presence of a peak relative to a distance of 1.7 nm, similar to our finding. Therefore, in both systems, the long residence time in solution induces a peak at higher $Q$. Different explanations could be given for the origin of these peaks. First of all, the presence of these peaks appear only after 100 min in solution. This finding suggests that the solution process has an influence on the ordering of the platelets of the two modified MMTs. However, the origin of the peaks could be a second order peak from some clay that forms tactoids. However, if this explanation seems reasonable, Figure 7.4(b) evidences that the EVA9:I44PA peak follows outside of the original I44PA scatter area. This could suggests that this peak does not correspond just to some I44PA tactoids but to some clay that lost part of the surfactant. Acharya *et al.* [181] suggested that expulsion of ions from the gallery leads to a collapse of the platelets

and gives rise to the peak at 1.7 nm. Filippi *et al.* [182] compared high density polyethylene loaded with a commercial clay prepared by melt-compounding and solution-blending. They found that the the MMT surfactant can be removed by the solvent and this was confirmed by X-ray diffraction with a decrease of the interlayer spacing. On the contrary, Kulia *et al.* [183] showed that exfoliation of an EVA nanocomposite is achievable only if a specific solvent is chosen. That is, the long residence time in solution can lead to a detachment of the surfactant from the clay. If this is the case, it is still not clear why the peak increase with increase of VA content. In summary, it can be conclude that 10 min solution blending with

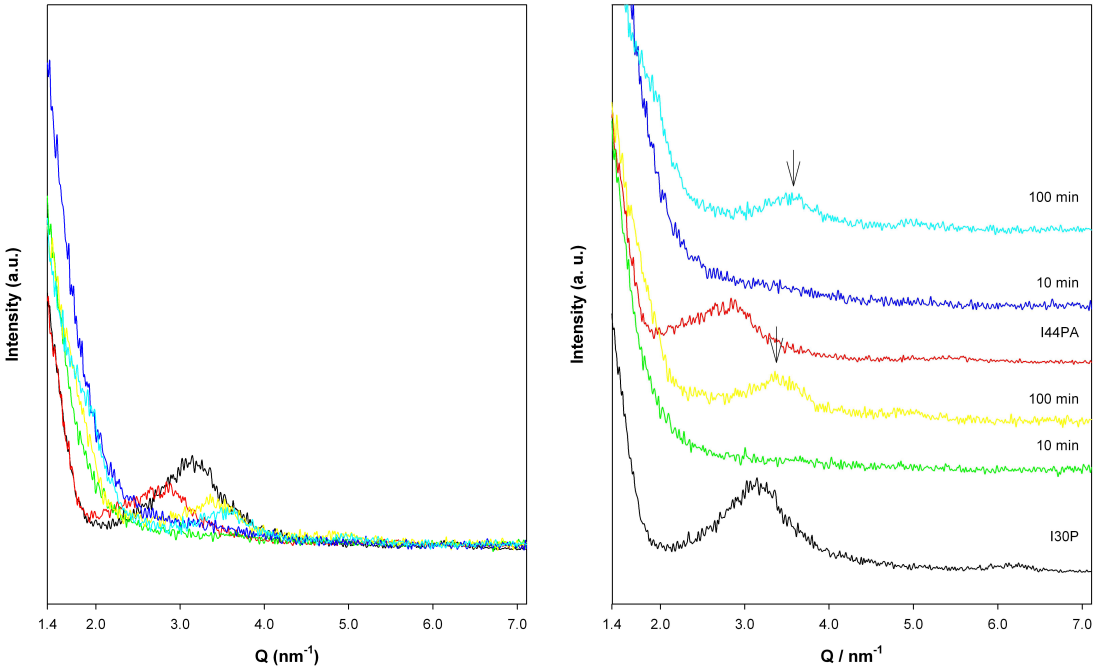


(a) WAXS on EVA18:MMT intercalation arrowed

(b) WAXS on EVA18:MMT: 2nd peak after 100 min solution blending

FIGURE 7.4: WAXS data of EVA18 5 % wt o-MMT: From the bottom I30P and I44PA reference clay, respectively. EVA18:o-MMT processed for 10 min show no evidence of diffraction peaks, whilst same materials processed for 100 min show diffraction peaks at 3 $nm^1$.

the aid of sonication can be a valuable way to increase the interlayer distances of the organomodified clays. However, the increase of solution processing seems to wash part of the surfactant out and therefore decreases the interlayer distance in at least a fraction of the clay. This conclusion is supported from other similar

results found in the literature ([181, 182, 184]).

## 7.5 Differential Scanning Calorimetry

Figure 7.5 shows melting traces obtained from quenched samples of EVA9 loaded with 5% wt of o-MMT. At the bottom, the EVA9 shows just one peak corresponding to the crystalline part of EVA9 at 95 °C. The same trend is seen in the case of EVA9 loaded with I30P and I44PA. The only difference is a slight depression

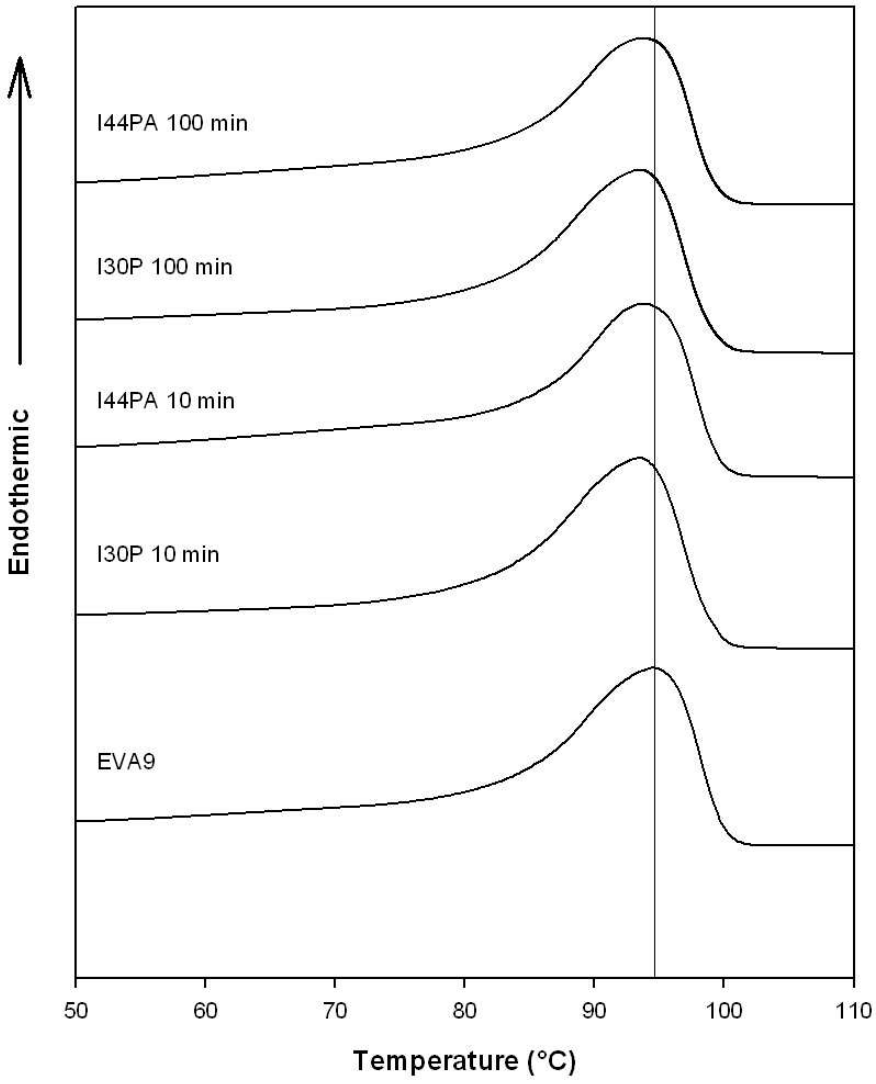


FIGURE 7.5: Melting traces of quenched EVA9, EVA9:I30P and EVA9:I44PA processed for 10 min and 100 min in solution blending.

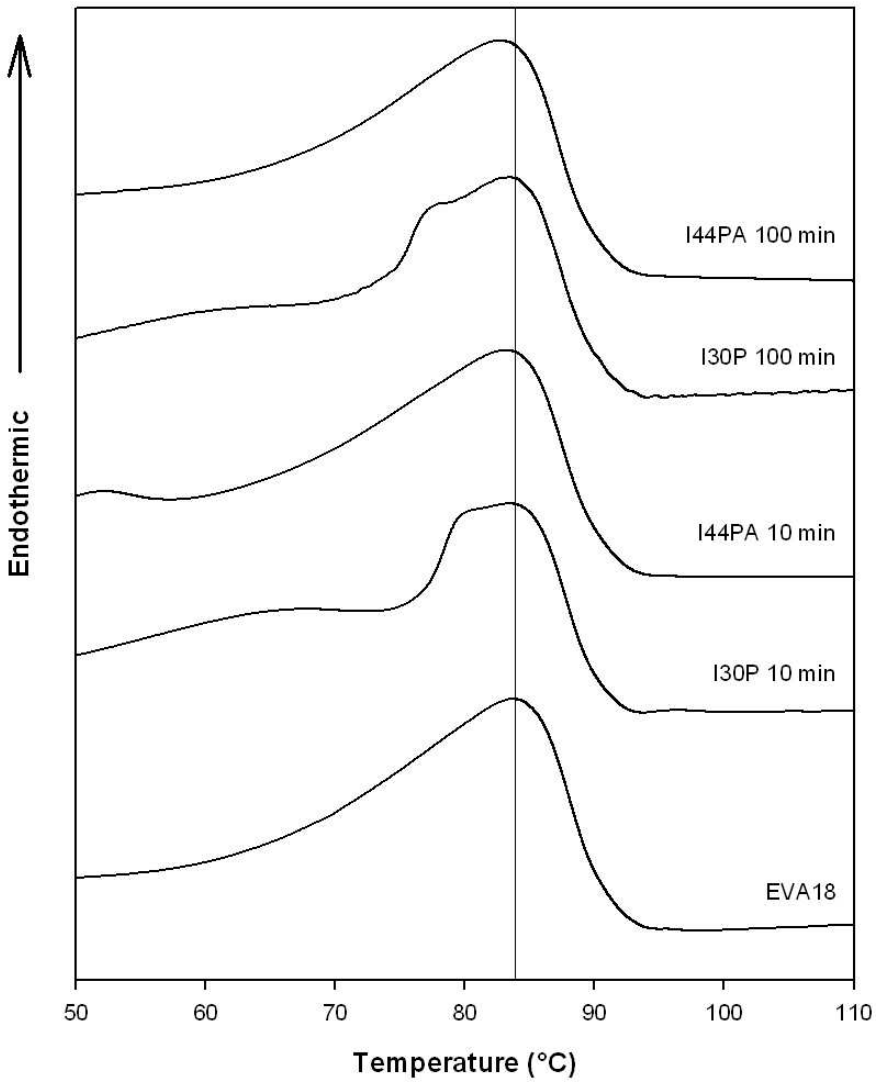


FIGURE 7.6: Melting traces of quenched EVA18, EVA18:I30P and EVA18:I44PA processed for 10 min and 100 min in solution blending.

of the peak, which is present in all the samples and which could be attributed to interactions between the EVA chains and the fillers. Figure 7.6 shows a different scenario from Figure 7.5. The EVA18 melting trace can be observed at the bottom of this figure with a melting peak at 84 °C. The addition of I30P gives rise to a secondary peak in the range of 77-80 °C. This peak could be attributed to some lamellar regions of different molecular weight. Increasing the solution melting time to 100 min, the same secondary peak on EVA18:I30P is observed. Vaughan *et al.* [177] observed an increase of $K_3$ in polyethylene/MMT nanocomposite and sug-

gested that the clay could act as a nucleation site for the polymer. Therefore, the increase in the secondary peak in EVA18:I30P could derive from some polymer chains that nucleate on the MMT. On the contrary EVA18:I44PA the EVA peak results similar to the unfilled EVA18.

### 7.5.1 Electrical Breakdown

Samples prepared in Specac press were degassed and then tested in the usual breakdown rig. Figure 7.7 shows Weibull plots of unfilled EVA9, compared with samples loaded with I30P processed through solution blending for 10 min and 100 min, respectively. A decrease in breakdown strength is noticed with the addition of the clay to the polymer. However, the processing time seems not to influence the breakdown. Figure 7.8 shows Weibull plots for the EVA9 samples loaded with I44PA and processed for 10 and 100 min in solution blending. In this case, the results from the various systems are largely indistinguishable from one another, indicating that the addition of I44PA seems not to affect the breakdown strength of the EVA9. These results suggest that the type of modified MMT and the time used to process it can both influence the breakdown behaviour of the final material. X-ray results show a less intense intercalation peak for EVA9:I44PA than EVA9:I30P, which could suggest that the increase in the disorder between the MMT layers play a key element in breakdown performance, as suggested by Vaughan [177]. EVA9 nanocomposites based on I30P seem to be affected by the solution blending time, which is related to different intercalation/exofoliation of the specimens.

However, Vaughan *at al* [177] observed a decrease in breakdown strength when the clay was poorly dispersed. This is in contrast with our results because presence of more ordered clay was observed when the specimens were processed for 100 min. The following table 7.1 summarises the $E_0$ and $\beta$ for all the EVA9. From these

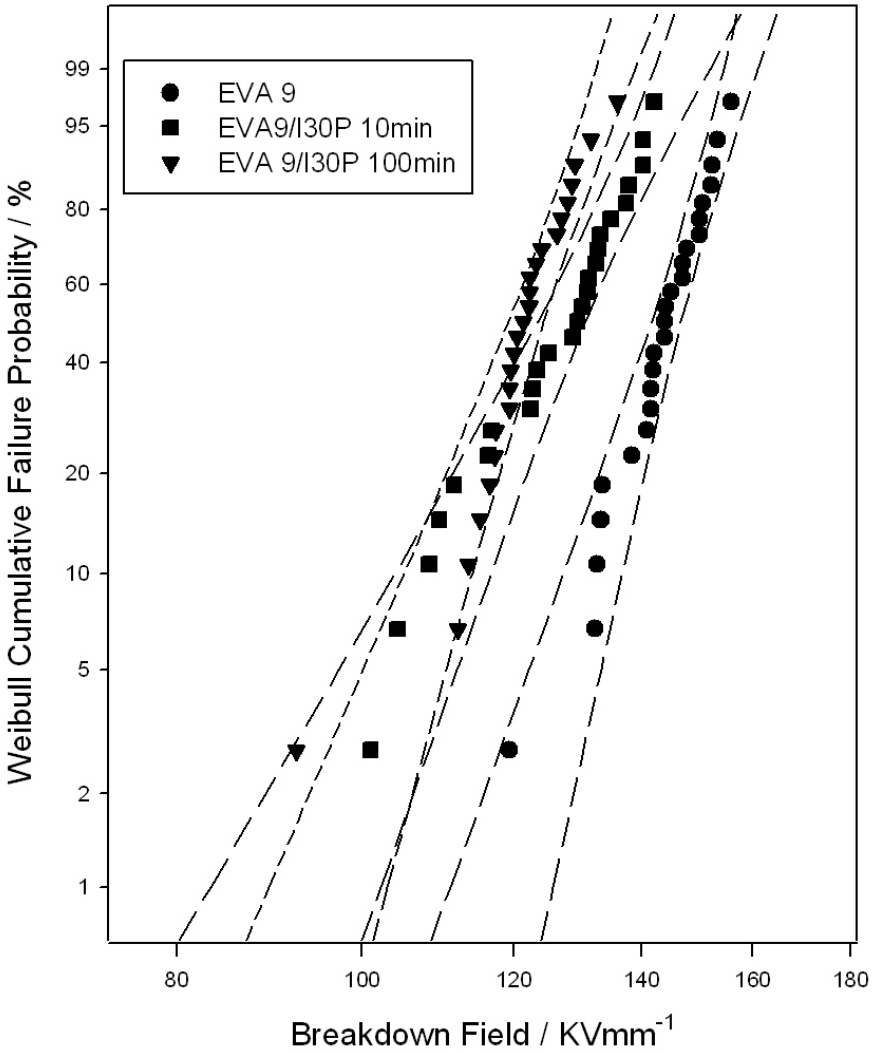


FIGURE 7.7: Breakdown strength of EVA9:I30P after 10 min and 100 min in solution.

TABLE 7.1: Weibull data derived from the plots of all the EVA9 nanocomposite systems

| **Materials** | $\beta$ | $E_0(kV/mm)$ |
|---|---|---|
| $EVA9$ | 22.45 | 146.8 ± 5 |
| $EVA9 : I30P$ 10 mins | 13.9 | 130.8 ± 3 |
| $EVA9 : I30P100mins$ | 18.6 | 124.4 ± 4 |
| $EVA9 : I44PA10mins$ | 16.32 | 142.36 ± 5 |
| $EVA9 : I44PA100mins$ | 15.2 | 151.59 ± 2 |

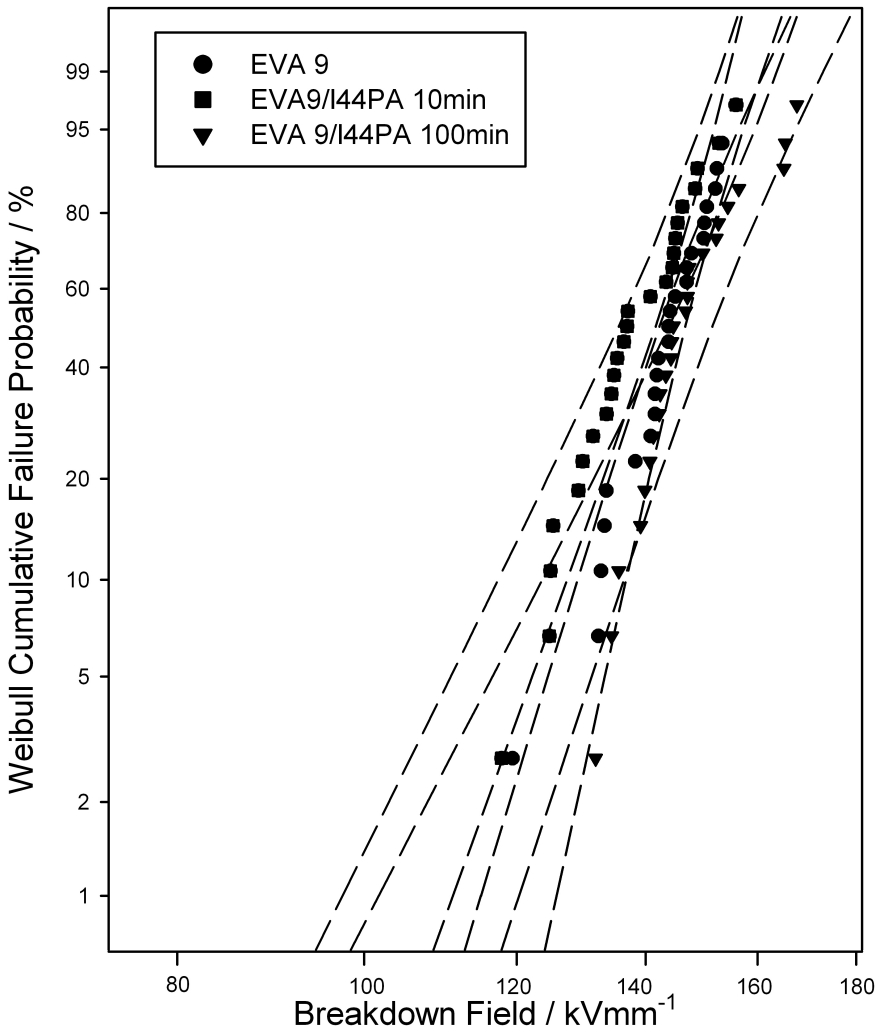


FIGURE 7.8: Breakdown strength of EVA9:I44PA after 10 min and 100 min in solution.

data, it can be seen that EVA9 loaded with I30P shows a decreases in breakdown strength from 146.8 kV for the unloaded material to the 124.4 kV for the loaded material that had been processed for 100 min. Conversely, specimens loaded with I44PA show similar breakdown strength within the uncertainties.

Figure 7.9 shows Weibull plots for samples EVA18 nanocomposites loaded with I30P. Although there are no real difference in breakdown strength, a trend can still be seen. In fact, only below 20 % of the cumulative failure probability the results are comparable. Above they can be treated as separate events. Therefore,

the introduction of I30P shows a decrease in the breakdown strength for samples processed in solution blending for 10 and 100 min. Figure 7.10 represents Weibull plots for the same EVA18 loaded with I44PA. In this case, EVA18:I44PA 10 min overlaps with the reference material, whilst EVA18:I44PA 100 min shows same decrease. Again, this could be attributed to the MMT aggregates seen from the X-ray and finds an agreement with other published works. [61, 177, 185].

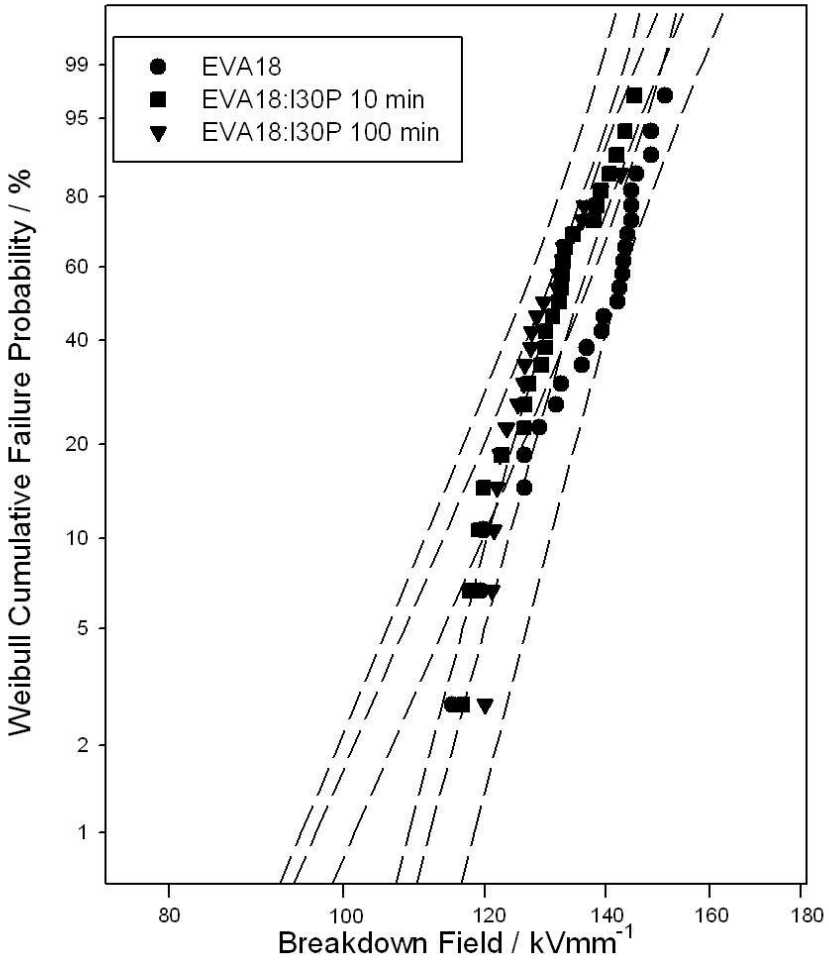


FIGURE 7.9: Breakdown strength of EVA18:I30P after 10 min and 100 min in solution.

Recently, Vaughan *et al.* [177] showed the effect of the processing method on the dispersion of the MMT and the effect on the breakdown characteristics. A noticeable decrease was observed in the case of the nanocomposite processed through solution blending. Table 7.2 shows the values for $E_0$ and $\beta$ of all the EVA18

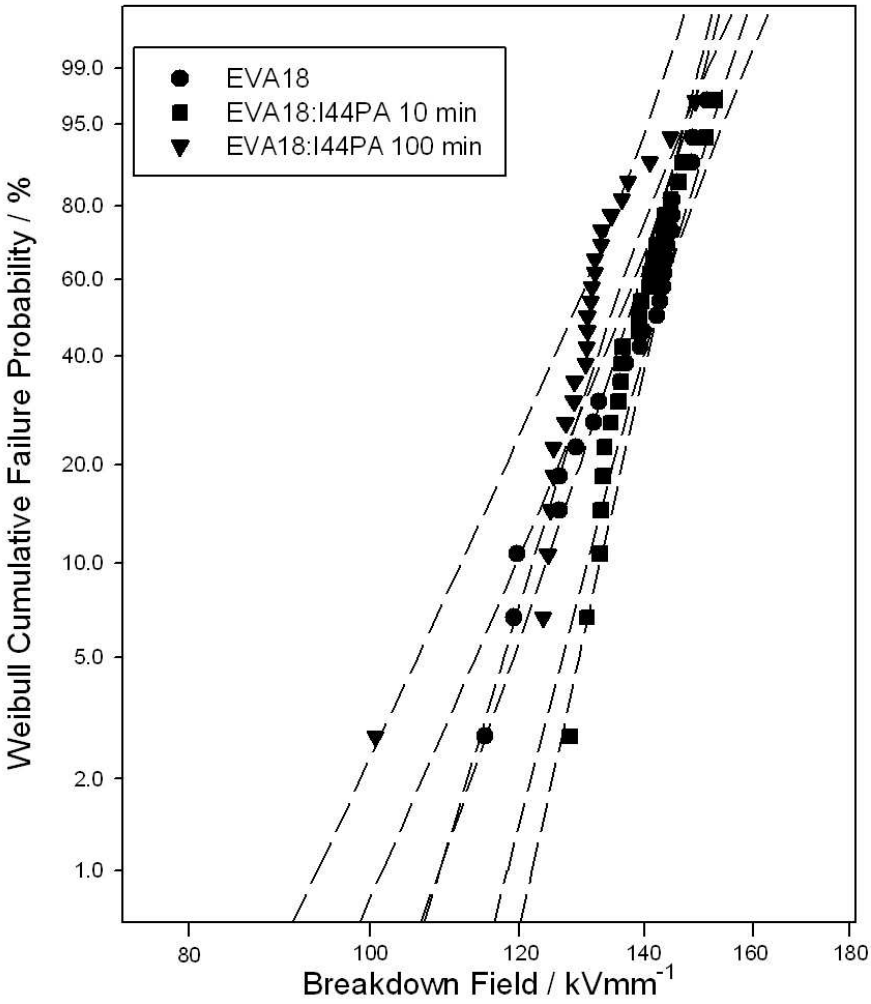


FIGURE 7.10: Breakdown strength of EVA18:I44PA after 10 min and 100 min in solution.

nanocomposites:

TABLE 7.2: Weibull data derived from the plots of all the EVA18 nanocomposite systems

| **Materials** | $\beta$ | $E_0(kV/mm)$ |
|---|---|---|
| $EVA18$ | 18.5 | 141.7 $\pm 4$ |
| $EVA18 : I30P10mins$ | 18.9 | 130.89 $\pm 5$ |
| $EVA18 : I30P100mins$ | 18.5 | 134.4 $\pm 3$ |
| $EVA18 : I44PA10mins$ | 22.8 | 142.15 $\pm 7$ |
| $EVA18 : I44PA100mins$ | 16.9 | 134.2 $\pm 5$ |

Comparing these results to the type of clay and the processing used, two major conclusions can be drawn. First, the processing of the materials through solution

blending can affect the interlayer galleries and play as a penalty in the intercalation/exfolation of the MMT with a relative polar copolymer as the ethylene vinyl acetate. However, the type of organomodified MMT can affect the dielectric properties of the materials. In fact, I44PA, a montmorillonite modified by displacing the sodium cation in the phyllosilicate by using a dimethyldialkyl ammoniumchloride, has shown a greater propensity for intercalation of both EVA9 and EVA18 which gives a comparable breakdown performance to that of the unfilled copolymer. However the I30P, a MMT organically modified with octadecylamine, give some decrease in the breakdown behaviour and this can be associated with the intercalation of the clay. Moreover, the long residence time in solution occurred the formation of tactoids which show to decrease the breakdown strength of the nanocomposites. This conclusion is supported by a previous study from Vaughan *et al.* [177], which investigated the breakdown strength of a polyethylene 5 % wt I30P processed through solution. They related the improvement of the breakdown strength to the structural ordering of the the polymer with the clay. More recently, Green *et al.* [61] reached a similar conclusion from the same material processed through extrusion.

## 7.6 Conclusion

The premises of this study was to investigate the intercalation of the two different organomodified MMT within ethylene vinyl acetates. Two relatively polar copolymers, EVA9 and EVA18, were chosen due to their dielectric properties in polyethylene blends shown in the previous chapter. The results shown here provide an indication of the intercalation that occurs in EVA/MMT nanocomposites, which was subsequently related to breakdown behaviour.

From these results it can be concluded that the EVA represents a potential material for the dispersion, intercalation and exfoliation of clay in the polymer matrix. The

EVA9:I30P nanocomposite showed a decrease the electrical properties ,whilst this was not the case for I44PA based nanocomposites. The X-ray scattering proved a shift in the clay peak from the organomodified clay to the EVA/MMT systems and confirmed the potential exfoliation of the clay in the matrix in the combined presence of ultrasound and short solution residence times. However, long residence times in the solvent appeared to result in surfactant being extracted from the two organomodified clays, such that the associated breakdown strengths were adversely affected by the presence of MMT clusters.

In conclusion, a relation between the chemical modification of the clay and the dispersion has been shown. This work is a first step for a polyethylene nanostructured dielectric.

# Chapter 8

# Conclusions

The aim of this thesis was to study the relationship between morphology and properties in the presence of polar additives of different nature. In Chapter 3, the morphology of a 20 % LPE : 80 % BPE blend was studied with the addition of DBS, a nucleation agent. It was found that the DBS forms a network of fibrils, when present above 1 % wt. SEM micrographs showed the nucleation of the PE blend perpendicular to the fibrils. When the DBS was present at 0.3 %, micrographs did not show direct evidence of the fibrils, but from Avrami analysis, a strong nucleation effect was evident. However, the nucleation effect of the DBS at all the concentrations was found to be temperature dependent. An abrupt decrease occurred in the range of 118-120 °C which, it was proposed, might be related to the ratio of polymer nuclei size and fibril size. Moreover, the nucleation of PE on DBS was studied through induction time analysis. A first approach suggested by Muchova and Lednický's theory was followed, but due to some of their assumptions, a new theory has been proposed. In this way, it was found that the DBS decreases the surface energy of the polyethylene crystals and therefore the nucleation of PE is favoured on the DBS. This study also showed a lower surface energy when the DBS is present in 0.3 % than 1-3 % and this finding has suggested that the nature of the DBS at low concentration may be different from

that at high concentrations. The relationship between the morphology and the space charge transport was examined in Chapter 4. Here, it was shown how the presence of a polar molecule can change the type of charge and the transport of it under an applied electric field. In particular, the addition of 0.3 % DBS has been revealed to be sufficient to improve the space charge transport with shallow traps, whilst the addition of more DBS created deep trap charges. From here it was clear that the amount of DBS plays an important role in charge transport, and that it can improve space charge characteristics.

In recent years the development of a new class of materials, polymer nanocomposites, has generated considerable interest in both the research and engineering fields. Although polymer nanocomposites have demonstrated improved many properties, some unsolved problem are still present. Among them, the dispersion of nanofiller in polyolefin can be difficult, due to the apolar nature of polymers, like polyethylene compared with the polar nature of the fillers. For this reason in Chapter 5 we studied the morphology of the 20 % LPE : 80 % BPE blend with the addition of a relatively polar EVA copolymer, as model for a future dispersion of organo modified MMT filler. The ratio between PE:EVA was varied together with the VA content. Two main conclusions were reached in this study. If the time in the melt is carefully chosen, a designed morphology can be achieved. Secondly, the phase separation of EVA in PE in form of droplets can be controlled choosing a relative low molecular weight of the EVA, as shown in the case of EVA40. In fact, in this particular case the dimension of the EVA droplets was significantly decreased from that seen in PE:EVA18, which had a higher molecular weight. This study was therefore a first potential step towards the fabrication of nanocomposites based on a non polar matrix and a low polar second phase, in order to maximise the exfoliation of the filler. In order to see if such blends mey be suitable for dielectric applications a further study of the breakdown behaviour of PE:EVA blends was conducted in Chapter 6. This work showed that the morphology of the blend

was not as important as the polarity of the EVA in determining the breakdown characteristics. In fact, a monotonic decrease of the breakdown behaviour was observed with increased VA content. Moreover, the breakdown characteristic were affected if water was present. However, the behaviour of the 80:20EVA40 blend was found to be independent from the water and it was suggested that, in this case, the morphology could play an important role. Therefore, the possibility of designing a polyethylene based nanocomposite through the presence of a relative polar EVA in the system has shown to be possible when the VA is present up to 18 % wt.

In chapter 7, a preliminary study was conducted with EVA based nanocomposite to determine if, in the presence of a filler, the dielectric properties of the nanocomposite would be affected. As seen from Chapter 6, the blends containing EVA40 showed the worst breakdown characteristics and, therefore, this copolymer was not studied further. Two relatively polar copolymers, EVA9 and EVA18, were processed by solution blending together with 5 % of o-MMT ( I30P and I44PA), and the time of solution blending was varied from 10 min to 100 min. X-ray scattering data showed intercalation in the case of EVA9 based nanocomposite and potential exfoliation for EVA18 based nanocomposite. However, the X-rays also showed the presence of an additional peak at higher $Q$ values when the materials were processed for 100 min. It was suggested that the solution blending could extract a fraction of the organo modified ions present between the MMT galleries, shrinking the clay spacing. If this suggestion is corrected, it was impossible to explain why the presence of the resulting tactoids did not affect the breakdown behaviour of these materials. The material preparation demonstrated to be important in the dispersion of the MMT in the polymer but a direct correlation with the dielectric properties was not obvious.

## 8.1 Future Works

The work presented in this thesis demonstrates that the morphology and dielectric properties of a polymeric material can be appropriately designed and controlled, even though the influence of factors such as the quantity and type of the filler, as well as the molecular weight of the copolymer need to be carefully assessed. The results obtained so far provide motivation for further investigations, some of which are briefly and outlined below. As shown in Chapter 3 the nature of the DBS is not clear, an issue which deserves more attention and experimental studies. The nucleation of ultrathin samples of PE:DBS could benefit from the use of AFM to elucidate its fundamental features. Space charge measurements suggested that the addition of DBS (0.3%) can represent an effective way to decrease the trapping of charges, but the effect of different crystallisation temperatures still needs to be investigated. Chapter 5 highlighted that different morphologies can be obtained by playing on just a small number of variables. Of particular interest was the finding that the molecular weight can play a major role in designing new blends. This can be considered to be part of a bigger project where EVA with the same VA content could be studied at various molecular weights, by applying the breakdown rig. Chapter 7 revealed some more interesting characteristics. It was found that the preparation method can influence the dispersion. A further study should thus investigate the same material prepared by extrusion, in order to see if the shear involved in such a process could increase the dispersion of the MMT. Finally, we aim at exploring the possibility of adding EVA:MMT to the PE blends in order to enhance the exfoliation of MMT in polyethylene blends via solution blending and extrusion and study the properties of the nanocomposite polymer as a model for a nanodielectric material.

# References


[1] F. Rodriguez. *Principles of Polymer Systems*. McGraw-Hill, 1985.

[2] G Natta, P. Pino, P. Corradini, F. Danusso, E. Mantica, G. Mazzanti, and G.i Moraglio. Crystalline high polymers of alfa-olefin. *J. Am. Chem. soc.*, 77:1708–1710, 1955.

[3] K. Ziegler. *Advanced in Organometallic Chemistry*, 6:1–17, 1968.

[4] K. Ziegler, E. Holzkamp, H. Breil, and H. Martin. *Angewandle Chemie*, 67: 426, 1955a.

[5] K. Ziegler, E. Holzkamp, H. Breil, and H. Martin. *Angewandle Chemie*, 67: 541–547, 1955b.

[6] R. J. Young and P.A. Lovell. *Introduction to Polymers*. Chapman & Hall, 1991.

[7] A. Keller. A note on single crystal in polymers: Evidence for a folded chain configuration. *Philosophical Magazine*, 2:1171–1175, 1957.

[8] U. W. Gedde. *Polymer Physics*. Kluwer Academic Publisher, 1995.

[9] I. L. Hosier. *Morphology and Electrical properties of Polyethyelene Blends*. PhD thesis, University of Reading, 1996.

[10] *Crystalline and Non Crystalline Solids Ch. 7*, volume 3. 1976.

[11] E.W. Fisher. Stufen- und spiralformiges kristallwachstum bei hochpolymeren. *Zeitschrift Naturforschung Teil A*, 12:753, 1957.

[12] P.H. Till. The growth of single crystal of linear polyethylene. *Journal of Polymer Science*, 24:301–306, 1957.

[13] P. J. flory. On the morphology of the crystalline state in polymers. *J. Am. Chem. Soc.*, 84:2857–2867, 1962.

[14] J. R. White. *Journal of Material Science*, 9:1860, 1974.

[15] A. S. Vaughan. The morphology of semicrystalline polymers. *Science Progress*, 76:1–65, 1992.

[16] D. C. Basset. *Principles of Polymer morphology.* Cambridge University Press, 1981.

[17] J. D. Hoffman and Jr. Lauritzen. Crystallisation of bulk polymers with chain folding: Theory of growth of lamellar spherulites. *J. Res. Natl Bur. Stand.*, 65A:297–336, 1961.

[18] J. D. Hoffman and R. Miller. Kinetics of crystallisation from the melt and chain folding in polyethylene fraction revisited: Theory and experiments. *Polymer*, 38:3151–3212, 1997.

[19] B. Wunderlich. Molecular nucleation and segregation. *Faraday Discuss. R. Chem. Soc.*, 68:239–243, 1979.

[20] D. M. Sadler and G. H. Gilmer. Selection of lamellar thickness in polymer crystal growth: a rate-theory model. *Phys. Rev.*, B38:2708–2711, 1988.

[21] J. L. Lauritzen and J. D. Hoffman. Extension of theory of growth of chain-folde polymer crystal to large undercoolings. *Journal of applied Physics*, 44: 4340–4352, 1973.

[22] M.L. Williams, R.F. Landel, and J.D. Ferry. The temperature dependence of relaxation mechanisms in amorphous polymers and other glass forming liquids. *Journal of American Chemical Society*, 77:3701–3707, 1955.

[23] J. J. Point, M. C. Colet, and M. Dosiere. Test of the validity of the classical kinetic theory of polymer crystallization. *Journal of Polymer Science Part B: Polymer Physics*, 28:1275–1281, 1990.

[24] M. Avrami. Kinetics of phase change. i general theory. *Journal of Chemical Physics*, 7:1103–1112, 1939.

[25] M. Avrami. Kinetics of phase change. ii transformation-time relations for random distribution of nuclei. *Journal of Chemical Physics*, 8:212–224, 1940.

[26] M. Avrami. Granulation, phase change, and microstructure kinetics of phase change. iii. *Journal of Chemical Physics*, 9:177–184, 1941.

[27] Morgan. The course of nucleation and crystallisation. *Phylosophical Transactions of the Royal Society of London, Serie A,*, 247:13–22, 1954.

[28] D. Grenier and R.E. PrudHomme. Avrami analysis: Three experimental limiting factor. *J. Polym. Sci., Polymer Physics*, 18:1655–1657, 1980.

[29] G. Greenway. PhD thesis, University of Reading, 2000.

[30] I. L. Hosier, A. S. Vaughan, and S. G. Swingler. Structure-property relationships in polyethylene blends: the effect of morphology on electrical breakdown strength. *Journal of Material Science*, 32:4523–4531, 1997.

[31] P.J. Barham, M. J. Hill, A. Keller, and C. A. Rosney. *Journal of Material Science Letter*, 7:1271–1275, 1988.

[32] J. Martinez-Salzar, M. Sanches Cuesta, and J. Plans. On phase separation in high- and low-density polyethylene blends. i: Melting-point depression analysis. *Polymer*, 32:2984–2988, 1991.

[33] J. H. Hildebrand. An improvement in the theory of regular solutions. *Proceedings of the National Academy of Sciences of the United States of America*, 76:6040–6041, 1979.

[34] P. J. Flory. Thermodynamics of high polymer solutions. *Journal of Chemical Physics*, 8:660, 1941.

[35] M. L. Huggins. Solution of long chain compound. *Journal of Chemial Physics*, 9:550, 1941.

[36] S. Krause. *Polymer Blends*. Accademic Press, New York, 1978.

[37] A. J. Ryan. Designer polymer blends. *Nature Materials*, 1:8–10, 2002.

[38] A. S. Vaughan and I. L. Hosier. The effect of dibenzylidene sorbitol on the crystallization behaviour of polyethylene. *Journal of Material Science*, 43: 2922–2928, 2008.

[39] M. Muller. Miscibility behavior and single chain properties in polymer blends: a bond fluctuation model study. *Macromolecular Theory Simulation*, 8:343374, 1999.

[40] L. Utracki. *Polymer Blends Handbook Vol. 1*. Kluwer Academic, 2002.

[41] C. P. Martin, A. S. Vaughan, and S. J. Sutton. Crystallization behavior of a propylene/ethylene copolymer: Nucleation and a clarifying additive. *Journal of Polymer Science: Part B: Polymer Physics*, 40:2178–2189, 2002.

[42] O. A. Serenko and V. S. Avinkin. Influence of an ethylene-vinyl acetate copolymer on the mechanical properties of a low-density polyethylene-rubber filler blend. *Polymer Science, Ser. A*, 43:129–133, 2001.

[43] T. Sterzynski, M. Lambla, H. Crozier, and M. Thomas. *Advanced Polymer Technology*, 13:25–36, 1994.

[44] M. Gahleitner, J. Wolfschwenger, C. Bachner, K. Bernreitner, and W. Neissl. Crystallinity and mechanical properties of pp-homopolymers as influenced by molecular structure and nucleation. *Journal of Applied Polymer Science*, 61:649–657, 1996.

[45] J. R. Ilzhoefer and R. J. Spontak. Effect of polymer composition on the morphology of self-assembled dibenzylidene sorbitol. *Langmuir*, 11:3288–3291, 1995.

[46] J M. Smith and Dimitris E. Kasoulis. Gelation of silicon fluids using 1,3:2,4-dibenzylidene sorbitol. *Journal of Material Chemistry*, 5:1899–1903, 1995.

[47] C. M. Nunez, J. K. Whitfield, D. J. Mercurio, J. R. Ilzhoefer, R. J. Spontak, , and S. A. Khan. Effect of molecular architecture on dbs-induced block copolymer gels: a rheological study. *Macromolecular Symposia*, 106:275–286, 1996.

[48] A. Thierry, B. Fillon, C. Straupe, B. Lotz, , and J. C.Wittmann. Polymer nucleating agents: efficiency scale and impact of physical gelation. *Progress of Colloid Polymer Science*, 87:28, 1992.

[49] T. Shepard, C. R. Delsorbo, R. M. Louth, J. L. Walborn, D. A. Norman, N. g. Harvey, and R. J. Spontak. Self-organization and pololefin nucleation efficacy of 1,3:2,4-di-*p*-methylbensylidene sorbitol. *Journal of Polymer Science: Part B: Polymer Physics*, 35:2617–2628, 1997.

[50] C. P. Martin. PhD thesis, University of Southampton, 2004.

[51] H. Beck. Heterogeneous nucleating agents for polypropylene crystallization. *Journal of Applied Polymer Science*, 11:673–685, 1967.

[52] J. C. Wittmann and B. Lotz. Epitaxial crystallization of aliphatic polyesters on trioxane and various aromatic hydrocarbons. *Journal of Polymer Science Polymer Physics*, 19:1853–1864, 1981.

[53] J. Siripitayananon, S. Wangsoub, R. H. Oleey, and G. R. Mitchell. The use of a low-molar-mass self-assembled template to direct the crystallisation of poly($\epsilon$-caprolactone). *Macromolecules Rapid Communication*, 25:1365–1370, 2004.

[54] C. Y. Kim, Y. C. Kim, and S. C. Kim. Crystallization characteristics of isotactic polypropylene with and without nucleating agents. *Polymer Engineering and Science*, 31:1009–1014, 1991.

[55] B. John, K. T. Varughese, Z. oommen, P. Potschke, and S. Thomas. Dynamic mechanical behavior of high density polyethylene/ethylene vinyl acetate copolymer blends: the effects of the blend ratio, reactive compatibilazation, and dynamic vulcanization. *Journal of Applied Polymer Science*, 87:2083–2099, 2003.

[56] B. Na, Q. Zhang, Q. Fun, G. Zhang, and K. Shen. Super polyolefin blends achived via dynamic packing injection molding: the morphology and the mechanical properties of hdpe/eva blends. *Polymer*, 43:7367–7376, 2002.

[57] M. Alexandre and A. Dubois. Polymer-layered silicate nanocomposites: preparation, properties and uses of a new class of materials. *Material science and Engineering*, 28(1-63), 2000.

[58] T. Tanaka, G. C. Montanari, and R. Mullhaupt. Polymer nanocomposites as dielectrics and electrical insulation: prespectives for processing technologies, material characterization and future application. *IEEE Trans. Diel. Electr. Insul.*, 11:763–784, 2004.

[59] T. J. Lewis. Interfaces: nanometric dielectrics. *Journal of Physics D-Applied Physiscs*, 38:202–212, 2005.

[60] J. K. Nelson and Y. Hu. Nanocomposite dielectrics - properties and implications. *Journal of Physics D-Applied Physiscs*, 38:213–222, 2005.

[61] C. D. Green, A. S. Vaughan, G. R. Mitchell, and T. Liu. Structure property relationships in polyethylene/montmorillonite nanodielectrics. *IEEE Transactions on Dielectrics and Electrical Insulation*, 15:134–143, 2008.

[62] G. P. Simon. *Polymer Characteristics Technology and Their Application to Blends*. American Publushing society, Oxford, 2003.

[63] L. L. Barrè. *Penetrant diffusion in polyethylene : the impact of water on the performance of novel XLPE cable designs*. Phd, University of Southampton, 2004.

[64] E. Hecht. *Optics*. San Francisco, 2002.

[65] A. M. Freedman, D. C. Basset, A. S. Vaughan, and R. H. Olley. On quantitive permanganic etching. *Polymer*, 27:1163–1543, 1986.

[66] R.H. Olley and D.C. Bassett. An improved permanganic etchant for polyolefines. *Polymer*, 23:1707–1710, 1982.

[67] M.M. Shahin, R.H. Olley, and M.J. Blissett. Refinement of etching techniques to reveal lamellar profiles in polyethylene banded spherulites. *Journal of Polymer Science Part B: Polymer Physics*, 37:2279–2286, 1999.

[68] A. S. Vaughan. *Polymer microscopy*. 1993.

[69] J.M. Huggett and H.F. Shaw. Field emission scanning electron microscopy a high-resolution technique for the study of clay minerals in sediments. *Clay Minerals*, 32:197–203, 1997.

[70] S. L. Flegler, J. W. Heckman, and K. L. Klomparens. *Scanning and Transmission Electron Microscopy, An Introduction*. W H Freeman and Co., New York, 1993.

[71] R. H. Olley, D. C. Bassett, A. S. Vaughan, V. A. A. Banks, P. B. McAllister, and S. M. Moody. Delineating water trees in cross-linked polyethylene: a new technique. *Journal of Material science*, 27:5192–5198, 1992.

[72] V. A. Bershtein and V. M. Egorov. *Differential Scanning Calorimetry of Polymers*. Ellis Horwood, 1994.

[73] Muchová and M. Lednicky. Investigation of heterogeneous nucleation using the induction time of crystallization: 1. theory of induction time. *Polymer*, 37:3031–3036, 1996.

[74] T. Kowalewski and A. J. Galeski. Influence of chalk and its surface treatment on crystallization of filled polypropylene. *Journal of Applied Polymer Science*, 32:2919–2934, 1986.

[75] A.S. Vaughan. Private communication.

[76] Muchová and M. Lednicky. Investigation of heterogeneous nucleation by the induction time of crystallization: 2. comparison of the theory and experimental measurement. *Polymer*, 37:3037–3043, 1996.

[77] M. Mucha, J. Marsalek, and A. Fidrych. Crystallization of isotactic polypropylene containing carbon black as a filler. *Polymer*, 41:4137–4142, 2000.

[78] J. D. Hoffman and J. J. Weeks. Melting process and the equilibrium melting temperature of polychlorotrifluoroethylene. *National Bureau of Standards-A. Physics and Chemistry*, 66A:13–28, 1962.

[79] J. T. Xu, F. X. Guan, T. Yasin, and Z. Q. Fan. Isothermal crystallization of metallocene-based polypropylenes with different isotacticity and regioregularity. *Journal of Applied Polymer Science*, 90:3215 – 3221, 2003.

[80] B.E. Warren. *X-ray Diffraction*. Dover Publication, 1990.

[81] H. C. Miller. *IEEE Transaction in Electrical Insulation*, 28:512, 1993.

[82] W. Weibull. A statistical distribution function of wide applicability. *Journal of Applied Mechanics - Transaction ASME*, 18:293–297, 1951.

[83] J. C. Fothergill and L. A. Dissado. *Space Charge in Dielectrics*. The Dielectric Society, 1998.

[84] *IEEE guide for the statistical analysis of electrical insulation voltage endurance data*. IEEE.

[85] C. Dang, J. Parpal, and J. Crine. Electrical aging of extruded dielectric cables: Review of existing theories and data. *IEEE Transaction Dielectrics and Electrical Insulation*, 3, 1996.

[86] C. Chauvet and C. Laurent. Weibull statistics in short-term dielectrics breakdown of thin polyethylene films. *IEEE Transaction Dielectrics and Electrical Insulation*, 28:18, 1993.

[87] M. Cacciari, G. Mazzanti, and G. C. Montanari. Comparison of maximum likehood method for the estimantion of the weibull parameters. *IEEE Transaction Dielectrics and Electrical Insulation*, 3:19, 1996.

[88] J. C. Fothergill. Estimating the cumulative probability of failure data points to be plotted on weibull and other probability paper. *IEEE Transaction Dielectrics and Electrical Insulation*, 25:489, 1990.

[89] R. Ross. Formulas to describe the bias and standard deviation of the ml-estimated weibull shape parameter. *IEEE Transaction Dielectrics and Electrical Insulation*, 1:247, 1994.

[90] G. C. Montanari, G. Mazzanti, M. Cacciari, and J.C. Fothergill. In search of convinient techniques for reducing bias in the estimation of weibull parameters for uncensored data. *IEEE Transaction Dielectrics and Electrical Insulation*, 4:307, 1997.

[91] T. Tanaka and T. Sakai. Measurement of electric field at a dielectric-electrode interface using an acoustic transducer techinique. *IEEE Transaction Dielectrics and Electrical Insulation*, 18:619–628, 1983.

[92] T. Maeno, T. Hoshino, T Funtami, and T. Takada. Application of ultrasonic techiniques to the measurement of spatial charge and electric field distribution in solid materials. *Electrical Engineering in Japan*, 109:58–64, 1990.

[93] M. fu, G. Chen, A. E. Davies, and J. Head. Space charge measurements in cables using the pea method - signal data processing consideration. In *IEEE International Conference on Solid Dieletrics*, pages 219–222, 2001.

[94] P. Terrech and R. G. Weiss. Low molecular mass gelator of organic liquids and the properties of their gels. *Chemical Review*, 97:3133–3159, 1997.

[95] S. Yamasaki and H. Tsutsumi. Microscopic studies of 1,3 : 2,4-di-*o*-benzylidene-d-sorbitol in ethylene glycol. *Bulletin of the Chemical Society of Japan*, 4:906–911, 1994.

[96] M. Watase and H. Itagoki. Thermal and rheological properties of physical gels formed from benzylidene-*d*-sorbitol derivatives. *Bulletin of the Chemical Society of Japan*, 71:1457–1466, 1998.

[97] D. J. Mercurio and R. J. Spontak. Morphological characteristics of 1,3:2,4-dibenzylidene sorbitol/poly(propylene glycol). *Journal of Physics Chemistry*, 105:2091–2098, 2001.

[98] E. A. Wilder, C. K. Hall, S. A. Khan, and R. J. Spontak. Effect of composition and matrix polarity on network development in organogels of poly(ethylene glycol. *Langmuir*, 19:6004–6013, 2003.

[99] S. Yamasaki, Y. Ohashi, H. Tsutsumi, and K. Tsujii. The aggregated higher-structure of 1,3 : 2,4-di-*o*-benzylidene-d-sorbitol in organic gels. *Bulletin of the Chemical Society of Japan*, 68:146–151, 1995.

[100] E. A. Wilder, R. J. Spontak, and C. Hall. The molecular structure and intermolecular interaction of 1,3:2,4-dibenzylidene-*d*-sorbitol. *Molecular Physics*, 101:3017–3027, 2003.

[101] A. Thierry, C. Straupé, B. Lotz, and J. C. Wittmann. Physical gelation: a path towards 'ideal' dispersion of additives in polymers. *Polymer Communications*, 31:229–301, 1990.

[102] A. Nogales, G. R. Mitchell, and A. S. Vaughan. Anisotropic crystallization in polypropylene induced by deformation of a nucleating agent network. *Macromolecules*, 36:4898–4906, 2003.

[103] M. Fahaländer, K. Fuchs, and C. J. Friedrich. Rheological properties of dibenzylidene sorbitol networks in poly(propylene oxide) matrices. *Journal of Rheology*, 44:1103–1119, 2000.

[104] D. J. Mercurio, A. K. Saad, and R. J. Spontak. Dynamic rheological behavior of dbs-induced poly(propylene glycol) physical gels. *Rheologica Acta*, 40:30–38, 2001.

[105] D. Mitra and A. Misra. Study on the agglomeration of nucleating agents in amorphous and semicrystalline polymer systems. *Polymer*, 29:1990–1994, 1988.

[106] M. Kristiansen, M. Werner, T. Tervoort, P. Smith, M. Blomenhofer, and H. W. Schmidt. The binary system isostactic polypropylene/bis(3,4-dimethylbenzylidene)sorbitol: Phase behavior, nucleation and optical properties. *Macromolecules*, 36:5150–5156, 2003.

[107] F. Silva, M. J. Sousa, and C. M. Pereira. Electrochemical study of aqueous-organic gel micro-interfaces. *Electrochimica Acta*, 42:3095–3103, 1997.

[108] A. Thierry, C. Straupé, J. C. Witmann, and B. Lotz. Organogelators and polymer crystallisation. *Macromolecular symposium*, 241:103–110, 2006.

[109] D. Patel an D.C. Bassett. On spherulitic crystallization and the morphology of melt-crystallized poly(4-methylpentene-1). *Proceedings Royal Society London*, 445:577–595, 1994.

[110] C. C. Puig. Enhanced crystallisation in branched polyethylenes when blended with linear polyethylene. *Polymer*, 42:6579–6585, 2001.

[111] I. L. Hosier, A. S. Vaughan, and S. G. Swingler. On the effects of morphology and molecular composition on the electrical strength of polyethylene blends. *Journal of Polymer Science: Part B: Polymer Physics*, 38:2309–22, 2000.

[112] C. Marco, G. Ellis, M. A. Gomez, and J. M. Arribas. Analysis of the isothermal crystallization of isotactic polypropylene nucleated with sorbitol derivates. *Journal of Applied Polymer Science*, 88:2261–2274, 2003.

[113] H. Marand, J. Xu, and S. Srinivas. Determination of the equilibrium melting temperature of polymer crystals: Linear and nonlinear hoffman-weeks extrapolations. *Macromolecules*, 31:82198229, 1998.

[114] Y. Zhao, A.S. Vaughan, S.J. Sutton, and S.G. Swingler. On the crystallization, morphology and physical properties of a clarified propylene/ethylene copolymer. *Polymer*, 42:6587–6597, 2001.

[115] C. Y. Kim, Y. C. Kim, and S. C. Kim. Temperature dependence of the nucleation effect of sorbitol derivatives on polypropylene crystallization. *Polymer Engineering and Science*, 33:1445–1451, 1993.

[116] J. Siripitayananon, S. Wangsoub, R. H. Olley, and G. R. Mitchell. The use of a low-molar-mass self-assembled template to direct the crystallisation of poly(-caprolactone). *Macromolecular Rapid Communications*, 25:1365–1370, 2004.

[117] A.J. Gresco and P.J. Philips. The role of epitaxy in the development of

morphology in carbon-fiber composites. *Journal of Advanced Materials*, 55: 51–60, 1994.

[118] A. Celli, E.D. Zanotto, and I. Avramov. Primary crystal nucleation and growth regime transition in isotactic polypropylene. *Journal of macromolecular science. Physics*, 42:387–401, 2003.

[119] H. Ishida and P. Bussi. Surface-induced crystallization in ultrahigh-modulus polyethyelene fiber reiforced polyethylene composites. *Macromolecules*, 24: 3569–3577, 1991.

[120] S.Ratner, P. Mona Moret, E. Wachtel, and G. Marom. New insights into lamellar twisting in transcrystalline polyethyelene. *Macromolecular Chemistry and Physics*, 206:1183–1189, 2005.

[121] K. Okada, K. Watanabe, I. Wataoka, A. Toda, S. Sasaki, K. Inoue, and M. Hikosaka. Size distribution and shape of nano-nucleus of polyethylene simultaneously determined by saxs. *Polymer*, 48:382–392, 2007.

[122] R. Greco, C. Mancarella, E. Martuscelli, and G. Ragosta. Polyolefin blends. ii. effect of epr composition on structure, morphology and mechanical properties of ipp/epr alloys. *Polymer*, 28:1929–1936, 1987.

[123] A. S. Vaughan, I. L. Hosier, S. J. Dodd, and S. J. Sutton. On the structure and chemistry of electrical trees in polyethylene. *Journal of Physics Publishing*, 39:962–978, 2006.

[124] R. Bartnikas. Performance characteristics of dielectrics in the presence of space charge. *IEEE Transactions on Dielectrics and Electrical Insulation*, 4: 544–557, 1997.

[125] G. Chen, T. Y. G. Tay, A. E. Davies, Y. Tanaka, and T. Takada. Electrodes and charge injection in low-density polyethylene-an experimental in-

vestigation using the pulsed electroacustic technique. *IEEE Transactions on Dielectrics and Electrical Insulation*, 8:867–873, 2001.

[126] Y. Tanaka, G. Chen, Y. Zhao, A. E. Davies, A. S. Vaughan, and T. Takada. Effect of additived on morphology and space charge accumulation in low density polyethylene. *IEEE Transactions on Dielectrics and Electrical Insulation*, 10:148–154, 2003.

[127] A. S. Vaughan, Y. Zhao, L. L. Barre, and S. J. Sutton. On additives, morphological evolution and dielectric breakdown in low density polyethylene. *European Polymer Journal*, 39:355–365, 2003.

[128] S. N. Kolesov. The influence of morphology on the electric strength of polymer insulation. *IEEE Transaction Electrical Insulation*, 15:81–86, 1980.

[129] L. Xiang, C. Yi, D. Qiangguo, Y. Yi, and T. Demin. Charge distribution and crystalline structure in polyethylene nucleated with sorbitol. *Journal of Applied Polymer Science*, 82:611–619, 2001.

[130] K. S. Suh, J. H. Koo, S H. Lee, J. K. Park, and T. Takada. Effects of sample preparation conditions and short chains on space charge formation in ldpe. *IEEE Transactions on Dielectrics and Electrical Insulation*, 10: 148–154, 2003.

[131] J. P. Jones, J. P. Llewellyn, and T. J. Lewis. The contribution of field-induced morphological change to the electrical aging and breakdown of polyethylene. *IEEE Transactions on Dielectrics and Electrical Insulation*, 12:951–966, 2005.

[132] J. Peon, J. F. Vega, B. D. Amo, and J. Martinez-Salazar. Phase morphology and melt viscoelastic properties in blends of ethylene/vinyl acetate copolymer and metallocene-catalysed linear polyethylene. *Polymer*, 44:2911–2918, 2003.

[133] M. Castro, C. Carrot, and F. Prochazka. Experimental and theoretical description of low frequency viscoelastic behaviour in immiscible polymer blends. *Polymer*, 45:4095–4104, 2004.

[134] M. Moan, J. Huitric, and P. Mederic. Rheological properties and reactive compatibilization of immiscible polymer blends. *Journal of Rheology*, 44: 1227–1245, 2000.

[135] H. A. Khonakdar, S. H. Jafari, A. Yavari, A. Asadinezhad, and U. Wagenknecht. Rheology, morphology and estimation of interfacial tension of LDPE/EVA and HDPE/EVA. *Polymer Bulletin*, 54:75–84, 2005.

[136] J. F. Palierne. Linear rheology of viscoelastic emulsions with interfacial tensionï¿. *Rheologica Acta*, 29:204–214, 1991.

[137] I. Ray and D. Khastgir. Correlation between morphology with dynamic mechanical, thermal, physicomechanical properties and electrical conductivity for EVA-LDPE blends. *Polymer*, 34:2030–2037, 1993.

[138] C. Li, Q. Kong, J. Zhao, Q. Fan, and Y. Xia. Crystallization of partially miscible linear low-density polyethylene/poly(ethylene-co-vinylacetate) blends. *Materials Letters*, 58:3613–3617, 2004.

[139] J. Peon, J. Vega, M. Aroca, and J. Martinez-Salazar. Rheological behaviour of LDPE/EVA-c blends: I. on the effect of vinyl acetate comonomer in EVA copolymers. *Polymer*, 42:8093–8101, 2001.

[140] I. L. Hosier, A. S. Vaughan, and W. Tseng. Effect of polyethylene on morphology and dielectric breakdown in EVA blends. In *IEEE 2007 International Conference on Solid Dielectrics (ICSD)*.

[141] D.C. Bassett and D. Patel. Isothermal lamellar thickening and the distribution of thermal stability in spherulitic isotactic poly(4-methylpentene-1). *Polymer*, 35:1855–1862, 1994.

[142] R. G. Alamo, J. D. Londono, L. Mandelkern, F. C. Stehling, and G. D. Wignall. Phase behavior of blends of linear and branched polyethylenes in the molten and solid states by small-angle neutron scattering. *MAcromolecules*, 27:411–417, 1994.

[143] G. Dreezen, M.H.J. Koch, H. Reynaers, and G. Groenickx. Miscible binary blends of poly(ethylene oxide) and an amorphous aromatic polyamide (aramide 34i): Crystallization, melting behavior and semi-crystalline morphology. *Polymer*, 40:6451–6463, 1999.

[144] N. Bulakh and J. P. Jog. Crystallization of poly(phenylenesulfide)/amorphous polyamide blends: DSC and microscopic studies. *Journal of Macromolecular Science - Physics B*, 38:277–287, 1999.

[145] C. Li, J. Zhao, and Q. Fan. Linear low-density polyethylene/poly(ethylene-ran-butene) elastomer blends: Miscibility and crystallization behavior. *Journal of Polymer Reasearch*, 11:323–331, 2004.

[146] M. L. Di Lorenzo. Spherulite growth rates in binary polymer blends. *Progress of Polymer Science*, 28:663–689, 2003.

[147] H. M. Shabana, R. H. Olley, D.C. Bassett, and B.-J. Jungnickel. Phase separation induced by crystallization in blends of polycaprolactone and polystyrene: an investigation y etching and electron microscopy. *Polymer*, 41:5513–5523, 2000.

[148] N. Okui and T. Kawai. Crystallization of ethylene/vinylacetate ramdom copolymer. *Die Makromolekulare Chemie*, 154:161–176, 1972.

[149] Y. Li and B.J. Jungnickel. The competition between crystallization and phase separation in polymer blends.2. small angle x-ray scattering stud-

ies on the crystalline morphology of poly($\varepsilon$-caprolactone) in its blends with polystyrene. *Polymer*, 34:9–15, 1993.

[150] M. Faker, M. K. Razavi Aghejeh, M. Ghaffari, and S. A. Seyyedi. Rheology, morphology and mechanical properties of polyethylene/ethylene vynil acetate copolymer (PE/EVA) blends. *European Polymer Journal*, 44:1834–1842, 2008.

[151] E. Martuscelli, M. Pracella, and Y. P. Wang. Influence of composition and molecular mass on the morphology, crystallization and melting behaviour of poly(ethylene oxide)/poly(methyl methacrylate) blends. *Polymer*, 1984.

[152] J. Wang, H. Zhang, F. Qiu, Z.G. Wang, and Y. Yang. Nucleation in binary polymer blends: Effects of adding diblock copolymer. *Journal of Chemical Physics*, 118:8997–9006, 2003.

[153] X. Zhang, X. Man, C. C. Han, and D. Yan. Nucleation induced by phase separation in the interface of polyolefin blend. *Polymer*, 49:2368–2372, 2008.

[154] Y. Ma, L. Zha, W. Hu, G. Reiter, and C. C. Han. Crystal nucleation enhanced at the diffuse interface of immiscible polymer blends. *Physical Review E*, 77:1–5, 2008.

[155] P Potschke and D. R. Paul. Formation of co-continuous structures in melt-mixed immiscible polymer blends. *Journal of Macromolecular Science Part C: Polymer Reviews*, 43:87141, 2003.

[156] C. Guoxiong and X. Jianfei. Breakdown properities of polyethylene-ethylene vinyl acetate copolymer composite under liquid nitrogen temperature. *Proceedings of the 3rd International Conference on Properties and Applications of Dielectric Materials*, pages 419–422, 1991.

[157] D.M. Tu, L. Kan, and K.C. Kao. Electric breakdown and space charge in ethylene vinyl acetate (EVA) incorporated polyethylene. *Proceedings of the*

*2nd International Conference on Properties and Applications of Dielectric Materials*, 2:598–601, 1988.

[158] J-H. Lee and M-K Han. A study of relationship between mechanical properties and watertreeing retardation in EVA blended XLPE. *Proceedings of the International Conference on Electrical Insulation and Dielectric Phenomena*, pages 638–643, 1992.

[159] Si-H Go, S.P. Kim, M.W. Seong, C.H. Lee, S.W. Lee, and J.W. Hong. A.c. dielectric strength due to the mixture ratio of LLDPE and EVA. *Proceedings of the 6th International Conference on Electrical Insulation and Dielectric Phenomena*, pages 911–914, 2000.

[160] S. Marais, Q.T. Nguyen, C. Devallencourt, M. Metayer, T.U. Nguyen, and P. Schaetzel. Permeation of water through polar and non polar polymers and copolymers: Determination of the concentration-dependent diffusion coefficient. *Journal of Polymer Science:Part B: Polymer Physics*, 38:1998–2008, 2000.

[161] R. Rhoton. *Particulate-filled Polymer Composites*. Rapra Technology Ltd, 2nd edition, 2003.

[162] M. Kawasumi. The discovery of polymer-clay hybrids. *Journal of Polymer Science. Part A: Polymer Chemistry*, 2004.

[163] A. Usuki, Y. Kojima, M. Kawasumi, A. Okada, Y. Fukushima, T. Kurauchi, and O. Kamigaito. *Journal of Materials Research*, 8:1179–1184, 1993.

[164] S. Sinha Ray and M. Okamoto. Polymer/layered silicate nanocomposites: a review from preparation to processing. *Progress in Polymer Science*, 28: 1539–1641, 2003.

[165] Y. Kojima, A. Usuki, M. Kawasumi, A. Okada, T. Kurauchi, and O. Kami-

gaito. One-pot synthesis of nylon 6-clay hybrid. *Journal of Polymer Science Part A: Polymer Chemistry*, 31:1755–1758, 1993.

[166] P. C. LeBaron, Z. Wang, and T. J. Pinnavaia. *Applied Clay Sience*, 1999.

[167] G. Lagaly. *Solid State Ionics*, 1986.

[168] A.R. Vaia, R.K. Teukolsky, and E.P. Giannelis. *Chemistry of Materials,*, 6: 1017–1022, 1994.

[169] M. Pramanik, S. K. Srivastava, B. K. Samantaray, and A. K. Bhowimick. Synthesis and characterization of organosoluble, thermoplastic elastomer/-clay nanocomposites. *Journal of Polymer Science: Part B: Polymer Physics*, 40:2065–2072, 2002.

[170] Y. Tian, H. Yu, S. Wu, and G. Ji. Study on the structure and properties of EVA/clay nanocomposites. *Journal of Materials Science*, 39:4301–4303, 2004.

[171] S. Pavlidou and C. D. Papaspyrides. A review on polymer-layered silicate nanocomposites. *Progress in Polymer Science*, 33:1119–1198, 2008.

[172] Y. Cao, P. C. Irwin, and K. Younsi. The future of nanodielectrics in the electrical power industry. *IEEE Transactions on Dielectrics and Electrical Insulation*, 11:797–807, 2004.

[173] F. Guastavino, G. Colettil, A.Dardanol, G.C. Montanari, F. Deorsola, M. Di Lorenzo, and Del Casale. Electrical treeing in EVA-layered silicate nanocomposites. *Annual Report Conference on Electrical Insulation and Dielectric Phenomena CEIDP*, 2005.

[174] F. Gustavino, A. Dardano, G. C. Montanari, F. Deorsola, and L. Testa. Electrical tree growth in eva-layered silicate nanocomposites. In *Conference on electrical Insulation and Dielectric Phenomena (CEIDP)*, 2006.

[175] T. J. Lewis. Nanometric dielectrics. *IEEE Transactions on Dielectrics and Electrical Insulation*, 1:812–825, 1994.

[176] R. J. Fleming, T. Pawlowski, A. Ammala, P.S. Casey, and K a. Lawerence. Electrical conductivity and space charge in ldpe containing TiO2 nanoparticles. *IEEE Transactions on Dielectrics and Electrical Insulation*, 12:743–753, 2005.

[177] A. S. Vaughan, S. G. Swingler, and Y. Zhang. Polyethylene nanodielecterics: the influence of nanoclays on structure formation and dielectric breakdown. *Transaction IEE Japan*, 126:1057–1063, 2006.

[178] D.S. Chaudhary, R. Prasad, R.K. Gupta, and S.N. Bhattacharya. Clay intercalation an influence on crystallinity of EVA-based clay nanocomposites. *Thermochimica Acta*, 31:187–195, 2005.

[179] C.M.G. De Souza and M.I.B. Tavares. High-resolution solid-state NMR and SEM study of the interaction behavior of poly(ethylene-co-vinyl acetate)/poly(vinyl acetate) blends. *Journal of Applied Polymer Science*, 86: 116–124, 2002.

[180] A.B. Morgan and J.D. Harris. Exfoliated polystyrene-clay nanocomposites synthesized by solvent blending with sonication. *Polymer*, 45:8695–8703, 2004.

[181] H. Acharya, S.K. Srivastava, and A.K. Bhowmick. Ethylene propylene diene terpolymer/ethylene vinyl acetate/layered silicate ternary nanocomposite by solution method. *Polymer Engineering and Science*, 46:837–846, 2006.

[182] Filippi, C. Marazzato, P. Magagnini, A. Famulari, P. Arosio, and S.V. Meille. Structure and morphology of HDPE-g-MA/organoclay nanocomposites: Effects of the preparation procedures. *Macromolecular Nanotechnology*, 44: 987–1002, 2008.

[183] Kulia, S.K. Srivastava, and A.K. Bhowmick. Rubber/ldh nanocomposites by solution blending. *Journal of Applied Polymer Science*, 111:635–641, 2008.

[184] M. Zanetti, G. Camino, R Thomann, and R Mulhaupt. Synthesis and thermal behaviour of layered silicate-eva nanocomposites. *Polymer*, 42:4501–4507, 2001.

[185] J. W. Wang, Q. D. Shen, C. Z. Yang, and Q. M. Zhang. High dielectric constant composite of P(VDF-TrFE) with grafted copper phthalocyanine oligomer. *Macromolecules*, 37:2294–2298, 2004.